UNIVERSITÀ DI PARMA

UNIVERSITÀ DEGLI STUDI DI PARMA

DOTTORATO DI RICERCA IN

"SCIENZE CHIMICHE"

CICLO XXXI

A bioinorganic approach to face two currently unsolved health issues: food poisoning and cancer

Coordinatore:

Chiar.mo Prof. Roberto Corradini

Tutore:

Chiar.mo Prof. Giorgio Pelosi

Dottoranda: Dott.ssa Marianna Pioli

Anni 2015/2018

Si ringraziano vivamente ***Fondazione Cariplo*** e ***Rotary Club Parma Est*** per aver cofinanziato rispettivamente la borsa di studio di dottorato (Progetto: Aflatox - "Un approccio biotecnologico per lo sviluppo di nuovi fitofarmaci antifungini per la tutela dell'ambiente e della salute umana" Rif. 2014-0555) e il periodo di studio presso l'Università di Warwick

&

“Il faut confronter des idées vagues avec des images claires"

Jean-Luc Godard

Table of contents:

1 Thiosemicarbazones

Thiosemicarbazones (TSs) are an extremely versatile class of compounds thanks to the variety of interesting physico-chemical properties they possess. Peculiar of most of these sulphur-containing organic molecules are the extensive electronic delocalisation and the presence of a thione-thiol tautomerism (*Figure 1*).

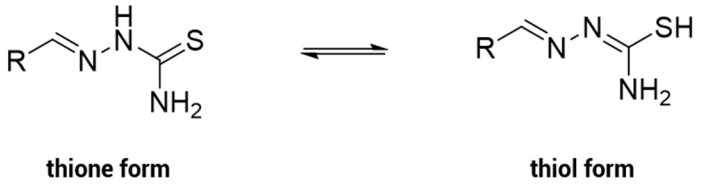

Figure 1: Thione-thiol tautomerism.

TSs are usually obtained from the condensation between the hydrazine group of a thiosemicarbazide with the carbonyl group of an aldehyde or ketone in protic solvents, like ethanol or methanol. One of the major assets of these compounds is the ease with which the TS structure can be modified, simply by using differentially substituted aldehydes (or ketones) or different aldehydes. The synthesis is usually fast, and the product is obtained usually in 12-24 hours. However, some reactions need a mild acidic catalysis especially when the carbonyl group is hindered by steric effects.
The most common nomenclature adopted to describe a TS structure follows a scheme in which every nitrogen is numbered as reported in *Figure 2*.

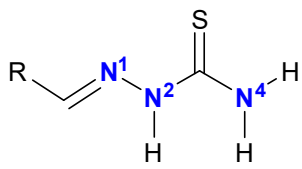

Figure 2: TS general structure.

Another crucial characteristic of TSs is the fact that they effectively act as bidentate ligands, using the sulphur and the iminic nitrogen, hence forming a 5-term coordination

ring. When the N^2 is not alkylated, TSs can also act as an anionic ligand through the deprotonation of the hydrazinic nitrogen (N^2). The TSs show high affinity to many different metals thanks to the presence of mixed hard-soft N-S donor atoms. Moreover, thanks to the N^2 deprotonation, TS's can also balance the positive charges of the metal. This electrostatic effect makes TSs very effective in chelating not only transition elements, but also alkaline and alkaline earth metals. Sulphur creates effectively metal-to-ligand charge-transfer (MLCT), an additional electrostatic stabilizing force for the final complex. The formation of a metal complex between a TS and a transition metal is usually indicated by a colour transition which can be explained by the well-known crystal field theory.

1.1 Applications

TSs (and their metal complexes) have been a very attractive class of molecules for many years and they found applications in many different fields. For example, the acetonethiosemicarbazone is commonly used in the plastic industry as "stopper" in the polyvinyl chloride polymerisation[1] and the Triapine® (3-aminopyridine-2-carboxaldehyde thiosemicarbazone) is a patented drug effective in the treatment of cancer which has successfully reached the phase II of clinical trials[2].

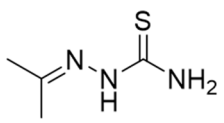

Acetonethiosemicarbazone

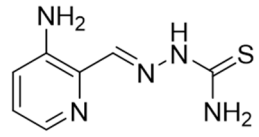

Triapine ®

Figure 3

TSs find also vast applications in analytical chemistry as sensing agents to detect metals in solution, acting as spectrophotometric or electrochemical indicators[3]. In particular, the most recent application explored in this field is the use of TS's as sensing agents to detect metals in food[4].

1.2 Aim of the thesis: thiosemicarbazones with biological properties

As mentioned in the previous paragraph, Triapine® showed promising anticancer ability, however it is not the only TS with interesting biological properties. Since their discovery in the 1950s, TSs have proven to be a very interesting bioactive agents, possessing antibacterial and antiviral activity[5,6], antifungal and anti-aflatoxigenic properties[7,8] and antitumor capacity[9].
In this thesis I focused my attention on two of these properties: anti-aflatoxigenic and anticancer effects.

1.2.1 Topic 1: antifungal and anti-aflatoxigenic properties

To our knowledge, the first example of TS designed and tested as antifungal agents was published by Benns et al. in 1960[10]. They evaluated the antifungal activity of a panel of fourty TSs and their copper complexes on *A. niger* and *Chaetomium globosum* cultures. The compounds were compared with two commercial fungicides: the 2,2'-dihydroxy-5,5'-dichlorodiphenylmethane and the copper/8-hydroxyquinolinolate mixture. The results were very interesting and showed that a few TSs resulted to be more effective than their corresponding copper complexes, indicating that the antifungal power was related not only to the presence of the metal ion but also to the TS molecule. The most effective compound was found to be the 9-undecenal thiosemicarbazone which showed an antifungal activity comparable with that of the standards used. Since this discovery, the research of TSs for antifungal purposes has grown rapidly and many other interesting TSs were identified. Their mechanism of action is still debated, some results ascribe the antifungal activity to the ability of TSs to modify the redox equilibrium in target cells acting both as anti-oxidant or ROS stimulating agents. Other studies revealed that TSs induce changes in sterol and membrane biosynthesis. In particular, it was reported that TSs can influence the regulation and biosynthesis of ergosterol, an essential vitamin for fungal cells strictly connected with the metabolism of lipids and membrane synthesis[11].

As mentioned before, TSs are very effective chelating agents for metal ions. In this context, the synthesis of TS metal complexes can be used to improve the TS antifungal and anti-aflatoxigenic effects through the optimisation of its chemical and physical properties, like water solubility, membrane crossing ability, bioavailability and uptake.

1.2.2 Topic 2: anticancer properties

The study of TS anticancer properties is probably the most addressed topic among those I reported. It is possible to find plenty of papers which describe the design, synthesis, characterisation and biological studies of TS derivatives. The very large amount of data available surely makes the TS very interesting, but, at the same time, all this information makes it difficult to extract from the literature general rules valid for the whole class of compounds. Moreover, many studies highlighted that TS activity in cells is often due to more than one target and that even small modification of the chemical scaffold can change dramatically the biological effect. Up to now, the main known effects related to the TS anticancer activity are, in order of discovery, ribonucleotide reductase inhibition[12], Reactive Oxygen Species production[13], topoisomerase II inhibition[14] and mitochondria disruption[15].

Ribonucleotide reductase inhibition

Ribonucleotide reductase (RNR) is an iron-dependent enzyme that promotes the reduction of ribose to deoxyribose. Since TSs have high formation constants for their metal complexes, many studies claim that these molecules might sequester iron and copper from the cell environment, leading to an inhibition of RNR. This would cause a block in the synthesis phase of the cell cycle and eventually bring the cell to death by apoptosis. The TS metal-sequestering effect in RNR have been reviewed by Yu and co-workers in 2011. They collected all the information available[16,17,18] and created a schematic summary of the effects of TS on thiol systems (*Figure 4*). The TS enters in cells and binds iron or copper, this binding raises the ROS level[15] which, as a cascade effect, decreases the GSH/GSSG (glutathione / oxidised glutathione) ratio and the GSH reductase (GR) activity, both fundamental steps in the prevention of oxidative stress in

cells. Moreover, the metal-sequestering decreases thioredoxin reductase (TrxR) levels, causing an increase in thioredoxin oxidation and then errors in the cell redox signalling system. Since GSH and Trx systems are crucial for the synthesis of deoxyribonucleotides (and then essential for the DNA synthesis), the RNR inhibition can induce errors in the DNA replication which usually lead to the arrest of the cell cycle and then to apoptosis.

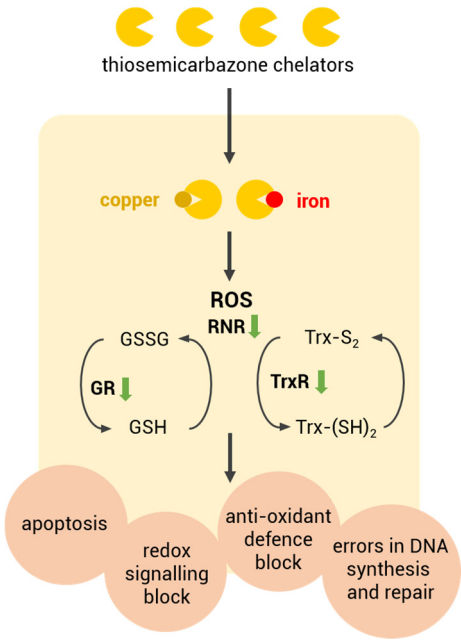

Figure 4: Scheme of the effect of TS on RNR.

Topoisomerase inhibition

The topoisomerases are a class of ubiquitous enzymes responsible for the regulation of the DNA supercoiling (the over- or under-winding of a DNA strand). They play a key role in many essential processes in which DNA is involved like its replication, its transcription and its recombination. Moreover, topoisomerase II is up-regulated in cancer cells, due to their higher proliferation rate, and this renders this enzyme a very interesting target. There are two classes of topoisomerases which differ for their catalytic mechanism. Topoisomerases I cut a single DNA strand of the double helix, whereas topoisomerases II cut both strands. In addition, topoisomerases II need the

hydrolysis of an ATP molecule to perform their function. Despite the differences, the two classes of topoisomerases have a similar molecular approach to cut the DNA strand. The oxygen of a tyrosine in the catalytic site binds the phosphate group of DNA inducing a break in the strand and the formation of a DNA-enzyme adduct. Many studies revealed that some TSs act as specific inhibitors of these enzymes and then they can stop the reproductive cell cycle inducing apoptosis in many different tumoral cell lines[19,20,21].

Reactive oxygen species production

The redox homeostasis in cell is crucial, for this reason compounds able to perturbate this condition appear attractive and promising for the development of new anticancer therapies. The ROS level in cancer cells is higher compared to normal cells due to oncogenic transformations which lead to a metabolic acceleration and to the loss of proper antioxidant control systems[22]. This higher level of oxidative stress and less mechanisms of control in tumour cells render them more sensitive to compounds able to induce oxidative stress. Many TS showed the ability to stimulate ROS production or to induce an even more significant down-regulation of the genes responsible for the antioxidant control. The complete destruction of the redox balance is considered a pro-apoptotic factor and therefore TSs with these characteristics are potentially very effective anticancer drugs[23]. Another effective method to increase the ability of TS to induce ROS in cells is the synthesis of TS metal complexes with redox active metals, such as copper, nickel and iron. These metals have redox potentials comparable with that we can find inside cells and therefore, after their uptake, they can easily induce redox reactions[24].

Mitochondria disruption

The ability to induce mitochondria disruption in cells is one of the latest mechanisms proposed to explain the great antiproliferative activity of some TSs. The evidence of mitochondrial damage came from the analysis of the mitochondrial potential prior to cell death which resulted reduced to zero. The ability to induce this effect is usually

related with the lipophilicity of the TS which can be effectively modulated using different bulky substituents[25]. The mitochondrial disruption leads to cell death because it stops cellular respiration and then all the metabolic pathways which ensure cell proliferation. In addition, a release of cytochrome c in the cytoplasm promotes the formation of the apoptosomes and this paves the way to apoptosis. Even if some tumour cells can live in hypoxia, mitochondrial damages are anyway considered pro-apoptotic and pro-necrotic factors responsible for the anti-proliferative activity.

TOPIC 1:

Anti-aflatoxigenic agents

2 Mycotoxins: a global threat

Filamentous fungi are ubiquitous species of mould able to grow and to contaminate almost every habitat. There are thousands of different genera known[26] and they usually occur in mixtures in which one or more genera dominate on the others depending on the environmental conditions. The presence of fungi is crucial to the functioning of natural ecosystems. They are fundamental, for instance, in the decomposition process of dead organic matter, which makes its chemical components available to living organisms. In addition, they are extremely important in plant nutrient uptake, absorbing nutrients from the soil and passing them to the plant roots.

However, some filamentous fungi are pathogens, especially for plants, since they damage cells and cause high level of stress to the host organism. Moreover, many species produce toxins that can be dangerous both for the plant and the surrounding organisms. These toxins, called mycotoxins, are secondary metabolites that are usually not essential for the fungal life and growth. In some case they can be produced in response to fungal stress or as signals, but their biological role is still not completely understood. What is certain is that mycotoxins are extremely hazardous substances for human and animal health.

To this day, more than 400 different mycotoxins have been identified and characterised[27], and most of them show severe effects on human health. It has been reported that mycotoxin exposure in the short term can lead to acute toxicity effects, mainly nephrotoxicity, hepatotoxicity and immunotoxicity[28]. In the long term, most of these substances are also mutagenic, teratogenic and carcinogenic.

Hazardous mycotoxins are produced chiefly by three different genera of filamentous fungi: *Aspergillus*, *Fusarium* and *Penicillium* which are unfortunately, the most widespread natural contaminants. They overrun and contaminate almost every agriculture and can be found in corn, wheat, rice, barley, rye and peanuts. They occur also in dried fruit, cocoa and coffee seeds, in spices, such as pepper and ginger, and in fruits and vegetables (i.e. grapes, apples, pears, carrots and tomatoes). As a consequence, high levels of mycotoxins can be detected also in meat and dairy products because mycotoxins remain unaltered during cooking and pasteurization due

to their high thermal stability, lasting long after the disappearance of the producer microorganism (*Figure 5*).

Figure 5: Schematic representation of aflatoxin contamination.

The spread of these moulds and the related mycotoxin contamination are a problem which is affecting the entire world community. Many countries are introducing increasingly stringent regulations on mycotoxin levels in food and feed with focus on mycotoxins with verified carcinogenic and genotoxic effect (i.e. Aflatoxin B_1). To ensure food and feed safety, the European Commission, through the EFSA (European Food Safety Authority), has established and constantly updates a guideline concerning the risk of the mycotoxin presence in foodstuffs. In addition, the official Journal of the European Union published in 2006 the regulation number 1881 which contains maximum levels for each contaminant in food matrices (updated and extended in reg. n. 1126/2007 and n. 565/2008).

Almost all the European countries released laws perfectly in agreement with the European guideline, but the situation is different in other parts of the world. However, the United States, India and China usually have adopted limits up to 15 times higher than Europe. Several Asian and African countries still have vague guidelines, with no distinctions between mycotoxin types and some other countries have no regulation at all[29]. These differences between nations are a significant problem for international trading and the import-export of foodstuffs is becoming more and more complicated.

On the other hand, due to these regulations, developing countries are often unable to export their products and this politics contribute to the raise of discrepancy between the economies. In addition, countries with lower restrictions have usually less control of storage conditions and cultivation practices with the results of higher level of food contamination and cases of mycotoxin related diseases are frequent and epidemic. For example, Kenya had continual aflatoxicosis epidemics between 1981 and 2008.[30]

However, these problems are not just localised in underdeveloped countries, they are a global threat. The FAO (Food and Agriculture Organization) recently estimated that about 25% of the world's foodstuffs are contaminated by mycotoxins, and that the number of foodstuffs subjected to contamination is increasing constantly[31]. In addition, mycotoxins are dangerous for the health, but also for the economy. In 2016, an extensive study estimated that every year the losses to the US corn industry due to the aflatoxin contamination are several tens of millions USD. These losses can even exceed 1 billion USD during years with warm summers and drought[32].

Considering all the above-mentioned facts, we can certainly affirm that mycotoxins are a dramatic threat to the global future and that all the countries should realise the importance of the development of new and reliable strategies to study, analyse and fight against mycotoxins spread.

2.1 Current strategies for the analysis and the control of mycotoxin contamination

Fungal growth and mycotoxin production are related to many different physical, chemical and biological factors. The most important are the climatic conditions in the areas of production, the agronomic techniques used to grow plants and the methods of harvest, storage and conservation of the foodstuffs. Therefore, raw materials are subject to contamination throughout all the production cycle, from the field to the final processing.

The first step to tackle the problem of mycotoxin spread is their detection and quantification. Many analytical techniques are applied to monitor foodstuffs and to quantify mycotoxin levels in food. The “bright greenish yellow fluorescence" (BGYF) is

the easiest and fastest method used. This technique is widely applied in the United States and consists in the analysis of a sample of the harvested matrix with a UV-lamp (365 nm). Most of the mycotoxins currently known emits at this wavelength and a sample can be considered positive when a fluorescence emission is recorded. Once that a sample results positive, it is analysed using more sophisticated analytical techniques. The High Pressure/Performance Liquid Chromatography (HPLC) is useful to separate and to characterise mycotoxins mixtures. In fact, using the hundreds of HPLC methods reported in literature is possible to detect almost every kind of toxins. Other widely used approaches are based on enzymatic tests, like the Rapid Immune Assay (RIA) or the *Enzyme-Linked ImmunoSorbent Assay* (ELISA). These assays are commonly used to detect and quantify specific mycotoxins in complex mixtures. They are usually expensive, but easy to use and extremely reliable. Once a contamination is detected, it is necessary to eliminate the associated risk. To do this there are several strategies currently used and we reported some of the newest and most effective ones[33] (*Table 1*).

Pre-harvest	Post-harvest
Enhancing host resistance	**Physical methods**
• Genetic engineering methods (transgenic or genetically modified crops)	• Improved storage and transportation (e.g. reduced humidity and temperature)
Altering growing environment	• Sorting to remove damaged kernels
• Good agronomic practices (e.g. hybrid choice, tillage, planting date, irrigation, crop rotation)	**Chemical methods**
• Biocontrol	• Use of antioxidants
• Chemical control (insecticides, fungicides)	• Food additives to bind or adsorb aflatoxins (e.g. clays)

Table 1: summary of the strategies for the analysis and the control of mycotoxin contamination.

The pre-harvest (or "in-field") contamination has the strongest impact on the final safety of a food product. In this period plants are exposed to natural events which can influence their contamination dramatically and often in an unpredictable way. In the

last decades, the most used approaches can be basically divided in two main categories: techniques to enhance host resistance and techniques to create an antifungal environment around the host. The first category is basically focused on the use of genetic engineering to induce the expression of RNA molecules in plants to silence genes expressed by pests and pathogens[34]. This approach is very effective and already applied with success to limit insects[35] and parasites infections[36]. Nevertheless, the European legislation forbids the use of genetically modified species and for this reason this biotechnological approach is limited to the United States.

Another strategy to avoid pre-harvest contamination is to develop methods for preventing the fungal growth on plants. Three different approaches are currently the most applied: the biocontrol using safe and competitive microflora, the use of pesticides, and the crop rotation.

An example of biocontrol is the development of fungal species which keep at bay phytophagous insects from plants. These insects promote fungal infection of plantations since they damage external integuments of kernels and, acting as spore vectors, facilitate the colonization by fungi. A possible solution consists in the use of non-toxigenic fungal strains which in turn act as biological competitors for the native and toxic species[37]. This approach is widely used in the United States, but, once again, not allowed in Europe, since the introduction and transplantation of non-indigenous species is prohibited in all the EU area. For this reason, the European research is mainly focused on the isolation and characterisation of local strains with the same bio-competitive properties[38].

Another pre-harvest strategy is the use of fungicides which is usually the easiest and cheapest approach. Nevertheless, this is often not effective in ensuring adequate protection against several types of mycotoxin, because toxic metabolites sometimes persist even after the disappearance of the moulds. It was even reported that the use of fungistatic compounds in some cases can increase mycotoxin production and this happens because the high stress condition induced by the fungicide can stimulate a strong mycotoxin production in the last part of the mould life[39].

The other crucial step in the foodstuff contamination is the post-harvest period. The prevention of the contamination during the storage, especially for cereals, is usually done by drying products to minimise the grain damage and to keep moisture levels

lower than those required to support mould (less than 15%). This is necessary to prevent further growth of fungal species that may be present on fresh grains[40].

Nowadays, the research is focused on the development of new techniques based on biocompatible and sustainable materials, with low environmental impact, cheap and easy to handle.

In these last few years, one of the most followed research lines has been the use of natural antioxidant additives able to inhibit the mycotoxin biosynthesis. In many studies it was reported that high levels of oxidative stress are strictly connected with the activation of many mycotoxin biosynthetic pathways. The use of antioxidant compounds resulted in many cases an effective strategy to limit toxin production.

For example, the *Lentinula edodes* (an edible mushroom native to East Asia) showed great ability in stimulating antioxidant mechanism in many different toxigenic moulds with significant reduction of mycotoxin production[41,42]. Moreover, the addition of *L. edodes* extract in *Aspergillus flavus* culture medium induces up-regulation of some anti-oxidant enzymes (Superoxide Dismutase (SOD), Catalase (CAT) and Glutathione Peroxidase (GPX) and the down-regulation of the gene expression related with the activation of the aflatoxin biosynthesis[43]. Some other natural derivatives showed great activity in inhibiting mycotoxin production. Caffeic acid, for example, can reduce aflatoxin production in *A. flavus* up to 95% without interfering with fungal growth[44]. Resveratrol, a stilbene produced by berries and grapes, resulted effective thanks to its anti-oxidant action through a strong inhibition of lipoxygenases (LOXs), enzymes involved in inflammatory response and related with the activation of many mycotoxin production enzymatic pathways. In particular, it seemed able to significantly inhibit the biosynthesis of ochratoxin A (OTA) in *A. ochraceus* e *P. viridicatum*[45]. Many of these natural extracts are very effective, however they are usually very difficult and expensive to prepare on a large-scale.

A different strategy is the use of mycotoxin adsorbents, food additives able to incorporate mycotoxins and to prevent their transition from the intestines walls in to blood system. These adsorbents are usually porous alluminosilicates called clays. The most studied is the HSCAS (Hydrated Sodium Calcium AluminoSilicate), a phyllosilicate clay that tightly binds aflatoxins in aqueous solutions[46,47]. It was reported that HSCAS alleviates aflatoxicosis in farm animals by reducing significantly the urinary aflatoxin

M_1 output if administered simultaneously with aflatoxin B_1[48]. Nevertheless, the applicability of adsorbents should be augmented by *in-vivo* experiments designed to demonstrate their safety for humans and animals.

2.2 Aspergillus flavus

First described by Link in 1809, *Aspergillus flavus* is a ubiquitous fungal eukaryote which acts as a pathogen for animals and plants. It is also widely studied because of its ability of producing aflatoxins and for causing aspergillosis in humans, animals and insects[49]. Its mycotoxins are responsible for the contamination of many economically important crops, such as maize and peanuts. *A. flavus* grow mostly in tepid climates located in the middle latitudes with an optimal temperature range of 28°C and 37°C [50].
Toxigenic species are spread mainly in Sub-Saharan Africa and South-East Asia where the climate is always warm and humid. In these areas *A. flavus* spores are omnipresent and human exposition to aflatoxin is chronic[51].Therefore, the presence of an *A. flavus* in every step of the agricultural food chain was revealed also in Europe.
In the South-Europe countries summer weather is extremely similar with the Asian one and this led to some massive contaminations of maize plantations. In 2003, the summer in Italy was particularly warm, the temperatures raised up to 40°C and the levels of mycotoxin detected in the maize used to feed animals were up to 10 times higher than the normal ones. This contamination led to a peak of aflatoxin M_1 in the milk produced by cows fed with contaminated maize derivatives. This emergency was so relevant that required the intervention of the Italian Ministry of Health which released specific measures to be taken to tackle the problem[52,53]. This was not the only event recorded in the past few years: the constant raise of temperatures due to the global warming, is causing an increasing number of these events in every part of the Europe and North America.

2.2.1 *A. flavus* biology

In nature, *A. flavus* colonises nutrient sources. It is a saprophyte and it usually grows on dead plants and animal tissues in the soil. Its appearance differs depending on the host species and climate condition.
For most part of its life the fungus appears as a mycelium (*Figure 6* - A): a mass of branching threads called hyphae (*Figure 6* - B). These hyphae absorb nutrients from the environment and bring them to the core of the mycelium.

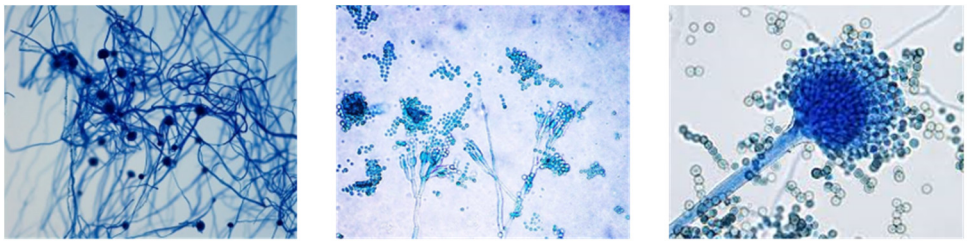

Figure 6: Pictures of A. flavus microscopic morphology.

Below 20°C the fungus enters a vegetative state and the mycelium evolves producing more resistant structures called sclerotia. When the climate becomes more favourable, sclerotia germinate to produce additional hyphae or conidia (asexual spores) (*Figure 6* - C), which can be dispersed in the soil and air using insects as unintentional carriers. Once the spores lie on a new substrate, they germinate again starting a new infection[54].
In cultures, *A.flavus* grows as yellow-green colonies with a diameter range of 65-70 mm and the Czapek's agar with the addition of yeast (CYA) is its optimal growth medium[55].

2.3 Aflatoxins

Aflatoxins became worldwide famous in 1960 due to the "Turkey-X disease", a severe aflatoxin intoxication of turkey farms in England. More than 100,000 turkeys died after consuming feed containing Brazilian peanuts contaminated with *A.flavus*. This

epidemic led to the discovery of the aflatoxin B_1 structure and biological dangerousness. After this outbreak, this topic became very popular and many other aflatoxins were discovered. Fourteen different aflatoxins have been discovered since 1960, but only five are nowadays considered the most harmful due to their high toxicity and diffusion (B_1, B_2, G_1, G_2 e M_1 - *Figure 7*).

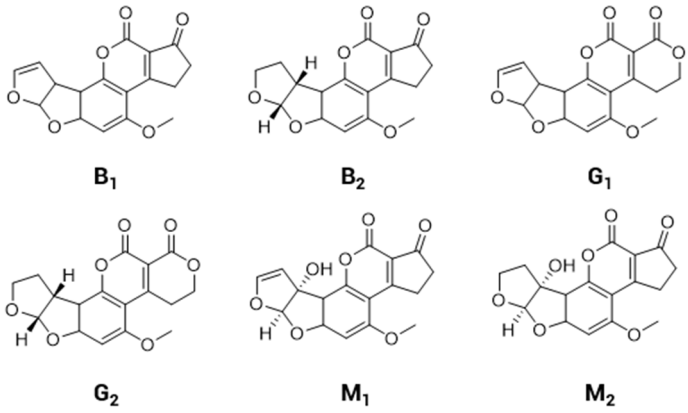

Figure 7: Most common and harmful aflatoxins.

Aflatoxins classification is based on their emission colour if irradiated with a 365 nm light (B = blue and G = green). Aflatoxins are also divided in class 1 or 2 depending on their mobility in TLC (Thin Layer Chromatography). Another interesting class (called M) indicates aflatoxins which contaminate milk. M_1 is the metabolite of aflatoxin B_1 found in humans and animals breast milk, whereas M_2 is the result of the metabolism of aflatoxin B_2 found in milk of cattle fed with contaminated foods.

Aflatoxins are a class of polyketides with low molecular weight (< 350 $g \cdot mol^{-1}$) and characterised by high melting and decomposition temperature (> 250 °C). The molecular structure is composed by a coumarin core fused with a double furane and a pentanone (in B_1, B_2, M_1 and M_2) or a lactone (in G_1, G_2).

Once ingested, aflatoxins are metabolised mostly in liver and kidneys by oxidases and other microsomal enzymes. The metabolites derived from this process are usually conjugated with glucuronic acid and excreted through urine or faeces. The aflatoxin toxicity is both acute and chronic. The acute toxicity is usually connected with tissue lesions (especially in the liver) and immune system suppression[56]. A collection of some

LD_{50} values (lethal dose which cause the death of the 50% of a test animal group) for aflatoxin B_1 exposure are reported in *Table 2* [57].

Animal	LD_{50} (mg/kg)	Zone of liver lesion
Duckling	0.335	Periportal
Rabbit	~0.3	Midzonal
Cat	0.55	Periportal
Pig	0.62	Centrilobular
Dog	~1.0	Centrilobular
Guinea pig	1.4	Centrilobular
Rat		
Neonate	0.56	Diffuse
Weanling	5.5	Periportal
Weanling	7.4	Periportal
100 gm	7.2	Periportal
150 gm	17.9	Periportal
Mouse	~9.0	
Hamster	10.2	

Table 2: LD_{50} values for aflatoxin B_1 exposure.

The chronic effects are mutagenicity and carcinogenicity and teratogenicity. Alfatoxins B1, G1 and M1 are classified carcinogenic to humans (Group 1) by IARC (International Agency for Research on Cancer).

The B_1 is the most harmful due to the *in-vivo* formation of an exo-8,9-epoxide in the terminal furane ring. This epoxide is extremely reactive, it creates covalent bonds with nucleic acids and induces DNA hydrolysis[58] which are considered the first step in the development of several different tumours (liver, lungs, kidneys, and colons)[59].

Interactions between aflatoxin B_1 and DNA

Aflatoxin B_1 needs to be metabolised to become toxic. The harmful species is created when B_1 interacts with cytochromes P450, an enzyme cluster able to mono-oxidise drugs and other lipophilic xenobiotics like aflatoxins. These enzymes are expressed in every tissue, mainly in liver, lungs and intestine. The reaction between B_1 and P450 is on the double bond of the furane to produce the B_1-exo-8,9-epoxide. This epoxide is extremely reactive and immediately interact with nucleophilic sites of proteins and nucleic acids. The key step in the cytotoxic process seems to be the DNA alkylation in the N^7-Guanine position (*Figure 8*). Moreover, at high pH values the B_1-N^7-Guanine adduct breaks the N^7-C^8 double bond with the formation of the B_1-FAPY. The irreparable DNA damage caused by B_1 interferes with the mechanism of the replicative or translesion polymerases causing primarily G→T mutations and other additional mutation processes which end with the onset of cancer[60].

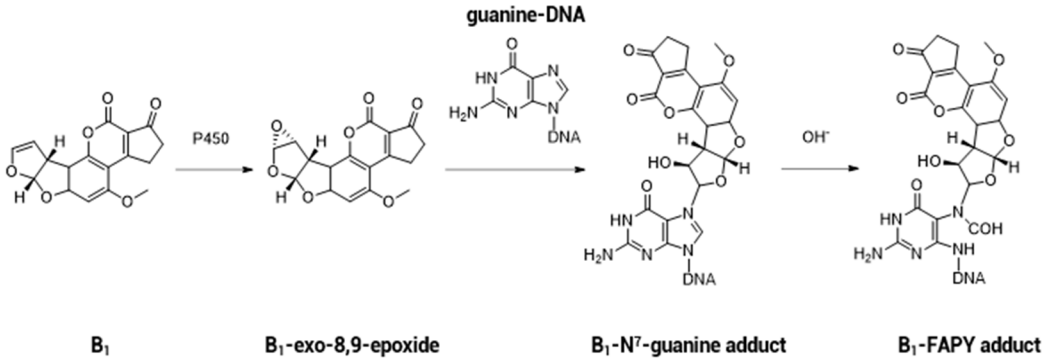

Figure 8: DNA alkylation induced by aflatoxin B_1.

2.4 Aflatoxin biosynthesis

The aflatoxin biosynthesis is a long and complex sequence of enzymatic processes. The biosynthetic pathway starts from Malonyl-CoA which is subsequently transformed into 15 different intermediates before the synthesis of the final toxin. A scheme of the entire aflatoxin bio-synthetic pathway is reported below (*Figure 9*).

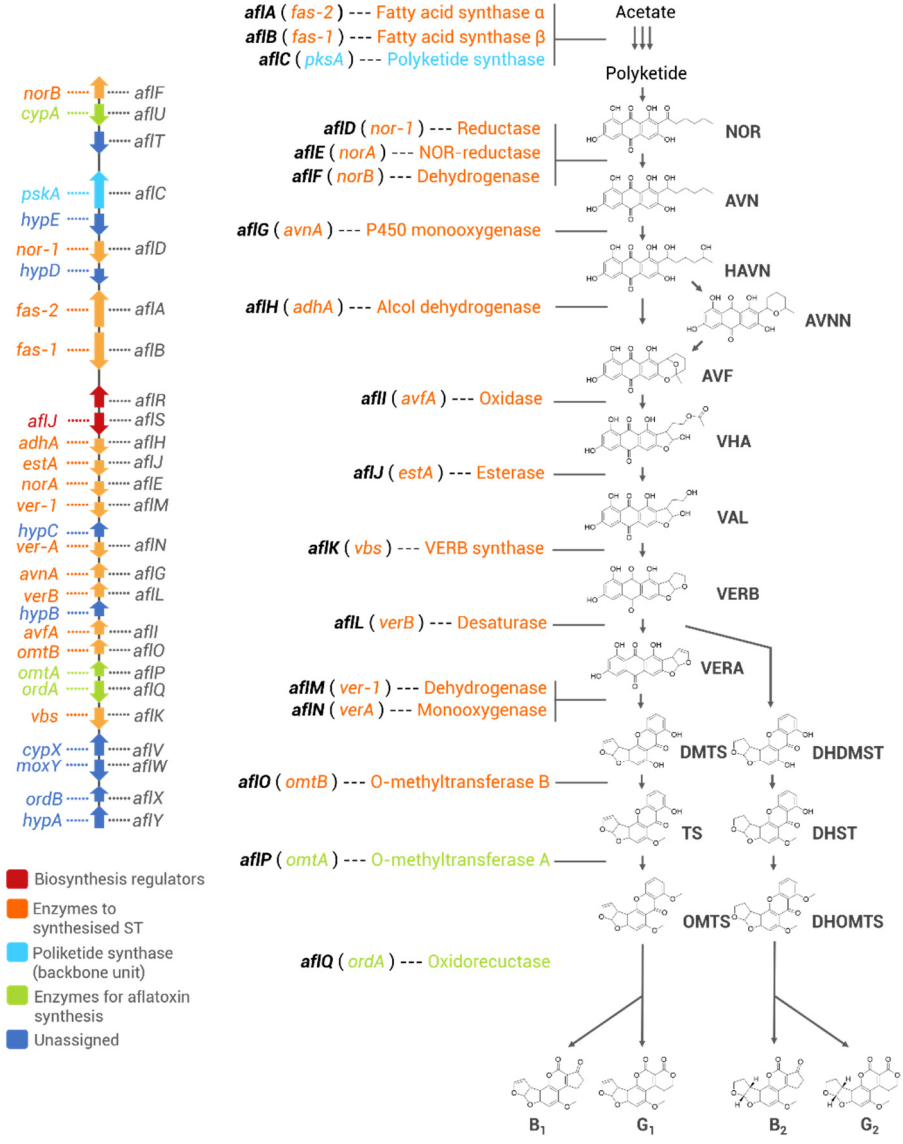

Figure 9: Aflatoxin biosynthetic pathway.

The genes involved in the biosynthetic pathway are organised in a cluster in the telomeric end of the chromosome 3. The contains 25 open reading frames (ORFs) and it is similar in every aflatoxigenic species of *Aspergillus*.

The majority of the 27 proteins produced are monooxigenases, a class of proteins responsible for selective oxidation of substrates. This monooxigenase activity is a key process in a synthesis like that of the aflatoxin production which requires a series of oxidations and cyclisations of palmitate (a C_{16} aliphatic chain). Biochemical precursors of aflatoxin are less toxic than the final products. However, they start to show toxicity already in the first steps of the pathway. Starting from norsolorinic acid (NOR) the mutagenicity increases almost directly with the metabolic proximity to the final toxin as reported in *Table 3* [61] (ames TEST on Salmonella typhimurium).

Intermediate	**mutagenicity ratio relative to B_1**
palmitate	-
NOR (norsolorinic acid)	$3.6 \cdot 10^{-7}$
AVN (averantin)	$6.2 \cdot 10^{-4}$
AVF (averufin)	$7.1 \cdot 10^{-7}$
VERA (versicolorin A)	$1.8 \cdot 10^{-2}$
TS (sterigmatocystin)	0.54

Table 3: mutagenicity of the intermediates of aflatoxin biosynthesis.

2.5 Thiosemicarbazones as antifungal agents

To our knowledge, the first example of TS designed and tested as antifungal agents was published by Benns et al. in 1960[62]. They evaluated the antifungal activity of a panel of fourty TSs and their copper complexes on *A. niger* and *Chaetomium globosum* cultures. The compounds were compared with two commercial fungicides: the 2,2'-dihydroxy-5,5'-dichlorodiphenylmethane and the copper/8-hydroxyquinolinolate mixture. The results were very interesting and showed that several TSs resulted significantly more effective than their corresponding copper complexes, indicating that

the antifungal power was related also to the TS structure and not only to the metal ion. The most effective compound was the 9-undecenal-TS which showed an antifungal activity comparable with that of the standards used. Since this discovery, the research of TSs for antifungal purposes has grown rapidly and many other interesting TSs were identified. Their mechanism of action is still debated, some results ascribed the antifungal activity to the ability of TSs to modify the redox equilibrium in target cells acting both as anti-oxidant or ROS stimulating agents. Other studies revealed that TSs induce changes in sterol and membrane biosynthesis. In particular, it was reported that TSs can influence the regulation and biosynthesis of ergosterol, an essential vitamin for fungal cells strictly connected with the metabolism of lipids and membrane synthesis[63].

TSs are also interesting because they are effective chelating agents for metal ions. The synthesis of TS metal complexes can be used to improve the TS biological effects through the modification of their chemical and physical properties, like the water solubility, membrane crossing ability, bioavailability and uptake.

2.6 Metal ions in agriculture

In agriculture, metals are usually applied as fertilizers but also as fungicides and anti-bacterial agents. Since metals are essential micro-nutrients, their biological effects are strictly connected with their amount and the level of each metal must be balanced to guarantee its homeostasis. Usually, low levels lead to poor growth, delayed flowering, and plant sterility, whereas high levels are responsible for plant stress, metabolism disfunctions and, in harsh conditions, the dead of the plants. Therefore, different biological effects can be obtained by modulating the bio-availability of metals in the environment around the target. The bio-availability indicates the fraction of adsorbed compound in an administered dose, therefore it is the actual dose metabolised by the target organism and it depends usually on the solubility of the metal source and on its uptake in cells. For metals, these characteristics can be modified by changing the oxidation state, by using different salts and by coordinating them with organic ligands. The synthesis of metal complexes is the most powerful method because organic ligands are very versatile and can be designed to obtain products with many different

properties. We focused our attention on copper and zinc. They are both essential micro-nutrients and widely applied in agriculture for many different purposes. As already mentioned, their biological effect is strictly connected with their concentration. They must be present in soil in the proper quantity, an excess usually induces problems because both metals bind effectively functional groups of proteins causing their denaturation with the consequent interference in plant metabolism.

Copper compounds are the most employed, especially copper(II)sulphate. It has been known since the XVIII century that the use of a mixture of copper(II)sulphate and lime in water – called "Bordeaux mixture" - has a strong fungistatic effect. If sprayed on crops, it inhibits mould growth and makes seeds unattractive for birds.
The fungicidal action of copper is often explained in terms of capacity to interfere with the redox processes which regulate respiration in cells. In fact, due to the easy redox interconversion between Cu(I)/Cu(II), it raises the number of reactive oxygen species (ROS) in cells inducing high levels of oxidative stress.

Zinc is widely used as fertiliser combined with other macronutrients (like potash, phosphate and nitrogen) and supports root growth increasing leaf size and resilience during stressful growing conditions. However, zinc is not only applied as fertilizer. Zinc dimethyldithiocarbamate is a broad-spectrum fungicide applied on the plant surface where it forms a barrier which inhibits the fungal growth on plant.

The role of copper and zinc in the aflatoxin biosynthesis is still poorly investigated, but there are evidences that they play a significant role[64]. Moreover, the production of mycotoxins is strictly connected with the redox equilibrium in mould cells. Even though the molecular details of this correlation are still unclear, evidence is coming out that the production of ROS (both from mould and host) during the mould/plant interactions are able to modulate the biosynthesis of aflatoxins[65].
This is why we decided to focus our research on the study of metal complexes with copper (a redox active metal) and zinc (an inert metal) because they can be very useful to study more in detail the correlations between aflatoxin production and ROS.

3 The Aflatox project

Figure 10: Aflatox logo and infographic of the project workflow.

A few years ago, the CARIPLO Foundation selected our group to develop a research aimed at discovering new antimycotic substances. The underlying idea was to conjugate the known inhibiting properties of natural aldehydes (the active component of spices, used for centuries to preserve food) and those of metal ions (metal salts, in particular copper, have been extensively used in agriculture to protect plants from molds, in particular in vineyards). As a link between these two components we have chosen a fragment also known to possess biological inhibiting properties: thiosemicarbazide. This molecule reacts easily with the carbonyl group of the natural aldehydes and possesses the right donor atoms to chelate metal ions, thus allowing the incorporation in a single molecule of three potentially active components. In the

course of the screening, focus has been placed on a specific problem that has an enormous impact on economy and health: the diffusion of molds of the genus *Aspergillus* and their production of aflatoxins. The aim of the Aflatox project was therefore to search among the new compounds those that inhibit aflatoxin production in *A. flavus*. It was organized in a systematic sequence of steps from the design of the molecules to the set-up of a practical screening procedure to identify the most effective and safe compounds. The project was based on a "funnel approach" in which the number of compounds decreases gradually during the stages. The infographic of the Aflatox project flowchart is reported in *Figure 10.*

3.1 Aflatox project stages

1. Design and synthesis of parent compounds

To obtain active and not toxic candidates we used TSs derived from natural aldehydes and ketones (the complete list of the natural starting materials in reported in *Table 4*).

2. Screening on *A.flavus* cultures

Each compound was tested to evaluate its ability to inhibit fungal growth and aflatoxin production. *A. flavus* cultures were exposed to different concentration of pesticide and then analyzed. The fungal growth inhibition was evaluated measuring the radial growth and the optical density of samples. The aflatoxin production inhibition was estimated through microplate fluorescence emission measurements.

3. Cytotoxicity evaluation

The compounds resulted efficient in the previous steps were tested on three different human cell lines: HFL1 (lung tissue), Crl1790 (colon tissue) and Hs27 (skin tissue). These lines were chosen to simulate the three typical points of contact between the pesticide and the final consumer. The cytotoxicity was tested using the MTT assay.

4. Compound derivatisation

Non-toxic candidates were used as parent compounds to create families of derivatives. Different TSs were obtained modifying the aldehyde, changing functional groups in N^2

and N^4 and replacing sulphur with oxygen. Moreover, these molecules were used as chelating agents for metal ions to obtain metal complexes.

5. Screening of the biological activity of derivatives

Each family of derivatives was tested on both *A. flavus* and human cells to obtain sets of data suitable for Structure-Activity Relationships studies (SAR).

6. Fill in a database

All the data obtained for each compound, including the physicochemical proprieties, were collected in a database. This tool was useful to record and manage the large volumes of data obtained and to analyse and match results came from different fields.

7. Study of the mode of action of active molecules

Active compounds are analyzed more deeply to understand the underlying mechanism for their anti-aflatoxigenic action. We used specific biological tests to evaluate possible mechanisms and biological pathways. In addition, we used computational chemistry to describe interactions between pesticides and targets and to create SAR models.

The Alfatox project was characterized by a multidisciplinary approach. In every step of the flowchart there were extremely different experiments which needed expertise in several fields: synthetic chemistry, medicinal and bio-inorganic chemistry, biology, micro-biology, toxicology and genetics. A group of 16 people from two Italian universities (The University of Parma and the University of Brescia) were involved in the project. Every compound was designed and synthesized in the department of Chemistry in Parma whereas the biological tests were performed both in Parma and Brescia. Due to the wide structure of this project, the database we built was a necessary and extremely useful tool to record and manage the large amount of information and results we obtained. My personal contribution to the Aflatox project has been the synthesis of a large part of the compound we tested, the creation of the database and the study of the mechanism of action of the best candidates. Therefore, the present thesis describes an overall analysis of the database contents and the detailed analysis of the families of derivatives I designed and synthesised.

raw material	natural source	raw material	natural source
 benzaldehyde	bitter almonds, apricot and peach seeds	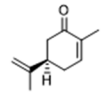 carvone	dill and spearmint leaves
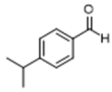 cuminaldehyde	cumin seeds	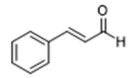 cinnamaldehyde	cinnamon essential oil
 2-acetylthiophene	tobacco leaves	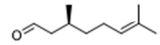 citral	lemon, lemongrass and orange essential oil
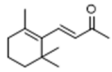 ionone	rose essential oil	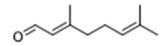 citronellal	kaffir lime essential oil
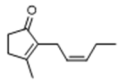 *cis*-jasmone	jasmine essential oil	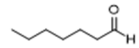 heptanal	clary sage, lemon, bitter orange and hyacinth essential oils
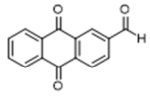 2-acethylanthraquinone	dyes in rhubarb root, alder tree bark, and aloe leaves	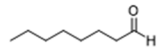 octanal	citrus essential oil
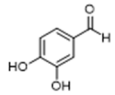 protocatechualdehyde	cork	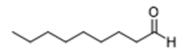 nonanal	citrus essential oil
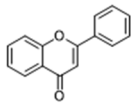 flavone	red berries	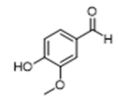 vanillin	vanilla beans
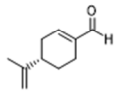 perillaldehyde	perilla leaves	 fenchone	fennel essential oil
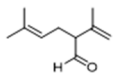 lavandulol	lavender essential oil	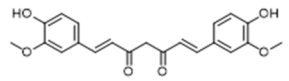 curcumin	curcuma essential oil
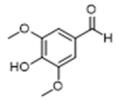 syringaldehyde	oak wood	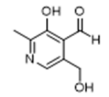 pyridoxal	vitamin B_6 derivative

Table 4: Natural aldehydes and ketones used in the Aflatox project.

3.2 The Aflatox Database

The database was built using *InstantJChem*, a software released by Chem Axon. Every compound was registered as a line of an interactive table in which every column corresponded with an experimental (or calculated) piece of information. Columns were also assembled in sections where data and experiments were linked together. The list of the eight sections of the database is reported below.

Chemical structure tool

The "chemical structure tool" allows to view and edit molecular structures. It is particularly useful in the data analysis to find correlations between structures and activity (SAR studies). It is possible to set up queries which use structures or fragments as input files combined with the chemical or biological properties.

***A. flavus* section**

The "*A. flavus* section" reports the results obtained from the fungal growth and aflatoxin production inhibition tests. The data are expressed as percentage of inhibition at different compound concentrations (50 µM and 100 µM).

Sclerotia section

The "sclerotia section" contains the data about the inhibitory effect that compound induce on sclerotia development. The data are reported as a percentage of inhibition compared with a control of the number of sclerotia per mycelium area.

Antioxidant potential section

The "antioxidant potential section" contains the results of the DPPH test. The DPPH (α,α-diphenyl-β-picrylhydrazyl) is a stable radical which is reduced by substances that can donate a hydrogen atom. This reaction can be followed using a spectrophotometer because DPPH is violet in the reduced form and yellow when oxidized. The antioxidant potential is measured as the % of DPPH which is reduced by a certain amount of compound.

Cytotoxicity section

The "cytotoxicity section" contains results from two different experiments: GI50 (50% cell growth inhibition) values obtained on three different healthy cell lines (HS27 skin, CRL1790 colon and HFL1 lung, and the AMES test which reports the compound ability to induce mutations in the DNA of *Salmonella typhimurium*.

Genotoxicity section

The "genotoxicity section" shows results of the Comet Assay. This biological test is a very effective method to measure deoxyribonucleic acid (DNA) strand breaks in eukaryotic cells. The analysis of the average DNA damage after the exposure to a compound is a measure of its genotoxic stress level.

Chemical and physical information section

The "chemical and physical information section" allows to analyse and find connections between chemicophysical properties of different compounds. Here some interesting parameters such as the molecular weight of the compound, the number of H-bond donor or acceptors and calculated value of logP (partition coefficient) and logS (aqueous solubility) and TPSA (Total Polar Surface Area) are reported.

***A. cepa* section**

The "*A. cepa* section" contains results of EC_{50}, the compound concentration which induces the 50% of *A. cepa* root growth inhibition. The MI (mitotic index) result, namely it is the number of cells in a population undergoing mitosis. If this value is different from the normal one, it suggests problems in the cell cycle due to the presence of the compound. The MNT (Micronucleus test) shows the compound concentration which induces genotoxicity in a specific organism. Finally, it is recorded the compound concentration which caused chromosomal aberrations.

All the detailed protocols and procedure used for the synthesis and biological assays are reported in the *Anti-aflatoxigenic agents: experimental* section.

3.3 Database overview and analysis of the results

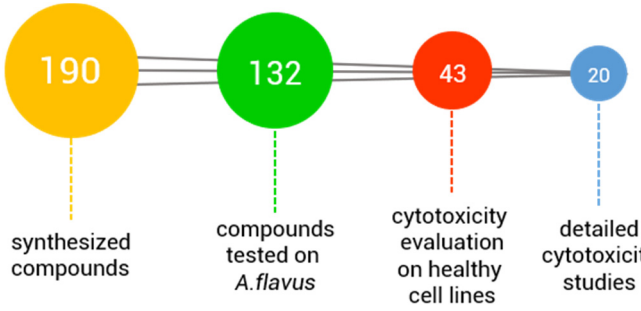

Figure 11: Number of compounds analysed in every step of the Aflatox project.

The database contains 190 molecules: 80 organic ligands, 75 metal complexes and 35 raw materials. The organic molecules are mainly TSs (74 of 80) and the 75 metal complexes were classified according to the metal centre (mostly Cu(II) and Zn(II)) (*Figure 12*).

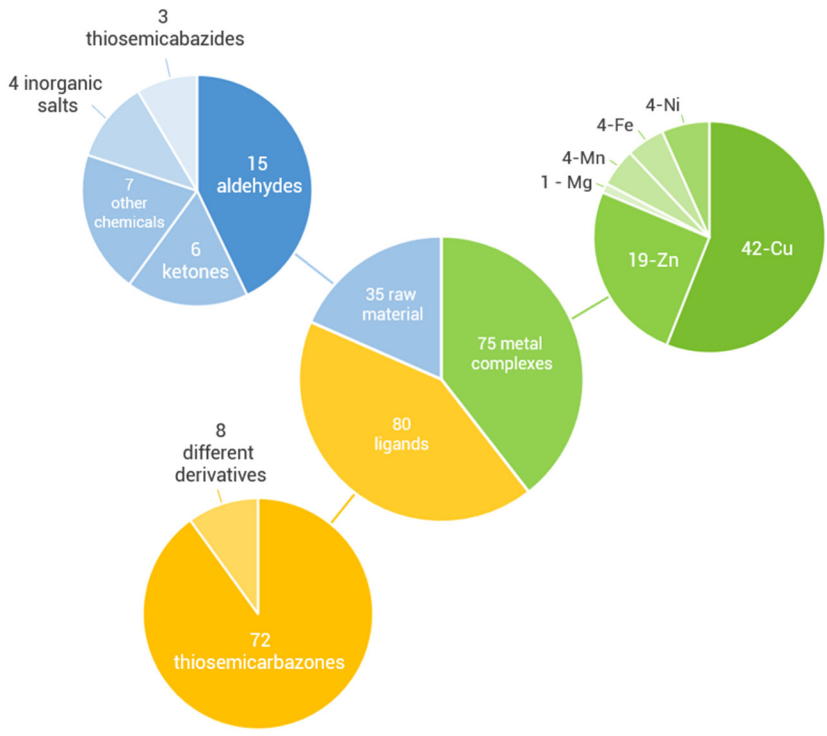

Figure 12: detailed description of the compounds collected in the Aflatox database.

The activity on *A. flavus* was determined for each compound. However, the database contains just 131 results concerning the inhibition of aflatoxin production and 132 from fungal growth inhibition, because some molecules resulted inadequate to be tested. For example, some of them were poorly soluble in the media used for the biological assays, especially in the fungal growth inhibition tests, and therefore it was impossible to define a reliable dose-response relationship. Moreover, 10 compounds gave rise to interferences in the fluorescence detection used for the aflatoxin inhibition quantification. At this stage of the screening, the parameters we used to define a good candidate were: inhibition of aflatoxin production higher than 75% and fungal growth inhibition lower than 30%. These parameters were chosen because, as already mentioned in the introduction, our goal was to find specific anti-aflatoxigenic molecules which do not influence significantly the fungal primary metabolism. Of the 190 compounds only 8 molecules showed these characteristics at a 100 μM treatment. They were directly submitted to the cytotoxicity evaluation, the subsequent step in the project workflow. However, we decided to enlarge the screening including also the cytotoxicity evaluation of some other interesting compounds which showed, for example, a strong fungistatic effect or very good anti-aflatoxigenic power even if associated with a significant fungistatic effect. In the end, the IG_{50} of 43 compounds were determined on the three healthy cell line (Hs27, Crl179 and HFL1) and they were considered not toxic only if 3 out of 3 IG_{50} values were higher than 100 μM, a threshold value which indicates a very strong exposure. Only 15 compounds displayed these characteristics. Combining in a database query the very good candidates from *A. flavus* tests and molecules with not toxic effect, we have identified 3 very interesting compounds (*Figure 13*). In the last part of the project, the potential toxicity of the most interesting compounds was studied in detail. We determined the genotoxicity of 14 compounds after 1 and 24 hours (COMET assay), the mutagenicity (AMES test) of 24 compounds and we performed 20 tests on *A. cepa* (to determinate the EC_{50}, MI and MNT) and 16 anti-oxidant power measurement (DPPH assay).

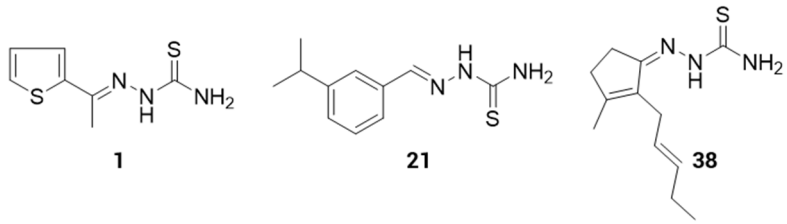

*Figure 13: best candidates of the Aflatox projects, namely 2-acetylthiophenethiosemicarbazone (**1**), 3-isopropylbenzaldehydethiosemicarbazone (**21**) and cis-jasmonethiosemicarbazone (**38**).*

3.4 Queries

To analyse the data contained in the Aflatox database, it was necessary to set up queries that combine different information. Examples of informative queries and their results are reported below.

How many compounds show an aflatoxin production (API%) more than 75%?

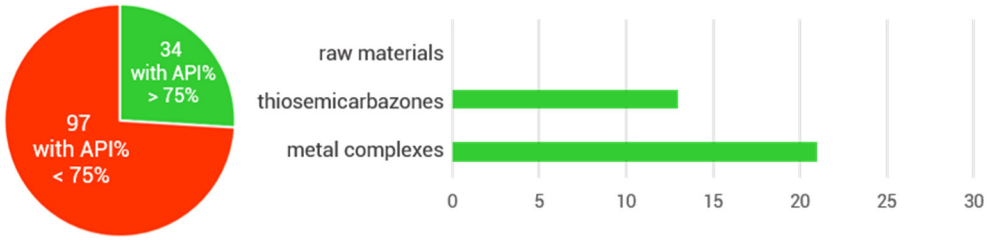

Figure 14

The compounds which show an aflatoxin production inhibition higher than 75% (at 100 μM) are 34. Active compounds are mostly metal complexes (21 out of 34) and no raw materials have significant anti-aflatoxigenic effect.

How many compounds show a fungal growth inhibition (FGI%) higher than 75%?

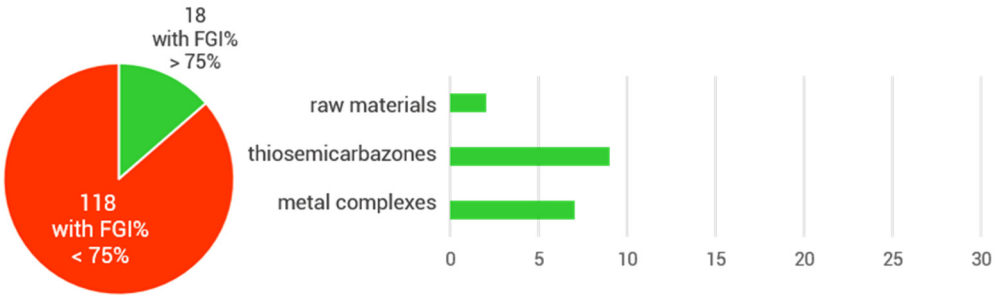

Figure 15

We considered fungistatic a compound able to inhibit the fungal growth more than 75% in a treatment at 100 µM. The fungistatic compounds in the database are 18 divided into 2 raw materials, 9 TSs and 7 complexes.

How many compounds showed higher aflatoxin production inhibition than fungal growth inhibition?

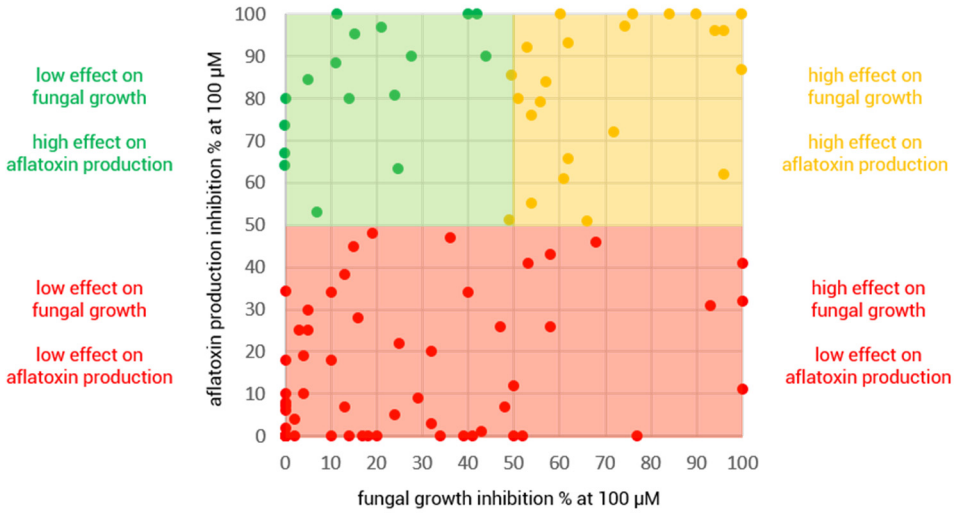

Figure 16

The compounds which resulted specific in inhibiting the aflatoxin biosynthesis were identified through a query which combines the aflatoxin production inhibition with the effects on fungal growth. The result was that 19 of the 119 molecules tested resulted more active in inhibiting aflatoxin production then on fungal growth (coloured in green in *Figure 16*). We considered promising also the 21 candidates we coloured in yellow. These molecules showed high anti-aflatoxigenic effect and, at the same time, high fungistatic effect. They are effective mycotoxigenic agents, even if their strong effect on fungal growth suggests a non-specific mechanism of action. For these reasons, these molecules are interesting but not completely suitable to be studied in detail according to the Aflatox project workflow.

Are there compounds with high anti-aflatoxigenic power and mild effects on sclerotia development?

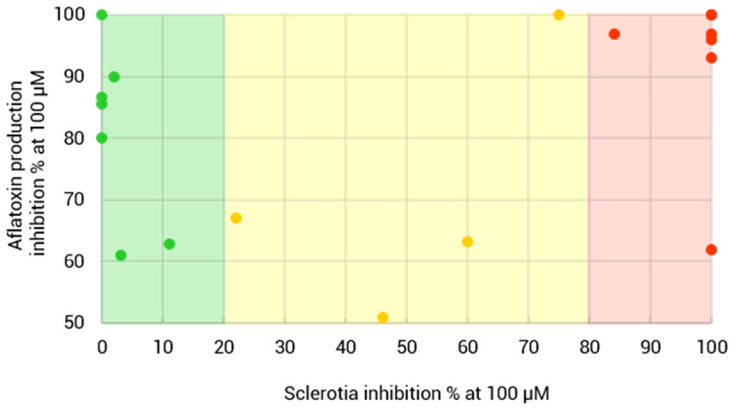

Figure 17: The graph describes the inhibitory effect on sclerotia biosynthesis of the anti-aflatoxigenic compounds (API% > 50%). Green area indicates compounds with no effect of sclerotia biosynthesis, the yellow area indicates those with light effect and the red area those with a strong effect.

It is known from literature that the majority of the anti-aflatoxigenic compounds have also the effect to inhibit and/or induce modifications in the sclerotia development. However, the exact metabolic event in common between the two pathways is still unknown. The anti-aflatoxigenic agents that inhibits also the sclerotia development are usually compounds which interfere with some primary functions of the fungus and then

the aflatoxin and sclerotia inhibition are just unintended consequences. For this reason, a compound which is effective on the aflatoxins but not on the sclerotia suggests higher specificity. To identify these compounds on the Aflatox database, we selected the compounds which showed aflatoxin production inhibition higher than 50% (at 100 μM) and then we applied a filter to divide the active derivatives according to their effect on sclerotia, namely null, low and high effect. This query showed that 7 out of the 18 compounds have no effect on sclerotia development.

What is the average molecular weight of the active compounds?

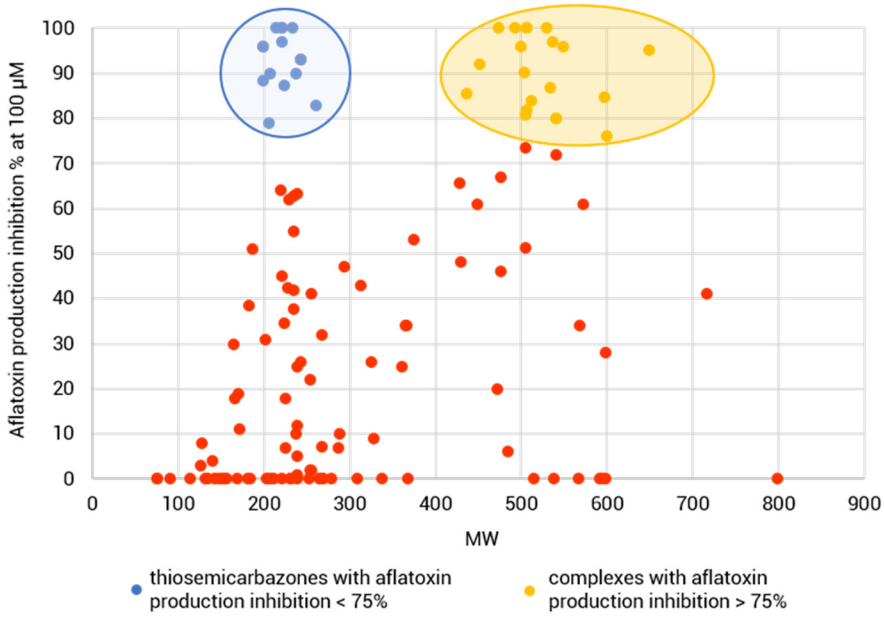

Figure 18

We plotted the molecular weight of each compound against its inhibitory effect on the aflatoxin biosynthesis. As a result, we identified a narrow range of MW (between 199.29 and 261.30) in which all the active ligands are comprised. We identified as 222.16 the average MW value to have TS with aflatoxin production inhibition higher than 75%. For the complexes, we identified a larger range (between 436.14 and 648.39) which did not identify a relationship between MW and the biological effect of this kind of compounds.

How many compounds have a significant cytotoxicity?

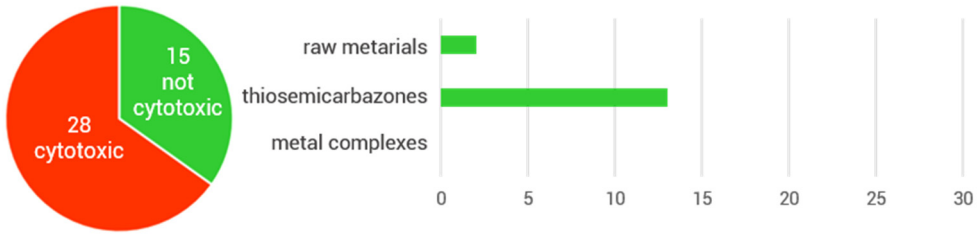

Figure 19

We evaluated the cytotoxicity through the determination of the GI_{50}, which estimates the antiproliferative effect of a compound. As mentioned before we tested the effect on three healthy cell lines and we considered "safe" a compound which has all the three IG_{50} higher than 100 μM. The compounds that satisfy this requirement in the database are 15 out of the 43 tested. Unfortunately, all the metal complexes we tested resulted cytotoxic. Among the 15 "safe" compounds 13 are TSs.

Which compounds show at the same time aflatoxin production inhibition > 75%, fungal growth inhibition < 30% and an IG_{50} > 100 μM in all the three healthy cell lines?

To set up this query we correlate the data from *A. flavus* with those from the cytotoxicity tests (*Figure 20*). In addition, we fixed threshold values in each test to identify the compounds that have all the characteristics required for our purposes. Thanks to this query, we found that 3 out of the 190 molecules synthesised satisfy all the requirements. These molecules are **1**, **22** and **38**. **1** and **38** are TSs of natural compounds, namely 2-acetylthiophene and *cis*-jasmone, whereas **22** is a structural modification of the cuminaldehyde-TS (**20**). They have all a strong inhibitory effect on the aflatoxin production, but low effect on fungal growth and on human cells. For these reasons they can be considered the best candidates of the Aflatox screening.

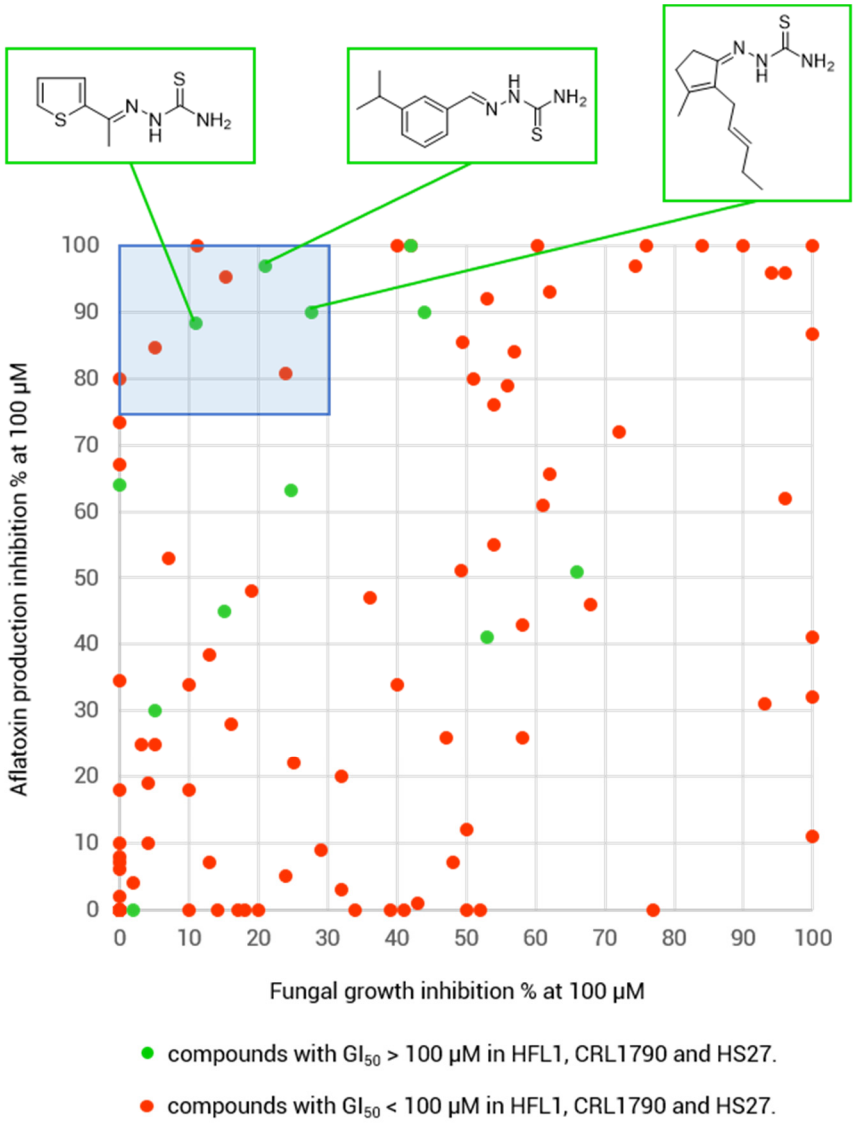
Aflatoxin production inhibition % at 100 µM
Fungal growth inhibition % at 100 µM
0
10
20
30
40
50
60
70
80
90
100
compounds with GI50 > 100 µM in HFL1, CRL1790 and HS27.
compounds with GI50 < 100 µM in HFL1, CRL1790 and HS27.

Figure 20

3.5 Pharmacophore model of the best candidates

The effects shown by **1**, **22** and **38** were similar, all the three TS showed great aflatoxin production inhibitory effect and negligible effects on fungal growth and healthy human cells. With these premises, we found it interesting to create the pharmacophore model of these three molecules. In medicinal chemistry a pharmacophore model is a scheme which describes the steric and electronic features necessary for the supramolecular interactions between molecules and their biological targets. It is useful to derive the structure-activity relationship of a set of molecules which showed similar biological properties[66]. In our work, we applied this technique to identify the structural characteristics in common between our active molecules to create a model to identify the potential key features on which the anti-aflatoxigenic effect could be based on. The pharmacophore model was created using *Gold* through the Hermes graphic interface. The first step was the creation of the 3D-models of **1**, **22** and **38** and then the generation of a set of 200 conformers for each molecule. After, the sets were used as input files for the "overlay calculation and ligand optimisation", namely the research of the conformer of each molecule that best fits with the others and the generation of a scheme which describes the features in common.
The overlay calculation of **1**, **22** and **38** generated two possible solutions, in *Table 5* are reported the scores obtained.

	Volume	**H-bond**	**Hydrophobic coplanarity**	**Internal energy**	**Dominance**
Solution1	271.125	72.000	15.638	5.841	0.000
Solution2	280.250	72.000	14.794	2.199	0.000

Table 5: overlay calculation solutions.

Solutions with dominance zero are considered the best compromise in the optimisation of the parameters used to score the solutions. Since the dominance resulted zero in both solutions, they are equivalent in terms of optimisation. However, we chose *solution 2* because it showed the lowest value of internal energy and therefore the lowest internal strain. In *solution 2* (*Figure 21* - A) the TS group of the three conformers were perfectly superimposed and the residue of the aldehyde/ketone, namely the *cis*-jasmone, the 2-acethylthiophene and the 3-isopropylbenzalhyde were positioned to maximise the overlay of the lipophilic groups.

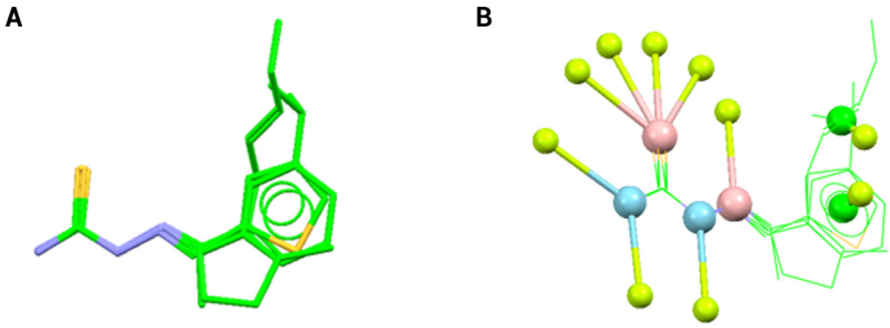

*Figure 21: Graphic visualisation of the overlay calculation (solution 2) (**A**) and the corresponding pharmacophore model (**B**).*

The pharmacophore model generated from the overlay solution 2 (*Figure 21* - B) showed the model of the possible interaction that **1**, **22** and **38** could generate in a similar way and with similar strength. The model was rendered to indicate the donor groups (cyan), the acceptor groups (pink) and the hydrophobic area (green). This model is useful to identify the requirements that could have triggered the strong and specific anti-aflatoxigenic effect we observed for these derivatives. It does not ensure that the molecules have the same target, however it describes the similarities between the active compounds which could be essential, for examples, for their uptake and/or recognition by the fungus. Finally, it can be used as model to keep as a reference in the design of new anti-aflatoxigenic compounds.

4 Detailed studies of the promising derivatives

4.1 2-acetylthiophene derivatives

The class of the 2-acetylthiophene derivatives was designed to test the effect of two different metal centres, namely copper(II) and zinc(II), on the anti-aflatoxigenic activity. In addition, we synthesised and tested the analogues of the 2-acetylthophene derivatives replacing the sulphur with oxygen in the 5-membered ring (2-acetylfuran derivatives) (*Figure 22*).

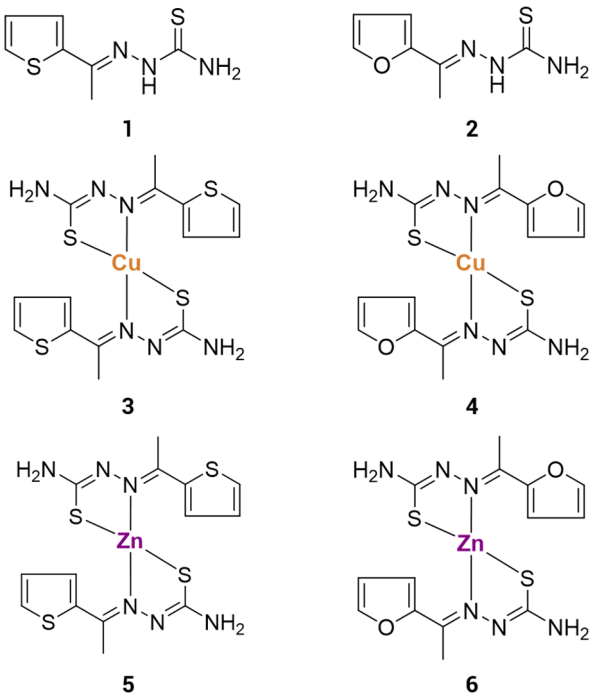

Figure 22: List of components of the 2-acetylthiophene family.

The entire family of derivatives resulted suitable to be tested on *A. flavus* cultures and the effects are reported in *Figure 23*. The derivatives of 2-acetylthiophene, **1** and **3**, resulted both anti-aflatoxigenic in a dose-dependent manner, whereas **5** (the zinc complex) showed just a mild inhibitory effect on aflatoxin production. All the three

derivatives showed a negligible effect on fungal growth. In fact, the highest fungistatic effect registered was a 29.3% fungal growth inhibition at 100 μM induced by copper complex **3**. The 2-acetylfuran series showed different results. The ligand (**2**) and its zinc complex (**6**) were almost inactive on both aflatoxin and growth inhibition. On the contrary, the copper complex (**4**) revealed higher effects in both tests. However, the entire series resulted less effective compared with the results of the 2-acetylthiophene derivatives. This result highlights a positive effect induced by the sulphur atom in the 5-membered ring.

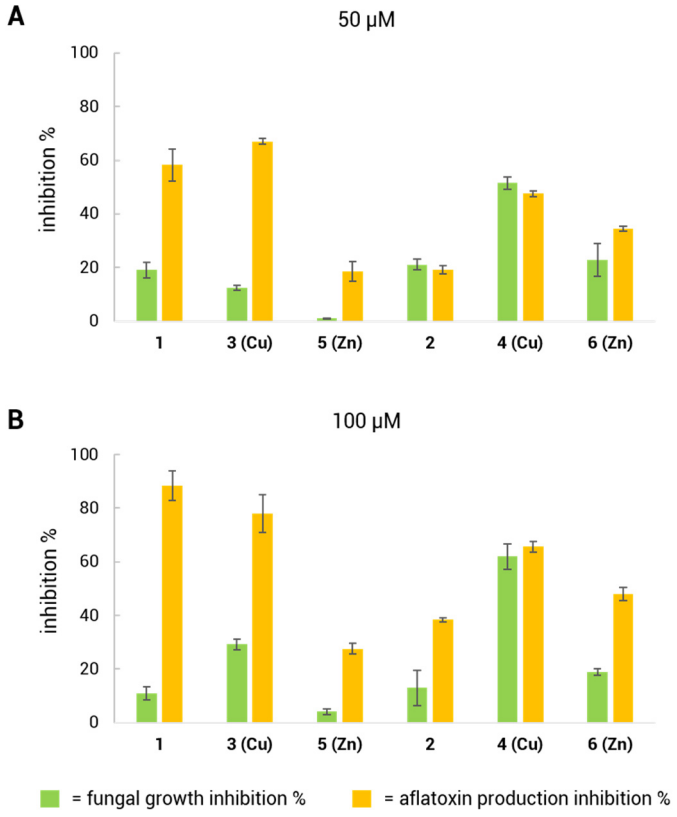

Figure 23: Effects of the 2-acetylthiophene derivatives on A. flavus. at two different sample concentration A. 50 μM and B. 100 μM.

The effects on gene expression induced by the most effective compound (**1**) were evaluated (*Figure 24*). In particular, we analysed the expression of genes involved in the secondary metabolism (aflatoxin cluster and sclerotia biogenesis) and the primary metabolism. The treatment with **1** induced a down-regulation of the genes belonging to the aflatoxin cluster (*OmtB* and *AflS*) and sclerotia development (*NsdC* and *NsdD*), and the up-regulation of the *Adh1*, a key gene of the fermentative metabolism. This evidence can explain the strong inhibitory effect of **1** on the aflatoxin production (88.4% at 100 μM) together with the absence of effects on primary metabolism. The down-regulation of *OmtB* and *AflS* induces a block of the aflatoxin biosynthesis, whereas the up-regulation of *Adh1* (pro-growth factor) is the signal of a fungal response to balance the dangerous and unspecific effects of **1**. Even if from these data it is impossible to define a single target, we can affirm that **1** interacts at some level of the metabolism by down-regulating the sclerotia and/or aflatoxin biosynthetic pathways which are known to be correlated[67]. The effect of this interaction is a selective inhibition of the aflatoxin production, a non-essential metabolism for the fungus, whereas all the other fungal functions remain apparently unaltered as demonstrated by the very mild effect of **1** on fungal growth (11.0% at 100 μM).

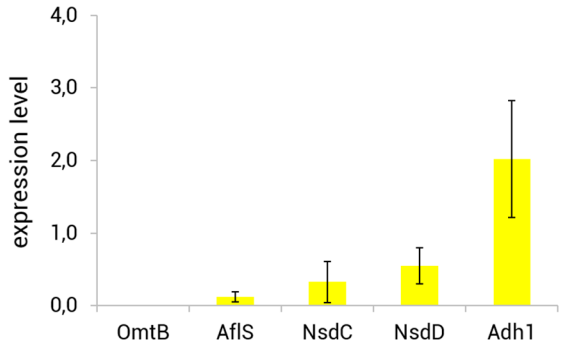

*Figure 24: Fold change of gene expression in response to the treatment with **1**.*

Since **1** resulted a perfect candidate in the first panel of experiment established in the Aflatox workflow, the potential toxic effect of **1** was investigated in depth (*Table 6*). The first experiment was the evaluation of the cytotoxicity on the three healthy cell lines Hs27, HFL1 and Crl1790 and **1** resulted not cytotoxic (GI_{50} > 100 μM) in all three cell

lines. Subsequently, the AMES test confirmed that **1** is also not mutagen and the Comet test does not highlight any effect both after 1 and 24 hours of exposure. Compound **1** did not affect *A. cepa* cells proliferation up to the highest concentration tested (100 µM) and the micronucleus test does not indicate genomic damage until 100 µM. The only experiment which showed an effect induced by **1** was the chromosomal aberration test. The 2-acetylthiophene derivative induced in *A. cepa* a light alteration of the chromosomes at 25 µM. This effect is commonly observed after exposure of *A. cepa* to pesticides or phyto-drugs and it can indicate also a potential risk for humans since correlations between *A. cepa* and mammalian systems are reported in the literature[68,69].

cytotoxicity		
Hs27 GI_{50} (µM)	**HFL1 GI_{50} (µM)**	**Crl1790 GI_{50} (µM)**
>100	>100	>100

***A.cepa* proliferation**		**mutagenicity**	**genotoxicity**			
EC50 (µM)	**Mitotic index reduction (µM)**	**AMES test**	**Micronucleus Test *A.cepa* (µM)**	**Chromosomal aberrations *A.cepa* (µM)**	**Comet test**	
					1 h	**24**
>100	100	not mutagenic	100	25	Not toxic	Not toxic

*Table 6: Collection of the data about the toxicity of **1**.*

The detailed study we made on the 2-acetylthiopnene family of derivatives led to the discovery of very interesting properties of 2-acetylthiophene-TS (**1**). This molecule results to be extremely effective in inhibiting the aflatoxin production (88.40% at 100

μM) without affecting fungal growth. In addition, it results non-toxic in all the *in vitro* tests made on healthy human cell lines and presents just a mild toxic effect detected in one of the four *in vivo* tests on *A. cepa*. These very good results obtained for **1** make it one of the best candidates in the Aflatox project.

4.2 Cinnamaldehyde derivatives

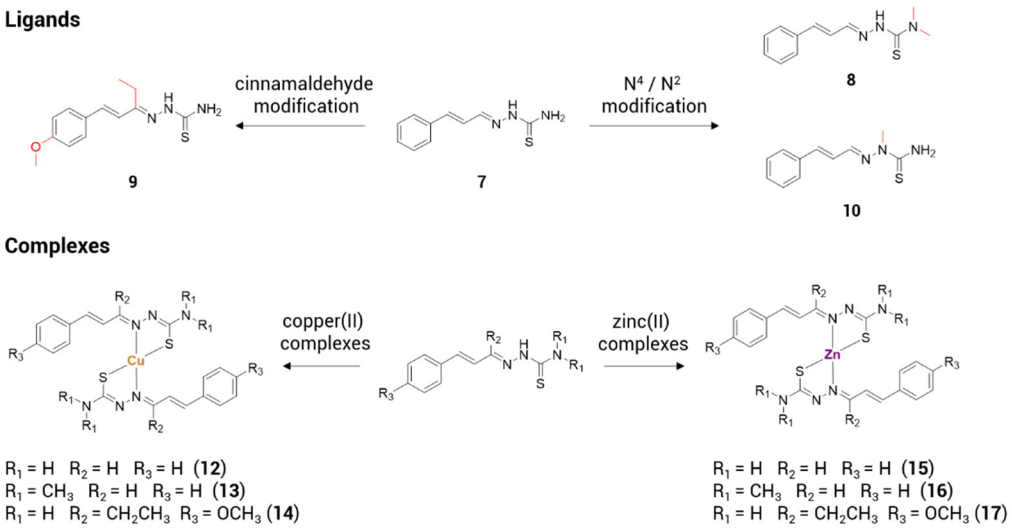

Figure 25: List of components of the cinnamaldehyde family.

Cinnamaldehyde is a natural volatile compound responsible for the smell of cinnamon. Cinnamon (and then cinnamaldehyde) has been known for a long time as a food preservative with extensive applications and no side effects, and traces of its use to preserve crops were identified in many ancient Egyptian documents. More recently, the effects of the cinnamon essential oil and of cinnamaldehyde, were studied in detail and they showed promising medical, antibacterial and fungicidal properties[70].

For our purposes, the most interesting paper in this field was published by Xie and co-workers in 2004[71]. They reported that *A. flavus* cultures exposed to cinnamaldehyde showed a severe inhibition of spore germination and changes in hyphae and spore morphology. In this context, we decided to use cinnamaldehyde as a reagent for the synthesis of the corresponding TS (**7**) and to explore its ability to inhibit fungal growth and aflatoxin production in the context of the Aflatox project. CinnamaldehydeTS (**7**) resulted to be an interesting parent compound because it showed an aflatoxin production inhibition higher than the corresponding fungal growth inhibition, namely 79% and 56% at 100 µM. Since at the same concentration cinnamaldehyde did not show

any effect, we found interesting to explore more in detail this TS by synthesizing a panel of derivatives, both compounds with structural modifications and metal complexes (*Figure 25)*. The panel of derivatives contains structural modifications of the parent compounds: one functionalised in the N^4, one modified in the N^2 and one modified in the cinnamaldehyde portion. The iminic bond of the N^2 methyl derivative (**10**) was also reduced to obtain **11**. In addition, each TS able to be deprotonated in N^2 was used as ligand to synthesise bis-TS complexes of copper(II) and zinc(II). The results of the screening of the activities on *A. flavus* are collected in *Figure 26*.

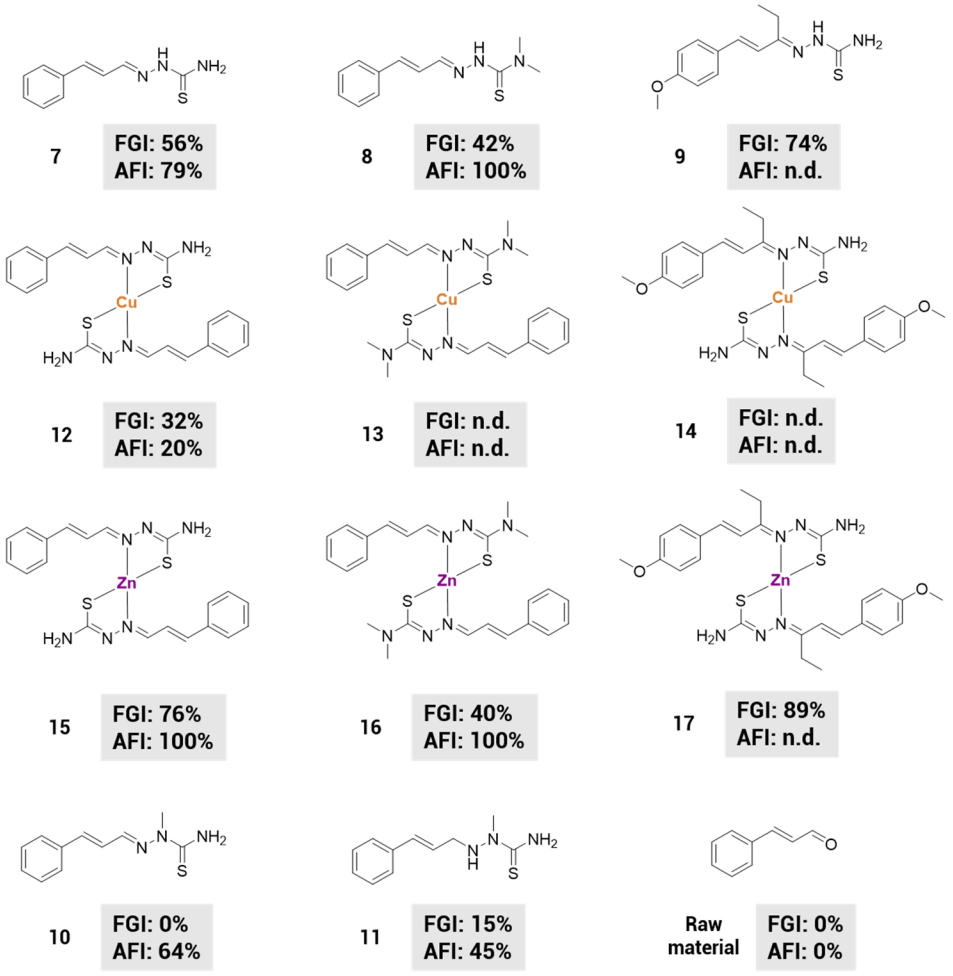

Figure 26: Effects of the cinnamaldehyde derivatives on A. flavus. FGI indicates fungal growth inhibition percentage at 100 μM and AFI indicates aflatoxin production inhibition percentage at 100 μM.

The two metal complexes of **7** (**12** Cu and **15** Zn) showed extremely different behaviours: **12** resulted less fungistatic than **7**, but also less able to inhibit aflatoxin production, while **15** was able to cancel completely the aflatoxin production even though it raised of the 20% the fungistatic effect of **7**. The screening highlighted that the modification of **7** in the cinnamaldehyde portion (TS **9**) led to raise the fungistatic effect. Unfortunately, **9** created interferences in the aflatoxin determination, due to its ability to partially absorb the fluorescence emission of aflatoxin B_1 which therefore resulted impossible to be quantified correctly. The same effects were observed for its zinc(II) complex **17**. Even the N^2 methylation (**10**) did not improve the aflatoxin production inhibition of **7**. However, it resulted completely ineffective on fungal growth and therefore it can be considered a good candidate. The reduction of its iminic bond (**11**) did not improved the biological effects. The functionalisation of N^4 led to more interesting results. In fact, **8** showed a total inhibition of aflatoxin production and a lower effect on fungal growth compared with the parent compound (**7**). Even its zinc complex (**16**) showed similar results, while the copper complex (**13**) could not be tested because it precipitated immediately after dissolution in the culture medium used for the *A. flavus* assays. The same problem was encountered with complex **14**. The issue of the solubility of TSs and of their metal complexes in culture media is an interesting topic, worth being examined in depth, because it can affect significantly the results of the biological assays. The insolubility of a compound can be clearly visible, like the ones we observed for **13** and **14**, but it can also be a very light effect, not directly observable during the experiment. For these reasons, we decided to analyse in detail the behaviour in solution of the copper complex **12** (compared with its zinc analogue **15**) to verify the solubility and stability of the sample.

4.2.1 Solubility and stability in solution of **10** and **13** in cell medium

The stability of complexes **12** and **15** in solution were evaluated by monitoring possible changes in their UV-vis absorption spectra during a 24-hour period. Two different types of changes can be observed in the spectra. The first is a change of the absorption profile that indicates a modification of the structure of the compound tested, for instance it could be due to its degradation or to the presence of secondary reactions

which modify the chemical scaffold of the chromophore. The second change which can be detected is the reduction of the absorbance of the entire spectrum, but without changes in the absorption profile. This phenomenon indicates that the compound is chemically stable, but its concentration decreases during time, and this means that its solubility is not optimal.

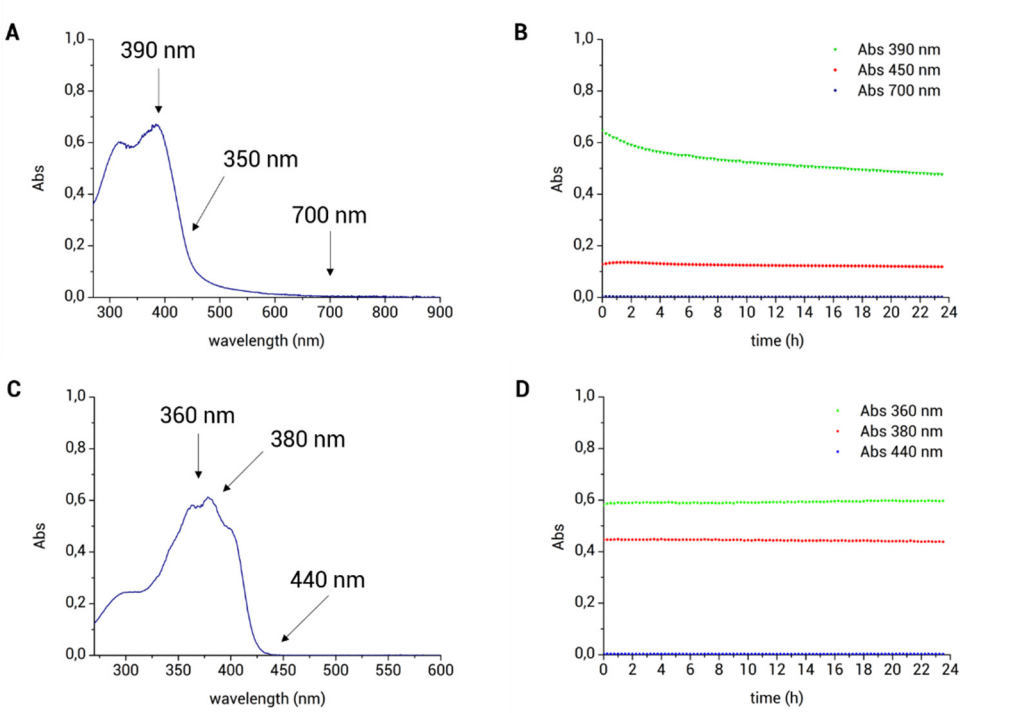

*Figure 27: Solution stability experiments. A and C are the UV-vis absorption profiles of freshly prepared solution of **12** and **15**, respectively. The wavelengths indicated are those used to monitor the stability. C and D are the evolution of the absorbances of **12** and **15** at different wavelengths during a 24-hour period.*

The decrease of the profile absorbance is usually associated with a raise of the base line because of the presence of precipitate in the optical path. With these premises, we considered stable a complex that do not change significantly its profile in a 24-hour period incubated at 37°C. It was impossible to use the actual culture medium as a solvent because it contains a highly lipophilic coconut proteins emulsion which interfere with the spectrum acquisition. We had therefore to simplify the system using a PBS-buffered aqueous solution in which the compounds were dissolved as DMSO

solutions. The DMSO percentage was kept below 2% as requested for the biological assays. Following this protocol, 100 µM solutions of **12** and **15** were prepared and their absorption spectra were recorded to identify the wavelengths to use for the stability evaluation. Subsequently, three different wavelengths were fixed for each complex: two from the absorption profile and one from the baseline as a control. Having fixed these wavelengths, the corresponding absorbances were recorded every 15 minutes for 24 h and the values were plotted versus time to obtain the stability profiles. The temperature was fixed at 37°C and kept stable during the entire experiment. The results are reported in *Figure 27*. The two complexes showed different stability. The zinc complex (**15**) did not change absorption profile significantly through time and the baseline remained stable on zero. On the contrary, the copper complex **12** showed a gradual decrease in the absorbance at 390 nm which indicated that something was happening in the solution. To better understand the phenomenon, we recorded the complete spectra of the two complexes also after 24 hours and we compared them with those acquired the day before (*Figure 28*). What we noticed was that the two absorption profiles of **15** resulted almost identical, while the spectrum of **10** after 24 hours showed a significant absorbance decrease. However, no significant changes in the profiles were observed, so we concluded that **10** has a lower solubility in the culture medium compared with **15** and that it slowly precipitates through time. Even if the precipitation of **15** was not dramatic, it could explain the milder effect observed for **12**, compared with **15** and **7**, in both the tests on *A. flavus*.

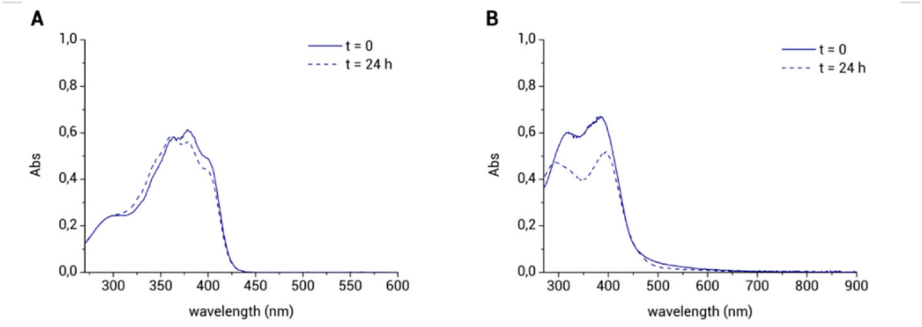

*Figure 28: Comparison between UV-vis absorption profiles of freshly prepared and 24-hour old solutions of **12** (A) and **15** (B).*

4.2.2 Toxicity assessment

Human cell lines

In the area of interest of the Aflatox project, five compounds of the cinnamaldehyde family reached the step of the cytotoxicity evaluation, namely **7**, **8**, **10**, **15** and **16**. The results of their cytotoxic effect on Hs27, HFL1 and Crl1790 is reported in the *Table 7* below:

	Hs27 GI_{50} (μM)	**HFL1 GI_{50} (μM)**	**Crl1790 GI_{50} (μM)**
7	>100	>100	>100
8	>100	>100	>100
10	>100	>100	>100
15	36.1	43.6	54.9
16	41.0	39.5	>100

Table 7: GI_{50} values of cinnamaldehyde derivatives on the three healthy cell lines Hs27, HFL1 and Crl1790.

All the three TSs resulted non-cytotoxic in all the three cell lines tested, while **15** and **16** (the two zinc complexes) resulted cytotoxic. In particular, **15** showed toxic effects in every cell line and **16** in two out of the three tested. This phenomenon is similar with what observed for other classes of derivatives, where the presence of a metal often raised the biological effects on *A. flavus*, but at the same time, it increased the cytotoxicity of human tissues.

***A. cepa* cultures**

The molecules tested on *A. cepa* cultures were four: three TSs (**7**, **8**, **10**) and one zinc complex (**15**). They represented the best candidates of the cinnamaldehyde family, since showed very good results in the previous steps: strong effects on aflatoxin

inhibition a low effect on fungal growth and human cell lines. *Table 8* collects all the data obtained from the screening on *A. cepa* and the results of the AMES test.

	***A.cepa* proliferation**		**mutagenicity**	**genotoxicity**	
	EC50 (μM)	**Mitotic index reduction (μM)**	**AMES test**	**Micronucleus test (μM)**	**Chromosomal aberrations (μM)**
7	1	10	non-mutagenic	10	1
8	50	>100	weakly mutagenic	>100	10
10	100	50	non-mutagenic	50	10
15	1	10	non-mutagenic	10	1

Table 8: Collection of the data about the toxicity on A.cepa of cinnamaldehyde derivatives.

7 and its zinc complex **15** resulted able to affect the *A. cepa* proliferation already at low concentration, while **8** and **10** showed this effect with 50- to 100-fold higher concentrations. The same results were obtained for the genotoxicity evaluation. The AMES test, which is a reliable method to evaluate the mutagenicity, showed a weakly mutagen effect only for **8**. Considering all the data collected, the best candidate of the cinnamaldehyde family of derivatives is the N^2-methyl-TS (**10**). It has a good inhibitory effect on fungal growth and low toxic effects on human and vegetal cell lines. The analysis of all the biological effects led us to believe that **10** has a specific anti-aflatoxigenic activity. It showed low cytotoxic, genotoxic and mutagenic effects probably because its preferential target is involved in the fungal secondary metabolism, which contains enzymes absent in human or vegetal systems. This hypothesis is supported by the null effect on fungal growth which indicates a specific effect on the fungal secondary metabolism.

4.3 Cuminaldehyde derivatives

The “hit-to-lead" strategy is a widely used approach for the drug discovery in medicinal chemistry. It consists in the identification of a promising compound from a preliminary screening and this is subsequently used as lead compound for the design of a panel of derivatives. In the following steps, the physicochemical and biological properties of every derivatives are compared with the parent compound to find the key requirements on which the biological effect is based. This result approach is also called “lead optimisation" and in contains the detailed study of the action mechanism of the most effective compounds. Even if we were not interested in a classic “drug discovery", the Aflatox project showed many similarities with research in medicinal chemistry, therefore the “hit-to lead" approach was an extremely powerful instrument for the discovery and optimisation of new anti-aflatoxigenic compounds. In the first part of the project, we identified an extremely interesting derivative of the cuminaldehyde **20**, which showed 100% of aflatoxin production inhibition and 90% fungal growth inhibition at 100 μM. This was therefore used as lead compound for the design of several derivatives (*Figure 29*). The main aim of the optimisation was to raise the selectivity of the cuminaldehyde-TS **20** for the aflatoxin production inhibition with a concomitant lowering of the effect on fungal growth. We started by modifying the hit compound constituting moieties: the TS and the cuminaldehyde fragments. Then, we used all the modified TSs as ligands for the synthesis of their Zn(II) and Cu(II) complexes and we also tested the effect of a sulphur replacement with oxygen by synthesising the cuminaldehydesemicarbazone (**27**). Finally, we tested the biological effects of the molecular fragments (cuminaldehyde, urea, thiourea, thiosemicarbazide, copper(II) and nickel(II) acetate) as a control.

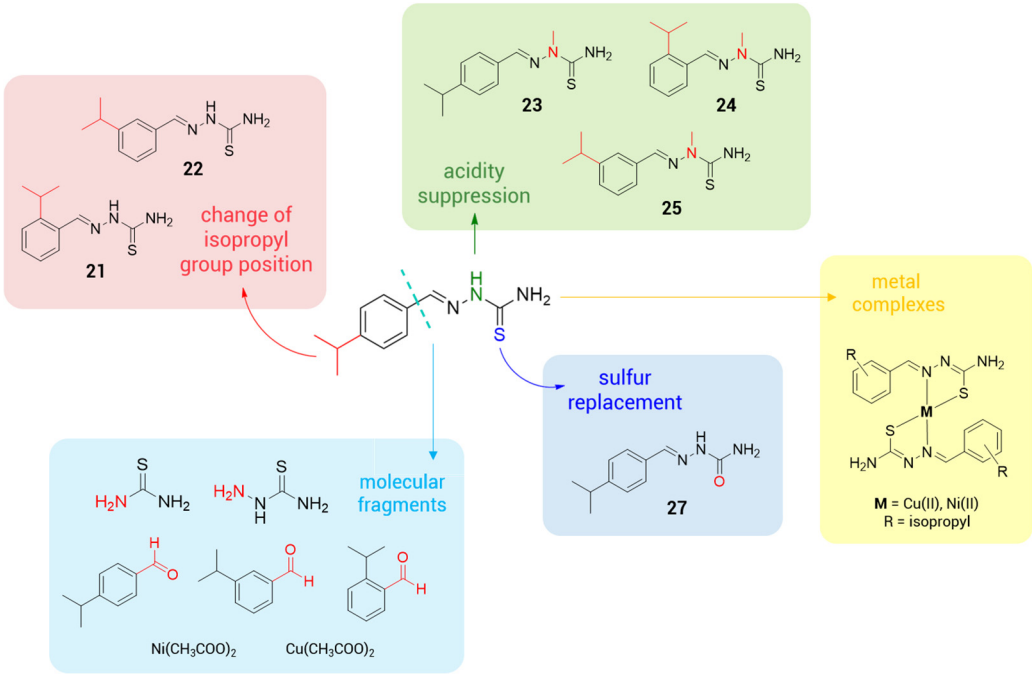

Figure 29: List of components of the cuminaldehyde family.

All the derivatives were obtained pure and in good yields according to the procedures reported in the *Chemical procedures* section. Their fungistatic and anti-aflatoxigenic powers were determined and compared with those previously obtained for cuminaldehyde-TS **20**. From the screening of the molecular fragments (*Figure 30*) did not emerge any significant activity, confirming that the TS structure is essential to obtain the biological effect. The same results came from the sulphur replacement, which highlighted the key role of the sulphur atom, which probably lies in its propensity to act as a reducer, as a reactive oxygen species (ROS) generator or as a radical scavenger.

However, the most surprising result came from the isomers of **20**. In this series, the shift of the isopropyl group induced a strong effect on the biological properties. The reference compound (*para* isomer **20**) was both fungicistatic and anti-aflatoxingenic, whereas the meta-isomer **22** registered a complete aflatoxin production inhibition with no fungistatic effect and the *ortho* isomer **21** resulted almost inactive in both tests. This behaviour observed for the *meta* isomer **22** suggests that it has a more specific anti-

aflatoxigenic action than **20** and that this specificity is related with the isopropyl group position.

We explored also a modification of the TS-fragment structure: the methylation of the N^2 postion. This substitution has the effect of removing the acidic proton involved in the thione–thiol tautomerism and then to significantly change the molecule hydrophilicity and ability to chelate metals. In our screening, all these derivatives (**23**, **24** and **25**) resulted less active than the corresponding N^2 free analogues (*Figure 30*). Moreover, in these derivatives also a change in the isopropyl position did not change the biological properties as much as in the compound reported above. These TSs have all the same mild and not-specific effect and this evidence suggests the crucial role of the free NH for the activity.

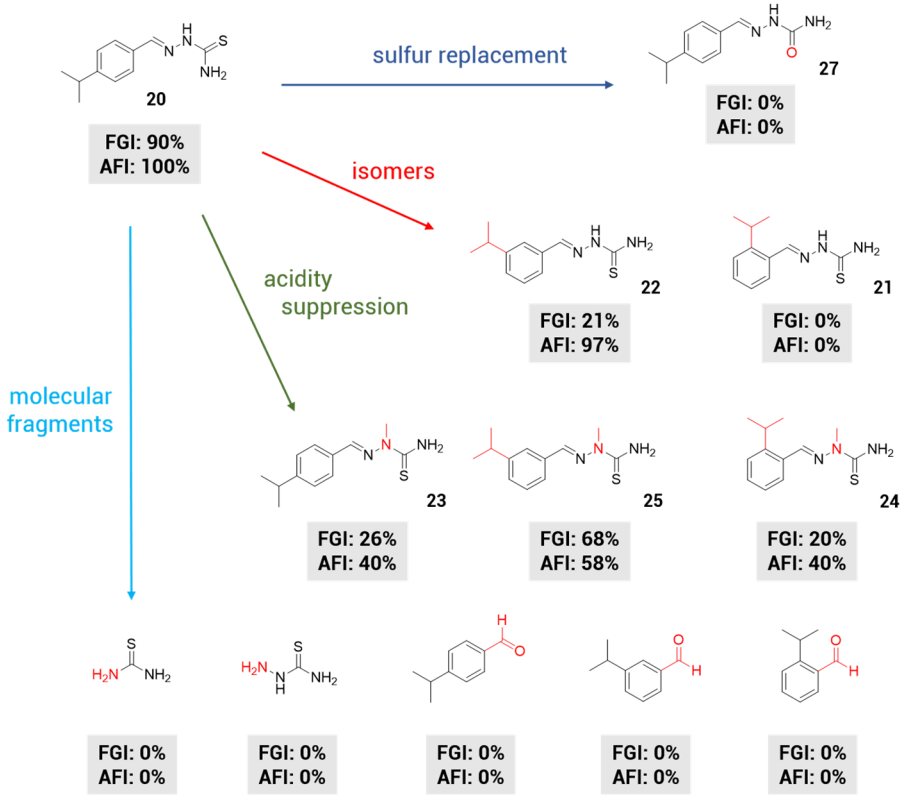

Figure 30: Effects of the cuminaldehyde structural modification on A. flavus. FGI indicates fungal growth inhibition percentage at 100 μM and AFI indicates aflatoxin production inhibition percentage at 100 μM.

The last class of derivatives were the metal complexes of zinc and copper. They were synthesised using **20**, **21** and **22** as anionic ligands to obtain neutral complexes with general formula [M(ligand)$_2$], where M = Zn(II), Cu(II). The complexes gave different results depending on their metal centre. Copper complexes showed lower antiaflatoxigenic power than the corresponding free ligands, whereas the zinc derivative was able to decrease the fungistatic effect of cuminaldehyde-TS **20**.

To sum up, we synthesised and tested sixteen different cuminaldehyde-TS derivatives. The N^2 methylation and the sulfur replacement were not effective derivatisations, whereas the shift of the isopropyl group from *para* to *meta* position gave origin to **22**, a very selective anti-aflatoxigenic compound which did not inhibit the fungal growth.

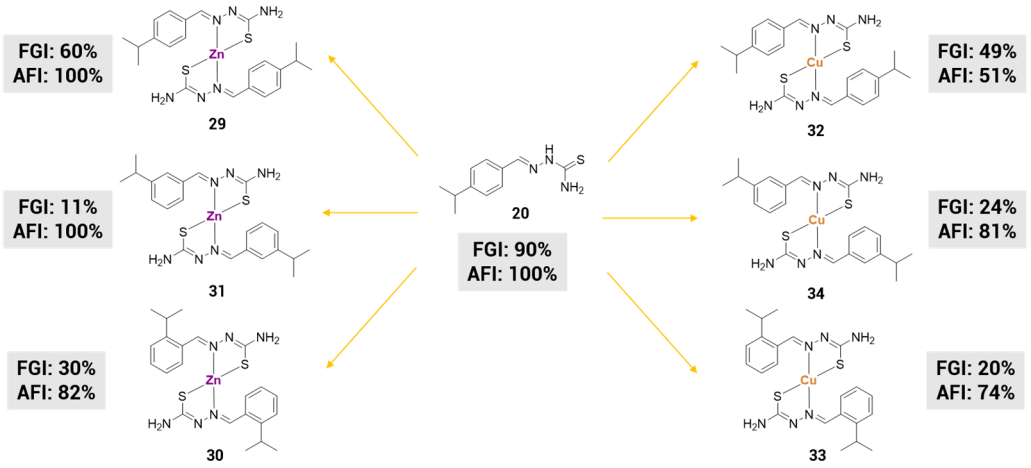

Figure 31 Effects of the cuminaldehyde family metal complexes on A. flavus. FGI indicates fungal growth inhibition percentage at 100 μM and AFI indicates aflatoxin production inhibition percentage at 100 μM.

The introduction of a metal ions (*Figure 31*) generally did not improve the ligands performances, except for [Zn(para)$_2$] which resulted less fungistatic than cuminaldehyde-TS **20**. In the light of these data, we decided to submit the para **20**, meta **22**, ortho **21** derivatives and their metal complexes to more detailed studies. The following step, according to the Aflatox project workflow, was the cytotoxicity evaluation on the three healthy cell lines HFL1, Hs27, Crl1790. These tests (*Table 9*)

revealed that the metal complexes are all cytotoxic, whereas the ligands have no effects on healthy cell proliferation.

	cytotoxicity		
	Hs27 GI_{50} (μM)	**HFL1 GI_{50} (μM)**	**Crl1790 GI_{50} (μM)**
20	>100	85	>100
22	>100	>100	>100
21	>100	>100	>100
32 (Cu)	insoluble	insoluble	insoluble
34 (Cu)	26	32.5	31.5
33 (Cu)	18	32	16
29 (Zn)	21	26	33.5
31 (Zn)	41.5	42	54
30 (Zn)	36	33	30

Table 9: GI_{50} values of cuminaldehyde derivatives on the three healthy cell lines Hs27, HFL1 and Crl1790.

All these experiments were inserted in the database that was subsequently used to cross-correlate the data. The query used to interrogate the database was designed to identify a non-harmful but anti-aflatoxigenic agent with a mode of action that does not interfere with the fungal primary metabolism. We applied the following filters: aflatoxin production inhibition higher than 75%, fungal growth inhibition lower than 25%, no cytotoxicity in all the three healthy cell lines and no mutagenicity. The compound which satisfied all the requests was **22**, and therefore we decided to further investigate its mode of action.

This was a successful example of the hit-to-lead approach applied to solve agricultural issues. We started by identifying an anti-aflatoxigenic and fungistatic lead compound from a preliminary screening, it was subsequently used to design a series of derivatives and these highlighted some interesting structure-activity relationships. Finally, using

the Aflatox database, we identified an optimised form of the lead compound which is perfectly suitable to be analysed in more in detail.

4.3.1 Action mechanism of **22**

This work was published as "*Structural modification of cuminaldehyde thiosemicarbazone increases inhibition specificity toward aflatoxin biosynthesis and sclerotia development in Aspergillus flavus*" (Applied Microbiology and Biotechnology **2017**, 101, 6683–6696).

The lead optimisation of cuminaldehyde-TS **20** led to the discovery of **22** which is both safe and anti-aflatoxigenic with a mode of action that seems not to interfere with the fungal primary metabolism. To investigate the mechanism of action of **22** we set up a series of different experiments:

The anti-oxidant activity

Since several studies reported that many synthetic and natural compounds effective to contrast AF biosynthesis had also high anti-oxidant power and significant ROS scavenging activity, we started with the analysis of the anti-oxidant activity. We tested **22**, and we compared the results also with the data obtained for **20**, **21** and cuminaldehyde to verify if there are any correlations between the anti-oxidant activity and the aflatoxin production inhibitory effect. We estimated the anti-oxidant power through both *in vitro* and *in vivo* tests. At first, we performed the *in vitro* DPPH reduction assay. Both **21** and **22** displayed a strong anti-oxidant activity, higher than those of **20** (about 70%) and of cuminaldehyde (no detectable anti-oxidant activity) (*Figure 32* - C). However, these results did not show any correlation with the trend of the anti-aflatoxigenic power observed before. In fact, the ortho-isomer **21** was almost unable to inhibit aflatoxin production even if it showed a very high anti-oxidant activity. To confirm this observation, we performed two different *in vivo* tests: the spot assay (*Figure 32* – A and B). and the Petite frequency assay (*Table 10*). The first uses *S. cerevisiae* as a model organism and the antioxidant activity is evaluated as the

beneficial effect that a compound shows in contrasting the oxidative stress induced by hydrogen peroxide. The second uses a mutant of the *S. cerevisiae* which has a particular phenotype (the *petite* phenotype) that is expressed only in oxidant conditions and it does not occur in the presence of antioxidant compounds. The measure of the "*petites*" in the cultures is a measure of the antioxidant activity. The results of the two *in vivo* tests confirmed the absence of correlation between antioxidant and anti-aflatoxigenic power.

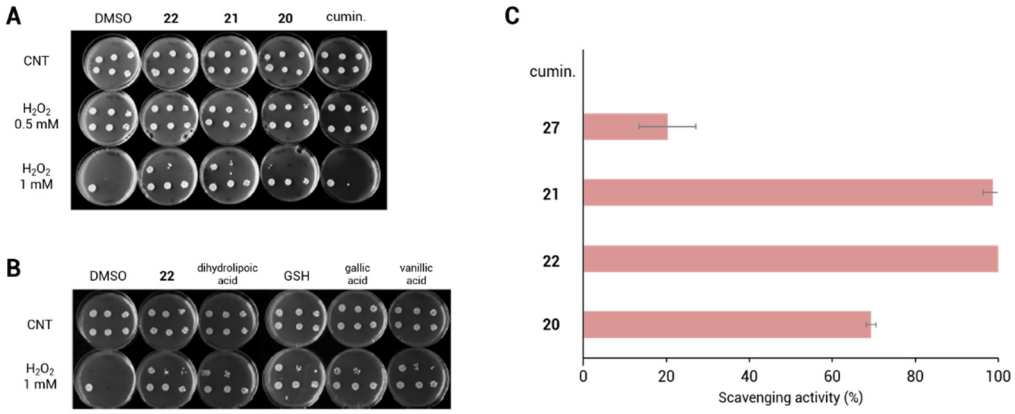

*Figure 32: Anti-oxidative response. A. Yeast bioassay. Three serial dilutions of yeast cultures were spotted at two different hydrogen peroxide concentrations and in presence of 50 µM samples of **20**, **21** and **22**. or 0.5% DMSO as control. B. **22** (50 µM) anti-oxidant power was compared to that of various natural anti-oxidants, namely dihydrolipoic acid, gallic acid, vanillic acid, and glutathione (GSH) in presence of H_2O_2 (1 mM). Yeast cultures were incubated for 7 days at 28 °C. C. In vitro anti-oxidant assay (DPPH assay). The values of the scavenging activity of the compounds (75 µM) are expressed in percentage of inhibition in relation to ascorbic acid (30 mM) which has scavenging activity (100%).*

Strain	22	DMSO	Dihydrolipoic acid	ethanol
mip 1^{Y757C}	9.8±1.3	20.5±0.2	10.5±0.4	23.6±3.3
mip 1^{G807R}	5.0±1.2	8.3±0.1	9.2±1.7	9.0±0.4

*Table 10: Effect of **22** on petite induction in two mip 1 yeast mutants. Petite frequency is reported as the percentage of colonies showing the petite phenotype after a 5-day incubation at 28 °C.*

Effect of 22 on *A. flavus* proteome

Since we had not found any direct correlation between the anti-aflatoxigenic action of **22** and its anti-oxidant power, we decided to investigate its mode of action through the analysis of changes in the protein expression between a sample treated and a control. The proteome separation was obtained by two-dimensional electrophoresis (2D PAGE), as described in detail in the *Biological test protocols* section (*Figure 33*).

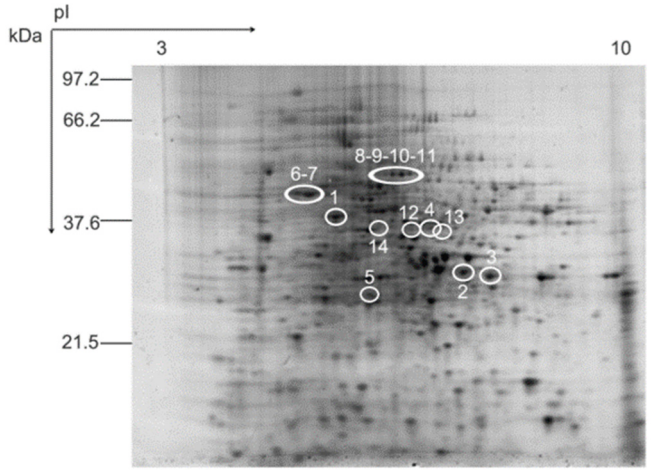

Figure 33: Gel showing the localization of the differentially expressed spots in A. flavus cultures treated with 50 µM solution of ***22****. Circles show the position of the identified spots. Protein extracts were separated on 7-cm-long IPG strips with a pH gradient from 3 to 10, followed by 12% SDS-PAGE. The protein spot number refers to the numbers with which are indicated proteins in Table 11.*

We obtained 434 spots per gel and 28 of them were differentially expressed (16 spots upregulated and 12 downregulated). We were able to recover 14 of these differential spots whose proteins were subsequently identified using LTQ-Orbitrap mass spectrometry and SEQUEST protein mass database (*Table 11*). Of the 16 recovered spots, 9 corresponded to unique proteins. Four spots matched with the same polypeptide (the aldehyde dehydrogenase (*aldA*) - B8N8T4) even if they showed different isoelectric points. This suggested that the relevant spots were affected by different post-translational modifications.

No.	SSP	Accession	Description	Score	Coverage	Number of protein	Number of unique peptides	Number of AAs	MW (kDa)
1↓ [a]	3604	Q9P900	Dimethyl sterigmatocystin 6-*O*-methyltransferase OS = *Aspergillus flavus* (OMTB_ASPFL)	63.37	54.92	22	10	386	43.1
2↓	6514	B8ND04	Malate dehydrogenase, NAD-dependent OS = *Aspergillus flavus* (B8ND04_ASPFN)	108.20	79.46	28	12	331	34.7
3↓	7407	I8TTW0	Malate dehydrogenase OS = *Aspergillus oryzae* (I8TTW0_ASPO3)	69.52	80.88	27	11	340	35.7
4↓	6601	P41747	Alcohol dehydrogenase 1 OS = *Aspergillus flavus* (ADH1_ASPFN)	15.73	31.71	1	2	350	37.0
5↓	4403	I7ZL55	Uncharacterized protein OS = *Aspergillus oryzae* (I7ZL55_ASPO3)	8.17	42.60	2	3	223	25.1
6↑	2704	B8NWC9	ATP synthase subunit β OS = *Aspergillus flavus* (B8NWC9_ASPFN)	158.71	80.08	12	18	517	55.4
7↑	2706	B8NWC9	ATP synthase subunit β OS = *Aspergillus flavus* (B8NWC9_ASPFN)	226.65	84.14	11	22	517	55.4
8↑	4706	B8N8T4	Aldehyde dehydrogenase AldA, putative OS = *Aspergillus flavus* (B8N8T4_ASPFN)	65.54	61.37	10	10	497	53.9
9↑	4712	B8N8T4	Aldehyde dehydrogenase AldA, putative OS = *Aspergillus flavus* (B8N8T4_ASPFN)	170.35	72.43	10	23	497	53.9
10↑	5707	B8N8T4	Aldehyde dehydrogenase AldA, putative OS = *Aspergillus flavus* (B8N8T4_ASPFN)	115.61	68.41	10	18	497	53.9
11↑	5712	B8N8T4	Aldehyde dehydrogenase AldA, putative OS = *Aspergillus flavus* (B8N8T4_ASPFN)	43.32	40.85	9	4	497	53.9
12↑	5608	B8NWT2	Zinc-binding oxidoreductase, putative OS = *Aspergillus flavus* (B8NWT2_ASPFN)	31.69	59.13	3	6	323	35.7
13↑	6501	B8NWT2	Zinc-binding oxidoreductase, putative OS = *Aspergillus flavus* (B8NWT2_ASPFN)	109.01	80.80	4	16	323	35.7
14↑	4607	I7ZW89	Transaldolase OS = *Aspergillus oryzae* (I7ZW89_ASPO3)	26.39	24.69	8	12	324	35.5

Table 11: Detailed information for each protein identified in the gel in Figure 33. Variation in spot abundance between A. flavus proteome treated with 22 (50 µM) and control (0.5% DMSO). Fold change was considered statistically significant when it exceeds both a fold of variation >2 and a $p < 0.05$.

Similarly, two spots were identified as ATP synthase subunit beta (B8NWC9) and two spots as zinc-binding oxidoreductase (B8NWT2). The remaining spots were identified as alcohol dehydrogenase 1 (*adh1*; P41747), transaldolase (I7ZW89), two malate dehydrogenase gene products (B8ND04 and I8TTW0), an *A. flavus* uncharacterised protein (B8NSV9), and dimethyl sterigmatocystin 6-O-methyltransferase (Q9P900). This last protein resulted particularly interesting because it belongs to the aflatoxin biosynthetic pathway and its expression is directed by the *aflO* gene. The downregulation of *OmtB* in the treated culture fits well with the observed anti-aflatoxigenic effect of **22**, whereas the other up or down regulations are associated with polypeptides involved mostly in the carbon/energy metabolism (like *adh1*), suggesting that **22** has also an effect on some crucial cell functions.

Gene expression analysis

To validate the proteomics, we analysed the expression of some of the genes encoding the proteins which resulted up or down regulated. We also added the study of a subset of genes that are involved in the regulation of aflatoxin biosynthesis (*Figure 34*). Specifically, using the Quantitative Real Time Polymerase Chain Reaction (qRT-PCR) we examined firstly the expression of *aflO* and *adh1* genes, then we studied the expression of *aflS*, *aflD*, *veA*, *laeA*, *nsdC*, and *nsdD* in *A. flavus* cultures grown either in the presence of **22** or in control condition. The proteomic results were confirmed since both *aflO* and *adh1* were downregulated in **22**-treated cultures. The analysis of the other genes belonging to the aflatoxin biosynthetic cluster showed that also *aflD* and *aflS* were downregulated. *aflD* encodes two enzymes that catalyse respectively an early and a later step of the AF biosynthetic pathway, whereas *aflS*, in conjunction with *aflR*, is an inherent regulator of many aflatoxin biosynthetic genes. Altogether, these data give evidence that **22** influence aflatoxin production modulating the transcription of genes that are directly involved in the biosynthetic process. However, we cannot exclude the possibility that the target of **22** is upstream of the regulatory genes located in the aflatoxin gene cluster. In this sense, it should be noted that **22** not only inhibits the aflatoxin production, but also impairs sclerotia development and the differentiation of proteins involved in primary metabolic functions.

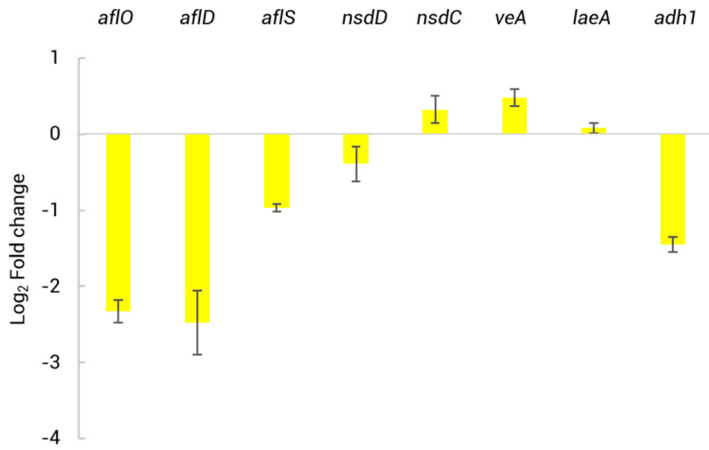

Figure 34: Fold change of gene expression in response to the treatment with ***22****.*

4.3.2 Molecular target of **22**

The data we collected so far are consistent with the hypothesis that at least one molecular target of **22** could be involved in the carbon flow and in the ox/red balance of the fungal cell. To best characterize this target, we decided to complement the previous analyses using *Saccharomyces cerevisiae* as a model system to validate our observations which are otherwise hard to be verified in fungus due to the lack of available literature and reliable protocols. In addition, *S. cerevisiae* is an organism in which it is possible to study separately the fermentative and non-fermentative metabolism. At first, we performed a disk diffusion assay to assess whether **22**, together with **20** and **21** as a control, differently affects yeast growth on a fermentable (2% glucose) or a non-fermentable (2% ethanol) carbon source. None of molecules affect cell growth on glucose medium, whereas **20** and **22** induce the formation of an inhibition halo in the presence of ethanol, not observed in the treatment with **21**. Interestingly, this is consistent with the observation that other anti-aflatoxigenic compounds affect yeast growth on ethanol, while compounds with no inhibitory effect on aflatoxin accumulation, share the same behaviour of **21**. Since *S. cerevisiae* in the presence of ethanol can proliferate only through mitochondrial respiration, the observation that **22** inhibits yeast growth in these conditions led us to hypothesise that

it induced a mitochondrial impairment. This effect is not detectable in fermentative condition, where glucose allows yeast to proliferate even with no mitochondrial activity. We then tested the effect of **22** on yeast cells respiration (levels of O_2 produced), and this allowed us to identify a reduction in response to the addition of **22**. Finally, to find the specific mitochondrial target, we tested the effect of **22** on the respiratory chain complexes. From the analysis, a concentration-dependent negative effect of **22** was observed on all the component of the respiratory chain when administrated to *in vivo* cultures (18 hours treatment). However, when the effect was assessed on isolated mitochondria, complex III activity resulted to be the only one inhibited.
(The experimental details of the experiments on the yeast model are not described in this thesis because they are out of the competence and purposes of this PhD project. They were performed by Dott.ssa Cristina Dallabona (*Molecular Genetics and Biotechnology Lab*. - University of Parma).

Molecular docking studies

A structure-based docking study was performed to investigate the intermolecular interactions responsible for the **22** activity on complex III (*bc1*) of the mitochondrial chain. It is known that molecules able to bind cytochrome *bc1* in Q_i site, like antimycin (AMY), can disrupt the Q-cycle and the entire enzyme turn-over[72]. This action is considered also responsible for the AMY ability to inhibit biosynthesis of aflatoxin in *A. flavus*[73]. In view of the similarities between AMY and **22** effects, we virtually studied the cytochrome *bc1* inhibition in the presence of **22** in the AMY binding site. The docking method was developed using *Gold v5.5* and optimised to compare **22** with AMY. Structural information about the protein was taken from the protein data bank (PDB ID: 3bcc). 3bcc is a cytochrome *bc1* structure with AMY as co-crystallized inhibitor located in Q_i region. The protein structure to be used in the calculations was prepared by deleting solvent molecules and AMY from the structure and by adding hydrogen atoms. A 6 Å cavity centred in the Q_i region of the protein was used as binding site. A 50-run docking approach was adopted, and the poses obtained were scored using the *Chemscore* fitness function (see *Molecular docking* section). In addition, all the poses were rescored using the *ChemPLP* function. The entire docking protocol was validated

using the self-docking approach and AMY was docked successfully[74,75] with RMSD 1.403 Å.

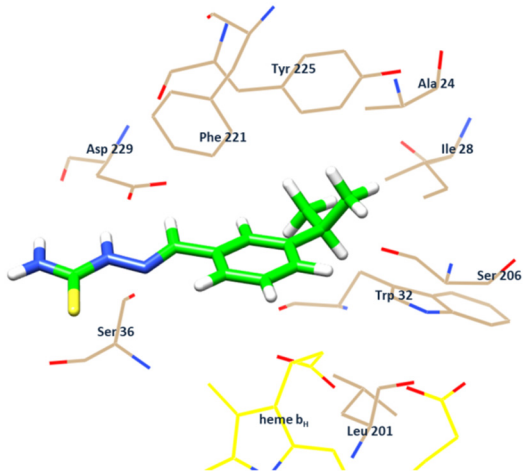

*Figure 35: Best docked pose of **22** into the 3bcc binding pocket.*

Figure 35 shows the best pose of **22** into the Q_i site. In detail (*Figure 36*), the hydrophobic environment formed by Phe221, Ile28, Tyr225, Ala24, Trp32 and Leu201[76] allowed to create a binding pocket in which the aromatic ring of **22** can be efficiently stabilised. In addition, **22** bound Asp229 with a strong hydrogen bond (2.001 Å) between the N^2 of the TS and the carboxyl group of the Asp229. This bond seemed able to lock **22** into the binding site, facing the aromatic portion of the ligand with the hydrophobic cavity of the protein. It is also interesting to notice that **22** (like AMY) resulted really close to heme b_H (3.376 Å). This proximity is considered fundamental in the mechanism of inhibition of AMY since the heme b_H is involved in the oxidation of ubiquinol to ubiquinone, a crucial step in the Q-cycle. The use of the *Chemscore* fitness function enabled us to predict a binding energy value to each pose[77,78]. This tool was very useful since energy value obtained from AMY self-docking was used as a reference to evaluate the binding strength of **22**in the Q_i region. The two binding energies obtained for **22** and AMY are really close: ΔG_{bind}(AMY) = -6.05 kcal/mol and ΔG_{bind}(**22**) = -5.96 kcal/mol. This result is perfectly in line with the experimental results that underlined a similarity between the **22** and AMY mitochondrial inhibition effect.

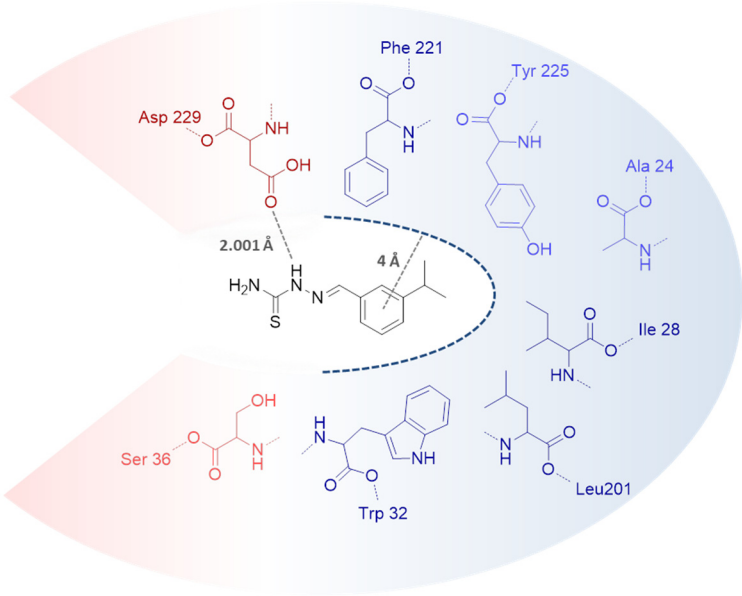

*Figure 36: Schematic representation of the binding mode of **22** into the 2bcc binding pocket. The hydrophilic area is indicated in red, while the hydrophobic pocket is indicated in blue.*

4.4 Jasmone derivatives

Many studies revealed that *cis*-jasmone is involved in plant defence systems. It is released from the leaves and the flowers of many plants (i.e. jasmine, neroli, bergamot) as a repellent for pests. Moreover, *cis*-jasmone and some other similar derivatives are produced by wounded plants to suppress the infection of fungi and herbivores including *A. flavus*, *Fusarium verticillioides*, and *Helicoverpa zea*[79]. *Cis*-jasmone is an oxylipin produced starting from α-linolenic acid through two possible multi-step biosynthetic pathways[80] involving lipoxygenases (*Figure 37*). Some natural metabolic routes for the α-linolenic acid oxidation were identified and several final products and many intermediates have specialized roles in plant defence systems. This class of compounds are called "death acids" because they can promote cytotoxicity and cell death in the biotic agents.

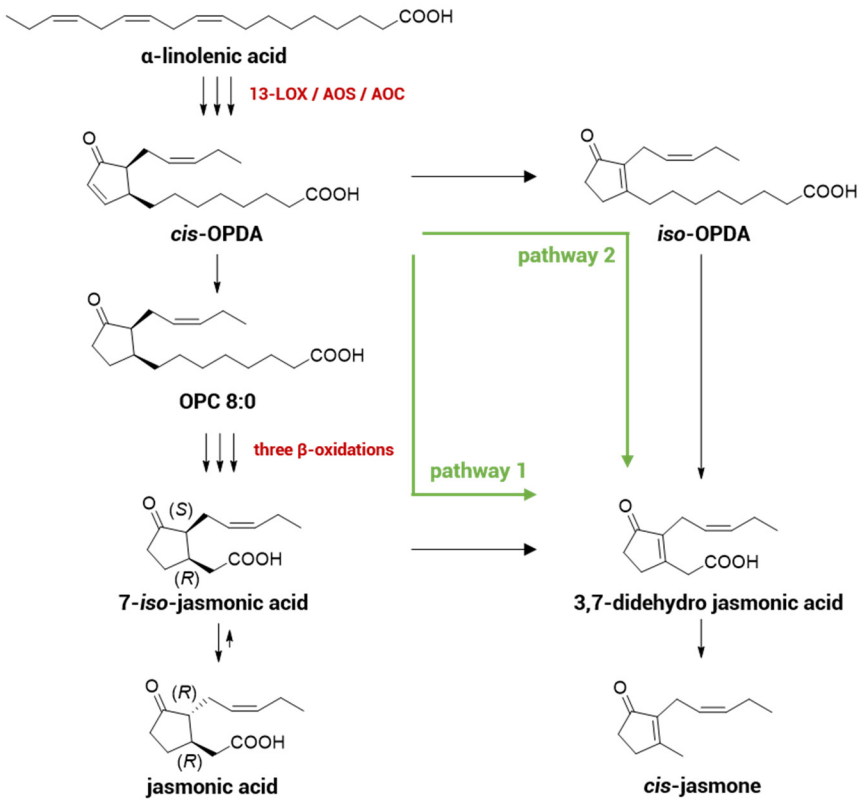

Figure 37: Cis-jasmone and jasmonic acid biosynthetic pathway.

Interestingly, one recent piece of evidence confirmed the *cis*-jasmone biosynthesis also in fungi[81]. Its biological role in these organisms is still debated, however it was reported that some fungi produce jasmonic acid (an intermediate of the *cis*-jasmone biosynthesis) as phytohormone to disturb signalling systems of plants and then to start their infection. This evidence brings to believe that *cis*-jasmone and its derivatives are crucial molecules for communication and signalling in plants and fungi and therefore interesting molecules to study for agricultural applications. For our purposes, the most interesting evidence is the effect of some *cis*-jasmone derivatives on *A. flavus* growth and development.

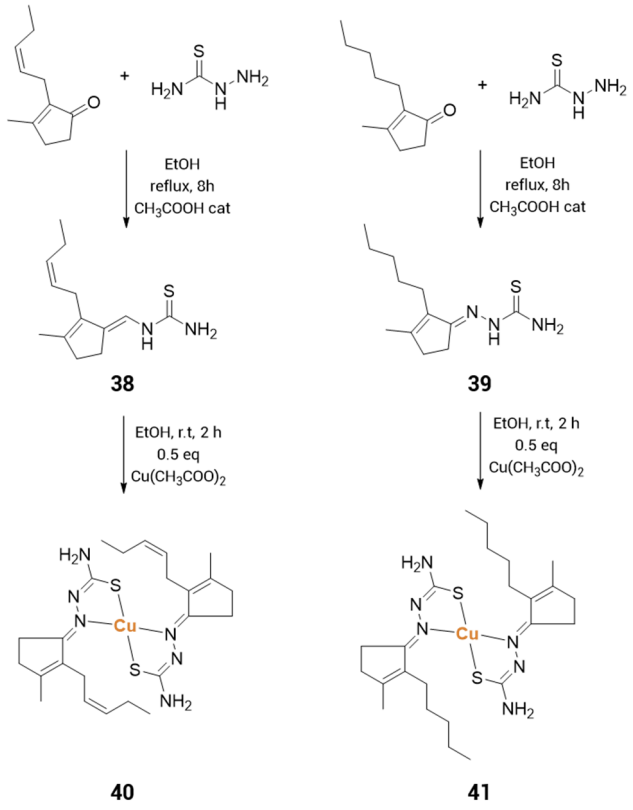

Figure 38: List of components of the cis-jasmone family.

Starting from these data, we decided to explore the effect of *cis*-jasmone on the aflatoxin biosynthesis within the Aflatox project. The first step was to compare the effects on *A. flavus* of the natural *cis*-jasmone with those of the corresponding TS (**38**). To gain deeper understanding of this class of molecules we synthesised and tested

also the TS of the dihydrojasmone (**39**), a natural analogue of the *cis*-jasmone hydrogenated in the aliphatic C_5 chain. Finally, we tested the corresponding copper complexes (**40** and **41**). The general scheme of the synthesis of all the derivatives is reported in *Figure 38*, whereas the *Jasmone derivatives* experimental section. The effects on *A. flavus* are reported in *Figure 39* and they show some interesting differences between the derivatives. In detail, the natural ketone (the *cis*-jasmone) showed a mild inhibitory effect on the aflatoxin production (about 25% at 100 μM) and no fungistatic effect. The two TSs **38** and **39** showed similar effects, a good aflatoxin production inhibition associated with a mild effect on the fungal growth. In particular, **38** resulted to be a very good candidate since it was able to reduce the aflatoxin production of the 88% already at 50 μM. However, even more interesting data came from the two copper complexes **40** and **41**. Unlike their free ligands, they show different activity trends. In **40** both the anti-aflatoxigenic and fungistatic effects raised significatly, whereas **41** raised the aflatoxin production inhibition of **39** and almost cancelled its fungistatic effect.

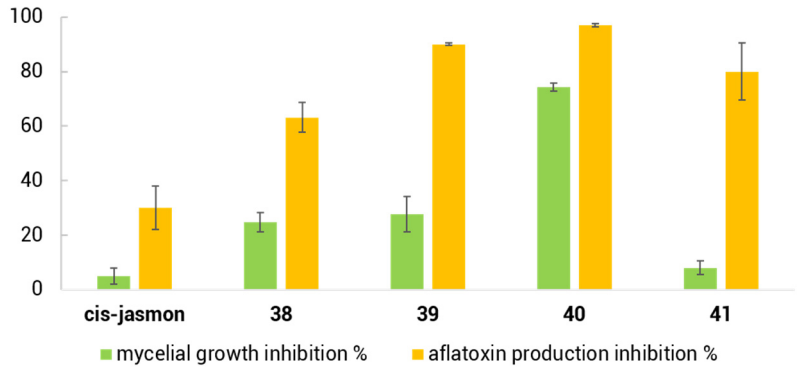

Figure 39: Effects of the cis-jasmone family on A. flavus. Fungal growth inhibition and aflatoxin production inhibition percentages correspond to a 100 μM treatment with the desired sample.

4.4.1 Toxicity assessment

Human cell lines

The *cis*-jasmone family resulted one of the most effective group of molecules of the Aflatox project since every derivatives showed an aflatoxin inhibition higher than 50% always associated with lower effect on fungal primary metabolism. For these reasons, every compound was submitted to the cytotoxicity evaluation. The IC_{50} values on the three healthy cell lines Hs27, HFL1 and Crl1790 are reported in *Table 12*. They unfortunately evidenced a strong antiproliferative effect of copper(II) complexes **40** and **41**. The cytotoxicity necessarily came from the metal, because both the organic molecules **38** and **39** resulted non-toxic.

	Hs27 GI_{50} **(μM)**	**HFL1** GI_{50} **(μM)**	**Crl1790** GI_{50} **μM**
cis-jasmone	>100	>100	>100
cis-jasmone-TS (**38**)	>100	>100	>100
dihydrojasmone-TS (**39**)	>100	>100	>100
Cu(*cis*-jasmone-TS)$_2$ (**40**)	28	5	38
Cu(dihydrojasmone-TS)$_2$ (**41**)	38	23	40

Table 12: GI_{50} values of cis-jasmone derivatives on the three healthy cell lines Hs27, HFL1 and Crl1790.

***A. cepa* cultures**

Since **38** and **39** had no effects on human cell lines, they were submitted to the last set of experiments provided in the Aflatox project, namely the in-depth analysis of the effects vegetal cell lines. In *Table 13* are summarised the results.

	***A.cepa* proliferation**		**mutagenicity**	**genotoxicity**	
	Mitotic index reduction	**AMES test**	**Micronucleus test (µM)**	**Mitotic index reduction (µM)**	**AMES test**
cis-jasmone-TS (**38**)	>100	100	Non-mutagenic	100	10
dihydrojasmone-TS (**39**)	>100	>100	Non-mutagenic	>100	10

Table 13: Collection of the data about the toxicity on A.cepa of cis-jasmone derivatives.

Both **38** and **39** resulted non-mutagenic and they did not interfere with *A. cepa* proliferation. They also did not show genotoxic effect in the micronucleus test, but they resulted toxic in the comet assay and able to induce chromosomal abnormalities in *A. cepa* starting from a 10 µM concentrations.

4.4.2 Anti-oxidant activity

Keeping in mind the potential harmful effect of **38** and **39**, we decided to investigate all the same the possible mechanism behind their anti-aflatoxigenic effect. In many *Aspergillus* species, anti-oxidative stress response is considered a prominent factor involved in the control of secondary metabolism, and several both synthetic and natural compounds that modulate secondary pathways - such as AF biosynthesis and sclerotia biogenesis - possess a ROS scavenging activity. In particular, the sclerotial metamorphosis in filamentous fungi seems induced by oxidative stress[82] according to the scheme reported in *Figure 40*.

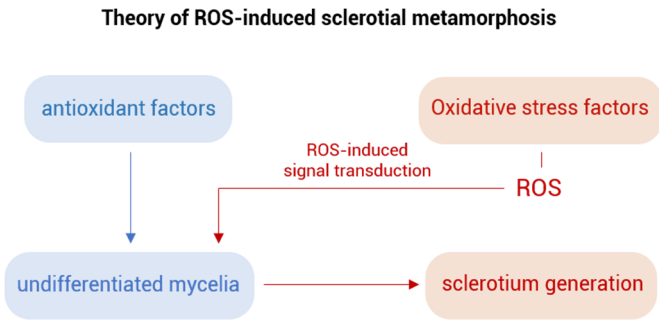

Figure 40: Schematic representation of the effect of ROS on sclerotia development.

In this context, we tried to find relationships between predicted antioxidant scavenging ability and secondary metabolism modulation through the comparison between the antioxidant power determined *in vitro* and the sclerotia development using the Aflatox database as a support. The *Figure 41* compares the results of the DPPH test (used to evaluate the antioxidant power *in vitro*) and those of the sclerotial development analysis. It also reports the images of the *A. flavus* cultures after the treatments to investigate the metamorphosis induced by our derivatives.

The effects induced by jasmone-derivatives on the biogenesis of sclerotia differed significantly depending on the molecule examined. *Cis*-jasmone had no effect, as confirmed also by the images (*Figure 41* - A) of the treated cultures which are similar to those treated with the control (DMSO). The free TSs **38** and **39** showed a high experimental variability, however both the treatments lowered significantly the number of sclerotia per colony area. The effect is also clearly visible in the pictures (*Figure 41* – A) of the treated cultures where only the white mycelium and not the brown sclerotia are visible. Surprisingly, **40** and **41** had completely different effects. **40** stopped completely the sclerotia biogenesis, whereas **41** did not have any effect on sclerotia. This difference between the effects on sclerotia development observed between **40** and **41**, were consistent with the data about the mycelial growth inhibition which highlighted the fungistatic effect of **40** and the null effect of **41**. The fungal growth inhibition induced by **40** is clearly visible in the pictures (*Figure 41* - A), where the area occupied by the *A. flavus* colonies is extremely reduced if compared with the control. The growth inhibition is ascribable to the complete absence of sclerotia, which prevented the germination and then the development of new colonies.

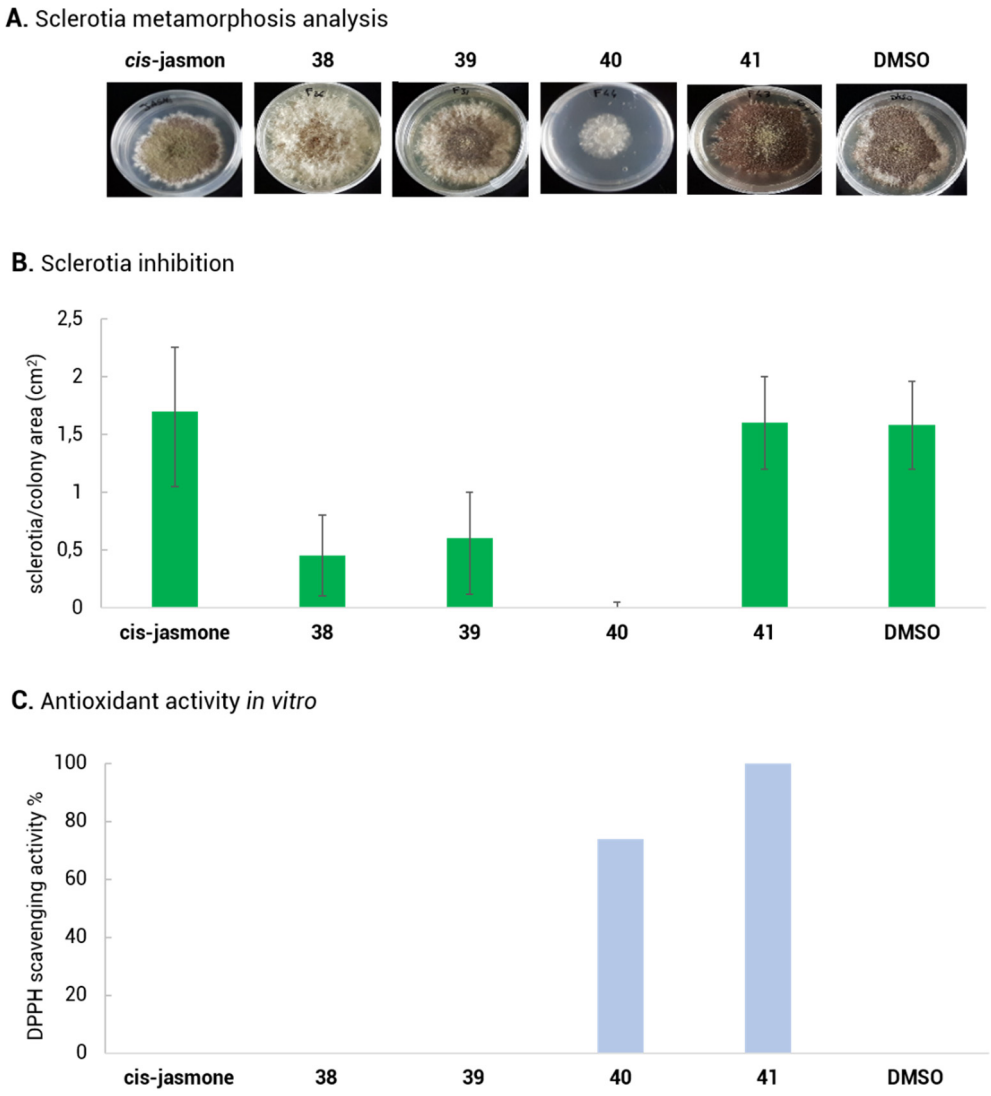

Figure 41: Comparison between antioxidant scavenging activity (DPPH assay) of jasmone-derivatives (C) and their effect on sclerotia development in A. flavus cultures (B: number of sclerotia per colony area – A: pictures of treated A. flavus cultures). Molecules were tested at a 50 µM concentration.

The antioxidant activity *in vitro* was estimated as the percentage of DPPH reduced by a certain concentration of the sample. This test showed that the two free ligands **38** and **39** have no antioxidant activity, whereas the two metal complexes are both

extremely effective if compared to the control. There results were necessarily related with the presence of copper, which is a redox active metal centre able to reduce DPPH. However, we did not find any correlations between the antioxidant power of our derivatives and their biological effects. The anti-aflatoxigenic effect of **38** and **39** seems related to the sclerotia inhibition and it suggests that their target(s) is/are involved in an upstream biochemical process in common between the aflatoxin and sclerotia metabolisms. The strong anti-aflatoxigenic effect of **40** is instead unspecific and related to the inhibition of the fungal primary metabolism. This explain its strong effect on fungal growth, which inhibits the aflatoxin and sclerotia biosynthesis as a ripple effect. Finally, **41** resulted the most interesting compound. The outcomes suggest a specificity of action and, unlike **38** and **39**, its target seems to be located in a downstream metabolic point closely related with aflatoxin biosynthesis. This assumption is supported by the biological results that showed the great inhibitory effect of **41** on aflatoxin biosynthesis and the negligible effects on sclerotia and fungal growth.

4.5 Long hydrophobic tail derivatives

As mentioned in the introduction, aflatoxins are produced by a sequence of almost 15 enzymatic reactions. The biosynthesis of aflatoxins is a complex system of cyclizations and oxidations which lead to the formation of the final poliketide. The enzymes involved in this process are called polyketide synthases (PKSs) and each enzymatic domain catalyse a specific cycle of the polyketide chain extension and/or β-keto processing[83]. Since the biosynthesis of aflatoxin is not part of the fungal primary metabolism, it uses as precursor a compound already present in the organism: palmitic acid.

Palmitate is a C_{12} aliphatic chain with a terminal carboxylic acid function produced in the first step of the fatty acid synthesis and used as precursor for longer fatty acids. The biosynthesis is initiated with the selection of the acyl starter unit, followed by its transfer to an acyl-carrier protein (ACP) and then to the pksA, the first enzyme of the aflatoxin biosynthesis pathway. The presence of different starters coming from alien sources in the pksA palmitate binding site triggers processes of structural variation on aflatoxin and/or the block of the entire pathway[84]. In this context, we designed a series of TSs with different aliphatic chain lengths from seven to eleven carbon atoms. The use of long aliphatic groups with these lengths is aimed at the synthesis of mimics of the palmitate able to inhibit effectively pksA. All the compounds were obtained from the corresponding natural aldehydes, namely heptanal, octanal, nonanal, decanal and undecanal condensed with thiosemicarbazide (see experimental details in *the Long hydrophobic tail derivatives* section). In addition, we synthesized some derivatives of these molecules to identify some structure-activity relationships. Finally, we synthesized the corresponding copper(II) complexes to evaluate the effect of a redox metal centre on the biological activity of the TSs.

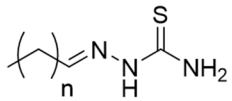

n = 5 Epta-TS (**42**) n = 8 Deca-TS (**48**)
n = 6 Octa-TS (**43**) n = 9 Undeca-TS (**49**)
n = 7 Nona-TS (**45**)

Figure 42: List of components of the cis-jasmone family.

4.5.1 Preliminary docking study

As a start, a structure-based docking approach was used to study the viability of an interaction between the TSs and pksA in the palmitate binding pocket. The molecular docking was performed with the *Gold* software (version 5.6.2) using the *ChemScore* function (see *Molecular docking* section). The computational method was validated measuring the RMSD (root-mean-square deviation) of atomic positions between palmitate in the crystal structure (the reference) and the best pose obtained for palmitate in the docking calculation. The RMSD value was 0.91Å which confirmed the accuracy of the method to predict the ligand position in the protein pocket[74,75]. The best pose of each TS was docked in a position similar to that of palmitate (*Figure 43*). All the aliphatic chains are unrolled and included in the hydrophobic pocket created by Tyr1568, Leu1511, Leu1508, Phe1551, Met1498, Met1495, Tyr1492 and Phe1501, whereas the TS moieties face the hydrophilic side of the binding pocked created by Gln1547, Asn1544, Asn1568 and His1345. In the hydrophilic environment the TSs, like the palmitate molecule, form some hydrogen bonds which stabilise the poses. Palmitate forms a strong hydrogen bond with Asn1568, whereas the TSs interact with Tyr1566 and Asn1544 creating single or multiple hydrogen bonds with different lengths using both the N^2 and N^4. All the hydrogen bonds are described in detail in *Figure 44* and *Table 14*.

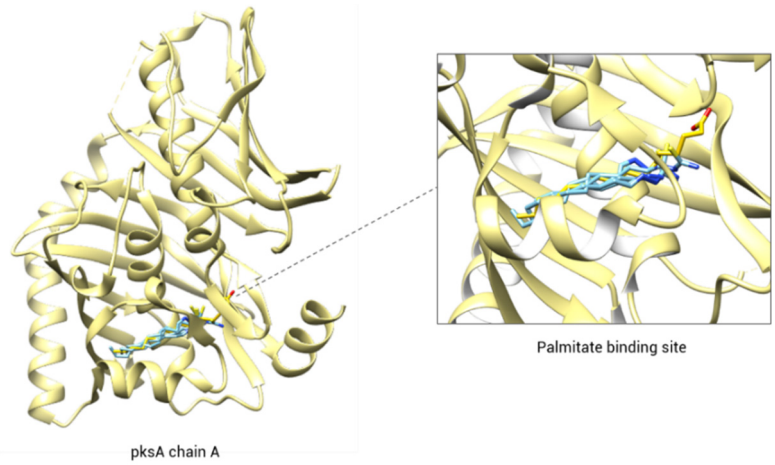

Figure 43: TS and palmitate docked into the palmitate binding site of pksA.

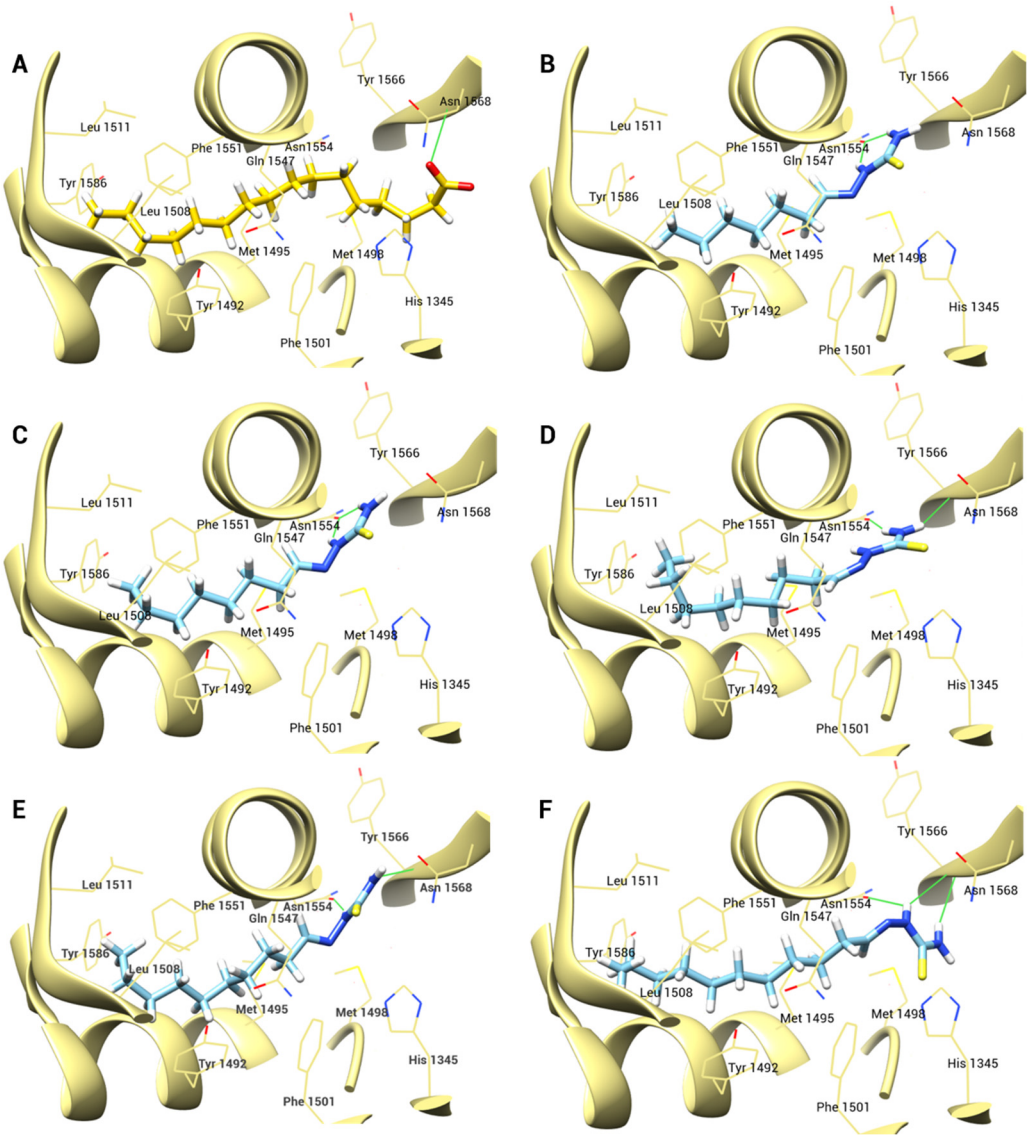

*Figure 44: Best docked position obtained for: A. palmitate, B. Hepta-TS (**42**), C. Octa-TS (**43**), D. Nona-TS (**45**), E. Deca-TS (**48**) and F. Undeca-TS (**49**).*

Analysing the hydrogen bonds, we noticed that every ligand uses the N^2 to bind Asn1554 and the N^4 to bind alternatively Tyr1566 (Nona-TS (**45**), Deca-TS (**48**) and Undeca-TS (**49**)) or Asn1544 (Hepta-TS (**42**), Octa-TS (**43**)). The only TS which creates

three hydrogen bonds is **49**: two with Tyr1566 (using the N^4 and the N^2) and one with Asn1554 (using the N^2).

	n° of carbon atoms in the aliphatic chain	n° of hydrogen bonds	pksA amino acid involved in the H-bond	ligand atom involved in the H-bond	H-bond length (Å)
Palmitate	16	1	Asn1568	O	1.785
Undeca-TS (**49**)	11	3	Tyr1566 / Asn 1554	2 x N^4 / N^2	2.163 / 1.992 / 2.736
Deca-TS (**48**)	10	2	Tyr 1566 / Asn 1554	N^4 / N^2	1.877 / 2.031
Nona-TS (**45**)	9	2	Tyr 1566 / Asn 1554	N^4 / N^2	1.757 / 1.893
Octa-TS (**43**)	8	2	Asn 1554	N^4 / N^2	1.907 / 2.009
Hepta-TS (**42**)	7	2	Asn 1554	N^4 / N^2	2.026 / 2.078

Table 14: List of the interactions between hydrophobic TSs and pksA binding site.

We estimated also the free energy of binding of each TS (*Table 15*). The calculation showed a direct relationship between the free energy of binding and the growing chain length. This relationship is ascribed to the growing importance of the lipophilic term in formula used to estimate the free energy of binding in the *GoldScore* function.

$$\Delta G_{binding} = \Delta G_0 + \Delta G_{h\,bond} + \Delta G_{metal} + \mathbf{\Delta G_{lipo}} + \Delta G_{rot}$$

	n° of carbon atoms in the aliphatic	ΔG kcal/mol	ranking
Palmitate	16	-8.88	#1
Undeca-TS (**49**)	11	-7.27	#2
Deca-TS (**48**)	10	-7.09	#3
Nona-TS (**45**)	9	-6.56	#4
Octa-TS (**43**)	8	-6.16	#5
Hepta-TS (**42**)	7	-5.65	#6

Table 15: Free energy of binding between hydrophobic TSs and pksA binding site.

4.5.2 Effects on *A. flavus*

The ranking obtained from the virtual screening was compared with the experimental ranking of the percentages of aflatoxin production inhibition (*Figure 45*- A) The trend of the anti-aflatoxigenic power seems to follow the trend predicted by the calculation, but surprisingly the TSs with an even-numbered aliphatic chains resulted more active than their closely related odd-chain derivatives. This structure-activity relationship led us to believe that odd-chain TSs induce a specific response in fungus and that the *in-silico* calculation cannot predict.

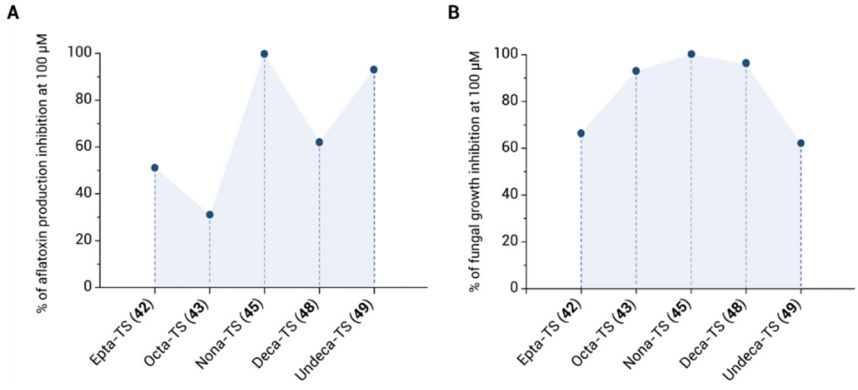

Figure 45: Effects of the hydrophobic TSs on A. flavus. (A. effects on aflatoxin production – B. effects on fungal growth). The data were plotted according to the carbon chain length.

An example of biochemical system which can distinguish substrates depending on the chain length is the fatty acids metabolism. In nature (including fungi), the most commonly occurring fatty acids have even aliphatic chains (i.e. palmitate) and they are metabolised through multiple steps of β-oxidations which create one acetyl-CoA molecule from each segment of two carbon atoms. Since an acetyl-CoA has two carbon atoms derived from the starting fatty acid, the final number of acetyl-CoA produced is half of the number of the chain length. When an odd chain fatty acid enters the mechanism, the β-oxidations produce acetyl-CoA molecules until the last step where the product is a propionyl-CoA molecule, which contains three carbon atoms of the starting chain (*Figure 46*). Since the metabolism of fatty acid is strictly related with polyketide biosynthesis and our TSs are compounds with structural characteristics similar to those of the lipids, we speculated that the reason of the higher anti-aflatoxigenic activity of odd chain derivatives could be related to this bio-chemical recognition system. Interestingly, in 2004, Zhang and co-workers examined the effect of propionyl- and acetyl-CoA on polyketide biosynthesis in *Aspergillus nidulans* and they claimed that propionyl-CoA has an inhibitory effect on polyketide production[85]. Since even in fungi the propionyl-CoA is produced by the β-oxidation of odd fatty acids and the docking studies confirmed the similarity of our derivatives with palmitate, we believe that our TSs are metabolised as lipids and that the odd chain TSs are responsible for the formation of propionyl-CoA that in turn inhibits polyketide biosynthesis and then the aflatoxin production. This hypothesis is consistent with the trend of the experimental data, but it cannot explain why Nona-TS (**45**) showed the highest anti-aflatoxigenic activity. A possible explanation of this phenomenon could derive from the docking analysis. In fact, looking at the estimated lengths of the hydrogen bonds (*Table 14*), **45** makes the shortest interactions. Since the length of a bond relates to its strength, the higher biological activity of Nona-TS (**45**) might be related to its ability to create more stable bonds with the pksA protein. The specific effect on aflatoxin biosynthesis shown by the odd chain TSs (**42**, **45** and **48**) was not visible in the results of the mycelial growth inhibition tests (*Figure 45*- B). However, the percentages of growth inhibition are rarely related to those of a very specific effect like aflatoxin production inhibition. On the contrary, it is usually the sum of all the possible effects induced by a molecule, and these rarely coincide with the inhibition of just one

target. The Nona-TS (**45**) clearly resulted to be the most effective fungicide, and the effect tends to be around this central value following a normal distribution.

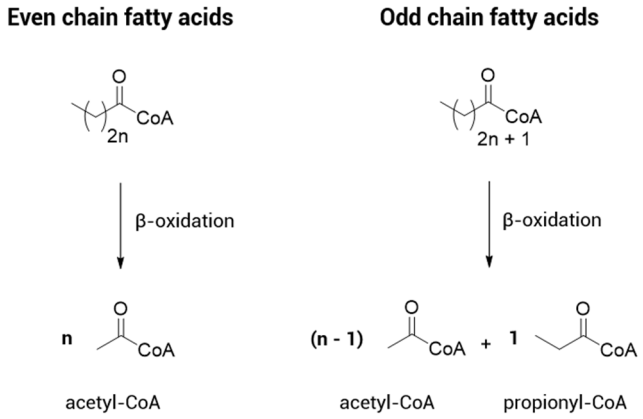

Figure 46: Schematic representation of the even and odd chain fatty acid metabolism.

4.5.3 Toxicity assessment

Human cell lines

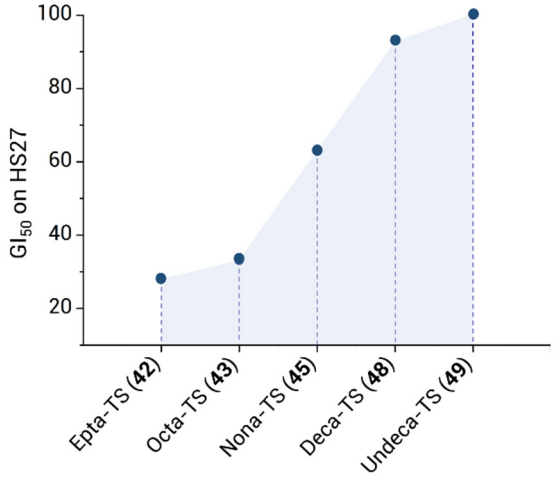

Figure 47: Relationship between the cytotoxicity on Hs27 and the chain length of the hydrophobic TS.

According to the Aflatox project workflow, we tested the cytotoxicity of our long aliphatic chain derivatives. Firstly, we tested all the five TSs on Hs27 cell lines and the IG_{50} obtained indicated that the cytotoxicity is directly proportional to the chain length (*Figure 47*). Subsequently, we completed the screening on the other two healthy cell lines with just odd chain derivatives **42**, **45** and **49**, the most interesting compound on fungus. The results (*Table 16*) confirmed a correlation between the cytotoxicity and the chain length in Crl1790, but not in HFL1. The raise of cytotoxicity along with the chain length is an interesting structure-activity relationship because, for example, in Hs27 the Hepta-TS (**42**) is not cytotoxic (GI_{50} > 100 µM), whereas the Undeca-TS (**49**) is strongly cytotoxic (GI_{50} 28.0 µM)

	n° of carbon atoms in the aliphatic chain	**Hs27 GI_{50} (µM)**	**HFL1 GI_{50} (µM)**	**Crl1790 GI_{50} (µM)**
Undeca-TS (**49**)	11	28.0	46.5	77.0
Deca-TS (**48**)	10	33.0	-	-
Nona-TS (**45**)	9	63.0	80.0	32.0
Octa-TS (**43**)	8	93.0	-	-
Hepta-TS (**42**)	7	>100	>100	>100

Table 16: GI_{50} values of hydrophobic derivatives on the three healthy cell lines Hs27, HFL1 and Crl1790.

The Hepta-TS (**42**) resulted not cytotoxic (GI_{50} > 100 µM) in all three cell lines and it was the only compound which showed the right characteristics to proceed to the last step

of the Aflatox project. It was therefore submitted to the genotoxicity analysis, mutagenicity and effects on *A. cepa* and the results are reported in *Table 17*.
Hepta-TS (**42**) resulted a weakly mutagenic agent and it was able to inhibit the *A. cepa* proliferation starting from 50 μM. The micronucleus test (which estimates the overall genetic damage) was negative, but we identified some chromosomal aberration already at 10 μM.

***A.cepa* proliferation**		**mutagenicity**	**genotoxicity**	
EC_{50} (μM)	**Mitotic index reduction (μM)**	**AMES test**	**Micronucleus Test (μM)**	**Chromosomal aberrations (μM)**
50	>100	Weakly mutagenic	>100	10

Table 17: Collection of the data about the toxicity on A.cepa of hydrophobic derivatives.

4.5.4 Metal complexes

Since we identified an interesting structure-activity relationship for Hepta-TS (**42**), Nona-TS (**45**) and Undeca-TS (**49**), we decided to synthesise and test also their corresponding copper(II) metal complexes. The anti-aflatoxigenic effects on *A. flavus* were compared using the results obtained at 100 μM for the free TSs and at 50 μM for the copper(II) complex taking into account the double amount of ligand contained in a single molecule of complex. Unfortunately, copper(II) did not improve the performances of the TSs (*Table 18*). The presence of the metal drastically lowered the activity of our best candidate Nona-TS (**45**), which as a free ligand was able to inhibit 100% the AF production, whereas when coordinated to copper the inhibition decreased to only 34.2%.

	n° of carbon atoms in the aliphatic chain	Aflatoxin production inhibition % at 100 µM free ligand	Aflatoxin production inhibition % at 100 µM copper(II) complex
Undeca-TS (**49**)	10	93.0	60.4
Nona-TS (**45**)	8	100.0	34.2
Hepta-TS (**42**)	6	51.0	16.3

Table 18: Effects of the hydrophobic TSs copper(II) complexes on A. flavus.

Even if the complexes did not improve the effects of our TSs on *A. flavus*, we tested anyway their cytotoxicity to complete the screening and to evaluate if the presence of the metal was able to affect the IG_{50} values of the free ligands (*Table 19*). However, the Nona-TS Cu (**53**) resulted more cytotoxic than Nona-TS (**45**), and Undeca-TS Cu (**55**) was impossible to test because insoluble in the cell culture medium. Moreover, the Hepta-TS Cu (**50**) (which contains the non-toxic ligand Hepta-TS (**42**)) showed a significant cytotoxicity in all three cell lines. This evidence indicates that the combination of a Cu(II) centre with this class of TSs worsens their performance and does not reach the thresholds/satisfy the characteristics required for the Aflatox project.

	n° of carbon atoms in the aliphatic chain	Hs27 IC_{50} (µM)	HFL1 GI_{50} (µM)	Crl1790 GI_{50} (µM)
Undeca-TS Cu (**55**)	10	insoluble	insoluble	insoluble
Nona-TS Cu (**45**)	8	30.5	35.0	44.0
Hepta-TS Cu (**42**)	6	29.0	10.0	30.5

Table 19: GI_{50} values of hydrophobic derivatives copper(II) complexes on the three healthy cell lines Hs27, HFL1 and Crl1790.

To sum up, the most interesting information we obtained from this study was the relationship between chain length and anti-aflatoxigenic activity. In the light of our results, the TSs functionalised with aliphatic chains that contain an odd number of carbon atoms are more active than compounds with similar chain length but with even numbers of carbon atoms. We attributed this effect to polyketide synthase inhibition by propionyl-CoA, which is selectively produced from the β-oxidation of odd chain fatty acids. The specificity of this structure-activity relationship onto the aflatoxin biosynthesis was confirmed from the evidence than the overall effect on fungal growth did not follow the same trend. The most effective compound on *A. flavus* resulted the Nona-TS (**45**) which completely inhibit both aflatoxin production and mycelial growth at 100 μM. However, it showed some cytotoxic effects on human cell lines. The safest compound was Hepta-TS (**42**), which was less effective on *A. flavus* than **45**, but capable of inhibiting aflatoxin production by 51% at 100 μM.

4.6 Non-effective compounds

1-(3-methoxyphenyl)-1-heptanone-TS

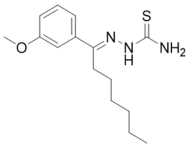

18

FGI: 36%
AFI: 47%

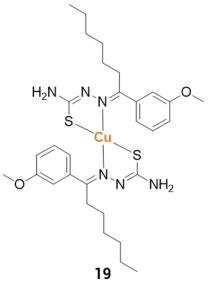

19

FGI: 15%
AFI: 35%

Khellinone-TS

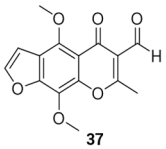

37

FGI: 0%
AFI: 10%

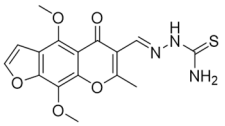

36

FGI: 5%
AFI: 25%

TS after the reduction of the iminic bond

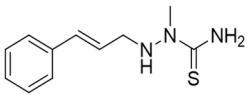

11

FGI: 15%
AFI: 45%

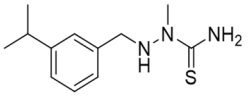

44

FGI: 4%
AFI: 10%

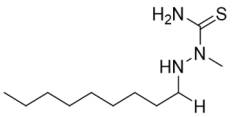

47

FGI: 50%
AFI: 6%

Octenal-TS

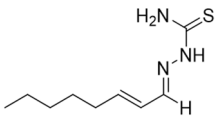

44

FGI: 96%
AFI: 87%

5 Topic 1 conclusions

The first section of the thesis describes the research and the experiments carried out to find innovative and effective compounds able to inhibit selectively the aflatoxin production in *A. flavus* cultures.

This project, called Aflatox, required three years of work and was divided in several stages. Firstly, we selected natural occurring aldehydes and ketones that were known to possess some interesting biological activity, like antioxidant power or plant growth inhibition. Then we prepared the corresponding TSs to create bio-active molecules able also to chelate metals like zinc and copper which have significant antifungal properties. All these molecules and the corresponding chemical components were tested on *A. flavus* to measure their inhibitory effects on fungal growth and aflatoxin production. In parallel, the cytotoxicity of each molecule was assessed using three different healthy cell lines (pulmonary, epithelial and intestinal) in order to find the safest candidates. In these stages we found a few interesting compounds that were subsequently used as parent molecules to develop families of derivatives which included modification of the chemical scaffold and the nature of the metal ion. All the derivatives were tested again, and the results were collected in a database to organise and optimise the search for the best hits. With this strategy we identified three very good candidates: the TSs of 2-acetylthiophene, 3-isopropylbenzaldehyde and cis-jasmone (**1**, **22**, **38**). These molecules showed at the same time aflatoxin production inhibition higher than 75%, fungal growth inhibition lower that 25% and no cytotoxicity (IC_{50} higher and 100 μM) in all the three human cell lines. These data highlighted that our three molecules are extremely selective anti-aflatoxigenic agents, since they have just a very low effect on the fungal growth and no cytotoxicity. We also found some extremely effective anti-aflatoxigenic metal complexes but all of them resulted toxic for the healthy human cell lines. The last step of the Aflatox project was the detailed study of the biological effects of the best candidates and the study of their mechanism of action. Derivative **1** (TS of 2-acetylthiophene) was submitted to several toxicity tests on *A. cepa*, used as vegetal system model. It resulted not to interfere with *A. cepa* cell proliferation, non-mutagenic and to non-genotoxic in two out of the three test we made. The only genotoxic effect

we observed was a very mild ability to induce chromosomal aberrations. Derivative **22** (TS of 3-isopropylbenzaldehyde) is a modification of the TS of cuminaldehyde.This molecule was widely studied to find its mechanism of action that we believe to be an inhibitory effect of the complex III (bc1) of the respiratory chain of *A. flavus*. This conclusion is supported by several experiments including proteomic studies, gene expression analysis, tests using a yeast model and a docking calculation of **22** into the binding pocket of the mitochondrial complex. Finally, an in-depth study of derivative **38** (the TS of the cis-jasmone) highlighted its ability to inhibit also sclerotia development which are known to have part of their biosynthetic pathway in common with aflatoxin biosynthesis. The inhibition of sclerotia development and aflatoxin production indicated that the target of **38** must be involved in an upstream biochemical process in common between the aflatoxin and sclerotia metabolisms. The thesis contains also the studies we made on other derivatives that were not as effective as **1**, **22** and **38** but that showed however interesting biological properties, for instance the class of long hydrophobic tail derivatives of the cinnamaldehyde family. All these results allow us to conclude that TSs are molecules that still have to be fully exploited for their potentials. In particular, we have observed that they can be metabolised and exert strong biological effects on fungi interfering only with specific biochemical pathways. For these reasons, we believe that the research on TSs potentialities cannot be considered exhausted and, on the contrary, this class of molecules may have in store for us new unexpected properties to be discovered and exploited in the future.

6 Anti-aflatoxigenic agents: experimental section

6.1 Chemical procedures

6.1.1 2-acetylthiophene derivatives

Ligands

The desired TSs were obtained mixing an equimolar amount of thiosemicarbazide with the appropriate aldehyde in absolute ethanol. A small amount of acetic acid was added to catalyse the condensation. The mixture was refluxed under stirring for 8 hours and left overnight at 0°C. The precipitate was filtered out, washed with cold ethanol and dried under *vacuum.*

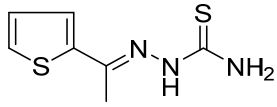

2-acetylthiophenethiosemicarbazone (1): thiosemicarbazide (0.36 g, 3.9 mmol), 2-acetylthiophene (0.50 g, 3.9 mmol). Yellow powder. Yield: 94%. ^{1}H-NMR (δ, ppm; DMSO-d^{6}): 2.33 (s, 3H), 7.10 (dd, 1H, *J* = 6.4 Hz, *J'* = 4.4Hz), 7.41 (s, 1H), 7.53 (d, 1H, *J* = 4.4Hz), 7.59 (d, 1H, *J* = 6.4Hz), 8.28 (s, 1H), 10.33 (s, 1H).

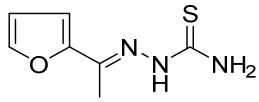

2-acetylfuranthiosemicarbazone (2): thiosemicarbazide (0.50 g, 4.5 mmol), 2-acetylfuran (0.41 g, 4.5 mmol). Orange powder. Yield: 46%. ^{1}H-NMR (δ, ppm; DMSO-d^{6}): 2.24 (s, 3H), 6.60 (dd, 1H, *J* = 3.6Hz, *J'* = 1.8 Hz), 7.12 (d, 1H, *J* = 3.6Hz), 7.71 (s, 1H), 7.77 (d, 1H, *J* = 1.8 Hz), 8.30 (s, 1H), 10.30 (s, 1H).

Metal complexes

The appropriate ligand was mixed with the appropriate metal salt in ethanol using a metal to ligand ratio of 1 : 2. The mixture was left under stirring at room temperature for 2 hours. Usually a change in the solution colour was observed during the reaction. Finally, the solvent was removed under reduced pressure and the product was washed twice with diethylether, then dried under *vacuum*.

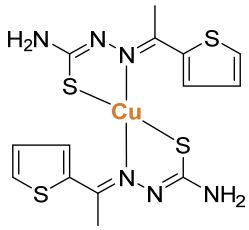

Bis(2-acetylthiophenethiosemicarbazonato)copper(II) (3): **1** (0.10 g, 0.50 mmol), copper(II) acetate (0.05 g, 0.025 mmol). Green powder. Yield: 59%. ESI-MS (+) m/z calc. 460.59 found 461.09.

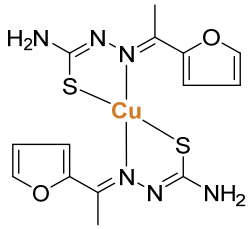

Bis(2-acetylfuranthiosemicarbazonato)copper(II) (4): 2 (0.11 g, 0.57 mmol), copper(II) acetate (0.06 g, 0.028 mmol). Dark green powder. Yield: 75%. ESI-MS (+) m/z calc. 428.98 found 428.11.

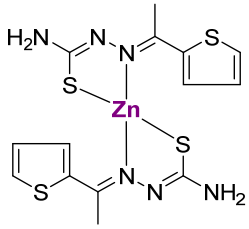

Bis(2-acetylthiophenethiosemicarbazonato)zinc(II) (5): 1 (0.10 g, 0.50 mmol), zinc(II) acetate (0.06 g, 0.25 mmol). Pale yellow powder. Yield: 74%. ^{1}H-NMR (δ, ppm; DMSO-d^{6}): 2.39 (s, 6H), 5.51 (sb, 2H), 7.54 (sb, 2H), 8.33 (s, 2H), 8.86 (m, 2H), 9.43 (s, 2H). ESI-MS (+) m/z calc. 462.94 found 461.76.

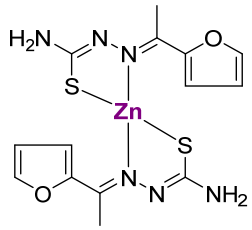

Bis(2-acetylfuranthiosemicarbazonato)zinc(II) (6): 2 (0.10 g, 0.55 mmol), zinc(II) acetate (0.06 g, 0.27 mmol). Pale orange powder. Yield: 82%. ^{1}H-NMR (δ, ppm; DMSO-d^{6}): 2.41 (s, 6H), 6.54 (sb, 2H), 6.76 (sb, 4H), 6.96 (s, 2H), 7.19 (s, 2H). ESI-MS (+) m/z calc. 430.82 found 431.42.

6.1.2 Cinnamaldehyde derivatives

Ligands

The desired thiosemicarbazones were obtained by mixing an equimolar amount of thiosemicarbazide with the proper aldehyde in absolute ethanol. The mixture was refluxed under stirring for 8 hours and left overnight at 0°C. The precipitate was filtered out, washed with cold ethanol and dried under *vacuum.*

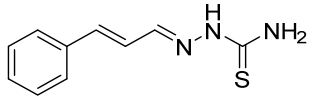

(*E*)-cinnamaldehydethiosemicarbazone (7): thiosemicarbazide (0.34 g, 3.8 mmol), (*E*)-cinnamaldehyde (0.50 g, 3.8 mmol). White powder. Yield: 96%. FT-IR (cm^{-1}): 1533 (s), 1254 (w), 966 (m). ^{1}H-NMR (δ, ppm; DMSO-d^{6}): 6.87 (dd, *J* = 16.1, *J'* = 9.2 Hz, 1H), 7.04 (d, *J* = 16.1 Hz, 1H), 7.34 (t, J = 8.2 Hz, 1H), 7.39 (t, *J* = 8.2 Hz, 2H), 7.58 (d, *J* = 8.2 Hz, 2H), 7.61 (s, 1H), 7.92 (d, *J* = 9.2 Hz, 1H), 8.18 (s, 1H), 11.40 (s, 1H). ESI-MS (+) m/z calc. 206.07 found 206.09.

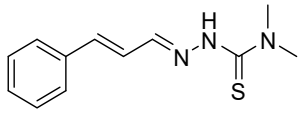

(*E*)-cinnamaldehyde-4,4-dimethyl-3-thiosemicarbazone (8): 4,4-dimethyl-3-thiosemicarbazide (0.44 g, 3.8 mmol), (*E*)-cinnamaldehyde (0.50 g, 3.8 mmol). Orange powder. Yield: 79%. FT-IR (cm^{-1}): 1545 (m), 1325 (w), 981 (m). ^{1}H-NMR (δ, ppm; DMSO-d^6): 3.26 (s, 6H), 6.97 (m, 2H), 7.33 (t, *J* = 7.2 Hz, 1H), 7.40 (t, *J* = 7.2 Hz, 2H), 7. 61 (d, *J* = 7.2 Hz, 2H), 8.04 (dd, *J* = 6.1 Hz, *J'* = 2.5 Hz, 1H), 10.83 (s, 1H). ESI-MS (+) m/z calc. 234.33 found 204.57.

Crystals suitable for XRD analysis were obtained from slow evaporation of a saturated ethanol solution of **8**.

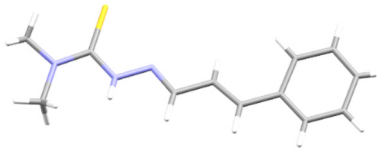

Space group *P*bca	
R 7.32%	
Z 8	
a 8.2252	α 90
b 10.954	β 90
c 27.937	γ 90

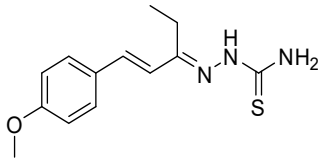

(*E*)-1-(4-methoxyphenyl)-1-pentene-3-one-4,4-dimethyl-3-thiosemicarbazone (9): thiosemicarbazide (0.10 g, 1.1 mmol), 1-(4 methoxyphenyl)-1-pentene-3-one (0.21 g, 1.1 mmol). Yellow crystals. Yield: 80%. Mp: 187 °C. FT-IR (cm^{-1}): 1577 (m), 1490 (w), 1242 (m). ^{1}H-NMR (δ, ppm; DMSO-d^6): 1.13 (t, *J* = 7.4 Hz, 3H), 2.56 (q, *J* = 7.4 Hz, 2H), 3.80 (s, 3H), 6.99 (d, *J* = 8.8 Hz, 2H), 7.10 (d, *J* = 16 Hz, 1H), 7.50 (d, *J* = 16 Hz, 1H), 7.59

(s, 1H), 7,74 (d, *J* = 8.8 Hz, 2H), 8.13 (s, 1H), 10.93 (s, 1H). ESI-MS (+) m/z calc. 264.36 found 264.09.

Crystals suitable for XRD analysis were obtained cooling the reaction mixture.

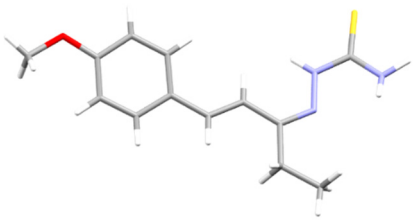

Space group *Cc*	
R 5.20%	
Z 4	
a 11.364	α 90
b 13.751	β 91.824
c 8.695	γ 90

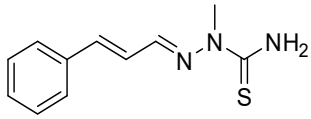

(*E*)-cinnamaldehyde-2-methyl-3-thiosemicarbazone (10): 2-methyl-3-thiosemicarbazide (0.16 g, 1.5 mmol), (*E*)-cinnamaldehyde (0.20 g, 1.5 mmol). Pale yellow powder. Yield: 52%. FT-IR (cm^{-1}): 1469 (m), 1426 (w), 971 (m). ^{1}H-NMR (δ, ppm; DMSO-d^{6}): 3.71 (s, 3H), 7.07 (m, 1H), 7.12 (m, 1H), 7.34 (m, 1H), 7.41 (t, *J* = 7.1 Hz, 2H), 7.57 (d, *J* = 6.8 Hz, 2H), 7.75 (s, 1H), 8.09 (s, 1H), 8.41 (s, 1H). ESI-MS (+) m/z calc. 220.31 found 220.50.

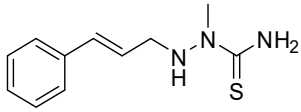

2-(*E*)-cinnamyl-1-methylhydrazine-1-carbothioamide (11): to reduce the imine bond of **10** (0.15 g, 0.68 mmol) was dissolved in 20 mL of EtOH with 4 eq. of $NaBH_4$ (0.10 g, 2.72 mmol). The mixture was refluxed and 2 eq. of $NaBH_4$ were added every 30 minutes until the complete disappearance of **10** (6 h). Finally, 20 mL of water and 1 mL of acetic acid were used to neutralise the solution. The product was extracted using CH_2Cl_2 (3 extractions of 15 mL each), then the organic solvent was removed under reduced pressure to obtain a white powder. Yield 25%. FT-IR (cm^{-1}): 3394 (m), 1581 (m), 964

(m). ^{1}H-NMR (δ, ppm; DMSO d^{6}): 3.71 (s, 3H), 7.04 (dd, *J* = 16.1, *J'* = 8.5 Hz, 1H), 7.14 (d, *J* = 16.1 Hz, 1H), 7.34 (d, *J* = 7.2 Hz, 1H), 7.41 (t, *J* = 7.2 Hz, 2H), 7.56 (d, *J* = 7.5 Hz, 2H), 7.74 (d, *J* = 85 Hz, 1H), 8.09 (s, 1H), 8.41 (s, 1H).

Metal complexes

The appropriate ligand was mixed with copper(II) or zinc(II) acetate in ethanol using a metal to ligand ratio of 1 : 2. The mixture was stirred at room temperature for 2 hours. The solutions changed colour gradually and the product precipitated during the reaction. Finally, the solid was filtered out, washed twice with diethylether, then dried under *vacuum*.

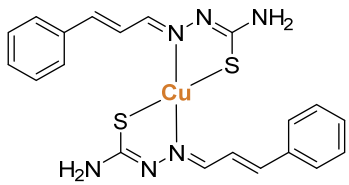

Bis[(*E*)-cinnamaldehydethiosemicarbazonato]copper(II) (12): 7 (0.10 g, 0.5 mmol), copper(II)acetate (0.05 g, 0.25 mmol). Brown powder. Yield: 60%. FT-IR (cm^{-1}): 1581 (s), 973 (s). ESI-MS (+) m/z calc. 471.09 found 472.16.

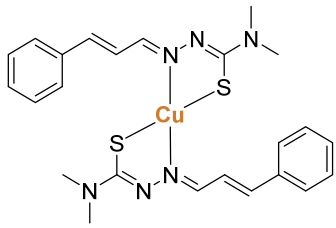

Bis[(*E*)-cinnamaldehyde-4,4-dimethyl-3-thiosemicarbazonato]copper(II) (13): 8 (0.10 g, 0.4 mmol), copper(II)acetate (0.04 g, 0.2 mmol). Brown powder. Yield: 73%. FT-IR (cm^{-1}): 1507 (m), 1353 (w), 1137 (m). ESI-MS (+) m/z calc. 528.20 found 520.20.

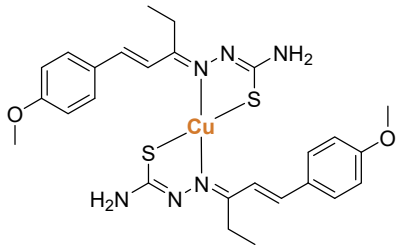

[(*E*)-1-(4-methoxyphenyl)-1-pentene-3-one-4,4-dimethyl-3-thiosemicarbazonato]copper(II) (14): 9 (0.10 g, 0.4 mmol), copper(II)acetate (0.04 g, 0.2 mmol). Brown powder. Yield: 87%. FT-IR (cm^{-1}): 1598 (m), 1477 (w). ESI-MS (+) m/z calc. 587.25 found 588.26.

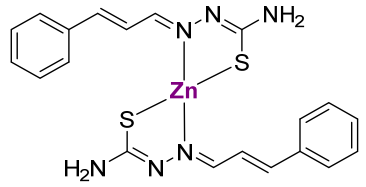

Bis[(*E*)-cinnamaldehydethiosemicarbazonato]zinc(II) (15): 7 (0.10 g, 0.5 mmol), zinc(II)acetate (0.05 g, 0.25 mmol). Yellow powder. Yield: 59%. FT-IR (cm^{-1}): 1631 (m), 1460 (s), 1185 (m), 963 (m). ^{1}H-NMR (δ, ppm; DMSO-d^{6}): 7.07 (d, *J* = 15.3, 1H), 7.13 (d, *J* = 15.3 Hz, 1H), 7.44 (m, 7H), 8.27 (d, *J* = 8.0 Hz, 1H). ESI- ESI-MS (+) m/z calc. 474.92 found 473.15.

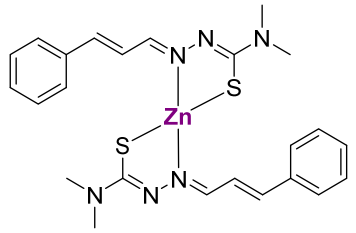

Bis[(*E*)-cinnamaldehyde-4,4-dimethyl-3-thiosemicarbazonato]zinc(II) (16): 8 (0.10 g, 0.4 mmol), zinc(II)acetate (0.05 g, 0.2 mmol). Yellow powder. Yield: 71%. FT-IR (cm^{-1}): 1579 (m), 1432 (w). ^{1}H-NMR (δ, ppm; DMSO-d^{6}): 2.52 (s, 12H), 7.03 (dd, *J* = 15.7 Hz, *J'* = 9.7 Hz, 2H), 7.09 (d, *J* = 17.7 Hz, 2H), 7. 32 (m, 4H), 7.40 (m, 6H), 8.37 (d, *J* = 9.7 Hz, 2H). ESI-MS (+) m/z calc. 529.03 found 529.22.

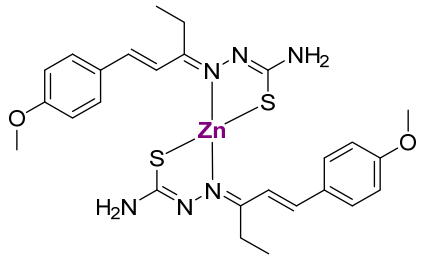

Bis[(*E*)-1-(4-methoxyphenyl)-1-pentene-3-one-4,4-dimethyl-3-thiosemicarbazonato]zinc(II) (17): 9 (0.10 g, 0.4 mmol), zinc(II)acetate (0.04 g, 0.2 mmol). Dark green powder. Yield: 87%. FT-IR (cm^{-1}): 1598 (m), 1477 (w). ^{1}H-NMR (δ, ppm; DMSO-d^6): 0.91 (t, *J* = 7.5 Hz, 6H), 2.73 (m, 2H), 2.91 (m, 2H), 3.78 (s, 6H), 6.82 (d, *J* = 16 Hz, 2H), 6.96 (d, *J* = 8.9, 4H), 7.05 (d, *J* = 16 Hz, 2H), 7.19 (s, 4H), 7.41 (d, *J* = 8.9 Hz, 4H). ESI-MS (+) m/z calc. 589.08 found 589.30.

6.1.3 1-(3-methoxyphenyl)-1-heptanone derivatives

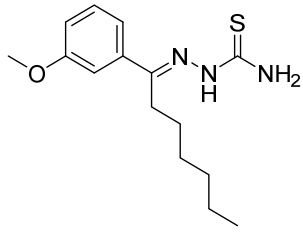

1-(3-methoxyphenyl)-1-heptanonethiosemicarbazone (18): thiosemicarbazide (0.21 g, 2.27 mmol) was dissolved in a hot solution of absolute ethanol (40 mL), then 1-(3-methoxyphenyl)-1-heptanone (0.50 g, 2.27 mmol) was added and the mixture was refluxed and stirred for 7 hours. The solvent was removed under reduced pressure and the oil obtained was sonicated for 2 hours to obtain a white solid which was washed three times with hexane and then dried under *vacuum*. White powder. Yield: 59%. Mp: 91 °C. FT-IR (cm^{-1}): 1595 (m), 1497 (w), 786 (m). ^{1}H-NMR (δ, ppm; DMSO-d^6): 0.85 (sb, 3H), 1.25 (sb, 4H), 1.36 (sb, 4H), 2.85 (sb, 2H), 3.80 (s, 3H), 6.96 (d, *J* = 7.9 Hz, 1H), 7.30 (s, *J* = 7.9 Hz, 1H), 7,41 (m, 2H), 7.89 (s, 1H), 8.26 (s, 1H), 10.34 (s, 1H). ESI-MS (+) m/z calc. 293.43 found 293.68.

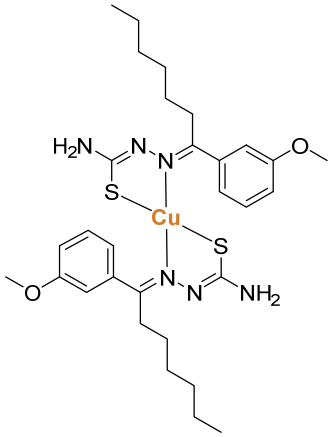

Bis[1-(3-methoxyphenyl)-1-heptanonethiosemicarbazonato]copper(II) (19): 18 (0.10 g, 0.34 mmol) was dissolved in 20 mL absolute ethanol and copper(II) acetate (0,03 g, 0.17 mmol) was dissolved in 10 mL of absolute ethanol. The solution containing copper was then slowly dripped into the ligand solution and the mixture turned from pale yellow to brown. The mixture was stirred for 2 hours and then the brown solid formed was recovered through centrifugation, washed twice with diethylether and dried under *vacuum*. Dark brown solid. Yield: 88%. FT-IR (cm^{-1}): 1480 (m), 693 (m). ESI-MS (+) m/z calc. 648.86 found 648.38.

6.1.4 Cuminaldehyde derivatives

Ligands

The desired TSs (and the semicarbazone) were obtained mixing an equimolar amount of thiosemicarbazide (or semicarbazide) with the appropriate aldehyde in absolute ethanol. The mixture was refluxed under stirring for 8 hours and left overnight at 0°C. The precipitate was filtered out, washed with cold ethanol and dried under *vacuum*.

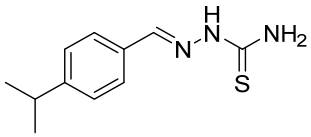

Cuminaldehydethiosemicarbazone (20): thiosemicarbazide (0.30 g, 3.3 mmol), cuminaldehyde (4-isopropylbenzaldehyde) (0.49 g, 3.3 mmol). Pale yellow powder. Yield: 86%. Mp: 144 °C. FT-IR (cm^{-1}): 3411 (m), 3280 (m), 3013 (m), 2957 (m), 1586 (s), 1537 (m), 1049 (m). ^{1}H-NMR (δ, ppm; DMSO-d^{6}): 1.21 (d, *J* = 6.7 Hz, 6H), 2.91 (m, 1H), 7.28 (d, *J* = 7.7 Hz, 2H), 7.71 (d, *J* = 7.7 Hz, 2H), 7.93 (s, 1H), 8.17 (s, 1H), 8.02 (s, 1H), 11.34 (s, 1H).

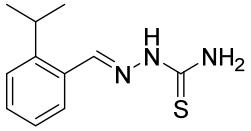

2-isopropylbenzaldehydethiosemicarbazone (21): thiosemicarbazide (0.30 g, 3.3 mmol), 2-isopropylbenzaldehyde (0.49 g, 3.3 mmol). White powder. Yield: 75%. Mp: 171°C. FT-IR (cm^{-1}): 3430 (m), 3256 (m), 3031 (w), 2955 (mw), 1594 (s), 1530 (m), 1093 (m). ^{1}H-NMR (δ, ppm; DMSO-d^{6}): 1.22 (d, *J* = 6.8 Hz, 6H), 3.26 (m, 1H); 7.21 (t, *J* = 6.8 Hz, 1H), 7.37 (m, 2H), 7.91 (s, 1H), 8.08 (d, *J* = 7.6 Hz, 1H), 8.19 (s, 1H), 8.56 (s, 1H), 11.32 (s, 1H).

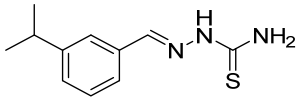

3-isopropylbenzaldehydethiosemicarbazone (22): thiosemicarbazide (0.30 g, 3.3 mmol), 3-isopropylbenzaldehyde (0.49 g, 3.3 mmol). White powder. Yield: 79%. Mp: 196°C. FT-IR (cm^{-1}): 3382 (m), 3230 (m), 3031 (m), 2952 (mw), 1597 (s), 1530 (s), 1090 (m). ^{1}H-NMR (δ, ppm; DMSO-d^{6}): 1.23 (d, J 0 6.8 Hz, 6H), 2.91 (m, 1H), 7.30 (m, 2H), 7.57 (d, *J* = 7.7 Hz, 1H), 7.69 (s, 1H); 8.00 (s, 1H), 8.03 (s, 1H), 8.20 (s, 1H), 11.41 (s, 1H).

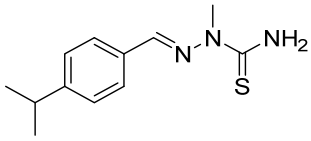

Cuminaldehyde-2-methyl-3-thiosemicarbazone (23): 2-methyl-3-thiosemicarbazide (0.14 g, 1.4 mmol), 4-isopropylbenzaldehyde (0.20 g, 1.4 mmol). White powder. Yield:

73%. Mp: 159°C. FT-IR (cm^{-1}): 3415 (s), 3235 (m), 3116 (m), 2868 (m), 2958 (m), 1582 (s), 828 (s).^{1}H-NMR (δ, ppm; DMSO-d^{6}): 1.22 (d, *J* = 6.7 Hz, 6H), 2.94 (m, 1H), 3.77 (s, 3H), 7.30 (d, *J* = 8.0 Hz, 2H), 7.58 (s, 1H), 7.84 (d, *J* = 8.0 Hz, 2H), 7.87 (s, 1H), 8.25 (s, 1H), 8.37 (s, 1H).

Crystals suitable for XRD analysis were obtained from slow evaporation of a saturated ethanolic solution of **23**.

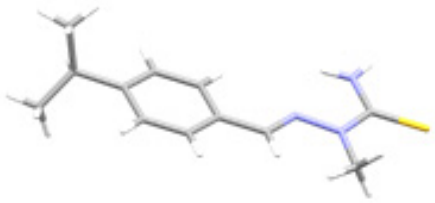

Space group *P*-1	
R 7.04%	
Z 2	
a 10.924	**α** 68.79
b 11.429	**β** 86.68
c 12.080	**γ** 69.89

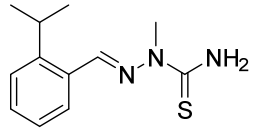

2-isopropylbenzaldehyde-2-methyl-3-thiosemicarbazone (24): 2-methyl-3-thiosemicarbazide (0.07 g, 0.7 mmol), 2-isopropylbenzaldehyde (0.10 g, 0.7 mmol). White powder. Yield: 81%. Mp: 157°C. FT-IR (cm^{-1}): 3398(s), 3257 (m), 3145 (m), 2862 (m), 2954 (s), 1585 (m), 786 (m).^{1}H-NMR (δ, ppm; DMSO-d^{6}): 1.25 (d, *J* = 6.7 Hz, 6H), 3.54 (m, 1H), 3.83 (s, 3H), 7.25 (m, 2H), 7.39 (m, 2H), 8.12 (m, 1H), 8.11 (s, 1H), 8.18 (s, 1H), 8.25 (s, 1H), 8.42 (s, 1H).

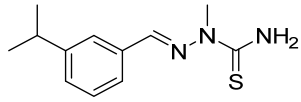

3-isopropylbenzaldehyde-2-methyl-3-thiosemicarbazone (25): 2-methyl-3-thiosemicarbazide (0.07 g, 0.7 mmol), 3-isopropylbenzaldehyde (0.10 g, 0.7 mmol). White powder. Yield: 81%. Mp: 157°C. FT-IR (cm^{-1}): 3398(s), 3257 (m), 3145 (m), 2862 (m), 2954 (s), 1585 (m), 786 (m).^{1}H-NMR (δ, ppm; DMSO-d^{6}): 1.25 (d, *J* = 6.6 Hz, 6H), 3.54 (m, 1H), 3.83 (s, 3H), 7.25 (m, 2H), 7.39 (m, 2H), 8.12 (m, 1H), 8.11 (s, 1H), 8.18 (s, 1H), 8.25 (s, 1H), 8.42 (s, 1H).

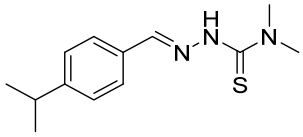

4-isopropylbenzaldehyde-4,4-dimethy-3-thiosemicarbazone (26): 4,4-dimethyl-3-thiosemicarbazide (0.10 g, 0.8 mmol), 4-isopropylbenzaldehyde (0.12 g, 0.8 mmol). White powder. Yield: 73%. FT-IR (cm^{-1}): 1565 (m), 783 (m).^{1}H-NMR (δ, ppm; DMSO-d^6): 1.23 (d, J = 6.7 Hz, 6H), 2.93 (m, 1H), 3.30 (s, 6H), 7.30 (d, *J* = 8.0 Hz, 1H), 7.37 (t, *J* = 8.0 Hz, 1H), 7.47 (d, *J* = 8.0 Hz, 1H), 7.50 (s, 1H), 8.17 (s, 1H), 10.93 (s, 1H).

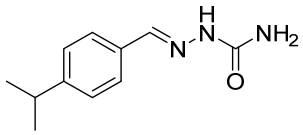

Cuminaldehydesemicarbazone (27): semicarbazide (0.30 g, 4.00 mmol), cuminaldehyde (4-isopropylbenzaldehyde) (0.59 g, 4.00 mmol). White powder. Yield: 81%. Mp: 224°C. FT-IR (cm^{-1}): 2959 (mw), 1682(s). ^{1}H-NMR (δ, ppm; DMSO d^6): 1.62 (d, *J* = 6.8 Hz, 6H), 2.87 (m, 1H), 7.29 (d, *J* = 7.2 Hz, 1H), 7.75 (d, *J* = 7.2 Hz, 2H), 7.70 (s, 1H), 8.00 (s, 1H), 8.02 (s, 1H), 10.60 (s, 1H).

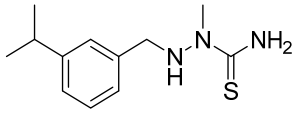

1-[(3-isopropylphenyl)methylamino]-1-methyl-thiourea (28): To reduce the imine bond, **25** (0.15 g, 0.6 mmol) was dissolved in 20 mL of EtOH with 4 eq. of $NaBH_4$ (0.09 g, 2.5 mmol). The mixture was refluxed and 2 eq. of $NaBH_4$ were added every 30 minutes until the complete disappearance of the reagent **25** (6 h). Finally, 20 mL of water and 1 mL of acetic acid were used to neutralise the solution. The product was extracted using CH_2Cl_2 (3 extractions of 15 mL each), then the organic solvent was removed under reduced pressure to obtain a white powder. Yield 22%. FT-IR (cm^{-1}): 3404 (m), 1577 (m), 1359 (m). ^{1}H-NMR (δ, ppm; DMSO d^6): 1.20 (d, *J* = 6.6 Hz, 6H), 2.87 (m, 1H), 3.40 (s, 3H); 3.82 (d, 2H), 5.38 (s, 1H), 7.19 (d, *J* = 7.5 Hz, 2H), 7.31 (d, *J* = 7.5 Hz, 2H), 7.46 (m, 2H).

Metal complexes

The appropriate ligand was mixed with the appropriate metal salt in ethanol using a metal to ligand ratio of 1 : 2. The mixture was left under stirring at room temperature for 2 hours. Usually it was observed a change in the solution colour during the reaction. Finally, the solvent was removed under reduced pressure and the product was washed twice with diethylether, then dried under *vacuum*.

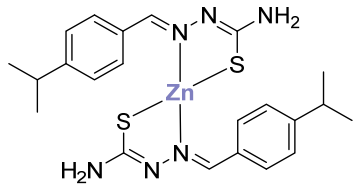

Bis(cuminaldehydethiosemicarbazonato)zinc(II) (29): 20 (0.06 g, .27 mmol),), zinc(II) acetate (0.03 g, 0.15 mmol). Pale yellow powder. Yield: 76%. FT-IR (cm^{-1}): 1652 (s), 934 (m). ^{1}H-NMR (δ, ppm; DMSO d^{6}): 1.62 (d, J = 6.7 Hz, 6H), 2.87 (m, 1H), 7.29 (d, *J* = 7.6 Hz, 2H), 7.75 (d, *J* = 7.6 Hz, 2H), 7.70 (s, 1H), 8.20 (s, 1H), 8.02 (s, 1H), 10.60 (s, 1H). ESI-MS (+) m/z calc. 507.02 found 506.29.

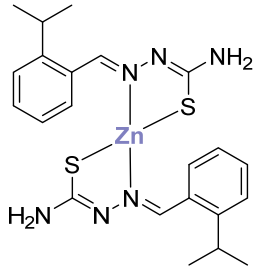

Bis(2-isopropylbenzaldehydethiosemicarbazonato)zinc(II) (30): 21 (0.06 g, 0.27 mmol), zinc(II) acetate (0.03 g, 0.15 mmol). White powder. Yield: 83%. FT-IR (cm^{-1}): 1639(s), 792 (m). ^{1}H-NMR (δ, ppm; DMSO-d^{6}): 1.23 (d, *J* = 6.8 Hz, 6H), 3.25 (m, 1H); 7.24 (t, *J* = 6.7 Hz, 1H), 7.37 (m, 2H), 7.90 (s, 1H), 8.10 (d, *J* = 7.7 Hz, 1H), 8.22 (s, 1H), 8.56 (s, 1H). ESI-MS (+) m/z calc. 507.02 found 506.32.

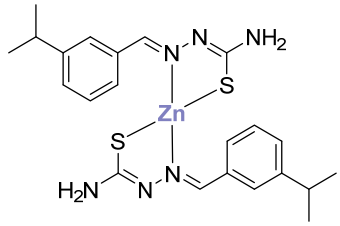

Bis(3-isopropylbenzaldehydethiosemicarbazonato)zinc(II) (31): 22 (0.10 g, 0.45 mmol), zinc(II) acetate (0.05 g, 0.23 mmol). White powder. Yield: 47%. FT-IR (cm^{-1}): 1677(s), 963 (m). ^{1}H-NMR (δ, ppm; DMSO d^{6}): 1.23 (d, 6H), 2.91 (ept, 1H), 7.30 (m, 2H), 7.56 (d, J = 7.4 Hz, 1H), 7.69 (s, 1H), 8.01 (s, 1H), 8.03 (s, 1H), 8.21 (s, 1H). ESI-MS (+) m/z calc. 507.02 found 506.20.

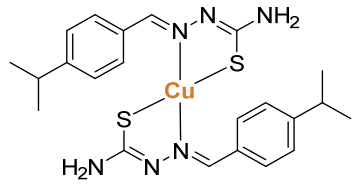

Bis(cuminaldehydethiosemicarbazonato)copper(II) (32): 20 (0.06 g, 0.27 mmol), copper(II) acetate (0.03 g, 0.14 mmol). White powder. Yield: 66%. FT-IR (cm^{-1}): 1662(s), 977 (m). ESI-MS (+) m/z calc. 505.19 found 505.24.

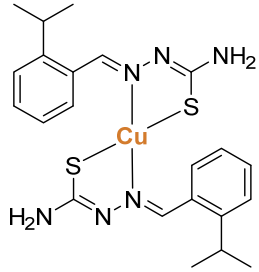

Bis(2-isopropylbenzaldehydethiosemicarbazonato)copper(II) (33): 21 (0.10 g, 0.45 mmol), copper(II) acetate (0.05 g, 0.23 mmol). White powder. Yield: 72%. FT-IR (cm^{-1}): 16752(s), 943 (m). ESI-MS (+) m/z calc. 505.19 found 505.22.

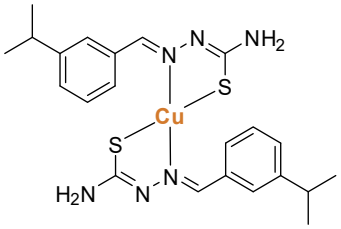

Bis(3-isopropylbenzaldehydethiosemicarbazonato)copper(II) (34): 22 (0.07 g, 0.32 mmol), copper(II) acetate (0.03 g, 0.16 mmol). White powder. Yield: 56%. FT-IR (cm^{-1}): 1669(s), 949 (m). ESI-MS (+) m/z calc. 505.19 found 505.25.

6.1.5 Khellinone derivatives

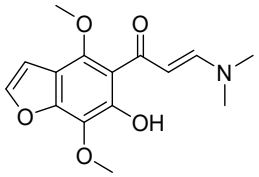

(E)-3-(dimethylamino)-1-(6-hydroxy-4,7-dimethoxybenzofuran-5-yl)-prop-2-en-1-one (35): khellinone (0.10 g, 0,42 mmol) was dissolved in 20 mL of dry toluene in N_2 atmosphere, then N,N-dimethylformamide dimethyl acetal (DMF/DMA) (0.06 g, 0.42 mmol) was added. The mixture was heated at 100°C for 3 hours and it turned from yellow to orange. The solvent volume was reduced under reduced pressure and then the solution was left at -4°C until the formation of orange crystals (ca. 3 days). The crystals were recovered by filtration and dried under *vacuum*. Orange crystals. Yield: 79%. ^{1}H-NMR (δ, ppm; DMSO d^6): 2.93 (s, 3H), 3.19 (s, 3H), 3.86 (s, 3H); 3.94 (s, 3H), 6.07 (sb, 1H), 7.06 (s, 1H), 7.84 (s, 1H), 7.91 (sb, 1H).

Crystals suitable for XRD analysis were obtained cooling the reaction mixture at -4°C.

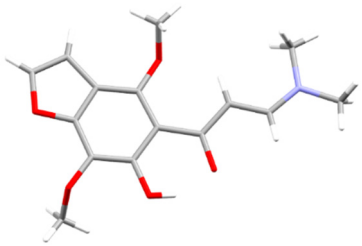

Space group $P2_1/n$	
R 4.78%	
Z 4	
a 7.2069	**α** 90
b 22.3288	**β** 104.875
c 9.0883	**γ** 90

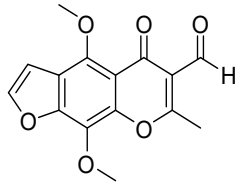

4,9-dimethoxy-5-oxo-5H-furo[3,2]chromene-6-carbaldehyde (36): 35 (0,10 g, 0.36 mmol) was dissolved in 10 mL of acetic anhydride, then 3.3 mL of pyridine were added. The mixture was stirred at room temperature for 15 hours and it turned from yellow to colourless. The solvent was removed under reduced pressure and the solid obtained was washed with hexane (2 x 7 mL) and dried under *vacuum.* Orange solid. Yield: 53%. ^{1}H-NMR (δ, ppm; DMSO d^{6}): 2.58 (s, 3H), 4.00 (s, 3H), 3.86 (s, 3H), 4.12 (s, 3H), 7.30 (d, *J* = 2.3 Hz, 1H), 8.17 (d, *J* = 2.3 Hz, 1H), 8.69 (s, 1H).

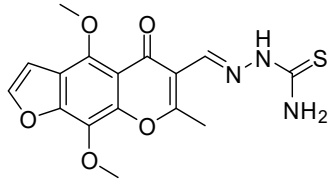

4,9-dimethoxy-5-oxo-5H-furo-[3,2]-chromene-6-carbaldehydethiosemicarbazone (37): 36 (0.05 g, 0.15 mmol) and thiosemicarbazide (0.01 g, 0.15 mmol) were dissolved in 5 mL of absolute ethanol, then few drops of acetic acid were added. The mixture was refluxed and stirred for 3 hours and the clear orange solution obtained was left at -4°C until the formation of orange needles. The crystals were collected, washed with diethylether (2 x 5 mL) and then dried under *vacuum*. Orange crystals. Yield: 87%. ^{1}H-NMR (δ, ppm; DMSO d^{6}): 2.71 (s, 3H), 3.97 (s, 3H), 4.13 (s, 3H), 7.27 (d, *J* = 2.4 Hz, 1H), 7.50 (s, 1H), 8.13 (d, *J* = 2.4 Hz, 1H), 8.22 (s, 1H), 8.35 (s, 1H), 11.55 (s, 1H).

Crystals suitable for XRD analysis were obtained directly from the reaction mixture cooled at -4°C.

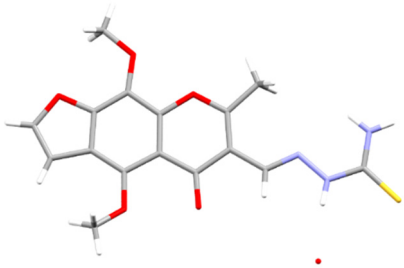

Space group $P2_1/n$	
R 5.58%	
Z 4	
a 6.217	**α** 90
b 17.461	**β** 92.94
c 15.240	**γ** 90

6.1.6 Jasmone derivatives

Ligands

The desired TSs were obtained mixing an equimolar amount of thiosemicarbazide with the appropriate aldehyde in absolute ethanol. A small amount of acetic acid was added to catalyse the condensation. The mixture was refluxed under stirring for 8 hours and left overnight at 0°C. The precipitate was filtered out, washed with cold ethanol and dried under *vacuum.*

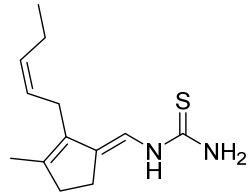

***cis*-jasmonethiosemicarbazone (38):** thiosemicarbazide (0.22 g, 2.4 mmol), cis-jasmone (0.40 mg, 2.4 mmol). White powder. Yield 26%. Mp. 149°C. FT-IR (cm^{-1}): 3401 (s), 3130 (m), 2964 (m), 1590 (s), 1507 (s) 874 (m). ^{1}H-NMR (δ, ppm; DMSO-d^{6}): 0.93 (t, *J* = 7.5 Hz, 3H), 1.89 (s, 3H), 2.13 (m, 2H), 2.44 (m, 2H), 2.59 (m, 2H), 2.98 (d, *J* = 9.2 Hz, 2H), 5.28 (m, 2H), 734 (s, 1H), 8.02 (s, 2H), 9.87 (s, 1H).

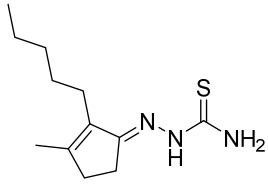

Dihydrojasmonethiosemicarbazone (39): thiosemicarbazide (0.22 g, 2.41 mmol), dihydrojasmone (0.40 g, 2.41 mmol. Pale yellow powder. Yield 41%. Mp. 177°C. FT-IR: 3403 cm^{-1} (s), 3130 cm^{-1} (m), 2925 cm^{-1} (m), 2852 cm^{-1} (s), 1590 cm^{-1} (m), 1507 cm^{-1} (s), 718 cm^{-1} (m). ^{1}H-NMR (δ, ppm; DMSO-d^{6}): 0.85 (t, *J* = 7.0 Hz, 3H), 1.25 (m, 4H), 1.37 (m, 2H), 2.22 (t, *J* = 7.4 Hz, 2H), 2.43 (m, 2H), 2.58 (m, 2H), 7.30 (s, 1H), 8.01 (s, 2H), 9.83 (s, 2H). Crystals suitable for XRD analysis were obtained from slow evaporation of a saturated ethanol solution of **39**.

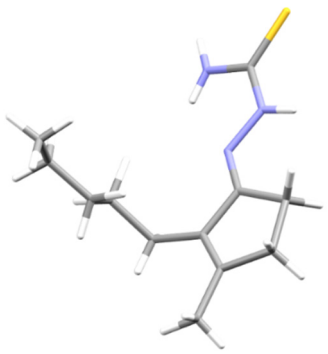

Space group $P2_1/a$	
R 5.98%	
Z 4	
a 10.635	90
b 8.272	107.45
c 16.687	90

Metal complexes

The solution containing the copper salt was dripped slowly into the **1** solution which rapidly turned to dark brown. The mixture was stirred at room temperature for 2 hours and then the solvent was removed under reduced pressure. The solid formed was collected and washed with diethylether, then dried under vacuum.

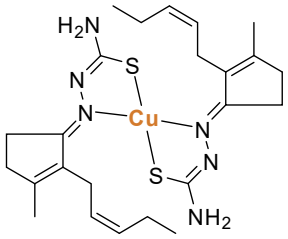

Bis(*cis*-jasmonethiosemicarbazonato)copper(II) (40): Copper(II) acetate (0.04 g, 0.21 mmol), **38** (0.10 g, 0.42 mmol). Dark brown powder. Yield 95%. FT-IR (cm^{-1}): 3416 (s), 2959 (m), 1570 (m), 1511 (m), 701 (m). ESI-MS (+) m/z calc. 537.28, found 537.39.

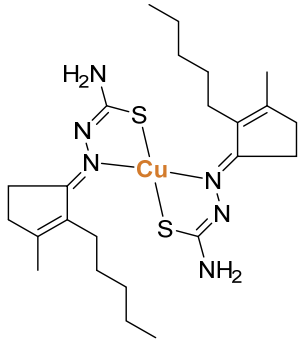

Bis(dihydrojasmonethiosemicarbazonato)copper(II) (41): Copper(II) acetate (0.04 g, 0.21 mmol), **39** (0.10 mg, 0.42 mmol). Dark brown powder. Yield 74%. FT-IR (cm^{-1}): 2920 (s), 2851 (m), 1550 (m), 618 cm^{-1} (m). ESI-MS (+) m/z calc. 541.31, found 542.42.

6.1.7 Long hydrophobic tail derivatives

Ligands

The desired TSs were obtained mixing an equimolar amount of thiosemicarbazide with the appropriate alkyl-aldehyde (from C_7 to C_{11}) in absolute ethanol. The mixture was refluxed under stirring for 8 hours. The solvent was removed using reduced pressure and the solid obtained was collected, washed with hexane and dried under *vacuum.*

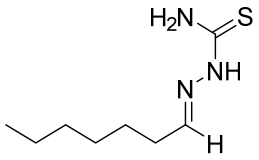

Heptanalthiosemicarbazone (42): thiosemicarbazide (0.32 g, 3.5 mmol), heptanal (0.40 g, 3.5 mmol). White powder. Yield: 79%. FT-IR (cm^{-1}): 1595 (s), 1531 (s), 825 (m). ^{1}H-NMR (δ, ppm; DMSO-d^6): 0.86 (t, *J* = 5.3 Hz, 3H), 1.27 (m, 6H), 1.45 (m, 2H), 2.18 (dd, *J* = 13.1 Hz, *J'* = 7.1 Hz, 2H), 7.40 (m, 2H), 7.95 (s, 1H), 11.03 (s, 1H).

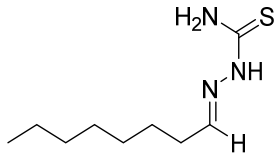

Octanalthiosemicarbazone (43): thiosemicarbazide (0.24 g, 2.6 mmol), octanal (0.13 g, 2.6 mmol). White powder. Yield: 91%. FT-IR (cm^{-1}): 1539 (s), 832 (m). ^{1}H-NMR (δ, ppm; DMSO-d^{6}): 0.86 (t, *J* = 5.6 Hz, 3H), 1.26 (m, 8H), 1.45 (m, 2H), 2.17 (m, 2H), 7.40 (m, 2H), 7.96 (s, 1H), 11.04 (s, 1H).

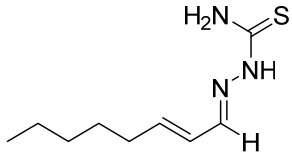

Octenalthiosemicarbazone (44): thiosemicarbazide (0.50g, 5.5 mmol), octenal (0.69 g, 5.5 mmol). White powder. Yield: 98%. FT-IR (cm^{-1}): 1541.08 (s), 963.58 (m). ^{1}H-NMR (δ, ppm; DMSO-d^{6}): 0.87 (t, *J* = 5.9 Hz, 3H), 1.28 (m, 6H), 1.40 (m, 2H), 2.15 (m, 2H), 6.11 (m, 2H), 7.69 (d, J = 6.9 Hz, 1H), 8.06 (m, 1H), 11.17 (s, 1H).

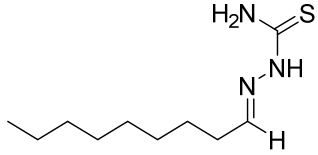

Nonanalthiosemicarbazone (45): thiosemicarbazide (0.26 g, 2.8 mmol), nonanal (0.40 g, 2.8 mmol). White powder. Yield: 81%. FT-IR (cm^{-1}): 1590 (s), 1537 (s), 820 (m) . ^{1}H-NMR (δ, ppm; DMSO-d^{6}): 0.86 (t, *J* = 6.9 Hz, 3H), 1.26 (m, 10H), 1.45 (m, 2H), 2.18 (td, *J* = 7.4 Hz, *J'* = 5.6, 2H), 7.41 (m, 2H), 7.96 (s, 1H), 11.03 (s, 1H).

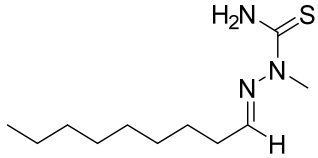

Nonanal-2-methyl-3-thiosemicarbazone (46): 2-methyl-3-thiosemicarbazide (0.30 g, 2.8 mmol), nonanal (0.40 g, 2.8 mmol). White powder. Yield: 81%. FT-IR (cm^{-1}): 1531 (s), 829 (m). ^{1}H-NMR (δ, ppm; DMSO-d^{6}): 0.82 (t, *J* = 6.9 Hz, 3H), 1.29 (m, H), 1.44 (m, 2H), 3.41 (s, 3H), 2.18 (m, 2H), 7.43 (m, 2H), 8.00 (s, 1H).

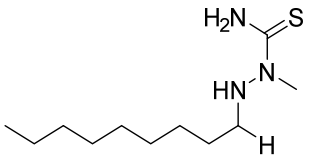

1-methyl-1-(nonylamino)thiourea (47): to reduce the imine, **46** (0.15 g, 0.7 mmol) was dissolved in 20 mL of EtOH with 4 eq. of $NaBH_4$ (0.10 g, 2.8 mmol). The mixture was refluxed and 2 eq. of $NaBH_4$ were added every 30 minutes until the complete disappearance of the reagent **46** (3 h) in TLC (hexane/ethyl acetate - 4 :1). Finally, 20 mL of water and 1 mL of acetic acid were used to neutralise the solution. A white precipitate appeared and was filtered out, washed twice with diethylether and dried under *vacuum*. Yield 40%. FT-IR (cm^{-1}): 1565 (s), 982 (m). ^{1}H-NMR (δ, ppm; DMSO d^6): 0.86 (t, *J* = 6.9 Hz, 3H), 1.25 (s, 3H), 1.35 (m, 14H), 2.68 (dd, *J* = 12.3 Hz, *J'* = 6.6 Hz, 2H), 5.05 (s, 1H), 7.45 (s, 2H).

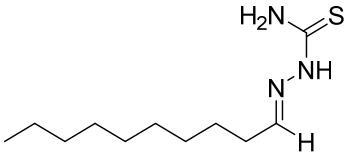

Decanalthiosemicarbazone (48): thiosemicarbazide (0.15 g, 1.6 mmol), decanal (0.26 g, 1.6 mmol). White powder. Yield: 65%. FT-IR (cm^{-1}): 1529 (s), 835 (m). ^{1}H-NMR (δ, ppm; DMSO-d^6): 0.86 (t, *J* = 6.4 Hz, 3H), 1.24 (m, 12H), 1.45 (m, 2H), 2.18 (dd, *J* = 13.3 Hz, *J'* = 7.4 Hz, 2H), 7.41 (m, 2H), 7.94 (s, 1H), 11.02 (s, 1H).

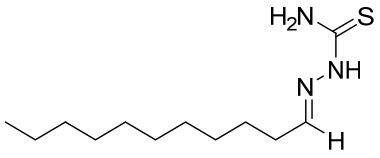

Undecanalthiosemicarbazone: (49): thiosemicarbazide (0.21 g, 2.4 mmol), undecanal (0.40 g, 2.4 mmol). White powder. Yield: 39%. Mp: 74 °C. FT-IR (cm^{-1}): 1594 (s), 1537 (s), 825 (s). ^{1}H-NMR (δ, ppm; DMSO-d^6): 0.86 (t, *J* = 6.8 Hz, 3H), 1.25 (m, 14H), 1.45 (m, 2H), 2.17 (td, *J* = 7.4 Hz, *J'* = 5.6 Hz, 2H), 7.40 (t, *J* = 5.5 Hz, 1H), 7.42 (s, 1H), 7.95 (s, 1H), 11.03 (s, 1H).

Metal complexes

General synthetic approach used for the synthesis of copper(II) complexes

The appropriate ligand was mixed with copper(II) acetate in ethanol with a metal to ligand ratio of 1 : 2. The mixture was left under stirring at room temperature for 2 hours. Usually a change in the solution colour was observed during the reaction. Finally, the solvent was removed under reduced pressure and the product was washed twice with diethylether, then dried under *vacuum*.

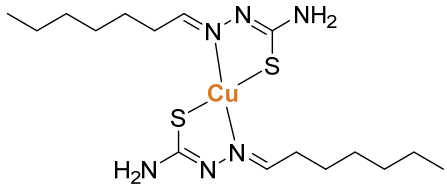

Bis(heptanalthiosemicarbazonato)copper(II) (50): 42 (0.10 g, 0.50 mmol), copper(II) acetate (0.05 g, 0.25 mmol). Black powder. Yield: 50%. FT-IR (cm^{-1}): 1584 (s), 1496 (s), 701 (m). ESI-MS (+) m/z calc. 437.17 found 436.33.

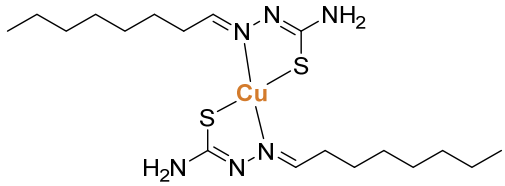

Bis(octanalthiosemicarbazonato)copper(II) (51): 43 (0.07 g, 0.35 mmol), copper(II) acetate (0.04 g, 0.18 mmol). Black powder. Yield: 50%. FT-IR (cm^{-1}): 1584 (s), 1496 (s), 701 (m). ESI-MS (+) m/z calc. 437.17 found 436.33.

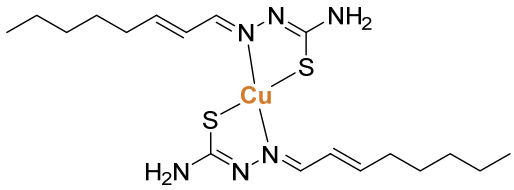

Bis(octenalthiosemicarbazonato)copper(II) (52): 44 (0.14 g, 0.71 mmol), copper(II) acetate (0.07 g, 0.35 mmol). Black powder. Yield: 86%. FT-IR (cm^{-1}): 1556 (s), 936 (m). ESI-MS (+) m/z calc. 465.21 found 464.35.

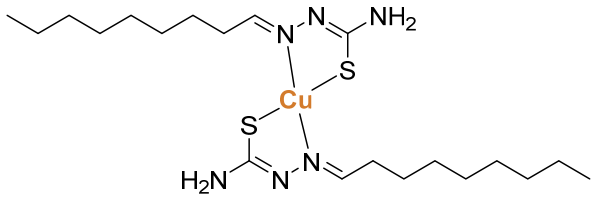

Bis(nonanalthiosemicarbazonato)copper(II) (53): 44 (0.07 g, 0.32 mmol), copper(II) acetate (0.03 g, 0.16 mmol). Black powder. Yield: 77%. FT-IR (cm^{-1}): 1496 (s), 1462 (s), 726 (s). ESI-MS (+) m/z calc. 493.27 found 492.35.

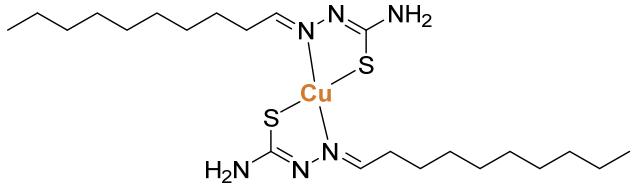

Bis(decanalthiosemicarbazonato)copper(II) (54): **48** (0.10 g, 0.43 mmol), copper(II) acetate (0.04 g, 0.22 mmol). Brown powder. Yield: 72%. FT-IR (cm^{-1}): 1518 (s), 855 (m). ESI-MS (+) m/z calc. 521.30 found 521.65.

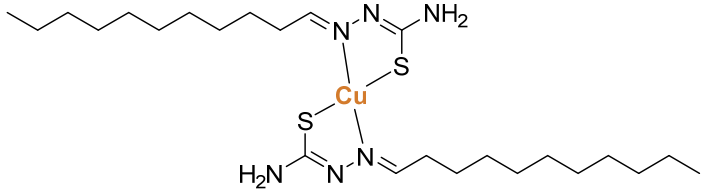

Bis(undecanalthiosemicarbazonato)copper(II) (55): 49 (0.08 g, 0.33 mmol), copper(II) acetate (0.03 g, 0.17 mmol). Brown powder. Yield: 59%. FT-IR (cm^{-1}): 1511 (s), 785 (m). ESI-MS (+) m/z calc. 549.37 found 548.55.

6.2 Biological test protocols

6.2.1 Aflatoxin production inhibition assay

A high throughput procedure performed in a multi-well plate was used to assess aflatoxin accumulation in a coconut milk-derived medium (CCM)[86]. The effect on aflatoxin biosynthesis was assessed by the microplate fluorescence-based procedure described by Degola and co-workers[87]. Standard flat-bottom 96-well microplates were used. Suspensions of conidia were diluted to the appropriate concentrations and brought to the final concentration of 5×10^2 conidia/well; cultures were set in a final volume of 200 µL/well of CCM medium added with TSs. The plates were incubated in the dark under stationary conditions for up to 6 days at 25 °C. Aflatoxin accumulation was monitored by fluorescence emission determination: readings were performed directly from the bottom of wells of the culture plate with a microplate reader (TECAN SpectraFluor Plus, Männedorf, Switzerland) using the following parameters: λ_{exc} = 360 nm; λ_{em} = 465 nm; manual gain = 83; lag time = 0 µs; number of flashes = 3; and integration time = 200 µs.

6.2.2 Mycelial growth inhibition assay

Conidia suspensions, obtained from 14-21-day solid cultures [YES medium: 2% (w/v) yeast extract, 5% (w/v) sucrose, 2% (w/v) agar], were extimated for concentration (OD_{600})[86]. Determination of *A. flavus* radial growth was performed in YES solid medium amended with: three single spots (5 µL of a 10^7 conidia/mL suspension each) of fungal strain were equidistant inoculated in 90-mm Petri dishes, plates were incubated for 4 days at 25 °C and the mycelial growth was evaluated daily by measuring the reverse of colonies along two orthogonal diameters. Radial growth was expressed as cm/day ± SD. Additionally, conidial germination rate and post-germination hyphal outgrowth were assessed by analyzing changes in optical density of spore suspensions over time: in a 96 well microtiter plate 10^4 spores were inoculated in a final volume of 200 µL of YES liquid medium amended with TSs and incubated at 28 °C. The optical density at

620 nm (OD_{620}) was recorded for each well every 120 min with a microplate reader (MULTISKAN EX, Thermo Electron Corporation, Vantaa, Finland) without shaking. Samples were inoculated in triplicate. Biomass variation was also determined: fresh or dry mycelium weight was obtained, for each sample, withdrawing the mycelium from eight wells of the microplate and pooling them. The pooled mycelia were then blotted dry on clean paper and weighed (fresh weight determination) and then incubated at 80 °C for 48 h before dry weight determination. Samples were inoculated in triplicate.

6.2.3 Determination of the effects on sclerotia production

A volume of 5 µL from a 1 × 105 spores/mL suspension of *A. flavus* strain was point inoculated centrally on four replicate CZ plates [1.5% (w/v) agar, 0.1% (w/v) di-potassium hydrogen phosphate, 0.05% (w/v) magnesium sulphate heptahydrate, 0.05% (w/v) potassium chloride, 0.3% (w/v) sodium nitrate, 3% (w/v) sucrose] added with samples at the concentration of 50 µM. Plates were incubated up to 10 days to obtain sclerotia production; then, the surface of colonies was scratched, and sclerotia were manually recovered, ethanol-washed to remove conidia, and counted. Data were recorded as number of sclerotia per mycelium colony.

6.2.4 Cytotoxicity assay in human cell lines

Cell lines and culture conditions

The cytotoxicity evaluation was performed on human fibroblast cell line Hs27 (ATCC, CRL1634), human lung epithelial cell line HFL1 (ATCC, CCL-153), human colon epithelial cell line Crl1790 (ATCC, CCD 841 CoN).
Hs27 cells were cultured in Dulbecco's Modified Eagle Medium (DMEM); HFL-1 cells in Kaighn's Modification of Ham's F-12 Medium (F-12K) and CRL1790 cells in Eagle's Minimum Essential Medium (EMEM). All media were supplemented with 10% (v/v) fetal bovine serum (FBS), 1% penicillin (100 U/ml)/streptomycin (100 µg/ml) and 1% L-Glutamine (2 mM). Adherent cells were grown as a subconfluent monolayer. Flasks and plates were maintained at 37°C and 5% CO_2 in a humidified atmosphere. Culture

medium was refreshed every two or three days during sub-culturing. Hs27, HFL-1 and CRL1790 cell lines were obtained from the American Type Culture Collection (ATCC); U937 cells were obtained from the American Tissue Culture Collection (Rockville, MD).

MTS assay in human cell lines

The antiproliferative activity was evaluated by CellTiter 96® AQueous One Solution Cell Proliferation Assay (Promega Corporation, Madison WI, USA), a colorimetric assay that allow us to determine the number of viable cells in proliferation.
The CellTiter 96® Aqueous One Solution Reagent contains a tetrazolium compound [3-(4,5-dimethylthiazol-2-yl)-5-(3-carboxymethoxyphenyl)-2-(4-sulfophenyl)-2H-tetrazolium, inner salt; MTS] and an electron coupling reagent (phenazine ethosulfate; PES). PES has enhanced chemical stability, which allows it to be combined with MTS to form a stable solution. The MTS tetrazolium compound is reduced by cells into a coloured formazan product that is soluble in tissue culture medium. This conversion is accomplished by NADPH or NADH produced by dehydrogenase enzyme in metabolically active cells.
Briefly, 100 µL of a suspension of cells in exponential growth (5×10^4/mL in complete medium without phenol red supplemented with 5% FBS) were added into 96-well plates (FALCON®, Becton Dickinson, Meylan Cedex, France) 24 hours before treatment. Plates were incubated at 37°C in a humidified 5% CO_2 incubator. After this recover period, increasing concentrations of compounds (0.5-1.0-5.0-10.0-50.0-100.0 µM) were added to the medium and cells were left exposed for 24 hours. After treatment period, MTS reagent was added to each well. At the end of exposure time, the absorbance of the formazan product was measured at 485 nm by a microwell plate reader (TECAN SpectraFluor Plus, Männedorf, Switzerland).
The percent growth was measured by the formula:

$$\textit{Percent growth} = [1 - (OD_{485}\ \textit{treated}/OD_{485}\ \textit{control})] \times 100$$

The cytotoxicity response parameter GI_{50}, concentration of compound inducing a 50% reduction of the cell number in comparison to untreated control cells cultured in parallel, were extrapolated from concentration-response curve.

COMET assay in human cell lines

The Alkaline Comet Assay in an approach for assessing DNA damage evaluating the presence, after electrophoresis, of fragmented DNA outside the core of the nucleus. Relaxed and/or broken DNA fragments, negatively charged, migrate toward the anode and the resulting image has the appearance of a comet. The amount of DNA migrated from the head of the comet indicates the extent of the DNA damage. This quantity is dependent on the size of DNA fragments and the number of broken ends in the strands. The comet assay is usually performed at pH>13 to detect single and double breaks, alkali-labile sites (adducts, purinic and pirimidinic sites, oxidation of the nitrogenous bases). U937 cells were seeded 24 hours before treatment at a concentration of 1×10^5 cell/mL in 1 mL wells. Cell were treated with increased concentrations of the compounds (25.0-50.0-75.0-100.0 µM) for 1 and 24 hours. Positive and negative controls were represented by ethylmethanesulfonate (EMS), 2 mM, and DMSO, 100 µM, respectively. After treatment period at 37°C, determination of cell numbers and viabilities was performed with the trypan blue exclusion method. Only the treatments that had a viability higher than 70% have been processed in the Comet assay. Cells were transferred onto degreased microscope slides previously dipped in 1% normal melting agarose (NMA) for the first layer. The agarose was allowed to set for 20 min at 4°C before addition of a final layer of low melting agarose (LMA). Cell lysis was carried out at 4 °C overnight by exposing the cells to a buffer containing 2.5 M NaCl, 10 mM Na_2EDTA, 10 mM Tris–HCl, 1% Triton X-100 and 10% DMSO, pH 10. The electrophoretic migration was performed in an alkaline buffer (1 mM Na_2EDTA, 300 mM NaOH, 0 °C) at pH > 13 (DNA unwinding: 20 min; electrophoresis: 20 min, 0.78 Vcm^{-1} 300 mA), to detect single and double DNA strand breaks and alkali-labile sites. Slides were then washed with a neutralisation solution (0.4 M Tris–HCl, pH 7.5). DNA was stained with 75 µl ethidium bromide (10 µg/mL) before the examination at 400 X magnification under a Leica DMLS fluorescence microscope (excitation filter BP 515–560 nm, barrier filter LP

580 nm), using an automatic image analysis system (Comet Assay IV – Perceptive Instruments Ltd). % DNA in the tail region of the comet (TI, tail intensity) provided representative data on genotoxic effects. For each sample, coded and evaluated blind, 100 cells were analysed. The cells showing completely fragmented chromatin (i.e. hedgehogs cells) were assessed as a further indicator of cytotoxicity. These cells were not evaluated by image analysis but were recorded separately.

6.2.5 Anti-oxidant power determination

DPPH assay

The *in vitro* measurement of the antioxidant power was measured as the scavenging activity of tested molecules against the 2,2-diphenyl-1-picrylhydrazyl (DPPH) radical. It was performed in accordance with Choi et al.[88], namely measuring the bleaching of a purple-coloured methanol solution of the stable DPPH radical. Briefly, a 4 mL solution containing the selected compound was added to 1-ml aliquot of freshly prepared 85 µM DPPH. The resulting mixture was stirred and then incubated for 30 min at room temperature. The sample concentration was 75 µM. The decrease in absorbance measured at 518 nm depicts the scavenging activity of the compound against DPPH. Ascorbic acid (30 mM) was used as positive control to determine the maximal decrease in DPPH absorbance. Values were expressed in percentage of inhibition of DPPH absorbance in relation to the control values without the sample (ascorbic acid maximal inhibition was considered 100% of inhibition).

Anti-oxidant spot assay

To examine the anti-oxidant effect of the test compounds, bioassays of *S. cerevisiae* (BY4741 strain) were performed as described by Kim et al. in 2005[89]; 1 × 106 cells/ml cultured in YPD at 28 °C overnight were serially diluted from 10- to 100-fold in liquid synthetic medium (SD; 6.9% w/v YNB (Formedium™, Swaffham, King's Lynn, Norfolk, UK) supplemented with 2% (w/v) glucose and appropriated amino acids and bases for auxotrophy), and then, cells from each serial dilution were spotted adjacently on SD

agar medium supplemented with 50 µM of each compound to be tested (0.5% v/v DMSO was used as control) and 0.5 or 1 mM hydrogen peroxide (H_2O_2). To examine alleviation of oxidative stress of vanillic, gallic, and dihydrolipoic acids; glutathione (GSH); and samples (all supplemented at the concentration of 50 µM) on cells, 0.5 or 1mM hydrogen peroxide (H_2O_2) was incorporated into the medium. Cell growth was monitored at 28°C for 7 days. Each assay was performed in triplicate. Compounds were considered to have anti-oxidant activity if cell growth improved compared to cohorts exposed to H_2O_2 without the sample.

Petite frequency assay

To determine the effect of samples on the yeast mitochondrial DNA (mtDNA) mutability, W303-1B and DWM-5A strains harbouring mip1Y757 and mip1G807R alleles, respectively, were pregrown on solid synthetic complete medium [SC; 6.9% (w/v) YNB (Formedium™, Swaffham, King's Lynn, Norfolk, UK), 0.1% (w/v) dropout mix] according to Baruffini et al.[90] supplemented with 2% (v/v) ethanol at 28 °C to counterselect the petite cells that could be present in the population. After approximately 60 h, strains were grown on liquid SC medium supplemented with 2% (w/v) glucose and the compound to test (50 µM) or dihydrolipoic acid (50 µM) for two 24-hours growth cycles. Control experiment in which equal amounts of DMSO (0.5% v/v) or ethanol (0.1% v/v)—the solvents used to solubilize the sample and dihydrolipoic acid, respectively—were added to untreated cells was done in parallel. Cells were then counted, diluted, and plated (200–250 cells/plate) on SC medium supplemented with 0.3% (w/v) glucose and 2% (v/v) ethanol. Petite frequency was defined as the percentage of colonies showing the petite phenotype after a 5-day incubation at 28 °C. Each experiment was repeated at least three times on two independent clones for each strain. Statistical analysis of petite frequency was performed by a *two-tailed Z test*.

6.2.6 Ames test

Molecules were dissolved in a compatible solvent (DMSO) and assayed with the *Salmonella*/ microsome test (Ames test) at increasing doses (0.1, 1, 10, 50, 100

μM/plate), with *S. typhimurium* TA98 and TA100 strains, with and without metabolic activation (S9 mix) to highlight the presence of indirect and direct mutagenic activity. The experimental procedure was the standard plate incorporation method[91]. Salmonella TA98 strain detects frame-shift mutagens and TA100 strain responds to base-pair substitution. Positive controls were 2-nitrofluorene (10 μg/plate) and sodium azide (10 μg/plate) for TA98 without S9 and TA100 without S9, respectively, and 2-aminofluorene (20 μg/plate) for both strains with S9. DMSO was tested as negative controls. The data obtained were showed as revertants per plates computed by means of two replicates with their relative standard deviation. Moreover, the results were expressed as mutagenicity ratio (RM) dividing the revertants/plate by spontaneous mutation rate. The results of the test were considered positive if two consecutive dose levels or the highest non-toxic dose level produced a response at least twice that of the solvent control and at least two of these consecutive doses showed a dose-response relationship[92].

6.2.7 *Allium cepa* test

The first step was a toxicity assay: 12 equal-sized young onion bulbs will be exposed for 96 hours in the dark to different dilutions of pure compounds dissolved in DMSO. Root length will be used to calculate the EC_{50} value of each compound and to identify the concentration to adopt in the *A. cepa* genotoxicity assay. Other macroscopic parameters (turgescence, consistency, change in colour, root tip shape) will be used as toxicity indexes. Two genotoxicity tests, using *A. cepa*, were carried out on molecules to detect **chromosome aberrations** (namely buds, bridges, binucleate cells, laggard or lost chromosomes, fragments, c-mitosis polar slip, rings and multipolar cells) and **micronuclei**[93,94]. Both tests were performed using six equal-sized young bulbs per sample and after 72-hour pre-germination in Rank solution; the bulbs were exposed to samples for 24 hours. After exposure the roots were fixed in acetic acid and ethanol (1:3) for 24 hours and lastly stored in 70% ethanol for the chromosome aberrations (CA) test. In the micronuclei (MN) test the bulbs, after exposure, were replaced in Rank's solution for 44 hours of recovery time (to cover two rounds of mitosis), fixed in acetic acid and ethanol (1:3) for 24 hours and lastly stored in 70% ethanol. Distilled water (24-

hour exposure) and maleic hydrazide (10-2M, 6-hour exposure) were used as negative and positive controls, respectively. The negative control was DMSO in Rank solution (the dose of DMSO corresponding to volume used in solution) and positive control was maleic hydrazide (10 mg/l, 6 h). Five roots of each sample were considered for microscopic analysis: 1,000 cells/slide (5,000 cells/sample) were scored for **mitotic index** (as a measure of cell division and hence of sample toxicity), 200 in mitosis cells/slide (1,000 cells/sample) for chromosomal aberrations and 2,000 in interphase cells/slide (10,000 cells/sample) were scored for micronuclei frequency. Statistical analysis was performed using *Chi square* test for mitotic index and chromosomal aberrations. All experiments were performed in duplicate (two independent assays).

6.2.8 *A. flavus* proteome analysis

Preparation of *A. flavus* total protein extracts

Mycelium (conidia were incubated for 4 days in the same culture conditions used for aflatoxin determination) was manually detached from wells and rinsed in ultrapure distilled water. Samples (200 mg each) were weighed into a prepared tube with 200 µL of glass microbeads, frozen in liquid nitrogen, ground into a powder with the action of a dental amalgamator (TAC 200/S, Linea TAC s.r.l., Montegrosso d'Asti, Italy), and added with 200 µL of lysis buffer [50 mM Tris-HCl pH 7.5, 2 M thiourea, 7 M urea, 2% (v/v) Triton X-100, 1% dithiothreitol (DTT), 2% (w/v) soluble polyvinylpolypyrrolidone (PVPP), 1 mM phenylmethylsulphonylfluoride (PMSF), and 0.2% (v/v) β-mercaptoethanol]. Samples were centrifuged twice for 20 min at 13,000 x g, and then, 200 µL 45% (w/v) trichloroacetic acid was added to the supernatant. After incubation on ice for 10 min, the samples were centrifuged for 15 min at 13,000×g at 4 °C and the pellet was washed with cold acetone; this washing step was repeated for three times. Pellets were dried in under a vacuum pump, then resuspended in rehydration buffer [8 M urea, 2% (w/v) 3-[(3-cholamidopropyl)dimethylammonio]-1-propanesulfonate hydrate (CHAPS)] and stored at −80 °C until further use. Total proteins content was determined according to the Bradford protein assay[95], using bovine serum albumin as standard.

Proteomic analysis

Analysis of differentially expressed proteins in *A. flavus* treated cultures was conducted by two-dimensional electrophoresis (2D-PAGE). Briefly, 125 µg of total proteins was loaded on 7-cm-long, pH interval 3–10, strips, isoelectrofocused and separated in a 12% polyacrylamide gels (second-dimension run). Gels were stained with SYPRO® Ruby Protein Stain (BioRad, Hercules, CA, USA); 2-D gel image elaboration and analysis was carried out with the PDQuest software version 8.0.1 (BioRad, Hercules, CA, USA). Three technical replicates for each of the three biological replicates were performed, for a total of nine gels for each class (control and treated samples). Spots differentially expressed were manually removed from the gels, subjected to an in-gel digestion, and addressed to a liquid chromatography–electrospray ionization–mass spectrometry (LCESI-MS/MS) and LTQ-Orbitrap analyses. Mass data were submitted to database searching using SEQUEST search engine Proteome Discoverer interface (Thermo Scientific, version 1.4; Thermo Fisher Scientific, Waltham, MA, USA).

Gene expression – Real-time PCR

Total RNA was extracted from 96-h-old microplate CCM cultures using TRIzol® Kit (Sigma-Aldrich, Saint Louis, MO, USA), according to the manufacturer's instructions. 2 mg of mycelium was flash frozen in liquid nitrogen, ground to a powder with an amalgamator (TAC 200/S, Linea TAC s.r.l., Asti, Italy; oscillation frequency 4.200 p/m), and overlaid with 300 µl of TRIzol® reagent. The RNA quality was confirmed by gel electrophoresis (1.5% agarose) and concentrations were measured using a BioPhotometer (Eppendorf, Hamburg, Germany). The A260/A280 ratio was measured. Two micrograms of total RNA sample were reverse-transcribed using theMaxima First-Strand cDNA Synthesis Kit for qRT-PCR with dsDNase (Thermo Fisher Scientific, Waltham, MA, USA), following the manufacturer instructions. The complementary DNA (cDNA) samples were used as templates of qPCR reactions conducted with ABI 7300 instrumentation (Thermo Fisher Scientific, Waltham, MA, USA) and SYBR® Green PCR Master Mix (Life Technologies, Waltham, MA, USA). The concentration of each primer pair was optimized in order to satisfy the requirements for mRNA-level quantification

according to the Livak method[96]. Primer validation was carried out with the best amplification curve, and dissociation curves were used to confirm the good amplification of each gene. At least three biological replicates were used to validate the amplification specificity. Target gene expression was normalized to the expression of tub1 gene, chosen as an internal standard. The ΔCT was calculated as CT target gene – CT internal standard; the expression level variations were then expressed as $2^{-\Delta\Delta CT}$ (with ΔΔCT = CT treatment – CT control). Three biological and three technical replicates per condition were performed. A negative control with no reverse transcriptase was also used to exclude DNA contamination. Amplification conditions were 50 °C for 2 min and 95 °C for 10min; followed by 40 cycles at 95 °C for 15 s and 60 °C for 1 min; and then, 95 °C for 15 s, 60 °C for 1 min, 95 °C for 15 s, and 60 °C for 15 s. The significance of differences between relative expression ratios of treated and control samples was determined using the *Mann-Whitney test,* with a $p \leq 0.05$ limit.

6.3 Molecular docking

The majority of biological processes are based on the principle of a molecular recognition between a substrate and its receptor. These interactions are very specific and ensure the success of extremely difficult biochemical reactions. The molecular docking is a computational technique able to predict and estimate the energies of the interactions between molecules[97]. It is useful to predict the mutual geometry of the two partners involved in the interaction both in energy and chemical affinity terms.

Docking techniques have been developed to be used mostly in the design of bio-active compounds in the field of medicinal chemistry, where the computational resources are widely used to perform virtual screening of huge libraries of compounds on different targets to guide the researchers in the identification of the most promising candidates. There are two different docking approaches: the ligand-based and the structure-based docking. In the ligand-based approach is applied to identify the target of an already known active molecule. The drug structure is kept fixed and many different potential target proteins are virtually tested to find the active site which better fits with the drug. The second, and most used, approach is the structure-based. In this docking technique a "guest" molecule (or a set of molecules) could be inserted in the active site of a previously fixed "host" molecule. This procedure is usually performed through specific software which guides the user in the research of the best host-guest combination (called "best pose"). There are three major categories of structure-based docking:

- Protein-protein
- Protein-DNA
- Protein-ligand (also called "substrate" or "inhibitor")

The best pose is a ligand position characterized by the highest affinity for the target protein. If the ligand is a small molecule, the affinity is considered the sum of different contributes:

- Hydrogen bonds
- Ionic interactions
- Van der Waals interactions
- Lipophilic interactions

To conclude, a reliable docking algorithm must take into account two major issues: the first is the research of the ligand conformation which better fits with the protein active site (shape selectivity) and the second is to score each position by estimating its binding affinity with the target from the energetical point of view.

Docking: limits and approximations

The research of the best pose has a huge number of variables, this leads to a non-negligible computational cost which can raise exponentially when the docking approach is applied with the aim of screening a large library of candidates. Therefore, it is impossible to apply the accurate methods based on quanto-mechanics and it is necessary to introduce molecular mechanics, based on easier concepts and approximations. The method applied is the force-field: a functional form which uses experimental parameters to calculate the potential energy of a system of atoms.
Of course, the simplifications introduced by the force-field method are a source of errors and uncertainty, which constitute the major limit of the docking technique.
The heaviest approximations usually introduced in a docking simulation are:

- The protein is kept in a blocked conformation, usually the crystallographic one. This simplification eliminates the common biological phenomenon of the induced-fit, namely the rearrangement of a protein in presence of a ligand.
- It is impossible to consider the formation or break of covalent bonds.
- The study of ligands with high degrees of freedom is usually not very reliable.

The *ChemScore* function

There is plenty of docking software, each of them has specific features that make them suitable for different purposes. To study interactions between proteins and small molecules that contains metal atoms one of the most efficient software is *Gold* (*Genetic Optimisation for Ligand Docking)* created by the Cambridge Crystallographic Data Centre (CCDC). According to its developers, "*Gold* has proven success in virtual screening, lead optimisation, and identifying the correct binding mode of active

molecules". *Gold* implemented some different algorithms to score the possible poses. The scoring functions used by *Gold a*re divided in those able only to classify conformations (like the *GoldScore* and ASP) and those who can also estimate the binding energy of each conformation with the protein like the *ChemScore.*

The *ChemScore* function[98,99] (the function we usually applied in our projects) has been optimised for the prediction of ligand binding positions considering factors such as H-bonding energy, van der Waals energy, metal interaction and ligand torsion strain. Through these parameters the algorithm estimates the total free energy change (ΔG) that occurs on ligand binding performing a regression against the binding affinity experimental data of 82 complexes. The function used to calculate the binding free energy is:

$$\Delta G_{binding} = \Delta G_0 + \Delta G_{h\,bond} + \Delta G_{metal} + \Delta G_{lipo} + \Delta G_{rot}$$

Each component of the equation is the product between the contribution of the physical or chemical feature and a factor determined with a regression of the type:

$$\Delta G_0 = v_0$$
$$\Delta G_{hbond} = v_1 \cdot P_{hbond}$$
$$\Delta G_{metal} = v_2 \cdot P_{metal}$$
$$\Delta G_{lipo} = v_3 \cdot P_{lipo}$$
$$\Delta G_{rot} = v_4 \cdot P_{rot}$$

Where the *v* terms are the coefficients of the regression and *P* indicates the different types of chemico-physical interactions.

Finally, the *ChemScore* function is obtained from the sum between the calculated $\Delta G_{binding}$ and some contributes which insert the effects of forces adverse to the binding like the internal torsions or the effect of collisions. Then, the final equation used by the algorithm to score each position is:

$$ChemScore = \Delta G_{binding} + P_{clash} + c_{internal} \cdot P_{internal} + (c_{covalent} \cdot P_{covalent} + P_{constraint})$$

All the parameters used in the functions like the energy and the direction of hydrogen bonds, atomic radii and torsion potentials, are part of the GOLD parameter file and taken from experimental data.

TOPIC 2:

Anticancer agents

7 Metal-based drugs

The use of metals in medicine has ancient roots. There is evidence of the use of gold in China to treat smallpox and lung diseases dating back to 2500 BC[100]. Egyptians are known to have used copper salts to sterilize water and during the 16th and 18th centuries galenic formulations containing mercury were applied to treat syphilis[101]. Throughout the 19th and early 20th centuries gastric problems were treated mostly using copper sulphate and lead acetate mixtures, whereas gold drugs have been in use for the treatment of rheumatoid arthritis[102]. Nowadays, metals are contained in many formulations, for instance lithium carbonate, used to stabilise the mood of people with manic-depressive disorders, and bismuth subsalicylate which is an antidiarrheal agent. However, a drug that dramatically changed the history of medicine is cisplatin. This platinum complex (*cis*-diamminedichloroplatinum(II)) has a strong anti-cancer activity in solid tumours thanks to its ability to bind DNA of cancerous cells and therefore to inhibit their proliferation. The cisplatin is the ancestor of a series of platinum-based drugs (i.e. carboplatin and oxaliplatin) which are still the only drugs to fight against extremely aggressive tumours in colon and lungs. Even if these compounds are very active, they have severe side effects and lead to intrinsic or acquired resistance phenomena when used for repetitive treatments[103]. These drawbacks have stimulated the research in the last two decades and scientists have discovered that also other metals have interesting anti-cancer properties. Gold and ruthenium are presently the most studied[104,105], but many other metals, such as osmium, silver, copper, zinc, nickel, etc, are currently under investigation[106] (*Figure 48*). Our research is aimed at finding new active metal-based compounds alternative to cisplatin which can be used in extremely low dosage and with the lowest possible effects on the organism.

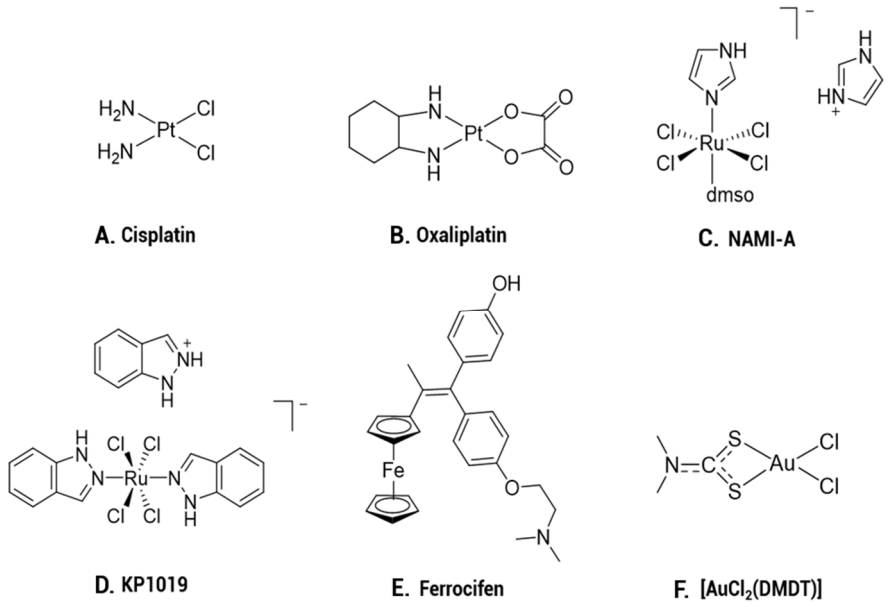

Figure 48: Examples of metal-based anticancer drugs. A. cis-platin[107], B. Oxaliplatin[108], C. NAMI-A[109], D. KP1019[110], E. Ferrocifen[111] and F. [AuCl$_2$(DMDT)][112].

7.1 Copper and nickel complexes as anticancer agents

In search of new anticancer metal complexes, we were interested in the study of two first-row transition metals: copper and nickel. We have focused our attention on these species because they are micronutrient elements for most living beings and in particular for humans. This characteristic makes them less toxic than platinum because cells recognize and handle them since they are under homeostatic control. This could in principle buffer the toxic side-effects observed for cisplatin and its analogues.

Our aim was therefore to obtain compounds containing these two metals and possessing new and selective mechanisms of action to overcome the limits of the current medical strategies.

Copper is a micronutrient element for humans. Its unique physicochemical properties allow copper to be the key element in many biological processes such as the electron transfer in mitochondria or the catalysis of enzymatic reactions. These processes are based on the copper ability to rapidly cycle between the +1 and +2 oxidation states, a process that takes place in the physiological range of redox potentials. Moreover, it can have a structural role in proteins, thanks to its ability to bind effectively medium-soft elements of some amino acids (mainly nitrogen and sulphur). As all the other micronutrients, copper amount in the human body is low (around 0.0001%) and finely controlled. It is essential for life, but high copper levels bring to acute and long-term toxicity[113]. The correct daily intake of copper seems to be around 900 μg/day (for adults)[114]. Therefore, to study new copper-based anticancer drugs we should be able to balance copper toxic activity to selectively kill carcinogenic cells without affecting the entire organism. The cytotoxic effect of copper-containing derivatives is usually connected with their ability to induce cell death either by necrosis and apoptosis, however some recent evidences describe also the ability of some copper compounds to induce cell-death through autophagy: an alternative and non-apoptotic process[115]. In general, copper derivatives display a different mechanism of action compared to other metal-based anticancer complexes. Classical anticancer drugs seem to be usually highly selective for their molecular target (for example, cisplatin with DNA), whereas copper complexes can affect both DNA and proteins inducing a general but lethal toxicity to cancer cells. One of its most effective mechanisms of action is the ability to induce high levels of oxidative stress through the production of large amounts of ROS in cells[116].

Nickel There are less examples of nickel-based anticancer drug in the literature compared to copper. Nevertheless, the number of nickel derivatives with promising therapeutic effects is growing rapidly. As mentioned above, nickel is considered a micronutrient, but its exact metabolism is still largely unknown. The daily intake of nickel is estimated between 5 and 50 μg per day and, as for copper, higher amounts are extremely toxic. Many people showed also allergies (mostly severe skin rash) even when nickel is present in traces. Human enzymes which contain nickel as cofactor have

not been identified yet, although rats grown in the lack of nickel exhibited severe consequences: depressed growth, low haemoglobin levels and low red blood cell counts. Moreover, this deficiency showed effects in the activity of many fundamental enzymes in liver and kidneys and the presence of altered levels of ATP, urea, and sugars and triglycerides in serum and liver fluids[117]. Nickel is essential for humans also because it is essential for the life of the gut microbiota. In fact, it has been known for years that nickel is involved in the metabolism of many prokaryotes and unicellular eukaryotes which constitute the intestinal microflora[118]. As potential anticancer drugs, nickel complexes were usually active in DNA binding, mostly as intercalating agents, and in DNA cleavage[119]. It is also able to produce high levels of ROS and oxidative DNA damage[120,121]. However, in the design of new nickel-based drugs, we need to consider that the biological properties of the complexes are usually largely dependent on the nature of the organic ligands.

TS of copper and nickel in literature

As mentioned in the introduction, TS are a very enticing class of molecules from which to develop anticancer agents. However, the antitumor activity of TS is extremely differentiated, and it often depends on the typology of tumour cells.

The presence of a metal ion almost systematically increases the activity of the TS ligand creating a cooperative effect. In fact, most of the TS metal complexes are more active than the corresponding reagents taken separately. The possible targets of the complexes are multiple, and up to now, a common mechanism of action to explain their activity has not been found. This variability comes from the number and nature of the components of the system, for instance the TS functionalisation or the metal used[122]. Currently, the effect of TS complexes can be grossly divided into compounds which contain redox-active or redox-inert metals. The presence of redox active metal (like copper and nickel) induces frequently oxidative stress phenomena and interference in the mitochondrial respiratory cycle. Our research group has studied these compounds for years and the most interesting copper complexes usually belong to these kinds of effects. We collected much evidence that high ROS levels have usually a key role in deciding the fate of the treated cells depending on the extent of the oxidative

damage[123]. The ROS can also act as intracellular signalling molecules implicated in the activation of the caspase proteins, the proteins that regulate and activate apoptosis[124] (*Figure 49*). In addition to these effects, we registered also the very interesting capability of some nickel(II) complexes to bind DNA without breaking it down into fragments, but altering the double-helix conformation and creating knot-like structures and hairpins[125].

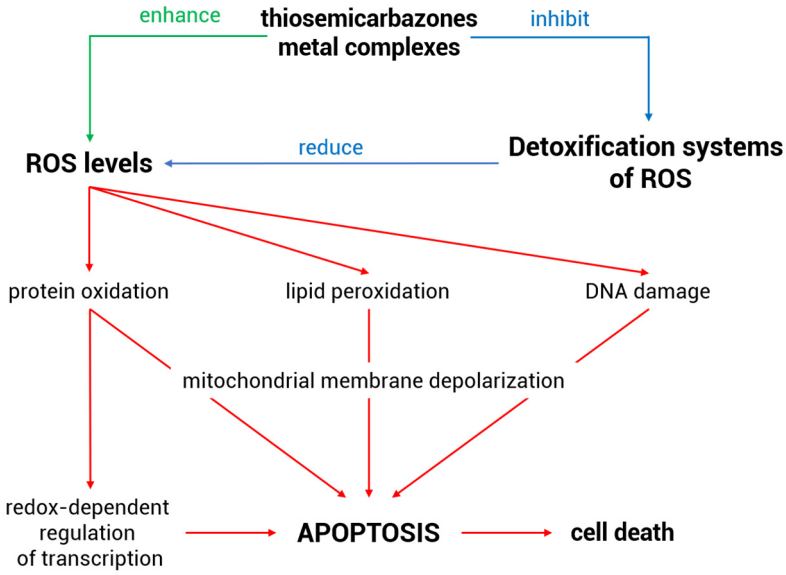

Figure 49: Schematic representation of the effects of TS metal complexes on cancer cells.

Our approach

Against this background, we decided to delve into this field by designing some new different TS copper and nickel complexes as new potential anticancer agents. The approach we used is inspired by the drug discovery cycle used by pharmaceutical industries. This approach starts from a large amount of potential active compounds that are screened to find the most effective ones. These are, in turn, subsequently studied in detail and optimised. Our project started from the idea to use copper(II) and nickel(II) as metal centres and to investigate how the thiosemicarbazone ligand can be

modified to improve the complex activity. In particular, we focused our work on the design of thiosemicarbazones with different denticity (*Figure 50*).

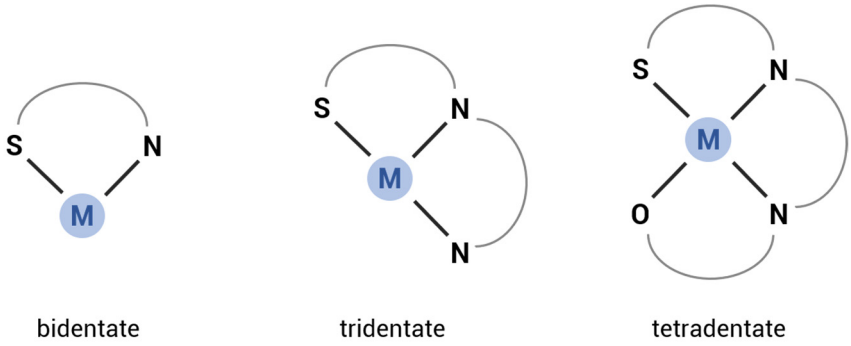

Figure 50: Schematic representation of TSs with different denticity.

The denticity is a technical word used in inorganic chemistry to describe the ability of a ligand to bind metal atoms based on the number of its donor groups. It is indicated with the Greek letter 'kappa' followed by the number of the linkage points (κ^n). Since thiosemicarbazones usually bind transition metals in an S,N-bidentate mode, we started from the design and synthesis of a panel of complexes in which two equivalents of ligand were used to bind and neutralise one divalent metal ion. Subsequently, we identified some interesting aldehydes and ketones able to increase the denticity of the final thiosemicarbazones. In this way, we obtained both tridentate and tetradentate ligands and their corresponding complexes. The antiproliferative activity of every derivatives was screened on different tumoral cell lines, then the most promising compounds were analysed more in detail according to their specific characteristics. Subsequently, we explored the possibility to modify some TS creating the analogue mono-thiocarbohydrazones (mono-TC). The biological properties of these derivatives were compared with the TS and then studied in detail finding some very interesting results.

7.2 Bidentate derivatives

The first step in the design of the bidentate ligands was the choice of the aldehydes to use in the condensation with the thiosemicarbazide. Analysing promising results obtained in our research group over the past few years, we choose to use four different natural aldehydes, namely citral, octanal, octenal and cinnamaldehyde.

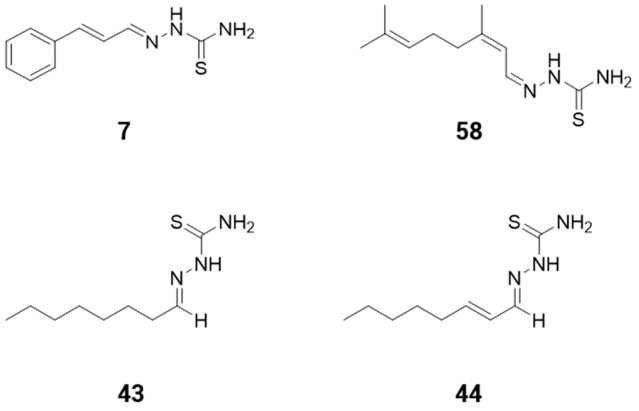

Figure 51: Bidentate TSs.

All the corresponding TSs were obtained pure and in good yields following the procedures reported in the *Anticancer agents: experimental* section (*Figure 51*). Since, these TSs did not have any functionalisation on the N^2, they were used as anionic ligand in the synthesis of metal complexes. A 2 : 1 ratio between ligand and metal ensures the charge neutrality of the final products. The characterisation was made mainly using ESI-MS at low and positive ionization voltages to observe the molecular ion peak. For nickel(II) diamagnetic derivatives, also the ^{1}H-NMR spectroscopy resulted in many cases very useful to verify the actual deprotonation of the ligand in the complex. For copper(II) this approach was not applied due to the paramagnetic nature of the metal ion. Every product was submitted to the cytotoxicity evaluation on U937, histiocytic lymphoma cells (experimental details are reported in the *Biological test protocols section*). *Table 20* shows the IC_{50} values obtained from the screening. Colours have been used to facilitate the reader in the comprehension of the data: the colour red

indicates non-active compounds, whereas colours from yellow to green indicate progressively lower IC_{50}, and therefore, the most interesting results.

	IC_{50} (μM) U937		
	free ligand	**Cu(II) complex**	**Ni(II) complex**
citral-TS	30.61±3.8	2.58±0.19	5.88±0.63
octanal-TS	>100	18.81±4.78	8.9±1.72
octenal-TS	>100	78.46±3.66	16.86±2.63
cinnamaldehyde-TS	>100	19.36±2.16	24.08±11.71

Table 20: IC_{50} values of bidentate TSs and their copper(II) and nickel(II) complexes on U937 cells.

The analysis of the IC_{50} values highlighted that the TSs themselves are always less active than their corresponding metal complexes. Three of the five TSs were considered inactive (having their IC_{50} higher than 100 μM), whereas the octanal-TS (**43**) and citral-TS (**58**) resulted moderately active with IC_{50} concentrations between 30 and 50 μM. Looking at the copper(II) derivatives, we can see that all the complexes showed an antiproliferative effect. Octanal-TS and cinnamaldehyde-TS copper(II) derivatives (**51** and **12**) showed similar and interesting results with both IC_{50} values lower than 20 μM. However, the best result of the series (and of the entire screening) was obtained with the citral-TS (**69**) with an IC_{50} of 2.58 μM. Regarding Ni(II) series, all the complexes resulted effective, with IC_{50} concentrations lower than 25 μM. The IC_{50} were generally similar to the corresponding copper(II) complexes except for the octenal-TS Ni(II) complex (**85**) which was five-fold more cytotoxic than its copper(II) analogue (**52**). To conclude, the TSs we designed are inactive alone, but when used as chelating agents for a metal ion (both Ni(II) and Cu(II)) they become very interesting candidates. The

following step was to modify our TSs in the N^4 position to evaluate the effects on the biological activity. We chose to modify the N^4 because it does not interfere with the ability of the ligand to undergo deprotonation and therefore to interact with metal ions. The modified products were obtained by condensing our starting aldehydes with two different N^4-substituted thiosemicarbazides, namely 4-methyl-3-thiosemicarbazide and 4-phenyl-3-thiosemicarbazide. The functionalisation on the N^4 changes significantly two important physicochemical properties of the ligands: the lipophilicity and the number of hydrogen bond donor sites. A TS not functionalised on N^4 has two terminal hydrogens which creates a hydrophilic and double hydrogen bond donor site. When one of the hydrogens is replaced with a methyl or phenyl group the lipophilicity raises significantly in agreement with the nature of the substituent. Moreover, the N^4 functionalised TSs have one less hydrogen bond donor site then the normal TSs. The partition coefficient $LogP_{ow}$ is a very useful parameter to estimate the effect on the lipophilicity caused by the different N^4 functionalisation. Its value, which can be determined experimentally or calculated, corresponds to the ratio of concentrations of a compound in two phases, hydrophilic and hydrophobic, represented by water and octanol when the system is at the equilibrium. The higher the $LogP_{ow}$ value, the more lipophilic is the compound. The $LogP_{ow}$ values calculated for each derivative are reported in *Table 21*. The table boxes have been coloured from red to blue in increasing order of lipophilicity.

$LogP_{ow}$ values	**$-NH_2$**	**$-NH(CH_3)$**	**$-NH(C_6H_5)$**
citral-TS	2.10	2.62	4.28
octenal-TS	2.07	2.59	4.25
octanal-TS	2.09	2.61	4.27
cinnamaldehyde-TS	1.58	2.10	3.77

Table 21: $LogP_{0w}$ values calculated for differentially substituted TSs.

The $LogP_{ow}$ values clearly showed than the lipophilicity grows significantly passing from TSs with no functional groups in N^4 to those alkylated in N^4 ($-NH_2$ < $-NH(CH_3)$ < $-NH(C_6H_5)$). The *Table 22* collects the IC_{50} values obtained from the screening on U937 cells of all the derivatives and their metal complexes.

	N^4 function	**IC_{50} (μM) 24h U937**		
		free ligand	**Cu(II) complex**	**Ni(II) complex**
citral-TS	$-NH_2$	30.61±3.8	2.58±0.19	5.88±0.63
	$-NH(CH)_3$	> 100	2.63±0.15	4.54±1.22
	$-NH(C_6H_5)$	54.55±6.94	>100	>100
octanal-TS	$-NH_2$	>100	18.81±4.78	8.9±1.72
	$-NH(CH)_3$	>100	3.57±1.42	24.38±5.39
	$-NH(C_6H_5)$	-	-	-
octenal-TS	$-NH_2$	>100	78.46±3.66	16.86±2.63
	$-NH(CH)_3$	>100	29.07±2.43	11.13±2.29
	$-NH(C_6H_5)$	-	-	-
cinnamaldehyde-TS	$-NH_2$	>100	19.36±2.16	24.08±11.71
	$-NH(CH)_3$	>100	3.89±1.07	>100
	$-NH(C_6H_5)$	-	-	-

Table 22: IC_{50} values of TSs and their copper(II) and nickel(II) complexes on U937 cells.

The citral-TS series was the first we submitted for a cytotoxicity evaluation. The N^4-methyl (**59**) and N^4-phenyl derivate (**60**) were both less active then the citral-TS (**58**). Regarding metal complexes, the N^4-methyl group (**70** (Cu) and **77** (Ni)) did not change significantly the activities, while the N^4-phenyl group (**71** (Cu) and **78** (Ni)) completely cancelled the cytotoxic power. This effect was due to the solubility problems we

encountered with these complexes. In fact, both copper and nickel compounds showed low solubility in the aqueous media used for the test, creating a light precipitate which is ascribable to the high lipophilicity of the two phenyl groups. In the light of this evidence, we decided to exclude the N^4-phenyl derivatives from the screening. The N^4-methyl TS of octanal (**61**), octenal (**63**), and cinnamaldehyde (**56**) were not as cytotoxic as their corresponding normal TS, while the copper(II) complexes (**71**, **74** and **67**) resulted all more active than the corresponding normal TSs, lowering the IC_{50} from 3 up to 5-fold. By contrast, for the nickel(II) complexes (**83**, **86** and **77**) of the N^4-methyl derivatives we evidenced a decrease of the cytotoxicity.

7.2.1 Stability of DMSO stock solutions and its effect on cytotoxicity

This paragraph describes the evaluation of the effects on the cytotoxicity results of the use of freshly or old prepared stock solutions of metal complexes. We took as an example the citral-TS series using both the normal and N^4-methyl derivatives. The first step was the evaluation of the cytotoxicity using a freshly prepared 10 mM stock solution of copper and nickel complexes in DMSO, then we repeated the same experiment after 6 months using the same stock solution which were stored in the dark at room temperature for the entire 6 months period. The comparison between the IC_{50} values obtained are collected in *Table 23*.

			IC_{50} (μM) 24h U937 Cu(II) complexes			**IC_{50} (μM) 24h U937 Ni(II) complexes**	
			freshly prepared solution	**6-month old solution**		**freshly prepared solution**	**6-month old solution**
derivatives of citral-TS	$-NH_2$	**69**	2.58±0.19	29.44±2.18	**79**	5.88±0.63	5.66±1.57
	$-NH(CH)_3$	**70**	2.63±0.15	39.27±1.98	**80**	4.54±1.22	4.25±2,29

*Table 23: Comparison between IC_{50} values of freshly prepared solution and 6-month-old solutions of **69**, **70**, **79** and **80**.*

The results showed a clear difference of behaviour between Cu(II) and Ni(II) complexes. As described before, in freshly prepared solutions copper derivatives showed better results than the nickel analogues with the two IC_{50} at around 2.5 μM. However, looking at the results of the same experiment performed after 6 months, we noticed that the copper complexes decreased significantly their cytotoxicity, whereas nickel derivatives maintained them almost unaltered. This evidence suggested that the two complexes have strongly different stability in solution and that the stability is strictly connected with their mechanism of action. In 2005, L. Helm and co-workers reviewed the inorganic and bio-inorganic solvent exchange mechanisms of metal complexes[126]. This review was very helpful to explain our experimental observations, it underlines a very high lability of copper(II) derivatives in the presence of coordinating solvents like water and DMSO. They compared also the rate constants of many solvent exchange reactions concluding that the substitution in Cu(II) derivatives is usually 5 orders of magnitude faster than in those of Ni(II). The cytotoxicity of our compounds reflected these considerations, underling a connection between complex stability and cytotoxicity. In fact, derivatives with nickel, being stable through time, retained their biological activity whereas the less stable Cu(II) complexes went toward DMSO substitution processes that lowered their cytotoxic power through time (*Figure 52*).

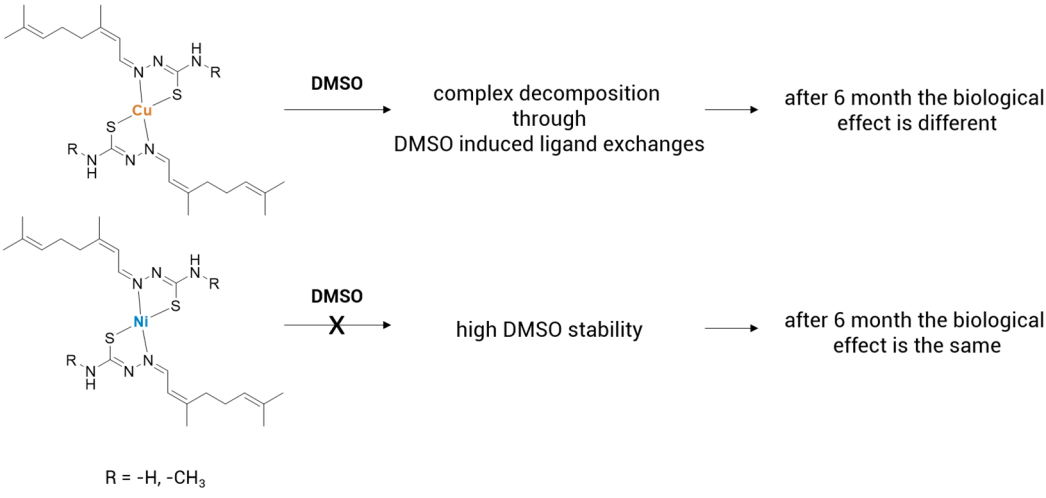

Figure 52: Different stability of copper(II) and nickel(II) complexes.

7.3 Tridentate derivatives

As mentioned before, we wanted to explore TSs with different denticity. This paragraph describes the study of two different κ^3 derivatives and the corresponding Cu(II) complexes, namely the TS of the quinoline-2-carboxaldehyde (**88**) and 5-fluorisatin (**89**). We chose these two derivatives because of the very interesting results they showed in previous works in our research group[21,127]. The quinoline-2-carboxaldehyde-TS (**88**) is a tridentate ligand because also the nitrogen atom of the quinoline is geometrically available to be coordinated by the metal, whereas in the 5-fluoroisatin-TS (**89**) the coordination is expanded through the oxygen atom of the cyclic amide (*Figure 53*).

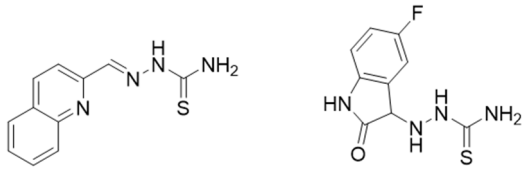

88 **89**

Figure 53: Tridentate TSs.

This kind of molecules promotes the formation of complexes with a 1 : 1 ratio between ligand and metal thanks to a classical chelate effect (entropic and enthalpic contributions). This explains why we used an equimolar amount of ligand and metal salts to synthesise the complexes. All the procedures used for the synthesis and characterisation of the products are described in the *Anticancer agents: experimental* section.

Following the same approach already used for bidentate TSs, we screened the anticancer activity of our tridentate candidates. Since we had already determined the IC_{50} values of quinoline-derivatives on U937 cell line[128], we tested the cytotoxicity on HeLa, a cervical cancer cell line (*Table 24*). The use of more than one cell lines is extremely interesting, because the comparison of the results allows to underline if there is specificity which could help to identify the mechanism of action.

		IC_{50} (μM) 24h free ligand			IC_{50} (μM) 24h Cu(II) complexes	
		U937[21]	**HeLa**		**U937**[21]	**HeLa**
quinoline-2-carboxaldehyde-TS	**88**	55.00	67.98±10.57	**90**	4.10	8.76±0.82
5-fluoroisatin-TS	**89**	-	>100	**91**	-	11.38±2.07

Table 24: IC_{50} values of tridentate TSs and their copper(II) complexes on U937 and HeLa cells.

The IC_{50} on HeLa confirmed the trend we previously observed on U937, but the IC_{50} values obtained for **88** and **90** on HeLa resulted a bit higher than those obtained on U937. However, the differences observed between the two cell lines do not justify any specificity of action, but they could be explained considering that the two cell lines have different nature: adhesive (HeLa) and suspension (U937), and then different response to external stimuli. In HeLa, the quinoline-TS (**88**) resulted moderately active, while the fluoroisatin-TS (**89**) completely inactive. On the other hand, the two copper(II) complexes (**90** and **91**) resulted both active with an IC_{50} of 8.76 and 11.38 μM respectively.

7.4 Tetradentate derivatives

This section contains the description of two different projects regarding κ^4 derivatives. The first one is the study of the cytotoxicity of a κ^4 quinoline derivative (**94**) and the second one is an extensive bio-inorganic study of two κ^4 bis-TS copper(II) complexes derived from 2,3-butanedione (**92** and **93**). This second project was published in *Metallomics* in 2016 with the title: "Autophagy and apoptosis: studies on the effects of bis-TS copper(II) complexes on p53 and p53-null tumour cell lines".

7.4.1 8-hydroxyquinoline-2-carboxaldehydethiosemicarbazone

This project completed our screening of the anti-cancer properties of TSs with different denticity and their metal complexes. We chose to functionalise with thiosemicarbazide the 8-hydroxyquinoline-2-carboxaldehyde (**94**) which has one more coordinative position than the previously described quinoline-2-carboxaldehyde (**88**). This ligand is able to bind metal ions through an S,N-coordination of the thiosemicarbazone plus the nitrogen of the quinoline and the oxygen of the phenolic group in position 8 of the quinolinic ring (*Figure 54,* synthesis and characterisation in the *Anticancer agents: experimental* section).

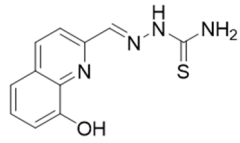

94

Figure 54

Some data about the cytotoxicity power of this molecule and its copper(II) were already available[129]. In the paper both ligand and complex were tested on SK-N-DZ, a cell line derived from human cisplatin-resistant neuroblastoma. Unlike us, they performed the MTT test using a 12 h cell treatment. The result was a strong anti-proliferative activity and marked cytopathological effects of the copper complex. They made also a cell-cycle analysis finding an accumulation of cells in the S and G2/M phases, and a

reduction of cell population in the G0/G1 phase which indicated inhibition of DNA synthesis. The copper complex was also able to induce apoptosis and necrosis and to dramatically increase the p53 expression which was a confirm of the damages of the cell DNA cycle.

We analysed the effects on HeLa cells and we confirmed the same trend observed for SK-N-DZ (*Table 25*): the ligand alone (**94**) was not effective whereas the copper complex (**97**) resulted to be a good inhibitor. Once again, these results confirm the key role of the metal for the anticancer activity.

	IC_{50} (μM) free ligand (94)			**IC_{50} (μM) Cu(II) complexes (97)**	
	SK-N-DZ NB 12h [129]	**HeLa 24h**		**SK-N-DZ NB 12h [129]**	**HeLa 24h**
94	>100	>100	**97**	0.64±0.03	2.14±0.20

*Table 25: IC_{50} values of **94** and **97** on SK-N-DZ NB and HeLa cells.*

7.4.2 2,3-butanedione-bis-thiosemicarbazones

In this section is reported the study of the anticancer properties of two bis-TSs and their copper(II) complexes (*Figure 55*). These molecules are two derivatives of 2,3-butanedione condensed respectively with 4,4-dimetyl-3-thiosemicarbazide (**92**) and 2-methylthiosemicarbazide (**93**). The products are symmetric κ^4 ligands with similar structure but different properties. The 2,3-butanedione-4,4-dimetyl-3-TS (**92**) is a S,N,N,S-ligand in which the two thiosemicarbazone moieties are arranged to effectively chelate a single metal ion thanks to the deprotonation of the two iminic nitrogen atoms. This molecule had been already studied as a chelating ligand for ^{64}Cu, a radioactive isotope of copper applied in radiochemical imaging[130], but we found no data about its cytotoxicity. We decided to study the anticancer activity of this molecule and to better understand its action we compared it with the 2,3-butanedione-bis-2-methyl-TS (**93**).

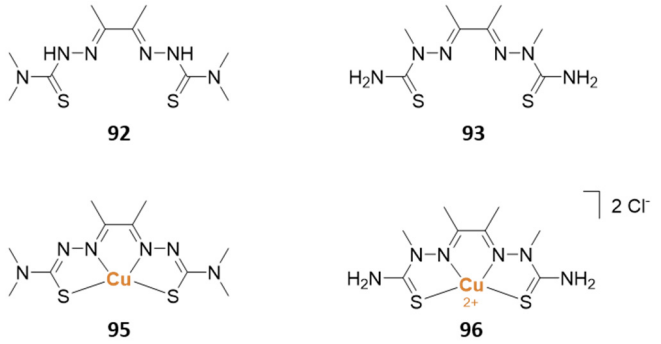

Figure 55: Bis-TSs and their corresponding copper(II) complexes.

The two molecules have a very similar chemical structure, but the 2-methyl derivative (**93**) cannot be deprotonated because of the N^2 methylation and consequently the complex it forms with copper(II) is bicationic (**96**). The biological effects due to these differences are very interesting to investigate especially because, up to now, there are only few examples in literature of cationic copper complexes studied for anticancer purposes and no one them is a bis-TS. We have focused our attention on the application of our compounds as drugs for treatment of solid and hypoxic tumours, which are extremely aggressive and there are still no effective drugs for their treatment. These pathologies are very aggressive because they can develop rapidly and in low oxygen concentration. Since the tissues of these tumours do not need oxygen to grow, they are poorly vascularised and this hinders the delivery of the majority of drugs. To test if our compounds were good candidates, we carried out a series of experiments designed to compare the effects on cell lines cultured both in normal and hypoxic environment. For this purpose, we used the A549, which are cells from adenocarcinoma that can growth both in normoxia and hypoxia. In addition, we used the U937, leukemic cells which do not express the p53 protein. The study of U937 has an added value because the comparison between data from p53 and p53-null cell lines (such as A549) can give a lot of interesting information. The p53 is a protein that is called the "the guardian of the genome" because of its ability to control and prevent genome mutations, phenomena which are at the basis of cancer development. It activates several mechanisms in humans, like the expression of DNA repair proteins, the suspension of cell growth at the G1/S checkpoint to give to the repair proteins the proper time to carry out their function, and eventually, when the damage is too severe,

it triggers the process of apoptosis to kill the defective cell[131]. In addition, it seems that p53 can also activate autophagy, namely a mechanism that induces the self-degradation and recycling of cell components. This mechanism is usually activated to preserve cell from death in high stress situations, but recent studies have shown that autophagy can also induce cell death in damaged cell[132]. The ability to stimulate cell death using biological pathways alternative to apoptosis is interesting because they could be a solution to many kinds of drug resistance phenomena. In *Table 26* are reported the IC_{50} values obtained from the screening on U937 and A549 cells (*see Biological test protocols* for experimental details).

		IC_{50} (μM) 24h free ligand			**IC_{50} (μM) 24h Cu(II) complexes**	
		U937	**A549**		**U937**	**A549**
2,3-butanedione-bis-4,4-dimetyl-TS	**92**	21.10±2.99	>100	**95**	2.53±0.81	7.52±2.13
2,3-butanedione-bis-2-metyl-TS	**93**	>100	>100	**96**	8.90±1.22	9.58±0.64

Table 26: IC_{50} values of bis-TSs and their Cu(II) complexes on U937 and A549 cells.

The two thiosemicarbazones resulted inactive, except for the 4,4-dimethyl derivative (**92**) which showed a moderate activity against U937 cells (IC_{50} 21.10 μM). By contrast, all the copper(II) complexes **95** and **96** showed much better results, with all the IC_{50} lower than 10 μM. Focusing on the 2-methyl derivatives **93** and **96**, the presence of metal raised the cytotoxic power of at least one order of magnitude. The general trend suggested also that the U937 cells are more sensitive than the A549, indicating once again the higher resistance of solid tumours.

Effects of hypoxia on cytotoxicity in A549 cells

As mentioned before, the A549 cells can grow also in oxygen deficiency (hypoxia), and therefore we studied the consequences of low oxygen levels on the biological effect of our derivatives. The IC_{50} values of the complexes determined under hypoxia were about 2.5-fold higher as compared to those obtained under normoxia (*Table 27*). This highlighted the fact that cells in hypoxia are less susceptible to cytotoxic effects of our compounds.

		IC_{50} (μM) A549 24h, free ligand			**IC_{50} (μM) A549 24h, Cu(II) complexes**	
		normoxia	**hypoxia**		**normoxia**	**hypoxia**
2,3-butanedione-bis-4,4-dimetyl-TS	**92**	>100	>100	**95**	7.52±2.13	14.09±3.29
2,3-butanedione-bis-2-metyl-TS	**93**	>100	>100	**96**	9.58±0.64	23.09±1.54

Table 27: IC_{50} values of bis-TSs and their Cu(II) complexes on A549 cells cultured in normoxia and hypoxia.

Thanks to these interesting preliminary results, we decided to study in detail the effects of our compounds. We arranged a series of experiment to explore their action in cells to formulate a possible description of their mechanism of action. All the experimental details and protocols used are described in the *Biological test protocols*.

Description of the different effects observed on U937 and A549

The cell cycle analysis was performed using the flow cytometer which allows to evaluate the cell phase distribution of a sample of cells by determining their nuclear DNA content. The analysis showed significant alterations of the cell cycle induced by the copper complexes in both A549 and U937 cultures (*Figure 56*). However, the two cultures had different responses.

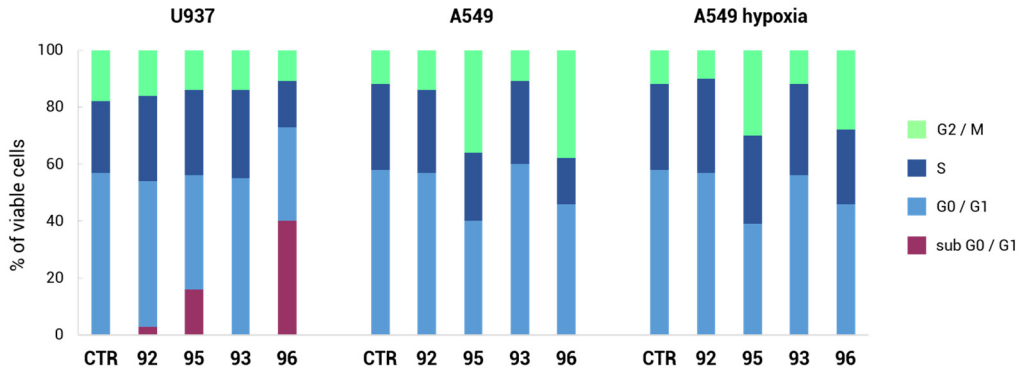

Figure 56: Cell cycle analysis of bis-TSs and their Cu(II) complexes in U937 and A549 (cultured normoxia and hypoxia).

In U937 every step of the cycle was affected suggesting an apoptotic process as indicated by the presence of cells in the sub G0/G1 phase in **92**, **95** and **96**. However, in A549 there is a significant accumulation in the G2/M phase but not in sub G0/G1, which indicates a different mode of action of our derivatives in this cell line. The hypoxia did not induce modification in the A549 cell cycle if compared with the same treatment performed in normoxia (*Figure 56*) suggesting that the oxygen deficiency did not modify the mode of action of out derivatives.

Side scatter analysis

Since the cell cycle analysis on A549 cells indicated the presence of an apoptotic event, we analysed if the treatment had induced changes in the internal cell granularity, a parameter that is related with changes in the morphology of cells and which can be measured through a Side Scatter analysis. A549 cultures treated with copper complexes showed a significant increase of the side scatter (SSC), which was not detected in U937 (*Figure 57*). This evidenced changes in the A549 internal structure and this is frequently related to autophagy.

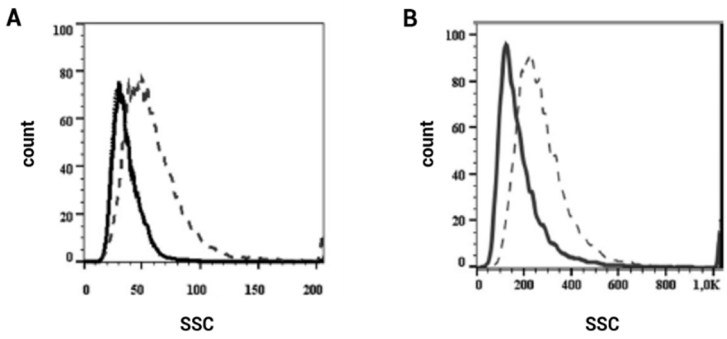

*Figure 57: Flow-cytometry analysis of side scatter (SSC) in A549 cells for compounds **95** (A) and **96** (B). Control: continuous lines. Cells exposed to IC_{50} conc. for 24 hours: dashed lines.*

These observations brought us to conclude that our copper complexes act through different cytotoxic mechanisms in the two cell cultures: apoptosis in U937 and autophagy in A549.

Caspase levels and flow cytometry

Two very useful methods to confirm our hypothesis were the test of the caspase levels and the flow cytometry analysis. Caspases are a class of enzymes involved in the apoptosis and, when their level grows, it means that an apoptotic process is occurring[133]. The caspase levels in U937 cultures treated with the two copper complexes were significantly higher than the control, this confirmed the ability of our compounds to induce apoptosis in the leukemic U937 cells (*Figure 58*).

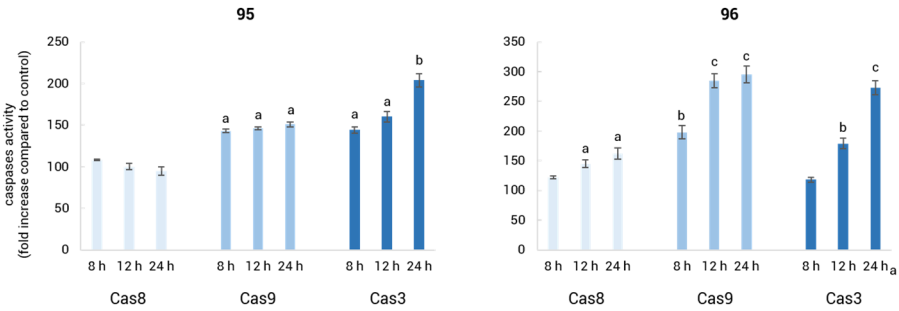

*Figure 58: Caspase levels (Cas8, Cas9 and Cas3) in U937 cultures treated with bis-TSs Cu(II) complexes **95** and **96**. Values expressed as percentage vs. control. Significant differences from the untreated control indicated as: **a** $p < 0.05$; **b** $p < 0.01$, **c** $p < 0.001$.*

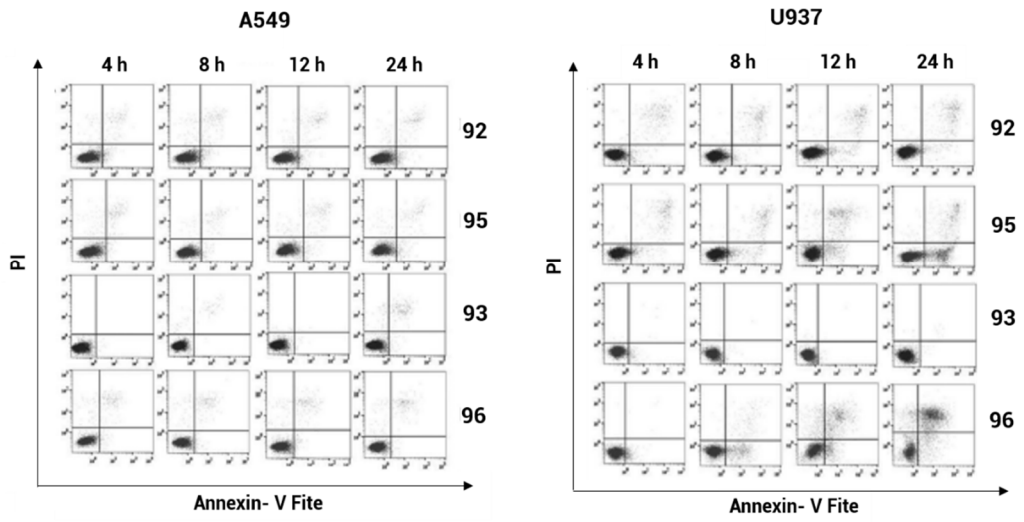

Figure 59: Flow cytometry analysis of apoptosis after cell staining with annexin V–FITC/PI. Annexin V–FITC(+)/PI(-) = early apoptotic cells and annexin V–FITC(+)/PI(+) = advanced apoptotic or necrotic cells.

Also the flow cytometry analysis confirmed the apoptosis in U937. In fact, the treatment with IC_{50} concentrations of **92** and of **95** resulted in a significant increase, compared to the controls, in the number of apoptotic U937 cells, while in the A549 cells no differences were observed (*Figure 59*).

Autophagy analysis in A549 cells

To study the behaviour of A549 cells, we performed an autophagy analysis using flow cytometry (FL-1 detector) and we identified an increase of FL-1 signal related to the presence of autophagosomes (the morphological characteristics of autophagy) (*Figure 60*). The autophagosomes in A549 cells were also clearly observed by microscopy (*Figure 61*). These evidences confirmed that the A549 cells, treated with copper complexes, are subjected to autophagy which induces cell death.

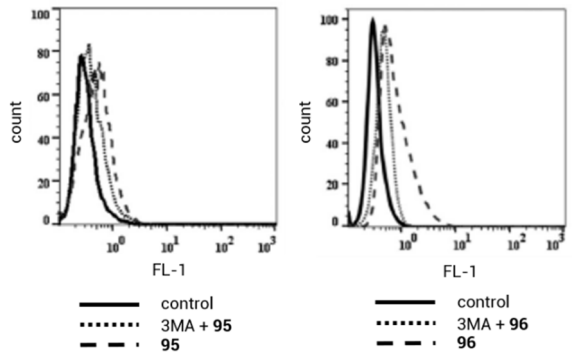

*Figure 60: Flow cytometry signal profiles on FL-1 detector of A549 cells treated with **95** and **96**.*

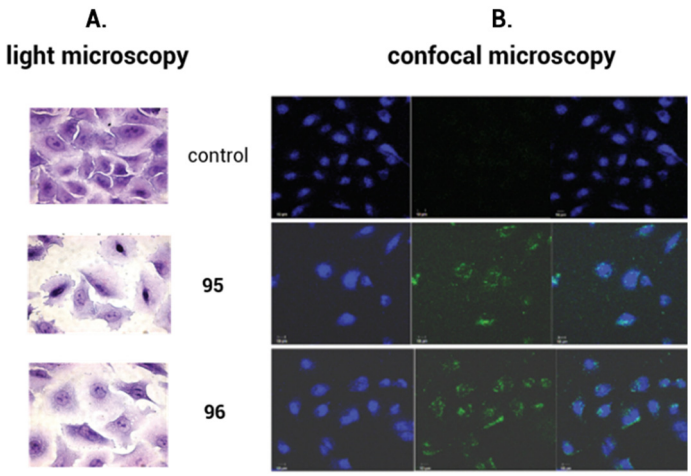

Figure 61: Morphological phenomena of autophagy in complex-treated lung cancer cells (5 mM for 24 h). (A) Direct observation under a light microscope (B) Samples stained with an autophagy probe were examined under a confocal microscope.

Interpretation of the two mechanisms of action: the role of p53

We finally focused our attention to the identification of the reasons why the two cell lines had such a different response. A good point to start with was the analysis of the p53 levels along the time course of treatment (24 h) (*Figure 62*).

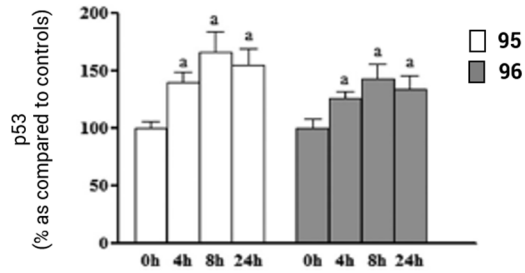

*Figure 62: p53 levels in A549 cells measured at different treatment periods with **95** and **96** (0, 4, 8 and 24 hours).*

This test was performed only on the A549 cells, because the U937 are p53 null cells for the lack of the corresponding gene[134]. The p53 expression increased in the presence of the copper derivatives with a maximum between 4–8 hours followed by a decline after 24 hours. It indicated a strong response of cells towards the treatment with metal complexes **95** and **96** and the p53 role in the initiation of the autophagic process as an alternative to the apoptosis.

ROS generation

The study continued by measuring the ROS levels in cells. High levels of oxidative stress were detected in both cell cultures treated with the two copper(II) complexes **95** and **96** and with **92**. The ROS generation induced by **95** was associated with lipid peroxidation (high TBARS levels) in both cell lines, while **96** enhanced TBARS levels only in U937 cells. The hypoxia in A549 cells induced a significant reduction of ROS levels for **92** and **95**. Since oxidative stress can induce cell death, the data matched with the IC_{50} values, but they did not help us to discriminate the autophagic and apoptotic behaviours (*Figure 63*).

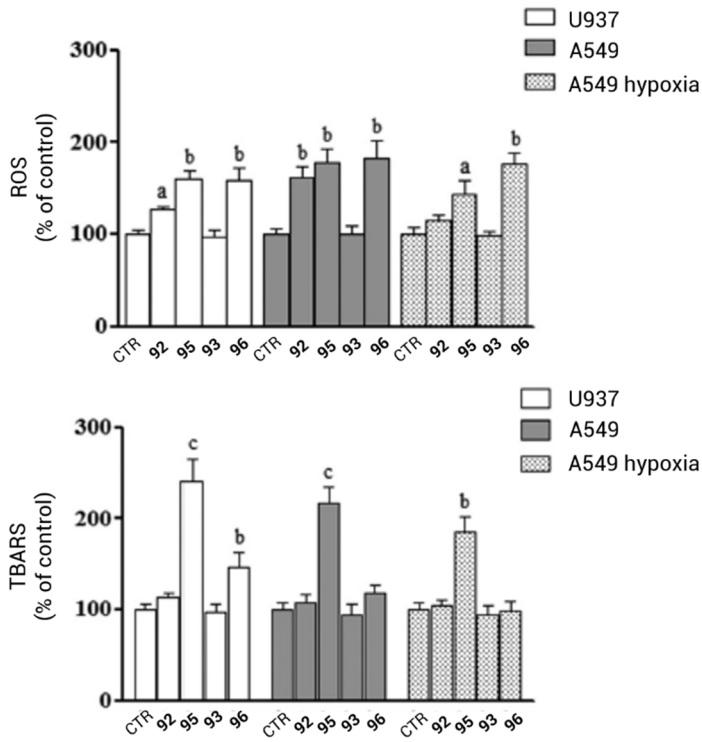

*Figure 63: ROS production (above) and lipid peroxidation levels (below) in cells treated with IC_{50} concentrations of **92**, **93**, **95** and **96**. Values expressed as a percentage of the control. Significant differences from the control: **a** $p < 0.05$; **b** $p < 0.01$; **c** $p < 0.001$.*

Metal uptake

Finally, we evaluated the metal content inside cells after their exposure to metal complexes in concentrations 1 μM (to avoid cellular damages). *Figure 64* shows the intracellular concentration of copper in U937 and A549 after 24 hours exposure. It seems that the complexes **95** and **96** easily entered in both cell lines and that the copper uptake increased during 24 hours with similar rates. The difference we noticed was that **96** was absorbed 4 times more than **95** by cell line U937 and 5 times more by cell line A549. In addition, the uptake was larger in the solid tumour than in the leukemic one.

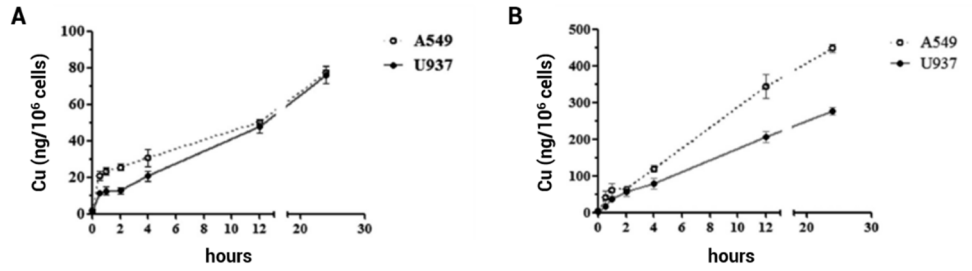

*Figure 64: Evaluation of Cu uptake in A549 and U937 cells treated with **95** and **96**. Intracellular metal was measured over a 24-hour period.*

This study is an example of how the autophagy can be a two-faced mechanism. It usually preserves cell life during stress situations or shortage of nutrients but, as in this case, it can also act as a mechanism to induce cell death. As a general trend, we noticed that the two metal complexes **95** and **96**, even though at different levels, induce ROS but, while in U937 the response is directly apoptotic, in cell line A549 autophagy prevails. We interpreted this phenomenon hypothesising that the reason of these differences comes from the differences between the two cells lines we used: the presence of p53 in A549 cells and its absence in U937. As stated above, protein p53 is responsible for the control of the genome and it is activated as a response to high level of stress to preserve the cell or to induce cell death when the damage is too extensive. Our copper(II) complexes induced in the short period a strong up-regulation of p53, indicating that the cells initially activated p53 to start the autophagic response as a mechanism of defence alternative to direct apoptosis. Subsequently, due to the strong cytotoxic effect of our compounds, autophagy becomes the mechanism which induces cell death. The p53-induced autophagy explains the higher resistance of A549 cells, because they can initially preserve themselves activating autophagy instead of apoptosis. This behaviour is confirmed by the higher IC_{50} values determined in A549 compared with those of U937 cells. This high resistance was highlighted by the fact that even though the A549 cells absorb much larger amounts of copper(II) than p53-null cell line U937, they do not undergo apoptosis. The same effect was even more evident in hypoxia, where the p53-induced autophagic response resulted higher than in normoxia and this led to higher IC_{50} values.

8 Thiocarbohyadrazones

Thiocarbohydrazones (TC) are a class of molecules that have two hydrazone fragments linked to a thiocarbonyl group (*Figure 65*). TCs are obtained, like TSs, from the condensation of one or both hydrazine groups of the thiocarbohydrazide with carbonyl compounds.

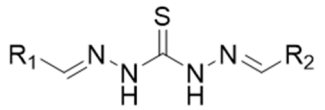

R_n = alkyl, aryl

Figure 65

TCs can be classified as symmetric if the thiocarbohydrazide is condensed on both hydrazine ends with the identical aldehyde or ketone ($R_1 = R_2$) or asymmetric if the two are different ($R_1 \neq R_2$). We decided to focus our attention on the use of the asymmetric functionalisation so as to create mono-TCs analogues of our TSs and then to explore the possibility to use the free hydrazine group as a linker to bind our TS to other systems of interest, such as drug delivery agents and so on. The ability to bind metal ions is, in principle, not affected by passing from a TS to a TC, thus this method can be used also for the functionalisation of the TS metal complexes. We decided to synthesise the mono-TC analogues of five of our TSs, choosing candidates with different denticity, namely the TS of cinnamaldehyde (**7**) and citronellal (**65**) (κ^2), TS of quinoline-2-carboxaldehyde (**88**) and 5-fluoroisatin (**89**) (κ^3) and TS of 8-hydroxiquinoline-2-carboxaldehyde (**94**) (κ^4). They were selected because of the good IC_{50} values previously obtained for the corresponding copper(II) complexes. A crucial step was to control if the presence of the free hydrazine group in the mono-TC would have affected significantly the biological properties of the parental compound. So, after the design of our candidates, we compared them with their analogue TS using as theoretical parameters those used in Lipinski's rules.

Lipinski's rules (also called the *Rule of Five* (RO5)) are general and empirical criteria which describe the guide lines to keep in mind in the design of a drug. They were

originally defined for drugs with oral administration and the limits they impose have been set analysing the correspondence between values of a collection of commercialised drugs. According to Lipinski, the crucial parameters that a potential drug should own are[135]:

- No more than 5 hydrogen bond donors (nitrogen or oxygen atoms with one or more hydrogen atoms)
- No more than 10 hydrogen bond acceptors (nitrogen or oxygen atoms)
- A molecular mass less than 500 Daltons
- An octanol-water partition coefficient LogP not greater than 5
- A Polar Surface Area (PSA) lower than 140 $Å^2$

The table containing the calculated parameters of each mono-TCs compared with the corresponding TSs is reported below (*Table 28*).

		H-bond donors	**H-bond accept.**	**MM (μ)**	**LogP**	**PSA ($Å^2$)**
Lipinski's recommended values		≤ 5	≤ 10	≤ 500	≤ 5	≤ 140
cinnamaldehyde	TS (**7**)	2	2	205.28	2.16	82.50
	TC (**98**)	3	3	220.29	1.82	94.53
citronellal	TS (**65**)	2	2	213.34	2.77	82.50
	TC (**99**)	3	3	228.36	2.44	94.53
quinoline-2-carboxaldehyde	TS (**88**)	2	3	230.29	2.41	95.39
	TC (**100**)	3	4	245.30	2.08	107.42
5-fluoroisatine	TS (**89**)	3	3	238.24	1.09	111.3
	TC (**101**)	3	4	245.30	2.08	107.42
8-hydroxiquinoline-2-carboxaldehyde	TS (**94**)	3	4	246.29	2.17	115.62
	TC (**102**)	4	5	261.30	1.84	127.65

Table 28: Lipinski's parameters of TSs and their corresponding TCs.

Looking at the values in the table, every TC maintained almost the same value of its parental TS and each molecule have Lipinski's parameters within the recommended levels. This was a good starting point to expect that the new molecule designed could be good potential anticancer agents like their analogues.

All the five compounds designed and their copper(II) complexes were synthesised and characterised following the procedures reported in the *Anticancer agents: experimental* section.

Subsequently, we submitted every mono-TC and copper(II) complexes to the IC_{50} determination on HeLa cell lines. The results are showed in the *Table 29* and compared with those obtained from the corresponding thiosemicarbazones.

	free ligands	**IC_{50} (μM) HeLa 24h**	**Copper(II) complexes**	**IC_{50} (μM) HeLa 24h**
cinnamaldehyde	TS (**7**)	>100	TS (**12**)	7.85±0.27
	TC (**98**)	>100	TC (**103**)	>100
citronellal	TS (**65**)	46.02±6.21	TS (**66**)	5.16±0.26
	TC (**99**)	>100	TC (**104**)	55.57±2.27
quinoline-2-carboxaldehyde	TS (**88**)	67.98±10.57	TS (**90**)	8.76±0.82
	TC (**100**)	>100	TC (**105**)	12.39±0.81
5-fluoroisatin	TS (**89**)	>100	TS (**91**)	11.38±2.07
	TC (**101**)	>100	TC (**106**)	7.60±1.95
8-hydroxiquinoline-2-carboxaldehyde	TS (**94**)	>100	TS (**97**)	2.14±0.20
	TC (**102**)	insoluble	TC (**107**)	34.70±3.83

Table 29: IC_{50} values of TSs, TCs and their copper(II) complexes on HeLa cells.

The biological results showed clearly that the presence of the copper complex is crucial to obtain a cytotoxic effect in both thiosemicarbazones and mono-TCs. In fact, the column which contains IC_{50} values of free ligands resulted almost completely red, indicating that no molecules had relevant effect on the cell proliferation. On the

contrary, the column of copper(II) derivatives was found to be almost completely green with the majority of the IC_{50} values lower than 15 μM.
The comparison between TSs and mono-TCs showed that the addition of a terminal NH_2 left almost unchanged the IC_{50} values of the TCs derived from the κ^3 TSs both in free ligands and Cu(II) complexes, whereas it modified the cytotoxicity of the κ^2 and κ^4 TS derivatives. The most evident difference between TSs and TCs was the series of the cinnamaldehyde derivatives, in which the TC metal complex (**103**) resulted not active whereas the TS (**12**) had an IC_{50} of 7.85 μM. The same negative effect was also recorded (even if with lower effects) for citronellal-mono-TC (**99** and **104**) and 8-hydroxiquinoline-2-carboxaldehyde (**102** and **107**) derivatives.

In the light of these results, the mono-TCs of quinoline-2-carboxaldehyde (**100**) and 5-fluorisatin (**101**) resulted to be the most promising complexes and we tested their cytotoxicity also on the A549 cell line. A549 is a cell line of adenocarcinomic human alveolar epithelial cells widely studied in medicinal chemistry as a target for the development of new drugs to overcome cis-platin resistance. We tested the two tridentate complexes **105** and **106** and we added to the screening also **107** because, even if it is less effective, it showed a non-negligible IC_{50} on HeLa (34.70 μM). The results of the screening on A549 cells are reported in *Table 30*.

Copper(II) complexes of	**IC_{50} (μM) A549 24h**
quinoline-2-carboxaldehyde-mono-TC (**105**)	42,73±5,66
5-fluoroisatin-mono-TC (**106**)	21,41±2,54
8-hydroxiquinoline-2-carboxaldehyde-mono-TC (**107**)	39,13±4,36

*Table 30: IC_{50} values of TC Cu(II) complexes **105**, **106** and **107** on A549 cells.*

The IC_{50} values for the **105** and the **106** are higher than the corresponding values previously obtained on HeLa. This result was probably due to the higher resistance of A549 cells compared with HeLa. Surprisingly, **107** gave on A549 an IC_{50} similar to those obtained on HeLa, suggesting a non-selective mode of action. To study in more detail

the effects of the active copper(II) complexes we performed a cell cycle analysis on both A549 and HeLa cells (*Figure 66*). The cell cycle of both the cell lines treated with complexes resulted significantly altered compared with the control. However, the compounds showed different effects depending on the cell line. In A549 the effect was a reduction of the cells in G0/G1 associated with cell accumulation in G2/M phase, whereas in HeLa we recorded the appearance of a significant number of cells in the sub G0/G1 phase and a decrease of cells in the S-phase. In A549 the accumulation in G2/M phase suggests a block in the G2/M transition, which is usually associated with DNA damage. In HeLa the presence of cells in sub G0/G1 phase suggests that the three complexes induce apoptosis. In addition, the decrease in cell number in the S-phase means that cells have problems in synthesising DNA and remain in the other phases highlighting strong replicative stress.

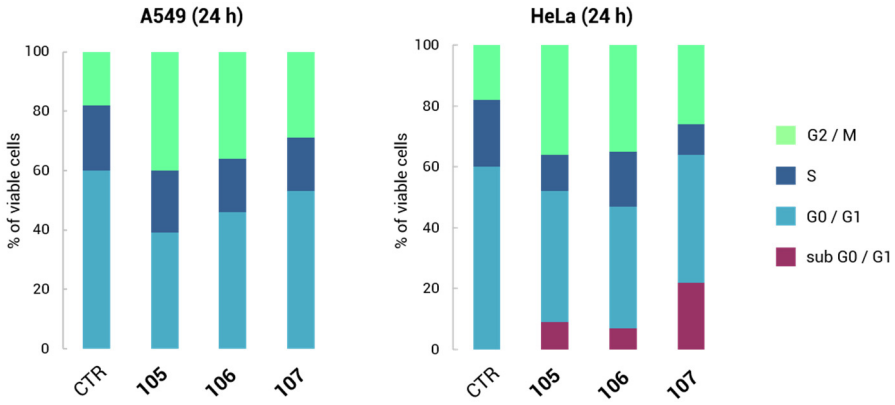

Figure 66: Cell cycle analysis of TC Cu(II) ***105****,* ***106*** *and* ***107*** *in HeLa and A549 cells.*

To confirm the occurrence of apoptosis in HeLa cells, we analysed the caspase 3 (Cas3) activity (*Figure 67*). This protein is activated in the execution-phase of cell apoptosis, then its up-regulation is an unequivocal signal of an apoptotic event. All the three complexes tested showed Cas3 levels higher than the control justifying the presence of the sub G0 / G1 phase in the cell cycle.

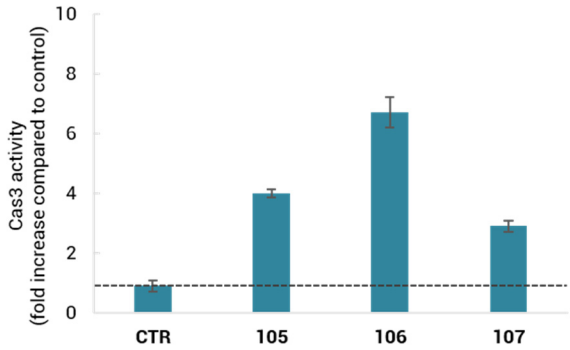

*Figure 67: Caspase3 (Cas3) levels in HeLa cultures treated with **105**, **106** and **107**. Values expressed as fold increase compared with the control.*

8.1.1 Topoisomerase IIA

As already reported in the introduction, topoisomerase A is considered one of the possible targets on which is based the TS activity. Therefore, we decided to test the ability of our derivatives (both TSs and TCs) to inhibit this enzyme. Topoisomerases are a large group of proteins, but for our purposes the most interesting one is that of the human topoisomerases IIα. The inhibition of these proteins has been proven to stop major cellular functions such as DNA replication, transcription, mitosis and, recombination[136].

From the structural point of view, topoisomerases IIα are dimeric proteins in which every monomer is subdivided in 3 domains. The N-terminal domain (the first 670 amino-acids) is that responsible for the ATP binding and hydrolysis. The central domain (from 671 to 1,200 amino-acids) contains the binding pocket necessary for the cut of a DNA strand. The C-terminal domain (from 1,201 to 1,521 amino-acids) is more variable and its actual role is still debated. It usually contains specific sequences which are considered essential for DNA recognition. Due to this high variability, there are still no X-ray structures of the C-terminal domain, whereas the Protein Data Bank (PDB) contains many structures of the other two domains, mostly resolved from proteins derived from yeast. Since our most promising copper complexes quinoline-mono-TC (**105**) and 5-fluoroisatin-mono-TC (**106**) showed high cytotoxicity and ability to induce apoptosis in HeLa cells, we decided to study their mechanism of action by testing their

inhibition power towards topoisomerase IIα. The *in vitro* evaluation of the enzyme inhibition was performed using a TopoGen kit containing the enzyme, a DNA segment and a DNA marker to show the effect of the tested compound. The DNA contained in the kit was a pHOT1, a circular double strand plasmid DNA that contains a single and specific binding site for topoisomerase IIα (see the *Biological test protocols* section).
We tested the inhibition power the cytotoxic copper(II) complexes containing TSs and TCs, namely **90**, **91**, **105** and **106**. All the candidates were tested using a 50 μM concentration and every compound resulted an inhibitor of the topoisomerase IIα (*Figure 68*). In fact, spots of supercoiled DNA and linear DNA were detected in every lane. In addition, evidences of DNA cleavage were found in every treated sample.

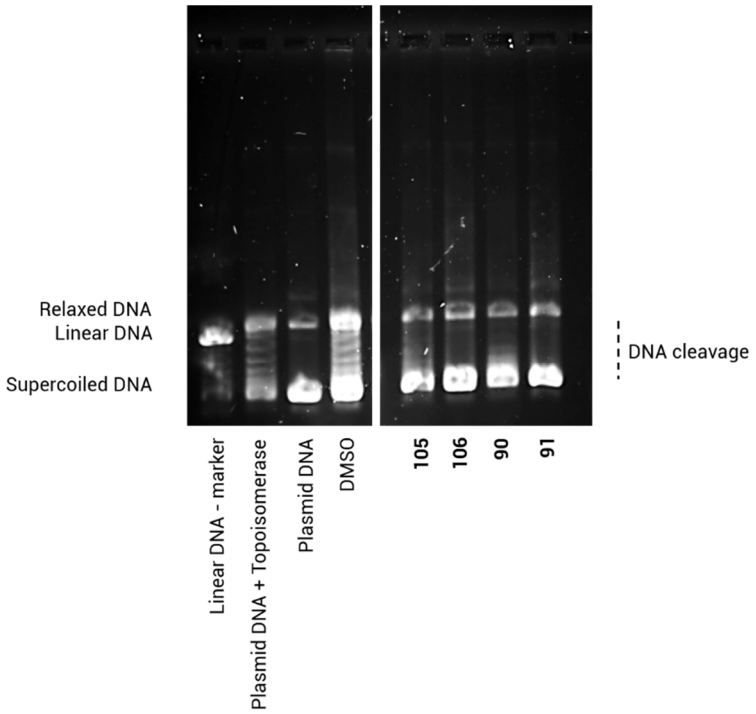

Figure 68: Gel of the topoisomerase II inhibition test. The first 4 lanes are references. Lanes 5-8 shows the reaction of Topo-II with supercoiled DNA in the presence of TSs and TCs tested at 50 μM.

8.1.2 Molecular docking studies on Topoisomerase IIα

To better understand the possible interactions of our inhibitors with topoisomerase Iiα, we used a structure-based docking approach. We based the study on a previous publication from our research group[21] in which the quinoline-2-carboxaldehyde copper(II) complex (**90**) was docked both in the ATP domain and in the DNA-cleavage domain of the topoisomerase IIα showing that the ATP binding pocket was the most reliable interaction site.

In that work, the calculations were performed using *AutoDock4*, a docking software which did not contain the parameters to handle copper ions and it was necessary to replace it with iron to perform the calculations. We decided to keep these values as reference, but to re-calculate the binding energies of the quinoline derivative using *Gold 5.5* and to extend this method to the other compounds. *Gold* is an innovative docking software specialised in the study of metal containing compounds, it uses a series of scoring functions which include in their algorithm specific parameters for every metal to quantify their contribute to the protein-substrate interaction.

The protein structure we used for the study was the X-ray solved structure of human topoisomerase IIα (1ZXM in the PDB database). In this structure, the ATP binding site is well-defined and contains the inhibitor ANP co-crystallized (called also AMP-PNP, an analogue of ATP with a nitrogen atom instead of the oxygen in the terminal phosphate group). The self-docking approach was applied for the validation of the docking method using the ANP crystallographic coordinates as a reference for the comparison with the ANP coordinates calculated from the docking run. A docking method, to be validated, needs a root-mean-square deviation of atomic positions (RMSD) lower than 2 Å between the crystallographic and the data calculated (excluding hydrogen atoms). The reliability of our method was confirmed from a RMDS of 0.898 Å[74,75].

The next step was the creation of the input file of our molecules. We created the 3D-input files of each ligand and complex using *ChemDraw v 15.0.* All the molecular geometries were optimised using the *Chimera v. 13.1* force field tool and, in the complexes, we eliminated the chlorine to obtain a +1 charge. Once every input file was optimised, we started with their virtual screening in *Gold* through the *Hermes* visual

interface. We fixed the docking cavity at 6 Å of radius around the ANP native binding site in the ATP pocket. Then, we set 100 runs of docking for each compound. Every docked position was scored using the *ChemScore* function, which allowed also to estimate a binding energy between every docked pose and the protein (for the detailed description of the docking method and set up see the *Molecular docking* section). The *Table 31* collects all the free energies of binding obtained from the docking study.

	Cu(II) complexes	**ΔG binding (kcal/mol) *Gold***	**ΔG binding (kcal/mol) *AutoDock****
ANP		-12.16	-13.8
Quinoline-2-carboxaldehyde	TS (**90**)	-6.60	-6.6
	TC (**105**)	-11.98	-
5-fluoroisatin	TS (**91**)	-9.13	-
	TC (**106**)	-11.24	-

*Table 31: Free energies of binding of TS and TC copper complexes calculated with Gold. The table contains also the reference values of **88** and ANP calculated with AutoDock.*

The results obtained with *Gold* are perfectly in line with those previously obtained with *AutoDock*, indicating a binding affinity of 6.60 kcal/mol for the copper complex **90**. The docking extended to all the derivatives showed that every compound can interact effectively with the ATP binding site of the topoisomerase IIα confirming the results from the *in vitro* inhibition test. Every derivative showed a binding energy lower than the reference ligand ANP. Another interesting result was the higher binding energy of TC complexes compared with TS complexes. This difference could be explained, in terms of calculation, considering that the TCs had the terminal hydrazine groups which contributes to an increase of the value of the term associated with hydrogen bonds in the *ChemScore* free energy equation (see *Molecular docking* section). This trend was confirmed by cytotoxicity results only for **106** but not for **105**.

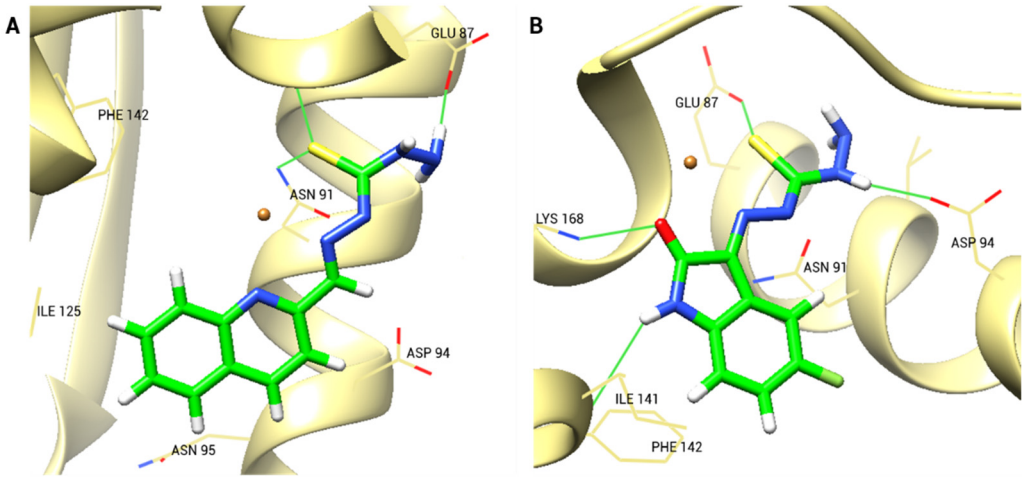

*Figure 69: Best-scored docking positions obtained for **105** (A) and **106** (B).*

In *Figure 69* are reported the best poses of **105** and **106** in the ATP binding site of the enzyme obtained from the docking simulation. The two complexes had similar poses in which the thiocarbohydrazide moiety pointed towards the hydrophilic space of the binding site created by Asn91, Glu87, Asp94 and Lys168. In this area were located most of the hydrogen bonds which involved the nitrogen atoms of the terminal free hydrazine and the sulphur of the TC. The lipophilic part of the TCs are stabilised by lipophilic interactions with amino acids like Ile125, Phe142 and Ile141 located at no more than 6 Å far from the aromatic rings of our two substrates.

How could these poses be responsible for the topoisomerase inhibition? The answer could be found analysing the ATP mechanism of action in this binding site. The hydrolysis of an ATP molecule is necessary for the DNA cleavage and this reaction is helped by the presence of a magnesium cation in the binding site which assists the cleavage of the bond between the α- and β-phosphates by its electron-withdrawing effect. The complex formed by ATP and Mg(II) in the binding site is also crucial both to neutralise the charges of the ATP phosphates and to provide additional points of interaction between the ATP and the enzyme, increasing the binding affinity and thus the efficiency of the entire process. Our complexes were positioned exactly in the place usually occupied by the Mg(II)-phosphates complex and the hydrazine of the TCs interacts with the amino acids responsible for the stabilisation of the magnesium. In

particular, the sulphur of the **105** complex forms a hydrogen bond with the residue Asn91 which is normally involved directly in the Mg(II) binding. In addition, the binding energies calculated for the complexes confirmed the strong binding affinity with the enzyme analogous with that obtained for the native ligand ANP. All these observations induced us to believe that our complexes possess the characteristics to be topoisomerase IIα inhibitors because they can interfere with the formation of the ATP-Mg(II) adduct preventing the correct energy supply necessary for the DNA cleavage.

9 Ruthenium(II) half-sandwiches as carriers for active molecules

9.1 New approaches to improve drug efficiency

Drug delivery

The number of potential effective drugs is very large, but most of them do not have the chemical and physical properties to ensure an actual use.
An approach to overcome these issues is the so-called "drug delivery", which consists in the development of methods of administration of pharmaceutical compounds aimed at optimising their absorption and therefore their selectivity. This approach is based on the use of a carrier which can transport effectively the drug improving its uptake. The most common carriers are bio or bio-mimetic molecules which are usually renewable, nontoxic, biocompatible, biodegradable and able to be recognised by specific receptors and transport mechanisms to cross barriers and reach the target tissue[137]. Nanoparticles are nowadays another very attractive kind of carriers for drug delivery. In the literature there are many examples of nanoparticles functionalised on the surface able to rise significantly the drug uptake[138]. Whichever method is adopted, the objective is a strict control over the drug delivery through the pharmacokinetics and pharmacodynamic optimisation to improve both therapeutic efficacy and safety.

The photodynamic therapy

The PhotoDynamic Therapy (PDT) refers to a particular kind of medical treatment in which the drug needs a light irradiation to be activated. These drugs, called photosensitizing agents or photosensitizers, are usually designed to have no biological activity before the irradiation, so they can diffuse into the body without side effects and reach the target tissue where they will be finally activated by light. These characteristics ensured several advantages:

- The PDT avoids systemic treatments because of its selectivity
- The reactive species are accumulated only in cancer cells (lower side-effects)
- The PDT is often applicable when surgery is not possible
- The PDT is repeatable even in the short time, unlike radiation and chemo-therapy which usually needs days of rest between treatments because of their strong side effects

The most common photosensitizers are effective anticancer agents because they produce reactive oxygen species (ROS) in the tissues in which they are localised after the irradiation. Nowadays, different cell death pathways induced by the PDT-ROS production have been reported[139]. In both cases, the theoretical basis of ROS production induced after light irradiation can be explained analysing the well-known Jablonski diagram (*Figure 70*).

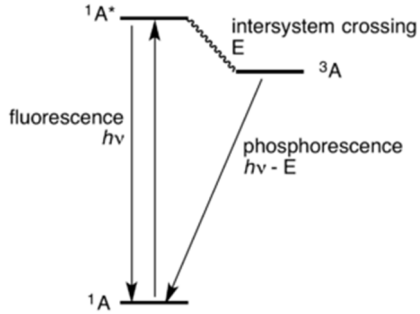

Figure 70: Jablonski diagram.

The energy level ^1A corresponds to the photosesitizer at the gound state (not irradiated). Once it is irradiated, the energy of the light is transferred to the photosensitizer that changes its electronic state into $^1A*$, the excited state. However, $^1A*$ is an unstable state for the photosensitizer that spontaneously decays to ^1A.
There are three mechanisms with which this decay can occur. The first two mechanisms are direct decays to ^1A. One is the fluorescence emission (radiative mechanism) and the second is the release of the energy of the exitation through non-radiative internal convertions and molecular vibrations. The third decay mechanism is undirect and it involves the formation of a intermediate ^3A excited state in which the

system is temporarily trapped before returning to the ground state. This ^3A state is called "triplet state" and it is the key step for the photodynamic process. The triplet state of the photosensitizer can either react directly with a neraby reductant molecule, acquiring a hydrogen atom or electron to form a radical and to produce a superoxide anion radical ($O2^{\bullet-}$), (type I), or it can transfer its energy to a molecular oxygen in the triplet ground state ($^3O_2$) to form the very reactive excited singlet oxygen ($^1O_2$) (type II). Both methods alter the redox balance in the cell inducing several death mechanisms. The mode of cell death observed after PDT depends on the photosensitizer localization and on which organelles are involved. In mitochondria PDT leads to membrane permeability modifications and the subsequent release of pro-apoptotic mediators (cytochrome c) which can lead both to apoptosis and necrosis. The damage of the endoplasmic reticulum induces lethal changes in the intracellular Ca^{2+} concentration, whereas in lysosomes the PDT can trigger the unregulated proteolytic enzymes production and the fusion with autophagosomes, organelles involved in the autophagy process[140].

Ruthenium anticancer drug with PDT applications

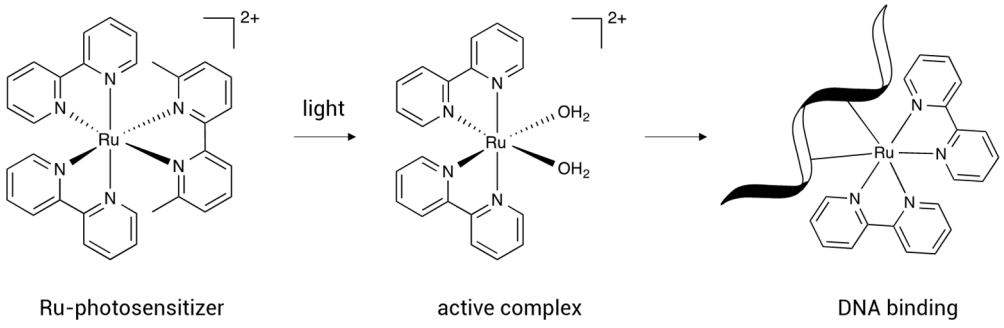

Figure 71: Schematic representation of the photoactivation of a ruthenium(II) polypyridyl derivative.

Some different ruthenium(II) polypyridyl derivatives have been synthesized and characterized as novel agents for the PDT. They are octahedral complexes which contain three bidentate ligands which are usually bonded to Ru(II) through nitrogen atoms. Once irradiated with light, these complexes immediately and selectively release

one of the bidentate ligands becoming extremely reactive molecules with two vacant positions. The complexes are inert in the dark, whereas after the ligand loss they effectively interact with DNA. A significant increase in cytotoxicity (1 or 2 order of magnitude) is usually observed with light activation in cancer cells, and these compounds display potencies superior to cisplatin in many different cell lines[141]. These complexes paved the way for the reasearch on new generation of metal-based anti-tumor agents which can be converted from nontoxic prodrugs to active cytotoxic species in a spatially and temporally controlled manner. These characteristics provide mechanisms of action capable to discriminate between malignant tissues and the surrounding healthy tissues, potentially reducing the dose-limiting side effects incurred with standard chemotherapies[142].

Sadler's strategy for the PDT

The photochemical activation of molecules has become an attractive approach for the development of new anticancer agents. In 2012 Sadler and co-workers published an article in which they described a series of photoactivatable ruthenium(II) half-sandwich complexes[143]. These complexes were all bi-cationic compounds of the type: $[(\eta^6\text{-arene})Ru(N,N')(L)]^{2+}$ containing some different η^6 coordinated arenes, some different κ^2 coordinated bipyridines (N,N') and many different pyridyl compounds as monodentate ligands. These complexes were able to selectively dissociate their monodentate pyridil ligand (L) when excited with UVA or white light, leading to the formation of the extremely reactive acqueous species $[(\eta^6\text{-arene})Ru(N,N')(H_2O)]^{2+}$ (*Figure 72*).

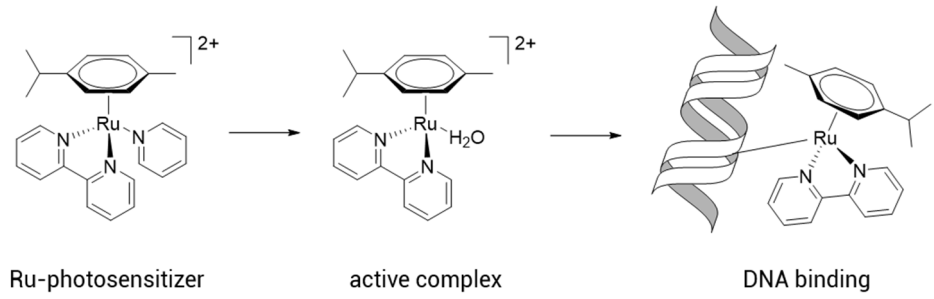

Figure 72: Schematic representation of the photoactivation of a general Sadler-type Ru(II) half-sandwich complex.

In the paper, the ability of the complexes to interact with two different nucleobases, namely the 9-ethylguanine (9-EtG) and 9-ethyladenine (9-EtA), was investigated. The results showed that light activation can be used to phototrigger the binding of these potential anticancer agents with discriminating preference toward 9-EtG. Moreover, they tested the interactions between the complexes and the Circulating Tumor DNA (CT-DNA), which consists in fragments of tumour origin DNA circulating into bloodstream. Some derivatives bound effectively the DNA both in irradiated and pre-irradiated samples, but usually, the non-irradiated forms, bound DNA negligibly. The irradiated species binding modes with DNA are a combination between monofunctional coordination and intercalation. Finally, the IC_{50} values of non-irradiated derivatives tested on A2780 cells (human ovarian cancer) showed that some of them were cytotoxic (with IC_{50} lower than 10 μM) suggesting that the complexes might be cytotoxic also using other mechanisms of action and that the photoactivation cuold be a strategy to even more raise the cytotoxicity. To conclude, this paper indicated that the photochemistry is a very interesting field to be integrated in the study of metal-based anticancer agents.

Naphthalenimides

Naphthalenimides (NIs) are a well known class of organic molecules which have found many different applications as anticancer drugs[144], luminescent[145] and sensing materials[146]. NIs are easy to synthesize and to functionalize and metal complexes containing NI-functionalized ligands are numerous in the literature. The structure of the NI moiety is planar, characterized by a high electron delocalization between the naphthalene rings and the symmetric imide. This structure provides NIs with a strong intercalating power which have been extensively studied in medicinal chemistry. The most famous example in this field is the Amonafide (trade names *Quinamed* and *Xanafide*, *Figure 73*) which in 2010 gained the FDA approval for the treatment of Secondary Acute Myeloid Leukaemia. Its mechanism of action is still debated but there are many studies about its ability to inhibit topoisomerase and to intercalate DNA.

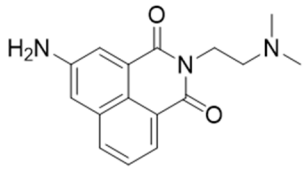

Figure 73: Amonafide.

The strong intercalating activity of NIs has been demonstrated through the solution of several X-ray structures of DNA strains in which Nis interact with nitrogenous bases. We report an example found in the Protein Data Bank (PDB code: 2KY7) in which it is clearly visible the intercalation of the pyrrolobenzodiazepine-NI conjugate[147].

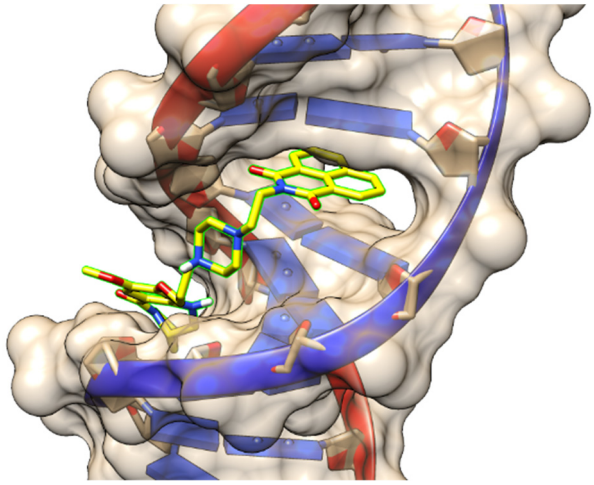

Figure 74: Pyrrolobenzodiazepine-NI conjugate intercalated into a DNA strand.

9.1.1 The project at Warwick

Given our interest in the subject, I came into contact with Prof. Sadler who hosted me in his laboratory for a six-month collaboration project between the University of Parma and the University of Warwick in 2017.
During this period, Sadler's strategy was applied to improve the performances of a series of Ru(II) half-sandwich complexes previously synthesised in our research group[148]. These compounds were designed as potential anticancer agents, but they resulted unsuitable for biological tests because they were unstable in DMSO/water medium. At Warwick, we decided to modify the coordination around the Ru(II) following Sadler's strategy and keeping fixed our original monodentate naphthalenimide-pyridyl (NI) ligands. We obtained some new complexes with general formula $[(\eta^6\text{-p-cym})Ru(N,N'\text{-bipy})(NI)]^{2+}$. Their stability in solution and photoactivation were tested and finally, they were submitted for biological tests. The success obtained with the NDI derivatives led us to believe that this strategy could be applied also to our TSs and TCs.

How to apply Sadler's strategy on our TSs and TCs

TSs are molecules usually poorly soluble in water. This characteristic has its pros and cons. It is useful, in principle, because a certain level of lipophilicity helps the membrane crossing ensuring a higher uptake. However, compounds insoluble in water are difficult to administrate, less bioavailable and, as a consequence, it is unlikely that they reach the target site intact or in a sufficient amount. We tried to solve this problem by applying the Sadler's strategy in the design of new photoactivatable Ru(II) half sandwich complexes containing TS as the ligand that is released upon photoactivation. These complexes were designed to raise the solubility of TSs because the final complex is a bi-cationic species which can be administered as a salt. After that, once the Ru(II) complex has reached intact the target site, it can be photoirradiated to release the TS which carries out its biological effects with the cooperative action of the Ru(II) photoproducts. In this way, we have envisaged a possible strategy to obtain the delivery of a water-insoluble TSs associated with its controlled photo-release. This strategy

combines the drug delivery concept with the photodynamic therapy approach to improve the activity of TSs.

In the literature, several examples report TSs used as ligands for Ru(II). They are complexes in which the TS act always as bidentate S,N-ligand. These complexes were designed and studied for several different purposes[149,150] among which there are also examples of potential anticancer agents[151,152]. Unfortunately, they usually show two important limits: the poor solubility in water and the rapid breaking up of the TS coordination in DMSO. We decided then to solve this problem by using a different and more stable coordination mood of the TS. Since in the Salder's strategy the requirement to obtain the photorelease was the presence of monodentate pyridyl derivatives, we decided to create a TS with a pyridyl function which binds Ru(II) instead of the typical S,N binding mode. To make possible this unconventional coordination, we designed a multistep synthetic strategy *ad hoc*. We firstly prepared the [(p-cym)Ru(N,N'-bipy)(4-formylpyridine)]$^{2+}$ which is stable and does not have coordinative vacant positions, then we synthesised the TS directly on the ruthenium complex. In this way we avoided the competition between the TS and the pyridine in the coordination to ruthenium.

The synthesis of naphthalenimides and its optimisation

During the collaboration with the University of Warwick we explored the possibility of using the NI ligands as fluorescent probes for cytofluorimeter and confocal microscopy analysis. Fluorescent active molecules in medicinal chemistry are extremely interesting because this characteristic helps in the research on the mechanism of action. In fact, the uptake and the location of fluorescent molecules can be followed in cells through many different techniques and in many cases with very good resolution and accuracy. In one of our previous works we described the fluorescent properties of **108** which resulted a good fluorophore with an emission band centred at 395 nm if excited at 336 nm[148]. Unfortunately, the **108** emission can only be obtained applying excitation wavelengths lower than 355 nm and this limit is unsuitable for confocal microcopy, where the lowest applicable excitation wavelength is 488 nm (Argon-Ion laser). In order to overcome this issue, we decided to modify the NI to shift its absorption-emission profile to higher wavelengths. In the literature there is an interesting review which

analyses the effects of the naphthalene functionalisation in NIs' on their fluorescence emission[153]. The authors claim that the 4-amino-1,8-naphthalimide derivatives have broad absorption and emission profiles usually centred at ca. 450 and 550 nm, respectivel. They assign the shift from the unfunctionalised NI values to a 'push–pull' internal charge transfer (ICT) caused by the electron-donating amine and the electron-withdrawing imide.

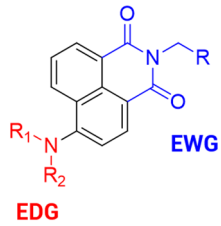

Figure 75

Following this principle we decided to functionalise **108** adding a piperidine group in position 4 of the naphthalene to obtain **111**. We chose this functionalisation because this molecule has already been studied by Braga et al. as a coformer for fluorescent co-crystals[154] with a broad absorption band between 350 and 500 nm. We synthesised this molecules simplyfing the original experimental procedure as follows:

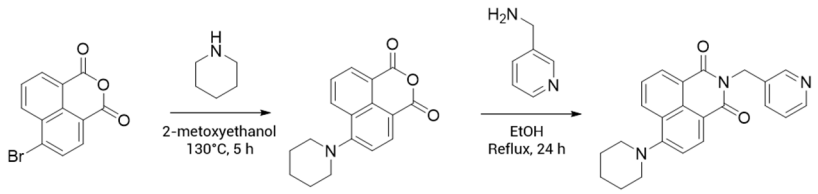

110 **111**

*Figure 76: Experimental details of the synthesis of the 4-piperidine-NI (**111**).*

The shifts of the absorbance and emission profiles were verified by the comparison between the UV-vis and fluorescence spectra (*Figure 77*). Passing from **108** to **111** the emission shifted to higher wavelength of 144 nm inducing a change in the colour of the fluoresence of the solution even when irradiated under the laboratory UV-lamp (365 nm).

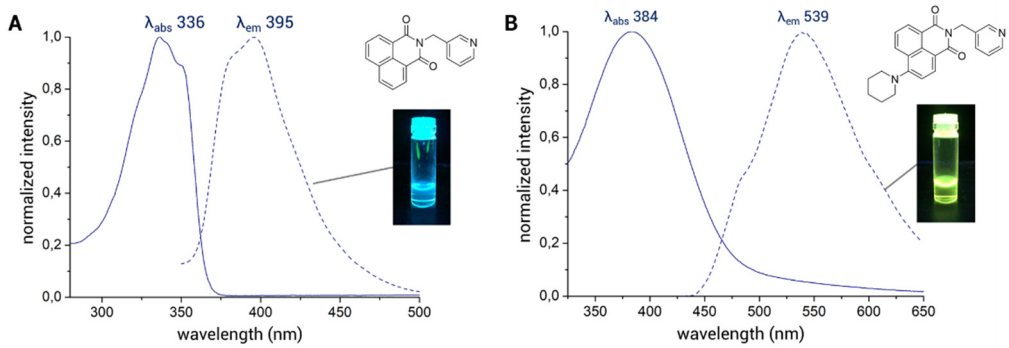

*Figure 77: UV-vis absorption and fluorescence emission spectra of **108** (A) and **111** (B).*

Synthetic approach

To obtain the final products we adopted a multistep synthetic approach optimised using a convergent synthesis. Although the final products were all ruthenium(II) half sandwich complexes with the general formula $[(\eta^6\text{-p-cym})Ru(\kappa^2\text{-bipy})(L)](TfO)_2$, the synthetic steps leading to the products containing NI or TC/TS ligands (L) were adapted according to the ligand desired.

Ru(II) half sandwich with NI derivatives

This synthesis was made for the first time at Warwick and later on optimised in Parma. The general scheme of the final and successful synthetic strategy is reported in *Figure 78.*

Step 1: *Synthesis of the bi-metallic complex* $[(\eta^6\text{-p-Cym})RuCl_2]_2$.
The product was obtained pure following an already known protocol which applied the microwaves to speed up and maximize the reaction yield[155].

Step 2a: *Synthesis of the NI ligand*.
The desired NI was obtained from the condensation of the aminomethylpyridine with the proper naphthalene anhydride.

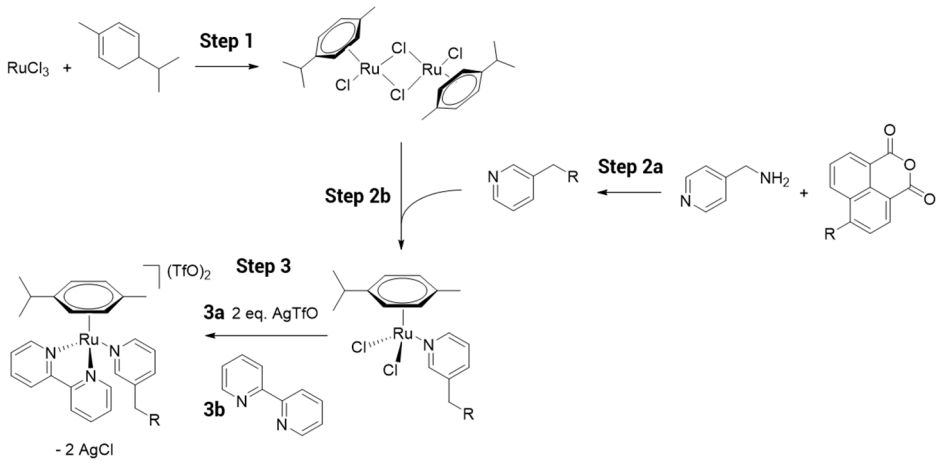

Figure 78: Synthetic route optimised to obtain Ru(II) half sandwich complexes with NIs.

Step 2b: *Synthesis of the [(η^6-p-cym)Ru(L)Cl_2] complexes.*

In this step, two equivalents of the ligand obtained in step 2a were mixed with one equivalent of [(η^6-*p*-Cym)$RuCl_2$]$_2$ in dry conditions to obtain two equivalents of the half-sandwich product. The complexes formed were neutral because the charges of Ru^{2+} were balanced by the two chloride anions.

Step 3a: *Halogen scavenging.*

The neutral complex was dissolved and two equivalents of silver triflate were added to get rid of the chlorides through the formation of AgCl. The salt formed was removed by filtration. This step was performed keeping the solution in the dark to avoid the silver photo-reduction.

Step 3b: *Insertion of the bipyridine.*

The last step was the addition of one equivalent of bipyridine to obtain the final product. Even in this step the solution was kept in the dark to preserve the photoactivatable products. The complexes obtained were bi-cationic complexes in which two triflate anions neutralised the charges without interfering with the metal cordination.

This procedure was optimised starting from a protocol published by Sadler and co-workers in 2012[143]. In that paper, it was reported that the complexes were obtained with

a strategy in which steps *2b* and *3a-b* were inverted. The protocol described the reaction of the $[(\eta^6\text{-}p\text{-Cym})RuCl_2]_2$ with the bipyridine to form a mono-cationic complex with the formula $[(\eta^6\text{-}p\text{-Cym})Ru(\kappa^2\text{-bipy})Cl]^+$. Subsequently the chloride was removed using a silver salt and finally it was added the desired ligand to complete the synthesis. This last steps needed a very large excess of ligand (10-20 equivalents) which created problems both in the purification of the products and in the recovery of the non-reacted ligand. We applied this procedure in the synthesis of the complex **114**, where it was necessary to use 10 equivalents of NI ligand and the yield was extremely low (17%) due to the multiple recrystallisations necessary to purify the product. All these issues were completely solved following the strategy we previously described, where reactants were always used in stoichiometric quantities and the products did not need any purification. Our optimised protocol resulted less laborious and it ensured higher yields (between 73% and 91%).

Ru(II) half sandwich with TS/TC derivatives

The same optimised strategy was applied also in the synthesis of a new series of complexes in which the monodentate ligand belongs to the class of thiosemicarbazones (or thiocarbohydrazones). In this case, the synthesis needed some additional steps and adjustments which are described in *Figure 79*.

Step 1: *Synthesis of the bi-metallic complex* $[(\eta^6\text{-}p\text{-Cym})RuCl_2]_2$.
For this step we used the same procedure described in the previous paragraph.

Step 2: *Synthesis of the* $[(\eta^6\text{-}p\text{-cym})Ru(4\text{-formylpyridine})Cl_2]$ *complex.*
This step was performed by mixing two equivalents of 4-formylpyridine with one equivalent of $[(\eta^6\text{-}p\text{-Cym})RuCl_2]_2$ in dry conditions to obtain two equivalents of the half-sandwich product.

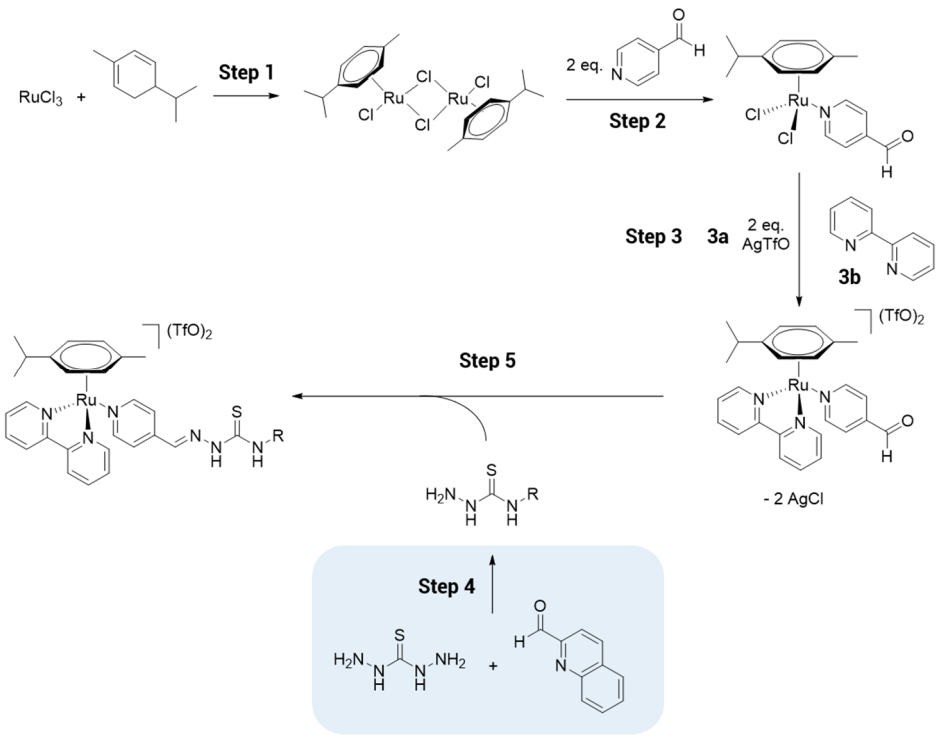

Figure 79: Synthetic route optimised to obtain Ru(II) half sandwich complexes with TSs and TCs.

Step 3a: *Halogen scavenging.*

As previously described, we used silver triflate for the replacement of the two coordinated chloride ions with two non-coordinated triflates.

Step 3b: *Insertion of bipyridine.*

Bipyridine was added after the halogen scavenging to obtain the bi-cationic half-sandwich derivative with formula $[(\eta^6\text{-}p\text{-Cym})Ru(\kappa^2\text{-bipy})(4\text{-formylpyridine})](TfO)_2$.

Step 4: *Synthesis of the mono-TC ligand.*

This step was necessary only for the syntheisis of **125** in which the monodentate ligand was a TC. It was obtained by the consensation of an equimolar amount of aldehyde and thiocarbohydrazide.

Step 5: *Condensation with the carbonyl group of 4-formylpyridine*.
The final product was obtained from the condensation between the carbonyl group of the Ru(II) complex and the hydrazine of the desired TS/TC in dark conditions. Routinely, the synthesis of the TC and TS is made by refluxing the reactant mixture in methanol for 6-8 hours. In this case it was necessary to use milder conditions to avoid the complex degradation. In the optimised protocol, we used a poorly coordinating solvent like dry THF instead of methanol and we did not heat the mixiture during the reaction.These changes in the protocol led to longer reaction times (24-48 hours), but they permitted to obtain the products pure and in good yields.

Stability in solution

The study of the stability in different solvents is a key step in the characterisation of the ruthenium(II) half-sandwich complexes, especially when they have been designed as molecules with biological and medical applications.
Biological assays are usually performed by dissolving the compound to test in DMSO (a 10 mM stock solution) and then by diluting it in the cell medium to create the desired concentration. However, the DMSO concentration must be kept as low as possible, because high concentrations can be lethal for the majority of cell lines. The biological effects of DMSO are due to its high polarity and dielectric constant which enhance membrane permeability, modifing cell hydration and homeostasis[156]. Since every cell line can be considered a different living system, it is always a good practice to include control cultures treated with the same DMSO concentration used to test compound. To ensure the correct cell growth and to avoid DMSO interferences, it is usually recommended to keep the concentration of DMSO lower then 2%.
As mentioned before, the compound dissolved in DMSO is subsequently diluted in cell medium to obtain the proper treatment concentration for the assay. The cell media used are usually extremely complex water mixtures of nutrients, mineral salts and buffers which ensure the proper enviroment for cell growth[157] but, at the same time, they could interact with the compound to test and interfere with its action.
It is then important to evaluate the solution behaviour of our candidates before submitting them to a biological screening. For metal complexes this study is more

crucial than with simple organic molecules, because their biological effects are usually connected with ligand exchange rates and binding constant with biological molecules. In addition, this parameter becomes even more important in the design of photoactivatable metal complexes, because to be selective they must be stable and inactive until the light irradiation. The stability test must be set up to prove that the drug is activated only by light and not by other components in the enviroment.

For ruthenium half-sanwich complexes the most critical test is the stability in DMSO. It is a strongly coordinating solvent and it can easily replace the neutral ligands of the complexes. Many ^{1}H-NMR studies unequivocally indicates that DMSO induces ligand exchange in complexes of the type [Ru(η^6-arene)Cl_2(L)], where L indicates a N-heterocyclic monodentate ligand[158]. The nature of all the coordinated organic molecules in the complex governs the amount of ligand displacement and the rate of the process, but DMSO is very often capable to immediately remove N-monodentate ligands. As already mentioned in the introduction, in the past we have already worked on half-sandwich complexes and they unfortunately confirmed this behaviour[148]. This is why we decided to change the design of our half-sandwich complexes following the outline used by Sadler and co-workerswhere one molecule of bipyridine replaces the two chlorides [(η^6-arene)Ru(N,N-bipyridine)(L)]$^{2+}$.

Against this background, we decided to test the stability of our complexes by monitoring changes in the ^{1}H-NMR spectra of samples measured immediately after their preparation and after 24 hours. To test the stability in different conditions the ^{1}H-NMR experiments were performed both in acetone (poorly-coordinating solvent) and in DMSO (highy-coordinating solvent)[159]. We decided also to store samples in the dark at 37°C to verify at the same time if complexes are also suitable for the subsequent photoactivation experiments. Finally, we tested also the stability in an aqueous media at physiological pH with the addition of 2% of DMSO to simulate the conditions of a biological assay. The use of water was also interesting in order to study the stability of compounds against hydrolysis. In this case, we used UV-vis absoption measurements (sample concentration 10-100 μM) because of the low solubility of our complexes in water in the range of concentration used for NMR experiments (5-10 mM). We considered stable a compound which did not change its ^{1}H-NMR spectra and profile of absorption in a 24 hours time period. All the complexes showed tha same trend then,

for the sake of simplicity, we show only the details of the **115**/**119** stability experiments (*Figure 80, Figure* 81*Figure 82*). All the other results are summarised in *Table 32*.

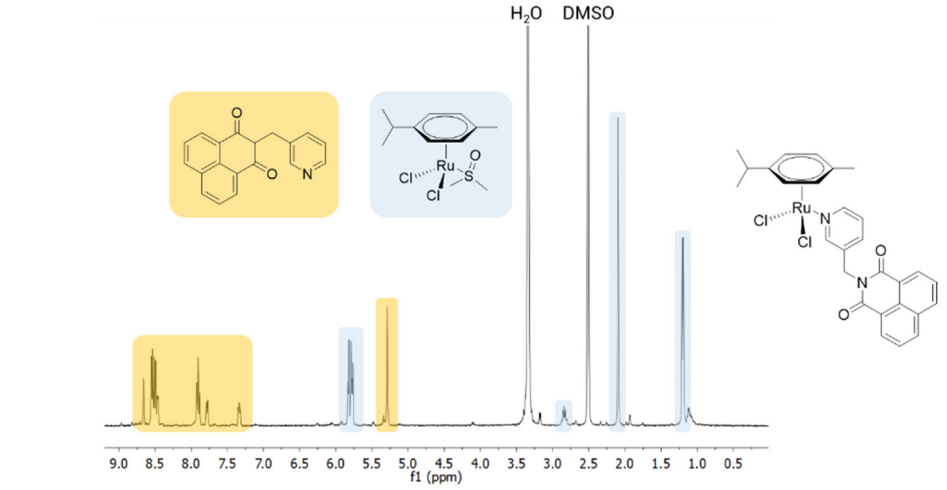

*Figure 80: ^{1}H NMR spectrum in DMSO-d^{6} of complex **115**. Signals of the free ligand **88** are coloured in orange and signals of the Ru(II)-DMSO adduct are coloured blue.*

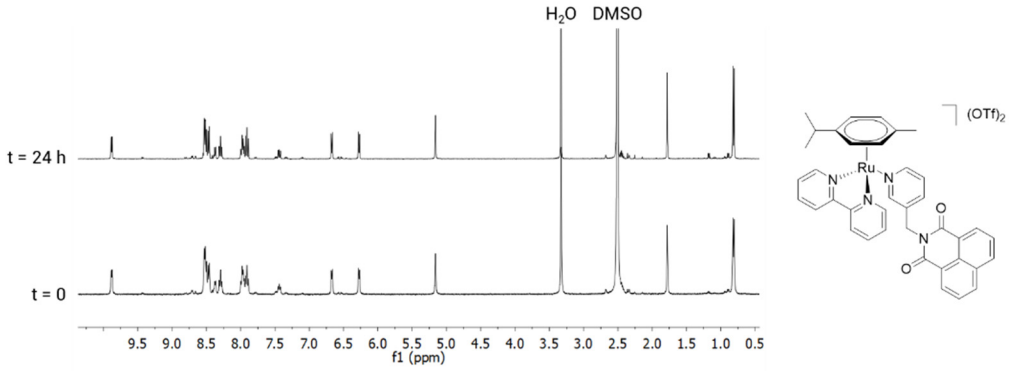

*Figure 81: Comparison between the ^{1}H NMR spectra in DMSO-d^{6} of complex **119** recorded immediately after the sample preparation and after 24 hours. No changes in the signals occurred.*

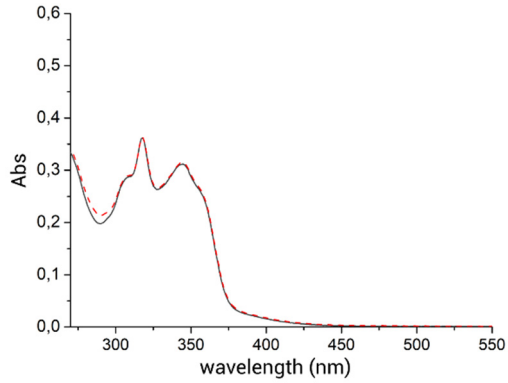

*Figure 82: Comparison between the UV-vis spectra of complex **119** collected in water buffered at physiological pH + 2% DMSO. Spectra were recorded immediately after the sample preparation (black line) and after 24 hours (red line). No changes in absorption profile occurred.*

complex	charge	stability in acetone	stability in DMSO	stability in water + 2% DMSO
119	bi-cationic	yes	yes	yes
115	neutral	-	no	insoluble
120	bi-cationic	yes	yes	yes
116	neutral	-	-	insoluble
121	bi-cationic	insoluble	yes	yes
117	neutral	-	no	insoluble
118	neutral	-	no	-
122	bi-cationic	yes	yes	yes
123	bi-cationic	yes	yes	yes
124	bi-cationic	yes	yes	yes
125	bi-cationic	yes	yes	yes

Table 32: Results of the stability experiments.

All the complexes with general formula $[(\eta^6\text{-arene})Ru(N,N\text{-bipyridine})(L)]^{2+}$ resulted stable in every solvent over a 24 hours time period. The only test that was impossible

to complete was the stability determination of complex **121** in acetone due to the poor solubility of the complex in this solvent. These great results indicated that the use of the N,N-bidentate bipyridine instead of two chlorides was able to stabilise effectively the coordination enviroment around the ruthenium, even when the complexes were dissolved in a very strong coordinating media such as the DMSO or water.

Acetone coordinating activity = 9%
Water coordinating activity = 46%
DMSO coordinating activity = 65 %

(*Dalton Tras.* **2011**, 40, 10742–10750).

9.1.2 Photoactivation experiments

As already mentioned, the final $[(\eta^6\text{-p-cym})\text{Ru(N,N-bipy)(L)}]^{2+}$ complexes were kept in the dark from the synthesis to the characterisation, including the storage. This precaution was applied to ensure the product stability in absence of light and to create at the same time the background data for photo-activation experiments. The data obtained in the dark (both NMR and UV-vis) were used as starting points, then the samples were irradiated with light and the spectra re-collected during the irradiation to monitor the light effect. Using this protocol, we were sure that any changes in the spectra were induced by light we applied and not by any other factor. The experiments were performed using a "photo-oven" we built in the lab. The apparatus (*Figure 83*) consists in a plastic box with a light source inside which can be regulated from the outside through a swictch. A lid ensures that the box is completely dark when the light inside is switched off. The sample can be placed from 0 up to 25 cm from the light source and the temperature inside is controlled by a thermometer. No temperature modifications induced by the light source were registered during the experiments.

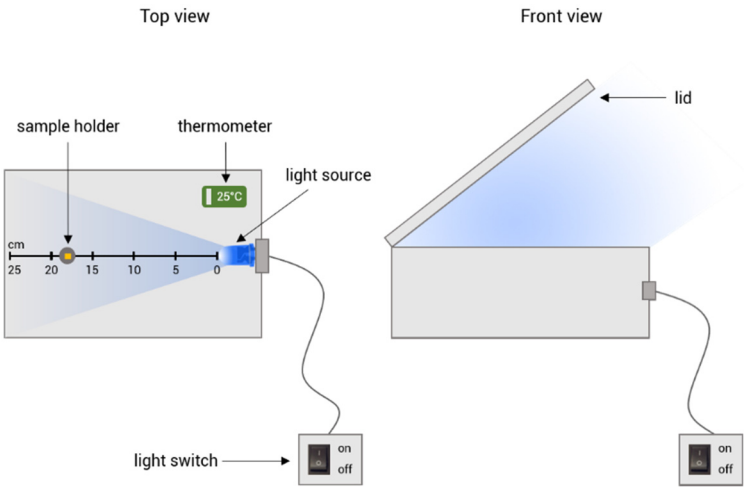

Figure 83: Schematic representation of the experimental apparatus used in the photoactivation experiments.

Photoactivation of Ru(II) half-sandwiches with NI derivatives

Complex 119

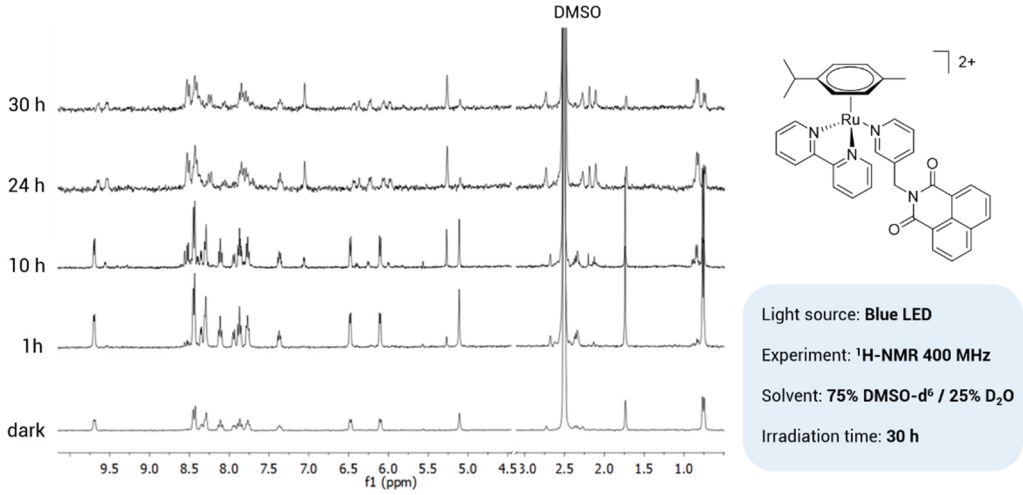

*Figure 84: Photoactivation of **119**.*

The photoactivation experiment was performed in an NMR glass tube and the sample was prepared in the dark by dissolving 5.03 mg of **119** in 500 µL (10.3 mM) of a solution 1 : 3 - D_2O/DMSO-d^6. The sample was irradiated directly in the NMR tube which was positioned in the photo-oven and 4 cm far from the light source. The effects of the light irradiation were analysed by collecting four different spectra of the same sample. The "dark" spectrum was collected immediately after the sample preparation. The following spectra were collected after 5, 20 and 25 hours of irradiation. The results are reported stacking the spectra in ascending order of time (*Figure 84*).

From the analysis of the data obtained, it was apparent that the light induced significative effects on **119** and some changes in the spectra were visible already after 1 hour of irradiation. During the irradiation, the singlet at 5.11 (the methylene group of the NI) decreased and simultaneously a new singlet appeared at 5.27 ppm, suggesting a relationship between the two species. Moreover, this new signal coincided with the signal of the same methylene group of the ligand **108** when it is not involved in the coordination with the ruthenium (*Figure 85*).

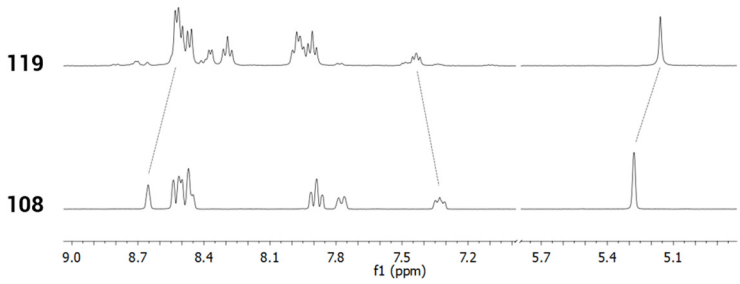

Signal	Free ligand	Complex	Δ Chem Shift
(s) CH_2	5.27	5.15	- 0.12
(t) Pyiridine	7.35	7.45	0.10
(s) Pyridine	8.65	8.52	- 0.13

*Figure 85: Comparison between diagnostic ^{1}H-NMR chemical shifts (75% DMSO-d^6 – 25% D_2O) of **108** and **119**.*

These observations suggested that the light was able to gradually induce the photodissociation of the NI ligand. Assuming this mechanism, we identified all the other signals of **108** uncoordinated and they resulted perfectly in agreement with those in the spectra of free **108** recorded in DMSO-d^6 (*Figure 85*). To identify the other product of the photo-reaction we analysed the remaining signals using their integrals as a reference. Starting from 5 hours of irradiation, we identified three different sets of signals: **119**, **108** released and $[(\eta^6\text{-p-cym})\text{Ru(N,N-bipy)}(\textit{solvent})]^{2+}$ (*solvent* could be DMSO or water because they are both coordinating). The complex $[(\eta^6\text{-p-cym})\text{Ru(N,N-bipy)}(\textit{solvent})]^{2+}$ was identified through the presence of the doublet at 9.53 ppm which correspons to the two equivalent protons close to the nitrogen of bipyridine shifted to lower field as an effect of the interaction with the metal. In fact, this signal is located at 8.63 ppm when bipyridine is free (in DMSO-d^6) and it shifts upper than 9 ppm when the bipy is coordinated. The starting complex **119** disappeared almost completely after 24 hours of irradiation and in the last spectra (24 and 30 hours) are clearly visible only the signal of two photoproducts **108** and $[(\eta^6\text{-p-cym})\text{Ru(N,N-bipy)}(\textit{solvent})]^{2+}$ (*Figure 86* and *Figure 87*).

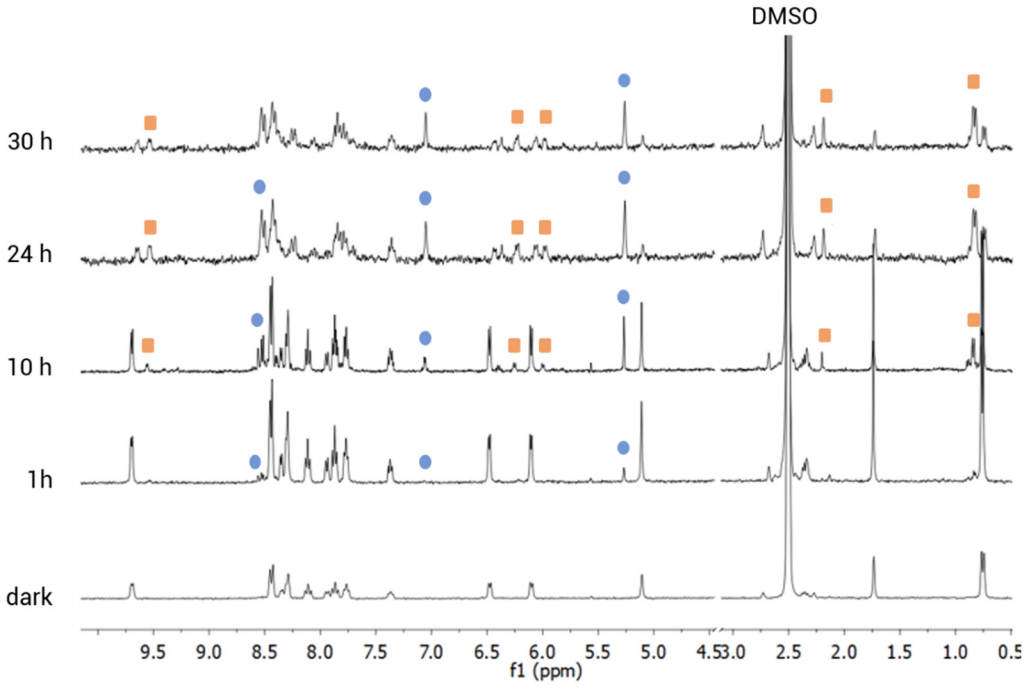

*Figure 86: Study of the photo-products obtained after the irradiation of **119.***

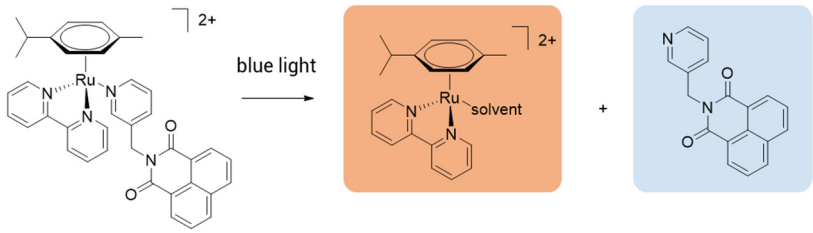

*Figure 87: Proposed mechanism for the photo-activation of **119**.*

These evidences led us to describe the photo-reaction as the selective detachment of the **108** ligand and the formation of a ruthenium complex with a vacant coordinative position[(η^6-p-cym)Ru(N,N-bipy)(*solvent*)]$^{2+}$. This experiment confirmed that **119** follows the same mechanism of photo-dissociation observed for the Sadler's pyridyl ruthenium(II) arene complexes. Same results were obtained from the photoactivation the analogue bi-cationic complex **120** which released selectively its NI ligand **109**.

Fluorescence emission as method to follow the photo-release of 108

Since the ligand **108** showed interesting fluorescent behaviour we measured also the emission profile of its complex **119**. The fluorescence profile of **119** was identical to **108** but significantly decreased in intensity. This suggested that the fluorophore in **119** is just **108** and that some quenching effect induced by the metal centre occurred. This behaviour was similar to what we previously observed for the neutral complex **115** [148]. Here we decided to use this phenomenon to study the photo-release of **108**. In particular, we monitored the photoreaction through the acquisition of emission spectra of the complex irradiated for 1, 5 and 24 hours. We recorded a very significant and progressive increase of the fluorescence during the irradiation time (*Figure 88*) and being the free ligand significantly more fluorescent than the complex, this phenomenon was ascribed to the selective photo-release of the ligand **108** from **119**.

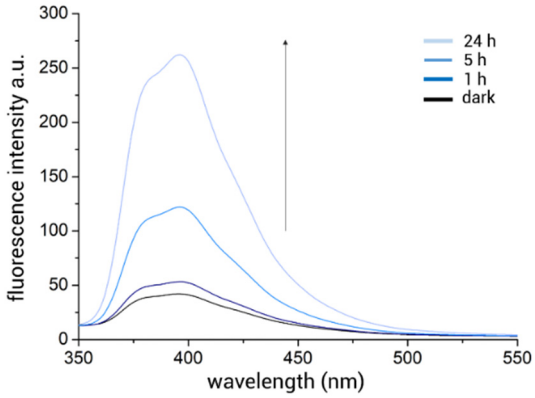

*Figure 88: Fluorescence emission spectra of complex **119** recorded at various irradiation time.*

Complex 121

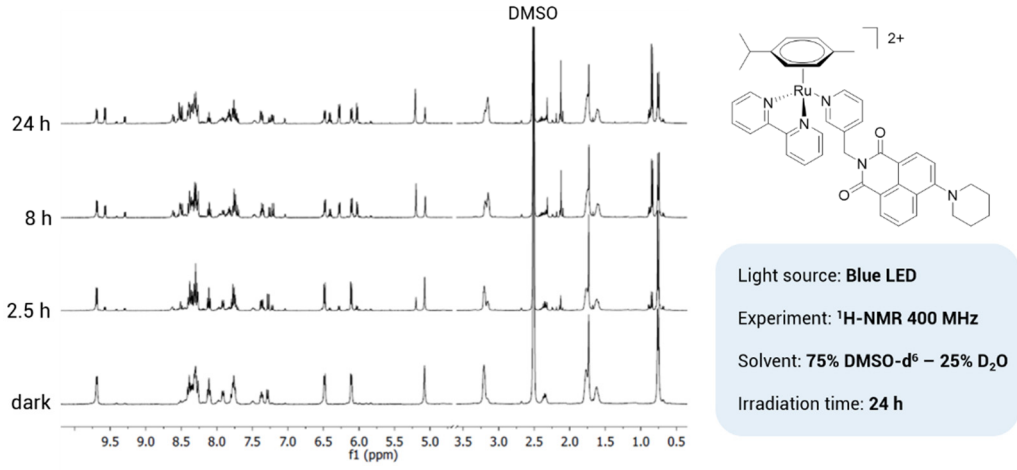

*Figure 89: Photoactivation of **121.***

To study the photoactivation of **121** we adopted the same experimental set-up applied for **119** (6.08 mg in 500 µL, final conc. 11.5 mM). Even in this case we used the singlet of the methylene group of the NI to follow the detachment because it shifts from 5.08 to 5.20 ppm passing from the coordinated to the uncoordinated ligand (*Figure 90*).

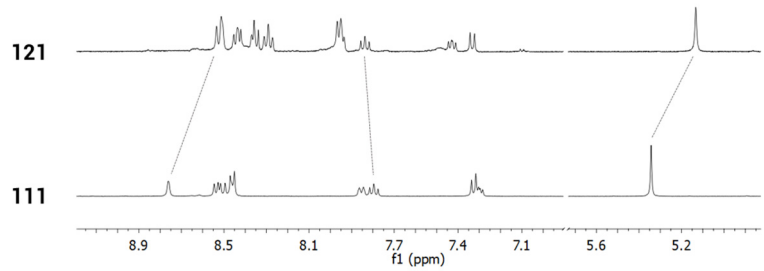

Signal	Free ligand	Complex	Δ Chem Shift
(s) CH_2	5.34	5.16	- 0.18
(t) Pyiridine	7.80	7.91	0.11
(s) Pyridine	8.76	8.53	- 0.23

*Figure 90: Comparison between diagnostic ^{1}H-NMR chemical shifts (75% DMSO-d^6 – 25% D_2O) of **111** and **121.***

However, between **121** and **119** we noticed some differences. **121** followed almost the same detachment kinetics of **119** until the release of the 56% of the ligand (after 8 hours of irradiation), then the percentage of released ligand did not raise any further. In fact, the spectrum of **121** registered after 24 hours of irradiation showed the same percentage of free ligand (56%) we measured in the spectra irradiated for 8 hours (*Figure 91*). In contrast to **119**, the photo-release of **111** from **121** was not complete and the reaction reached a chemical equilibrium after 8 hours of irradiation. To analyse the photo-products we applied the same method used for **119**. We started from the singlet at 5.20, then we used the integrals to identify the other signals of the free **111**. Subsequently we identified the signals of the complex [(η^6-p-cym)Ru(N,N-bipy)(*solvent*)]$^{2+}$ using the doublet of the bipy at 9.57 ppm and the aromatic p-cymene signals at 6.02 and 6.27 ppm. Starting from 8 hours we noticed also another set of aromatic p-cymene signals (6.38 and 6.42 ppm) which is related with a bipy doublet at 9.29 ppm. It was impossible to identify other signals related to this species and we classified it as a byproduct of the [(η^6-p-cym)Ru(N,N-bipy)(*solvent*)]$^{2+}$. The amount of

this byproduct raised passing from 8 to 23 hours of irradiation and in the final spectrum 4 species were are contemporarily present: **121**, **111**, [(η^6-p-cym)Ru(N,N-bipy)(*solvent*)]$^{2+}$ and its unknown byproduct. The mechanism we speculated for this photo-activation is reported in *Figure 92* and it involved a DMSO / water exchange processes in complex [(η^6-p-cym)Ru(N,N-bipy)(*solvent*)]$^{2+}$ which led to the formation of a different ruthenium arene species.

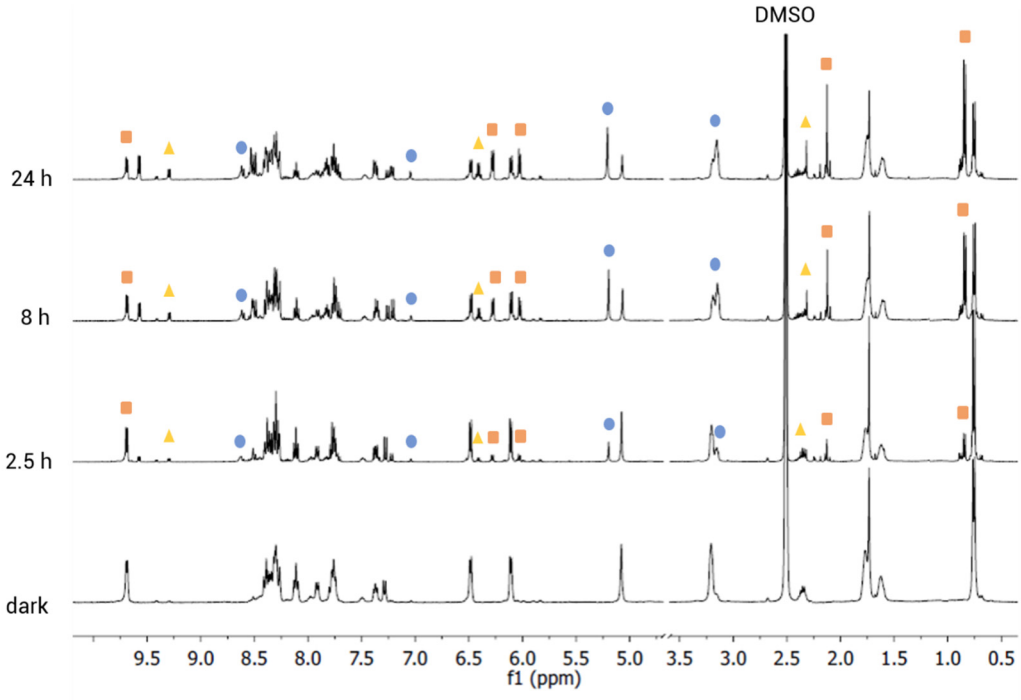

Figure 91: Study of the photo-products obtained after the irradiation of ***121.***

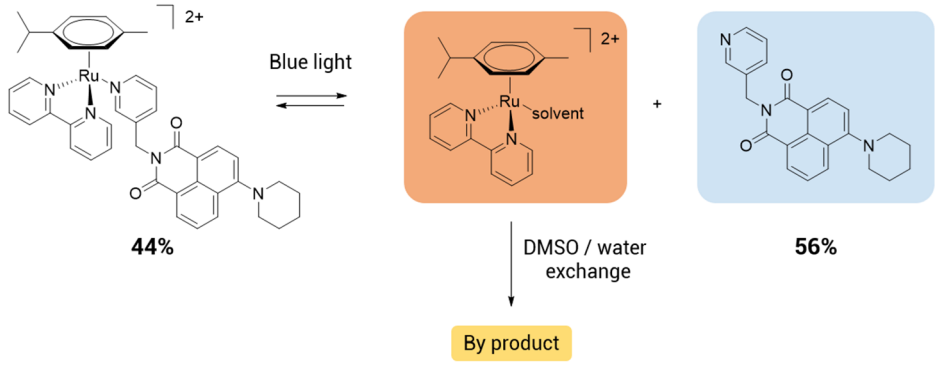

Figure 92: Proposed mechanism for the photo-activation of ***121.***

Photoactivation of Ru(II) half-sandwich with TS derivatives

Complex 123

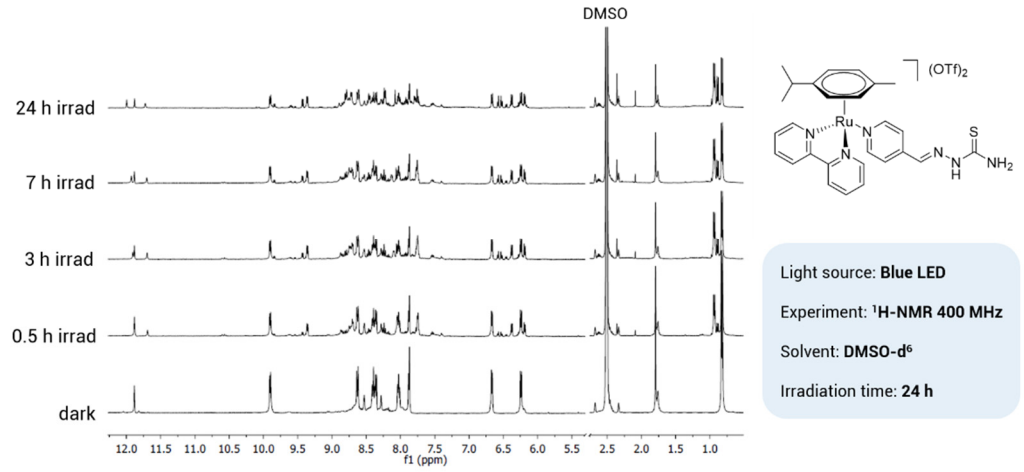

*Figure 93: Photoactivation of **123.***

Even the photoactivation on **123** was performed as already described for **119**, **120** and **121**. However, the solvent used for this experiment was just DMSO-d^6 because the presence of water in the system would have exchanged the -NH- and -NH_2 protons of the TS molecule. Despite this precaution, the results of this experiment were difficult to describe because the TS ligand has just one signal that can be monitored during the detachment, namely the singlet of the terminal iminic -NH- at 11.88 ppm. We recorded the NMR spectra of **123** after 0.5, 3, 7 and 24 hours of irradiation (*Figure 93*).

Analysing the spectra (*Figure 94*), we noticed the appearance of the peak at 11.69 ppm after half an hour of irradiation which corresponded with the free TS ligand. At the same time, the set of the p-cymene signals of the complex [(η^6-p-cym)Ru(N,N-bipy)(*solvent*)]$^{2+}$ appeared between 3.2 and 3.5 ppm. The percentage of these two photo-products was 35% after 0.5 hour and it increased with time. Even in this case we noticed the formation of a second ruthenium-containing species. It appeared in traces after 0.5 hour, but after 7 hours it was present in almost equal amounts with [(η^6-p-cym)Ru(N,N-bipy)(*solvent*)]$^{2+}$. Another important aspect, was that even **123** did not complete the monodentate ligand release and the reaction reached the chemical equilibrium after 7 hours. In fact, the signals in the spectra recorded after 7 and 24

hours of irradiation did not change significantly. In the spectra from 3 hour and beyond some traces of other unidentified byproducts also appeared. This behaviour suggested a mechanism of photoactivation similar to **121**, but characterised by a lower specificity of action. The large amount of byproducts caused by light irradiation highlighted that **123** is a light sensitive complex but also that the mechanism of this phenomenon is more complicated than what observed in NI-containing and Sadler's derivatives. A possible explanation is that when **123** releases the TS ligand it could start interacting with ruthenium also with the N,S-TS group generating different species. One piece of evidence that supports this hypothesis could be found in the singlet which appeared at 11.99 ppm after 3 hours of irradiation. This could be reasonably assigned to an -NH- proton of the imine group of the TS involved in a different interaction with the ruthenium half-sandwich (*Figure 95*Figure 95). Same results were obtained from the photoactivation of the analogue bi-cationic complex **124**.

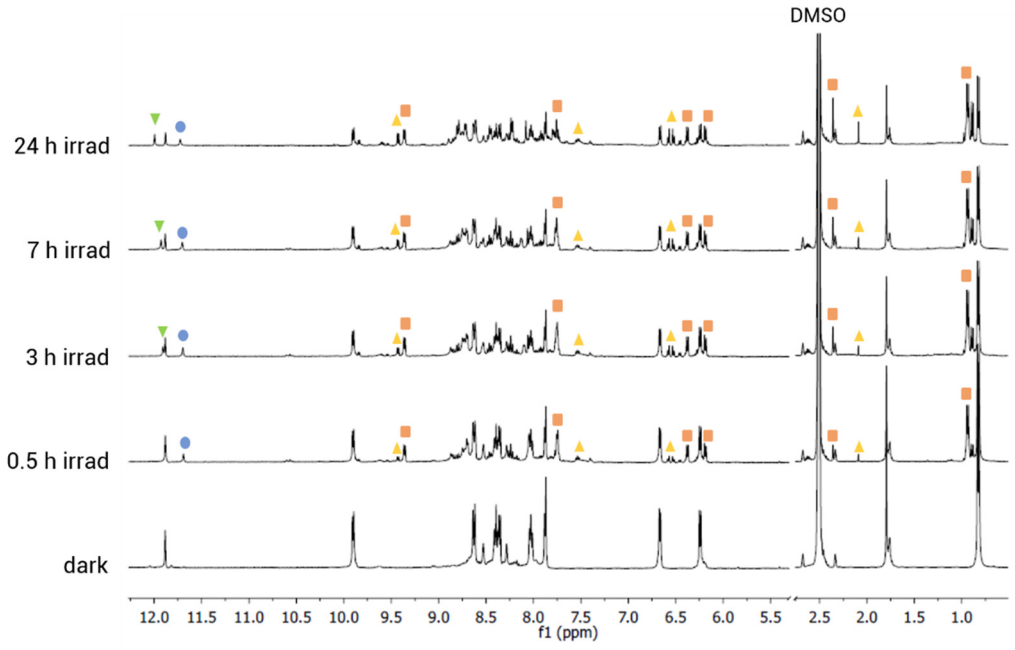

*Figure 94: Study of the photo-products obtained after the irradiation of **123.***

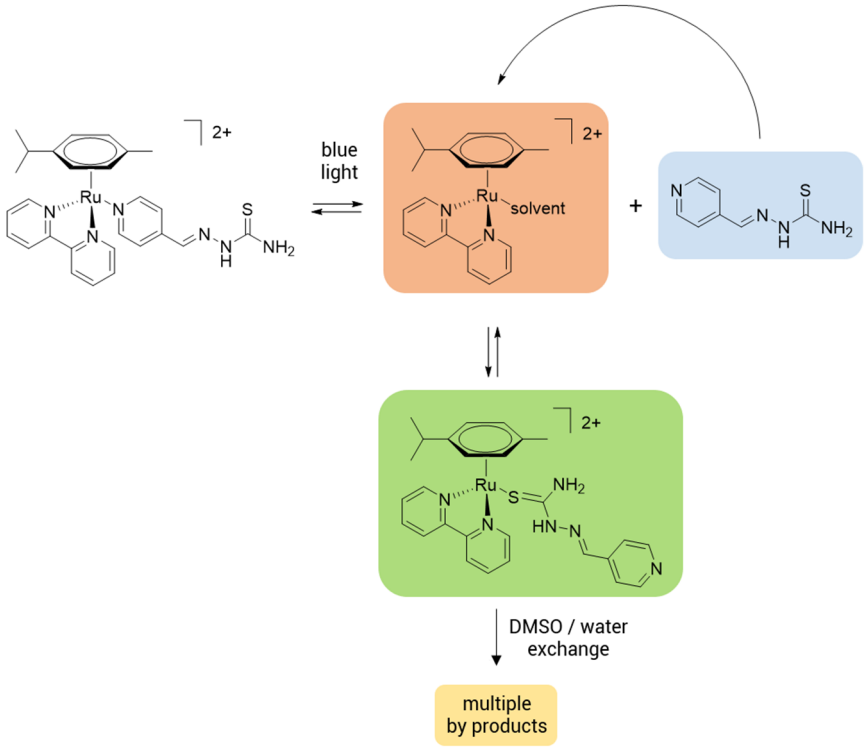

*Figure 95: Proposed mechanism for the photo-activation of **123.***

Complex 125

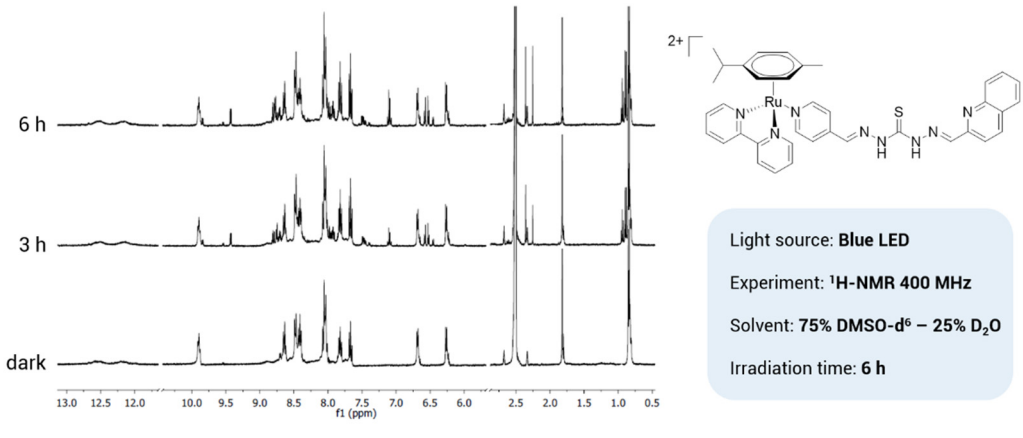

*Figure 96: Photoactivation of **125**.*

Also the photoactivation of **125** was performed using the method applied for the other complexes and in pure DMSO-d^6 because, even in this case, we wanted to avoid the water induced exchange of the hydrazone protons and the ^{1}H-NMR spectra were recorded after 3 and 6 hours of irradiation. In this experiment, compared with the previous ones, it was not possible to identify clearly the species [(η^6-p-cym)Ru(N,N-bipy)(*solvent*)]$^{2+}$. However, we identified sets ascribable to the free TC and to two (p-cymene)Ru-containing species which was impossible to assign accurately (*Figure 97* and *Figure 98*). One of this Ru-species seemed also containing a coordinated bypiridine, according to the doublet at 9.43 ppm. These two by-products were present already after 3 hours of irradiation and their amount raised proportionally with the irradiation time. After 6 hours of light the NMR experiments were stopped because the solution became turbid, indicating that one (or more) by products were insoluble. This evidence is consistent with the poor solubility of TCs in water containing media. Nevertheless the mechanism of the photoactivation of **125** is not completely understood, we verified that this complex is light sensitive and then suitable for PDT-tests on cancer cells.

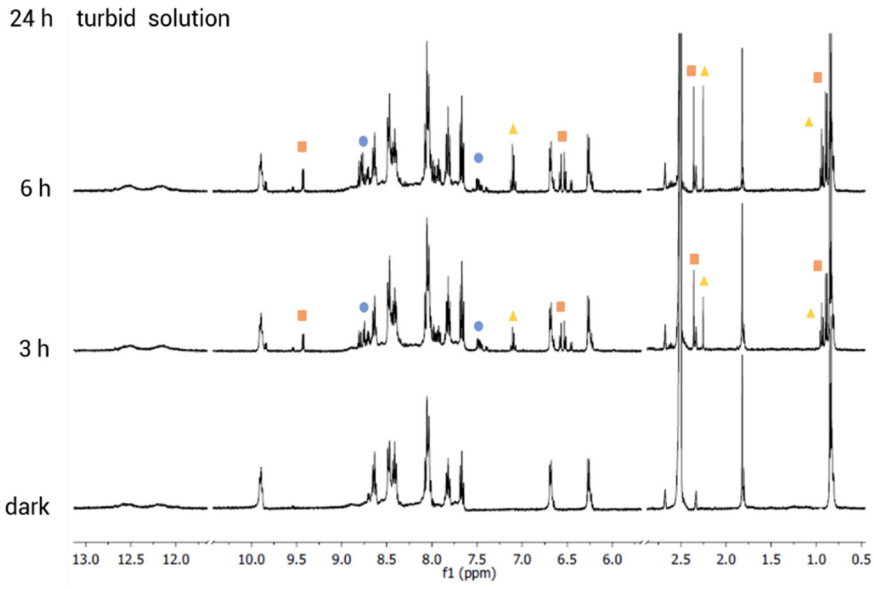

*Figure 97: Study of the photo-products obtained after the irradiation of **125.***

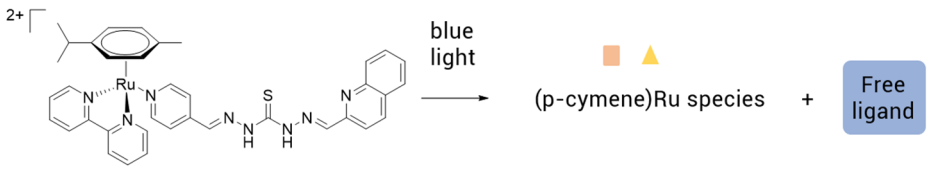

*Figure 98: Proposed mechanism for the photo-activation of **125.***

9.1.3 Photoactivation in cells

Since we confirmed the ability of our derivatives to be activated by light in solution, we decided to verify if this characteristic make them potential photosensitizers even in cells. We chose A549 cells as target since they represent a solid lung tumour that currently have no effective cure and, in principle, it is suitable for PDT treatments. In this context, we evaluated the cytotoxicity in A549 using the MTT assay inserting in the protocol different periods of light irradiation. Briefly, the MTT test consists in a 24-hour treatment in which cells are exposed to the drug. During the treatment we added periods of light irradiation, from 0.5 to 24 hours and in the end we measured the cell viability using MTT. In addition, to be sure to avoid the potential harmful effect of light we used, as control, cells non treated with drug, but irradiated. The results of this experiment are reported in *Table 33* .

The complexes containing non-functionalised NIs (**119** and **120**) and TSs (**123** and **124**) as monodentate ligands resulted not cytotoxic in the dark and this behaviour did not change in presence of light irradiation, indicating that these compounds are not effective photosensitizers in cells. on the other hand, completely different results were obtained from **121**. This complex, that contains the NI functionalised with piperidine (**111**), resulted mildly cytotoxic in dark condition, but in raised significantly its IC_{50} during irradiation, passing from 76.74 to 1.98 μM. Similar very good results were obtained also for **125** that showed an IC_{50} of 84.62 μM in dark condition and of 17.53 μM after 24 hours of irradiation.

	IC_{50} (µM) A549 24 hours		
	dark	**3 hours of irradiation**	**24 hours of irradiation**
119	>100	>100	>100
120	>100	>100	>100
121	76,74 ± 1,32	10,94 ± 1,75	1,98 ± 0,87
123	>100	>100	>100
124	>100	>100	>100
125	84,62 ± 3,90	10,52 ± 1,95	17,53 ± 2,28

Table 33: IC_{50} values of Ru(II) half-sandwich complexes determined in dark condition and after 3 and 24 hours of irradiation.

The best candidate of this screening was undoubtedly **121**, then we decided to explore more in detail its photoactive behaviour in cells. Keeping in mind a possible application of **121** as a drug for a real medical treatment, we decided to set 3 hours as maximum light exposure and we analysed the evolution of cytotoxicity in this period by determining the IC_{50} after 0.5, 1, 2, and 3 hours of irradiation *Table 34* .

121 IC_{50} (μM) A549 24 hours					
dark	**light**				
-	**30 min**	**1 hours**	**2 hours**	**3 hours**	**24 hours**
76,74 ±1,32	12,50 ±1,75	10,52 ±3,22	12,47 ±0,71	10,94 ±1,75	1,98 ±0,87

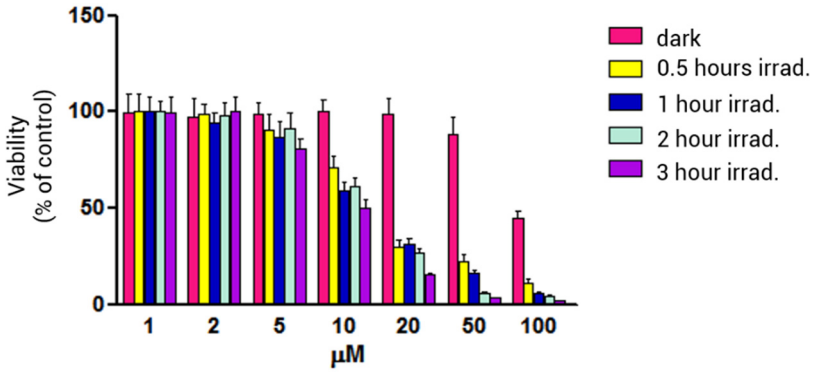

*Table 34: IC_{50} values of **121** determined in dark condition and after 0.5, 1, 2, 3 and 24 hours of irradiation.*

Surprisingly, the cytotoxicity of **121** did not raise during time as shown by the IC_{50}'s determined between 0.5 and 3 hours of irradiation that were all around 12 μM. This result is extremely important because suggests that the photoactivation is a very fast phenomenon in cells and this makes **121** an even more interesting potential photosensitizer. The activity of **121** on A549 was also explored through the analysis of the cell cycle over a 24-hour period *Figure 99*. The graph shows that light alone did not induce any effect on the cell cycle and that **121** not irradiated only lightly modified the percentage of cells in the G2/M phase (from 13.8% to 17.6%). Stronger effects on the cell cycle were highlithed in presence of **121** irradiatiated. The percentages showed a strong accumulation of cells in G2/M phase (32.1%) indicating that the irradiation of

121 is able to induce problems in the mitotic process. No apoptosis signals were detected, since were not found cells in the sub G0/G1 phase.

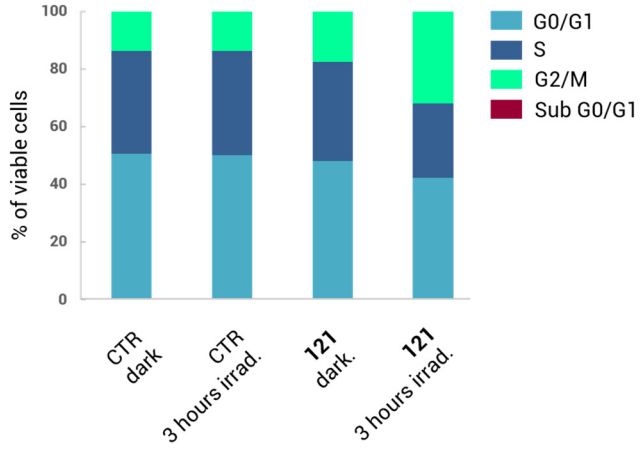

*Figure 99: Cell cycle analysis of A549 cells treated with irradiated and non-irradiated **121.***

Side scatter analysis

Finally, we tested the effect of **121** by measuring the Side Scatter (SSC) to identify the presence of modification in the granularity and internal morphology of cells. As shown in *Figure 100,* **121** (both irradiated and non-irradiated) did not induce any modification in the SSC signal and then no mutation of the internal granularity and complexity of cells.

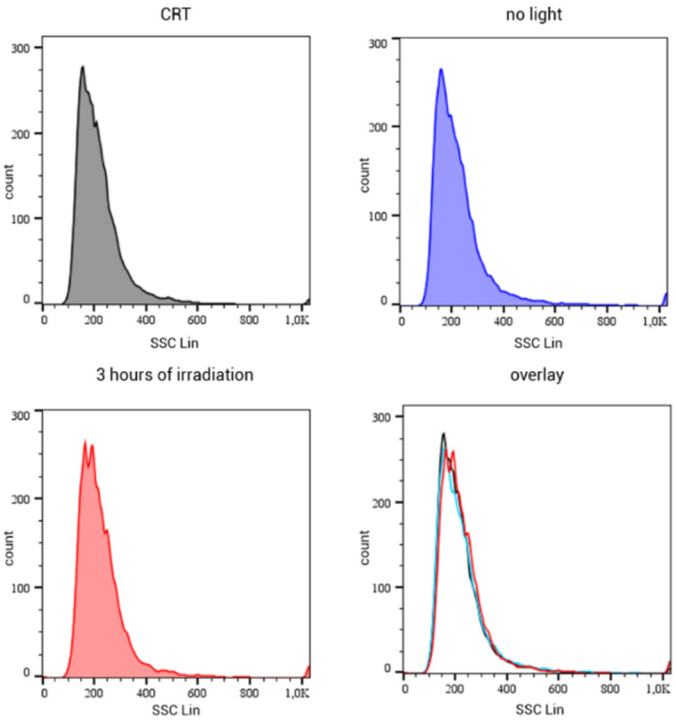

*Figure 100: Side Scatter (SSC) analysis of A549 cells treated with **121.***

Fluorescence in cells

121 contains **111** as NI ligand, which is a molecule that we previously described as an efficient fluorophore, able to emit in the range of 500-600 nm. To exploit this interesting property of **111**, we though to make the evaluation of the uptake of **121** in cells using fluorescence measurements. The flow cytometry is useful for this purpose, since it can be used to monitor changes in internal cell fluorescence. In particular, we used the laser at 488 nm as light source and we monitored the emission in the FL1 detector channel (500-550 nm). The results are collected in *Figure 101* and showed that, in both the samples treated with **121**, the emission intensity raised significantly and the FL1 signal was completely different (> 97%) compared with the control. This evidence indicated that cells absorbed a very strong fluorophore with characteristics that are perfectly in line with those observed for **111**. With these evidences, we have no reasons to doubt that the shift of the internal fluorescence is due to the uptake of **121** in cells.

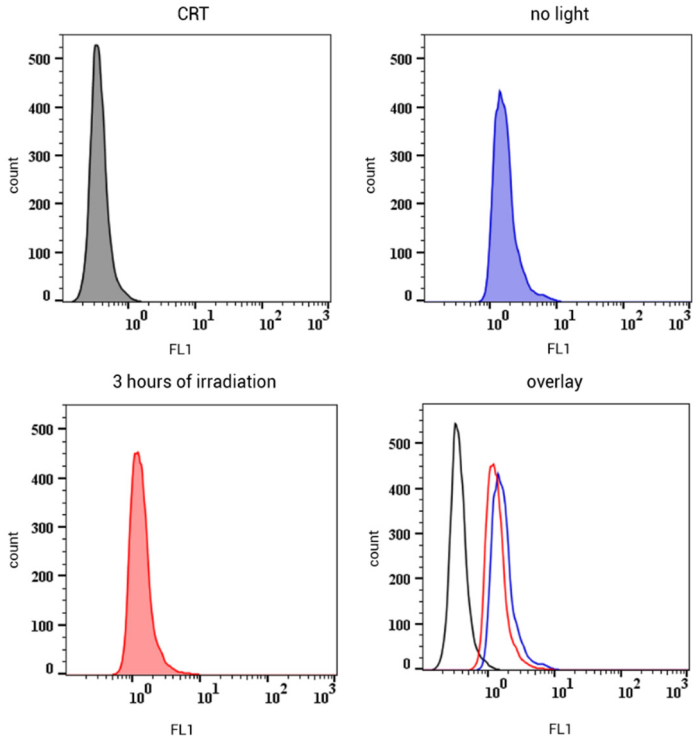

*Figure 101: Flow cytometry (FL1 signal) applied to detect in-cell fluorescence in A549 treated with **121**.*

10 Bimetallic anticancer-drugs

Up to now, the research of new metal based anticancer drugs alternative to cisplatin has been centred mostly on monometallic complexes. Since the metal is often the core centre of the antineoplastic action, the use of bimetallic complexes could be an interesting approach to improve the performance of this class of drugs. In these last few years some examples of bimetallic complexes have been tested as potential anticancer agents successfully[160,161,162]. Among these examples, there were also some dimeric TSs of copper, zinc or iron[163,164]. Most of these examples were homo-dinuclear complexes, however the presence of two (or more) metals in a single molecule seems to induce extremely interesting properties. The hetero-nuclear compounds can be active simultaneously in different biological targets using two or more metals in a single molecule. Very fascinating examples, were the Pt(IV)/Ru(II) complexes synthesised by Ma and co-workers in 2016. They designed and tested a series of complexes (called *ruthplatins*, *Figure 102* - A) in which the synergic action of the two metals led to 2-orders of magnitude enhanced cytotoxicity in cisplatin-resistant cells and strong inhibition of metastasis diffusion.

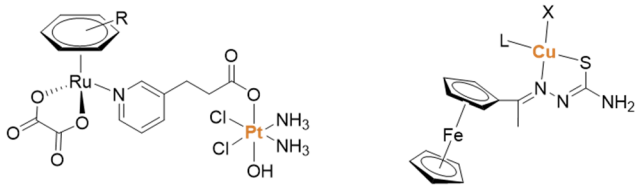

A. Ruthplatin 4 **B**. Ferrocene TS with Cu(II)

Figure 102

Very few hetero-bimetallic thiosemicarbazones have been studied. As an example, a paper reported the synthesis and spectroscopic characterisation of a thiosemicarbazone of monoacetylferrocene used as chelating agents for Cu(II) halides (*Figure 102* - B)[165]. Unfortunately, the authors did not evaluate the biological properties or possible medical application of the complexes, even if they were in principle very

good candidates. To our knowledge, no hetero-dinuclear thiosemicarbazones have been tested as anticancer agents yet.

10.1 Complex **125** as a chelating agent for copper and nickel ions

In *Chapter 7* we described the ability of the quinoline-TC **100** to chelate copper ions to create **105**, a cytotoxic complex. **105** was tested on A549 and HeLa cells and it induced apoptosis in HeLa cells. Furthermore, we described the ability of **105** to inhibit topoisomerase IIA and a docking study speculated about the interaction between the complex and the protein. Thanks to these interesting background, we used **100** to synthesise the photolabile Ru(II) half-sandwich **125** (*Figure 103*).

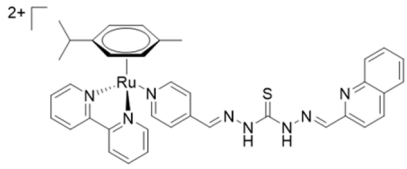

125

Figure 103

Since **125** contains the TC function not involved in any coordination, we explored its ability to chelate copper and nickel ions in order to obtain new hetero-dinuclear complexes (*Figure 104*- top). We studied the formation of the complexes through a UV-vis titration of a **125** solution with known portions of metal salts ($CuCl_2$ and $NiCl_2$) in DMSO.

The titration was made in a quartz cuvette filled with 600 µL of a 4.85 µM solution of **125** in which one equivalent of the desired metal salt was added in five portions (0.2 eq. each). We used metal salt solutions more than three orders of magnitude more concentrated than **125** to avoid dilution interferences ([$CuCl_2$] = [$NiCl_2$] = 2.92 mM). The UV-vis spectra were recorded after every addition, but it was extremely important to wait for the end of the complexation before recording the spectrum. This precaution

was necessary because during the first attempts we noticed that the spectra we registered immediately after the metal addition were time-dependent and non-reproducible. We estimated the proper time to wait by measuring the time necessary to stabilise the UV-vis profile after a metal salt addition. It resulted 7 and 30 minutes for copper and nickel, respectively. In addition, we registered the absorption spectra of the 4.85 μM solutions of the metal salts to verify that they would not have any absorption band which could interfere with the titration experiment. The result of the two titrations are reported below (*Figure 104* - bottom):

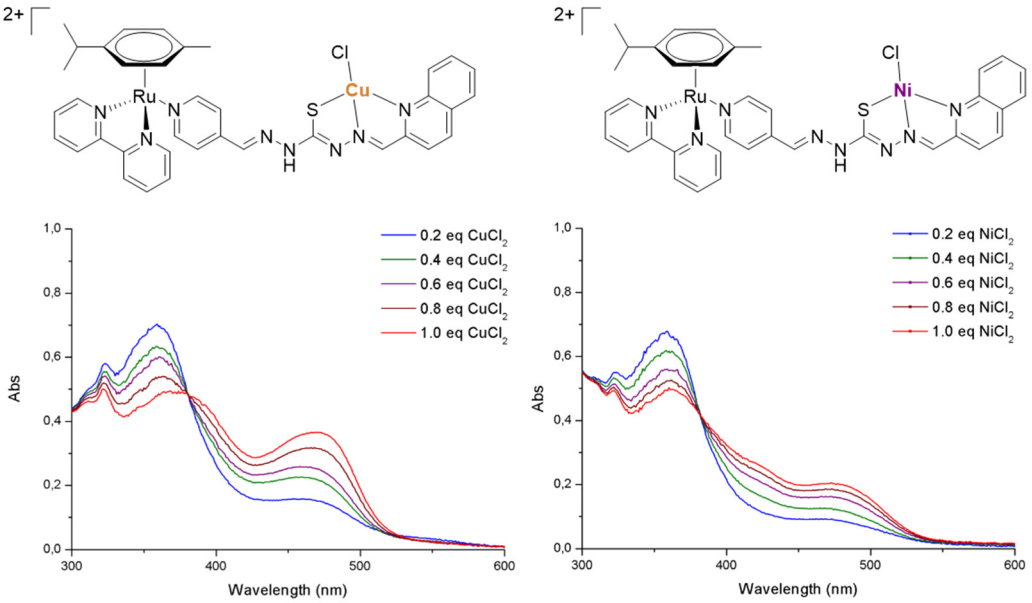

*Figure 104: UV-vis titrations of **125** with copper(II) chloride (left) and nickel(II) chloride (right).*

The two titrations showed a very similar result: the gradual formation of an absorption band between 450 and 500 nm associated with the decrease of the absorption bands below 380 nm. In both cases, these changes created an isosbestic point which clearly indicated that the initial species (**125**) gradually converted in another single species (the hetero-dinuclear complex with copper or nickel, respectively).

To prove that metals were κ^3-coordinated by the quinoline-TS moiety we performed a titration using **100** instead of **125**. **100** can interact with metals just as an S,N,N-tridentate ligand. Therefore, the use of **100** is very useful to simplify the system and to

collect information on the "quinolineTS + metal" system and the wavelengths associated with the complex formation. The results of this second titration are reported in *Figure 105*.

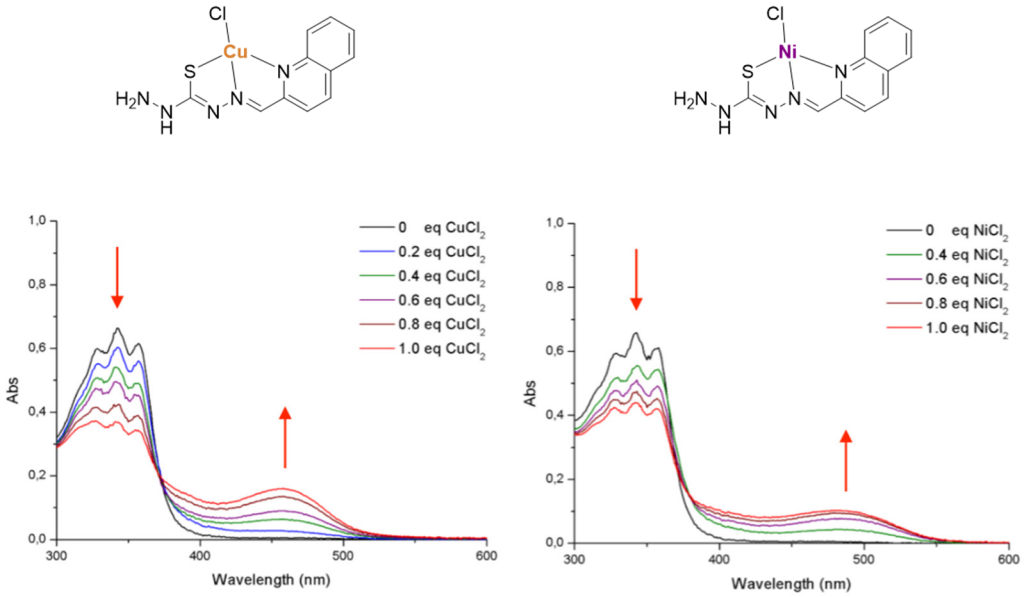

*Figure 105: UV-vis titrations of **100** with copper(II) chloride (left) and nickel(II) chloride (right).*

Even in these spectra the addition of both metals led to the formation of isosbestic points. This evidence confirmed once again that the species involved are linearly related by a stoichiometry process which, in this case, we could certainly assume was the formation of the complexes between **100** and Cu(II) or Ni(II) . If we now compare the absorption profiles of the **100** and **125** bands created after the metal ion addition, they are identical and centred in the same wavelength interval. After all these observations we have no reasons to doubt that Ni(II) and Cu(II) are coordinated in the same way in the two systems and then that 125 can creates hetero-dinuclear complexes.

10.1.1 Cytotoxicity of **125** mixed with copper(II) and nickel(II) chlorides

To test if **125** can increase the uptake of copper and nickel chlorides in cells through the formation of the above mentioned hetero-dinuclear complexes, we decided to compare the IC_{50} values of **125**, $NiCl_2$, $CuCl_2$ with those obtained from the administration of a 1 : 1 mixture of **125** with $NiCl_2$ and $CuCl_2$. The results are reported in *Table 35* and show a strong raise of the cytotoxicity passing from the free components to the mixtures. However, the IC_{50} values are affected by uncertainty because the mixtures coloured the medium and this affected the colorimetric quantification of MTT. To remedy to this setback, we show the pictures of cell treated with the two mixtures (Figure 106). They clearly show that cells suffered for the treatment with mixtures because they changed morphology, becoming more spherical and less attached to the flask an unequivocal signal of cell damage. In addition, for cells treated with the mixture **125** + $NiCl_2$ was visible also a change in the colour of cells that clearly indicated the internalization of the compound.

IC_{50} (μM) A549 24 hour				
125	$CuCl_2$	**125** + $CuCl_2$	$NiCl_2$	**125** + $NiCl_2$
84.62 ± 3.90	>100	~ 20	>100	~ 10

*Table 35: IC_{50} values determined for A549 cells treated with **125** mixed with copper(II) and nickel(II) chlorides.*

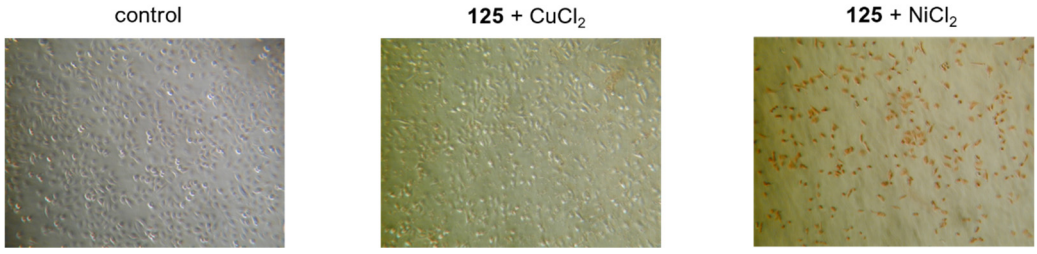

*Figure 106: Pictures of A549 cells untreated and treated with **125** mixed with copper(II) and nickel(II) chlorides.*

These interesting, even if preliminary, results confirmed that the creation of hetero-dinuclear metal complexes is an extremely fascinating field to explore and that it could be, in the future, a very effective way to raise and optimise absorption and selectivity of metal-based drugs.

11 Topic 2 conclusions

In the second part of the thesis I described the scientific approach we applied to develop new metal-based drugs for anticancer purposes. We used TSs as chelating agents for copper and nickel ions to explore the anticancer properties of these two micronutrient elements as an alternative to the widely studied and extremely toxic heavy metals, like platinum and gold. Initially, we designed our TS ligands in order to obtain three different types of chelating agents. We started from a panel of bi-dentate TSs we used as anionic ligands to obtain neutral complexes of Cu(II) and Ni(II) with a metal to ligand ratio of 1 : 2. We tested them on U937 cells (a leukemic cell line) and we found as best candidate the citral-TS copper(II) complex (**69**) (IC_{50} of 2.58 μM). Subsequently, we modified the TS portion of our compounds raising their lipophilicity to evaluate the effect of this parameter onto the cytotoxicity. We noticed that replacing the terminal -NH_2 with a -$NH(CH_3)$ group the activity did not change significantly, whereas using a -$NH(C_6H_5)$ the products became insoluble in water + 2% DMSO mixtures. Then, we moved on to the study of some tridentate-TS and the corresponding metal complexes with metal to ligand ratio 1 : 1. We obtained promising results on HeLa cells with the two copper(II) complexes of quinoline-2-carboxaldehyde-TS (**90**) and 5-fluoroisatin-TS (**91**) (IC_{50} 8.76 and 11.38 μM, respectively). As last type of chelating agents we designed three different tetradentate-TSs. Two of them (the derivatives of the 2,3-butanedione **95** and **96**) were studied in-depth on U937 and A549 cells and we found that these compounds can induce cell death with two different mechanisms depending on the cell line: U937 apoptosis and A549 autophagy.

The last part of the topic concerned the possibility of using our most effective compounds as ligands for Ru(II) half-sandwich moieties to obtain bi-functional drugs with higher biological activity. We chose to use the Ru(II)-arene structure to exploit its great ability to act as a carrier for active molecules. In fact, this kind of organometallic structure can selectively release ligands after a proper light irradiation. To bind our TSs with Ru(II), we decided to synthesise the corresponding mono-TCs and to use their free -NH_2 in a condensation with a carbonyl group placed in the Ru(II) moiety. All the mono-TCs we obtained were compared in terms of cytotoxicity with the corresponding TSs

and we found that tridentate compounds were those that better maintained the biological activity. In particular, we used quinoline-2-carboxaldehyde-TC (**100**) as TC in the synthesis of the Ru(II)-TC complex **125**. Finally, the photoactivation mechanism of **125** (and of some other Ru(II)-TS and Ru(II)-NDI complexes) was analysed in-depth and then tested on cells. Two derivatives (**121** and **125**) showed a significant increase of their cytotoxicity after light irradiation indicating that they are very promising to become new photodynamic therapy agents. All the data and results we collected in this context are encouraging and extremely useful to widen our knowledge in the field and to open up new pathways to innovative strategies to fight cancer, possibly allowing us to overcome the limits of conventional treatments.

12 Anticancer agents: experimental section

12.1 Chemical procedures

12.1.1 Bidentate derivatives

General synthetic approach for the synthesis of the κ^2-TS

The desired thiosemicarbazones were obtained by mixing an equimolar amount of the desired thiosemicarbazide with the proper aldehyde in absolute ethanol. The mixture was refluxed under stirring for 8 hours and left overnight at 0°C. The precipitate was filtered out, washed with cold ethanol and dried under *vacuum.*

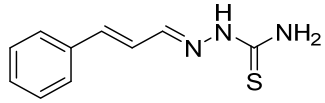

(*E*)-cinnamaldehydethiosemicarbazone (7): see the *Anti-aflatoxigenic agents: experimental* section.

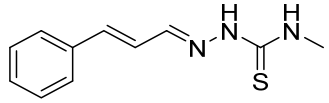

(*E*)-cinnamaldehyde-4-methyl-3-thiosemicarbazone (**56**): 4-methyl-3-thiosemicarbazide (0.50 g, 4.8 mmol), (*E*)-cinnamaldehyde (0.62 g, 4.8 mmol). Light yellow powder. Yield: 94%. FT-IR (cm^{-1}): 1549 (s), 976 (m). ^{1}H-NMR (δ, ppm; DMSO-d^6): 2.98 (d, *J* = 4.6 Hz, 3H), 6.86 (dd, *J* = 16.1 Hz, *J'* = 9.2 Hz, 1H), 7.33 (t, *J* = 7.3, 1H), 7.40 (t, *J* = 7.4 Hz, 2H), 7.55 (d, *J* = 7.2 Hz, 2H), 7.90 (d, *J* = 9.2 Hz, 1H), 8.28 (d, *J* = 4.6 Hz, 1H), 11.44 (s, 1H). ESI-MS (+) m/z calc. 220.08 found 220.17.

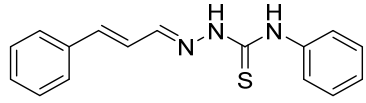

(*E*)-cinnamaldehyde-4-phenyl-3-thiosemicarbazone (57): 4-phenyl-3-thiosemicarbazide (0.10 g, 0.6 mmol), (*E*)-cinnamaldehyde (0.08 g, 0.6 mmol). Light

yellow powder. Yield: 52%. FT-IR (cm^{-1}): 995 (m). ^{1}H-NMR (δ, ppm; DMSO-d^6): 6.99 (dd, *J* = 16.2 Hz, *J'* = 9.0 Hz, 1H), 7.10 (d, *J* = 16.2 Hz, 1H), 7.18 (t, *J* = 7.3, 1H), 7.34 (m, 3H), 7.41 (t, *J* = 7.3 Hz, 2H), 7.59 (d, *J* = 7.5 Hz, 2H), 7.64 (d, *J* = 7.6 Hz, 2H), 8.01 (d, *J* = 9.0 Hz, 1H), 9.90 (s, 1H), 11.78 (s, 1H). ESI-MS (+) m/z calc. 282.38 found 282.16.

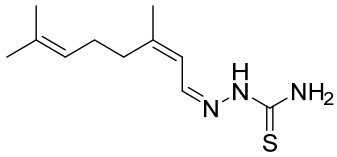

Citralthiosemicarbazone (58): thiosemicarbazide (0.10 g, 1.1 mmol), citral (0.17 g, 1.1 mmol). Pale brown powder. Yield: 96%. FT-IR (cm^{-1}): 1537 (s), 1097 (m). ^{1}H-NMR (δ, ppm; DMSO-d^6): 1.58 (s, 3H), 1.65 (s, 3H), 1.82 (t, *J* = 0.9, 2H), 1.86 (d, *J* = 0.9 Hz, 1H), 2.13 (s, 3H), 2.21 (m, 1H), 5.08 (s, 1H), 5.87 (s, *J* = 9.8 Hz, 1H), 7.47 (m, 1H), 8.05 (m, 2H), 11.05 (s, 1H). ESI-MS (+) m/z calc. 226.13 found 226.11.

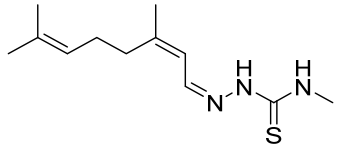

Citral-4-methyl-3-thiosemicarbazone (59): 4-methyl-3-thiosemicarbazide (0.10 g, 1.0 mmol), citral (0.15 g, 1.0 mmol). Light yellow powder. Yield: 88%. FT-IR (cm^{-1}): 1539 (s), 941 (m). ^{1}H-NMR (δ, ppm; DMSO-d^6): 1.58 (s, 3H), 1.65 (s, 3H), 1.81 (s, 2H), 1.86 (s, 1H), 2.14 (s, 3H), 2.21 (m, 1H), 2.94 (d, *J* = 4.6 Hz, 3H), 5.08 (s, 1H), 5.88 (s, *J* = 9.4 Hz, 1H), 8.05 (dd, *J* = 9.4 Hz, *J* = 6.3 Hz, 1H), 8.14 (m, 1H), 11.08 (s, 1H). ESI-MS (+) m/z calc. 240.38 found 240.21.

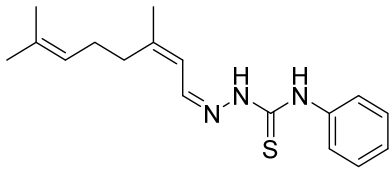

Citral-4-phenyl-3-thiosemicarbazone (60): 4-phenyl-3-thiosemicarbazide (0.10 g, 0.6 mmol), citral (0.09 g, 0.6 mmol). Brown powder. Yield: 95%. FT-IR (cm^{-1}): 1536 (s), 935 (m). ^{1}H-NMR (δ, ppm; DMSO-d^6): 1.59 (s, 3H), 1.66 (s, 3H), 1.86 (s, 3H), 2.17 (m, 4H),

5.11 (sb, 1H), 6.00 (d, *J* = 9.8 Hz, 1H), 7.16 (t, *J* = 7.4 Hz, 1H), 7.33 (t, *J* = 7.9 Hz, 2H), 7.61 (d, *J* = 8.4 Hz, 2H), 8.17 (dd, *J* = 9.8 Hz, *J* = 7.4 Hz, 1H), 9.76 (sb, 1H), 11.43 (s, 1H). ESI-MS (+) m/z calc. 302.45 found 302.24.

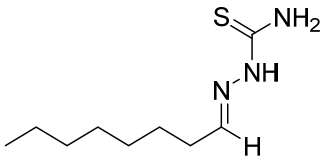

Octanalthiosemicarbazone (43): see the *Anti-aflatoxigenic agents: experimental section.*

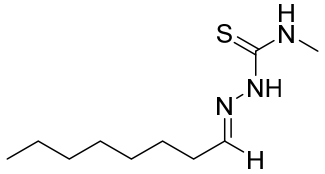

Octanal-4-methyl-3-thiosemicarbazone (61): 4-methyl-3-thiosemicarbazide (0.20 g, 1.9 mmol), octanal (0.25 g, 1.9 mmol). White powder. Yield: 98%. FT-IR (cm^{-1}): 1536 (s), 973.08 (m). ^{1}H-NMR (δ, ppm; DMSO-d^{6}): 0.86 (sb, 3H), 1.27 (sb, 8H), 1.45 (sb, 2H), 2.18 (sb, 2H), 2.94 (s, 3H), 7.39 (s, 1H), 8.05 (s,1H), 11.02 (s, 1H). ESI-MS (+) m/z calc. 216.36 found 216.10.

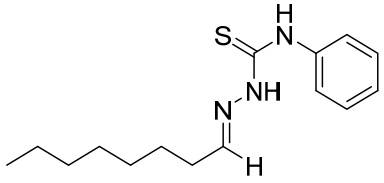

Octanal-4-phenyl-3-thiosemicarbazone (62): 4-phenyl-3-thiosemicarbazide (0.20 g, 1.2 mmol), octanal (0.15 g, 1.2 mmol). Yellow powder. Yield: 97%. FT-IR (cm^{-1}): 1492 (s), 1008 (m). ^{1}H-NMR (δ, ppm; DMSO-d^{6}): 0.86 (sb, 3H), 1.20 (sb, 8H), 1.43 (m, 2H), 2.26 (m, 2H), 7.33 (t, *J* = 7.9 Hz, 1H), 7.41 (d, t, *J* = 8.3 Hz, 2H), 7.56 (t, *J* = 8.1 Hz, 2H), 9.70 (s, 1H), 11.44 (s, 1H), 13.68 (s, 1H). ESI-MS (+) m/z calc. 278.43 found 278.19.

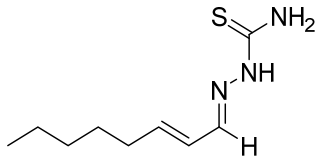

2-octenalthiosemicarbazone (44): see the *Anti-aflatoxigenic agents: experimental* section.

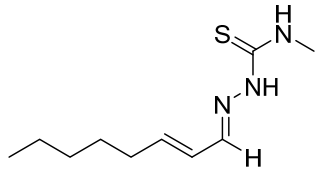

2-octenal-4-methyl-3-thiosemicarbazone (63): 4-methyl-3-thiosemicarbazide (0.31 g, 3.0 mmol), 2-octenal (0.38 g, 3.0 mmol). Orange powder. Yield: 95%. FT-IR (cm^{-1}): 1549 (s), 979 (m). ^{1}H-NMR (δ, ppm; DMSO-d^{6}): 0.87 (t, *J* = 6.9 Hz, 3H), 1.27 (m, 4H), 1.41 (m, 2H), 2.17 (dd, *J* = 13.2 Hz, *J'* = 7.1 Hz, 2H), 2.95 (d, *J* = 4.3 Hz, 3H), 6.13 (m, 2H), 7.70 (d, *J* = 8.2 Hz, 1H), 8.13 (d, *J* = 4.3 Hz, 1H), 11.15 (s, 1H). ESI-MS (+) m/z calc. 200.32 found 200.13.

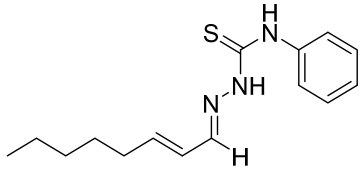

2-octenal-4-phenyl-3-thiosemicarbazone (64): 4-phenyl-3-thiosemicarbazide (0.10 g, 0.6 mmol), 2-octenal (0.08 g, 0.6 mmol). Brown oil. Yield: 92%. FT-IR (cm^{-1}): 1511 (s), 1036 (m). ^{1}H-NMR (δ, ppm; DMSO-d^{6}): 0.85 (t, *J* = 7.0 Hz, 3H), 1.29 (sb, 4H), 1.39 (m, 2H), 2.17 (sb, 2H), 6.24 (m, 2H), 7.28 (t, *J* = 7.9 Hz, 1H), 7.36 (d, *J* = 8.3 Hz, 2H), 7.54 (t, *J* = 8.1 Hz, 2H), 7.70 (d, *J* = 8.2 Hz, 1H), 8.13 (d, *J* = 4.3 Hz, 1H), 11.15 (s, 1H). ESI-MS (+) m/z calc. 276.45 found 276.20.

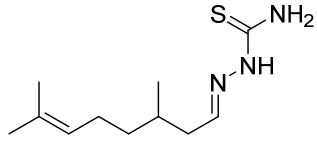

***S*-citronellalthiosemicarbazone (65):** thiosemicarbazide (0,18 g, 1.95 mmol), *S*-citronellal (0.30 g, 1.95 mmol). Transparent oil. Yield: 72%. FT-IR (cm^{-1}): 1592 (s),

1093(m), 822 (m). ^{1}H-NMR (δ, ppm; DMSO-d^{6}): 0.88 (d, *J* = 7.0 Hz, 3H), 1.15 (m, 1H), 1.29 (m, 1H), 1.56 (s, 3H), 1.64 (s, 3H), 1.69 (m, 1H), 1.91 (d, *J* = 7.0 Hz, 1H), 1.97 (m, 1H), 2.04 (m, 1H), 2.18 (m, 1H), 5.08 (dd, *J* = 7.8 Hz, *J*' = 6.5 Hz, 1H), 7.41 (t, *J* = 5.9 Hz, 2H), 7.98 (s, 1H), 11.03 (s, 1H). ESI-MS (+) m/z calc. 228.37 found 228.17.

General procedure to synthesise Ni(II) and Cu(II) complexes

The copper(II) and nickel(II) complexes were obtained by mixing the desired κ^{2}-TS ligand with copper(II) or nickel(II) acetate in ethanol. The reagents were dissolved separately in two portion of ethanol and then the solution containing the metal salt was slowly dripped into the ligand solution. The colour turned immediately from clear to dark. The mixture was stirred at room temperature for 2 hours and finally the solvent was removed under reduced pressure and the solid obtained washed twice with diethylether and dried under *vacuum*.

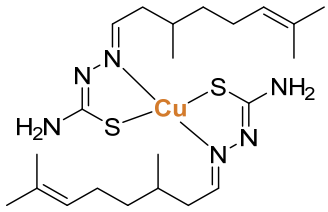

Bis(citronellalthiosemicarbazonato)Cu(II) (66): 64 (0.11 g, 0.48 mmol), copper(II) acetate (0.05 g, 0.24 mmol). Brown powder. Yield: 80%. FT-IR (cm^{-1}): 1626 (s), 963 (m). ESI-MS (+) m/z calc. 517.27 found 516.03.

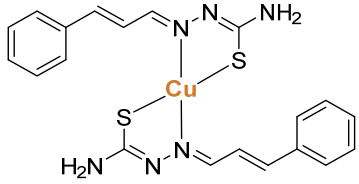

Bis[(*E*)cinnamaldehydethiosemicarbazonato]Cu(II) (12): see the *Anti-aflatoxigenic agents: experimental section*.

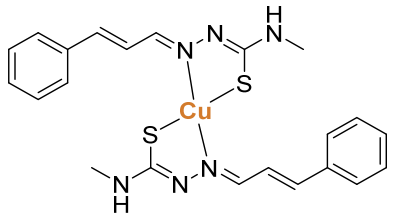

Bis[(*E*)-cinnamaldehyde-4-methyl-3-thiosemicarbazonato]Cu(II) (67): 56 (0.10 g, 0.45 mmol), copper(II) acetate (0.05 g, 0.22 mmol). Brown powder. Yield: 94%. FT-IR (cm^{-1}): 1491 (s), 937 (m). ESI-MS (+) m/z calc. 500.71 found 500.16.

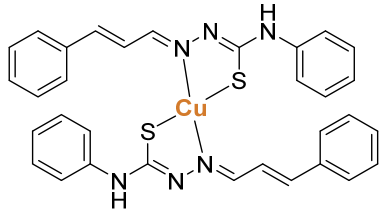

Bis[(*E*)-cinnamaldehyde-4-phenyl-3-thiosemicarbazonato]Cu(II) (68): 57 (0.04 g, 0.14 mmol), copper(II) acetate (0.02 g, 0.07 mmol). Brown solid. Yield: 86%. FT-IR (cm^{-1}): 1495 (s), 988 (m). ESI-MS (+) m/z calc. 625.30 found 626.04.

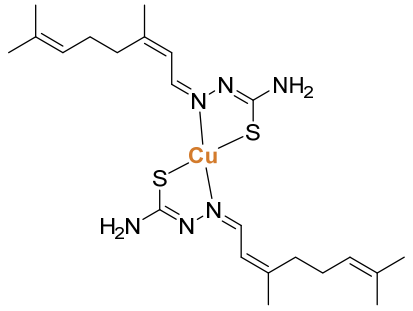

Bis(citralthiosemicarbazonato)Cu(II) (69): 58 (0.50 g, 0.20 mmol), copper(II) acetate (0.02 g, 0.10 mmol). Dark green powder. Yield: 86%. FT-IR (cm^{-1}): 1553 (s), 954 (m). ESI-MS (+) m/z calc. 513.25 found 512.87.

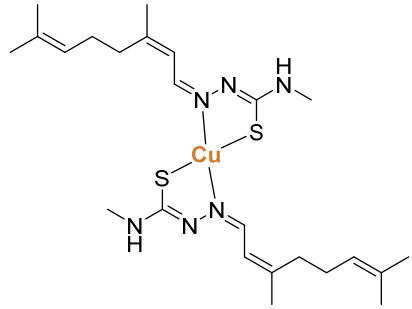

Bis(citral-4-methyl-3-thisemicarbazonato)Cu(II) (70): 59 (0.05 g, 0.20 mmol), copper(II) acetate (0.02 g, 0.10 mmol). Black powder. Yield: 89%. FT-IR (cm^{-1}): 1559 (s), 910 (m). ESI-MS (+) m/z calc. 541.29 found 541.65.

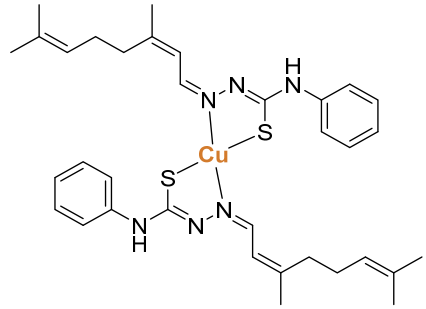

Bis(citral-4-phenyl-3-thisemicarbazonato)Cu(II) (71): 60 (0.07 g, 0.23 mmol), copper(II) acetate (0.02 g, 0.12 mmol). Dark red powder. Yield: 75%. FT-IR (cm^{-1}): 1495 (s), 824 (m). ESI-MS (+) m/z calc. 665.42 found 664.97.

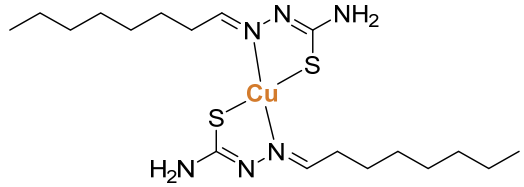

Bis(octanalthiosemicarbazonato)Cu(II) (51): see the *Anti-aflatoxigenic agents: experimental* section.

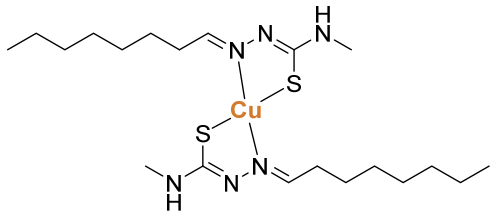

Bis(octanal-4-methyl-3-thiosemicarbazonato)Cu(II) (72): 61 (0.07 g, 0.34 mmol), copper(II) acetate (0.03 g, 0.17 mmol). Black powder. Yield: 91%. FT-IR (cm^{-1}): 1602 (s), 1012 (m). ESI-MS (+) m/z calc. 493.25 found 492.29.

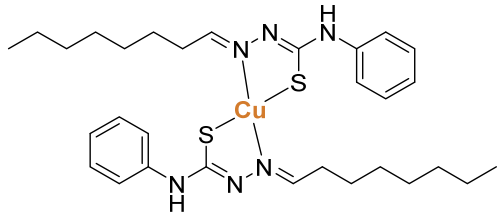

Bis(octanal-4-phenyl-3-thiosemicarbazonato)Cu(II) (73): 62 (0.10 g, 0.36 mmol), copper(II) acetate (0.04 g, 0.18 mmol). Brown powder. Yield: 87%. FT-IR (cm^{-1}): 1587 (s), 1019 (m). ESI-MS (+) m/z calc. 617.39 found 617.22.

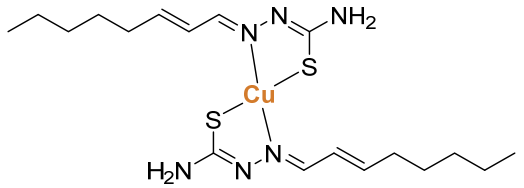

Bis(octenalthiosemicarbazonato)Cu(II) (52): *see the Anti-aflatoxigenic agents: experimental* section.

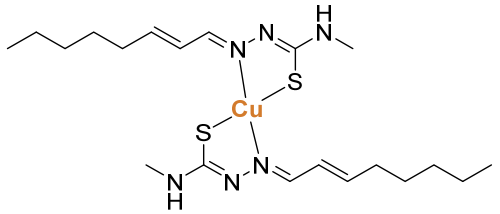

Bis(octenal-4-methyl-3-thiosemicarbazonato)Cu(II) (74): 63 (0.11 g, 0.51 mmol), copper(II) acetate (0.05 g, 0.25 mmol). Brown powder. Yield: 88%. FT-IR (cm^{-1}): 1551 (s), 939 (m). ESI-MS (+) m/z calc. 489.23 found 489.20.

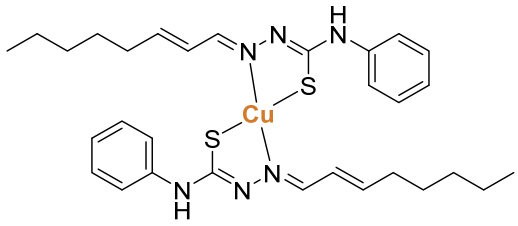

Bis(octenal-4-phenyl-3-thiosemicarbazonato)Cu(II) (75): 64 (0.11 g, 0.51 mmol), copper(II) acetate (0.05 g, 0.25 mmol). Brown powder. Yield: 88%. FT-IR (cm^{-1}): 1551 (s), 939 (m). ESI-MS (+) m/z calc. 489.23 found 489.20.

Nickel(II) complexes

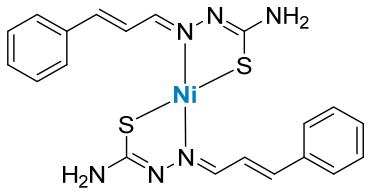

Bis[(*E*)-cinnamaldehydethiosemicarbazonato]Ni(II) (76): 7 (0.06 g, 0.28 mmol), nickel(II) acetate (0.03 g, 0.14 mmol). Green powder. Yield: 86%. FT-IR (cm^{-1}): 1632 (s), 933 (m). ^{1}H-NMR (δ, ppm; DMSO-d^{6}): 6.96 (s, 4H), 7.15 (m, 4H), 7.40 (m, 8H), 7.52 (m, 4H). ESI-MS (+) m/z calc. 468.23 found 467.11.

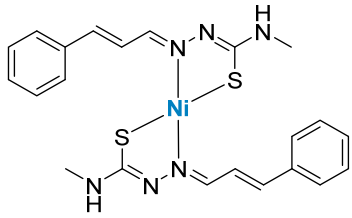

Bis[(*E*)-cinnamaldehyde-4-methyl-3-thiosemicarbazonato]Ni(II) (77): 56 (0.07 g, 0.30 mmol), nickel(II) acetate (0.04 g, 0.15 mmol). Brown powder. Yield: 75%. FT-IR (cm^{-1}): 1551 (s), 939 (m). ^{1}H-NMR (δ, ppm; DMSO-d^{6}): 2.87 (m, 6H), 6.95 (s, 4H), 7.19 (m, 4H), 7.45 (m, 6H), 7.52 (m, 4H). ESI-MS (+) m/z calc. 496.29 found 495.17.

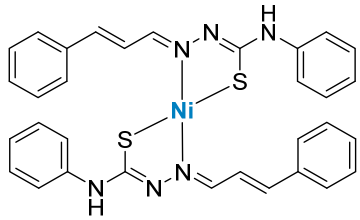

Bis[(*E*)-cinnamaldehyde-4-phenyl-3-thiosemicarbazonato]Ni(II) (78): 57 (0.10 g, 0.35 mmol), nickel(II) acetate (0.04 g, 0.17 mmol). Brown powder. Yield: 61%. FT-IR (cm^{-1}): 1005 (m), 978 (m). ^{1}H-NMR (δ, ppm; DMSO-d^{6}): 6.94 (sb, 2H), 7.10 (m, , 2H), 7.19 (t, *J* = 7.2, 2H), 7.35 (m, 6H), 7.41 (t, *J* = 7.2 Hz, 4H), 7.60 (d, *J* = 7.5 Hz, 4H), 7.66 (d, *J* = 7.6 Hz, 4H), 8.03 (sb, 2H), 9.94 (sb, 2H). ESI-MS (+) m/z calc. 620.43 found 620.39.

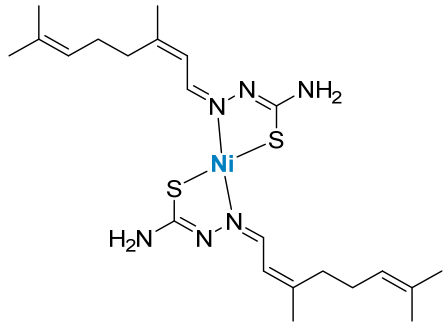

Bis(citralthiosemicarbazonato)Ni(II) (79): 58 (0.07 g, 0.31 mmol), nickel(II) acetate (0.03 g, 0.10 mmol). Dark green powder. Yield: 91%. FT-IR (cm^{-1}): 1518 (s), 874 (m). ^{1}H-NMR (δ, ppm; DMSO-d^{6}): 1.67 (m, 12H), 1.83 (s, 6H), 5.05 (s, 4H), 6.52 (m, 4H), 7.17 (m, 2H), 6.79 (m, 8H). ESI-MS (+) m/z calc. 508.39 found 507.54.

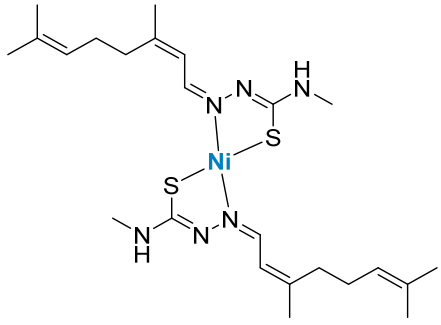

Bis(citral-4-methyl-3-thiosemicarbazonato)Ni(II) (80): 59 (0.07 g, 0.29 mmol), nickel(II) acetate (0.03 g, 0.15 mmol). Brown powder. Yield: 93%. FT-IR (cm^{-1}): 1519 (s),

864 (m). ^{1}H-NMR (δ, ppm; DMSO-d^{6}): 1.62 (m, 16H), 1.12 (m, 6H), 2.18 (m, 4H), 2.69 (m, 6H), 5.05 (s, 2H), 6.59 (m, 2H), 7.19 (m, 4H). ESI-MS (+) m/z calc. 535.97 found 536.35.

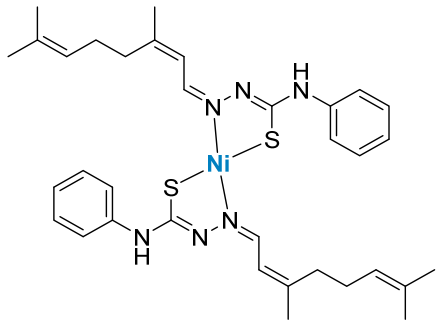

Bis(citral-4-phenyl-3-thiosemicarbazonato)Ni(II) (81): 60 (0.07 g, 0.23 mmol), nickel(II) acetate (0.03 g, 0.11 mmol). Brown powder. Yield: 79%. FT-IR (cm^{-1}): 1531 (s), 853 (m). ^{1}H-NMR (δ, ppm; DMSO-d^{6}): 1.58 (s, 6H), 1.64 (s, 6H), 1.12 (s, 6H), 2.20 (bs, 8H), 5.10 (s, 2H), 6.64 (bs, 2H), 6.95 (m, 2H), 7.24 (m, 4H), 7.57 (bs, 6H), 9.66 (s, 2H). ESI-MS (+) m/z calc. 660.68 found 659.97.

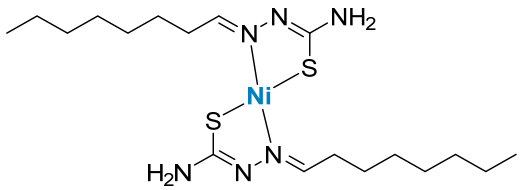

Bis(octanalthiosemicarbazonato)Ni(II) (82): 43 (0.07 g, 0.36 mmol), nickel(II) acetate (0.04 g, 0.18 mmol). Light brown powder. Yield: 82%. %. FT-IR (cm^{-1}): 1456 (s), 938 (m). ^{1}H-NMR (δ, ppm; DMSO-d^{6}): 0.91 (sb, 6H), 1.20 (m, 16H), 1.40 (m, 4H), 2.21 (m, 4H), 7.44 (m, 2H), 7.75 (m, 2H), 8.18 (sb, 2H). ESI-MS (+) m/z calc. 488.39 found 487.98.

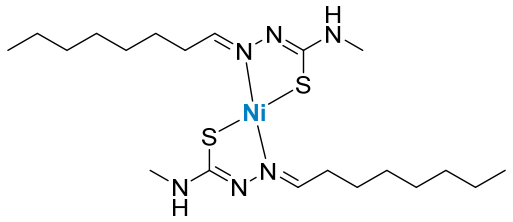

Bis(octanal-4-methyl-3-thiosemicarbazonato)Ni(II) (83): 61 (0.06 g, 0.30 mmol), nickel(II) acetate (0.04 g, 0.15 mmol). Brown powder. Yield: 79%. FT-IR (cm^{-1}): 1551 (s),

939 (m). ^{1}H-NMR (δ, ppm; DMSO-d^{6}): 0.91 (sb, 6H), 1.20 (m, 16H), 1.40 (m, 4H), 2.21 (m, 4H), 3.08 (m, 6H), 7.44 (m, 2H), 8.18 (sb, 2H). ESI-MS (+) m/z calc. 488.39 found 487.98.

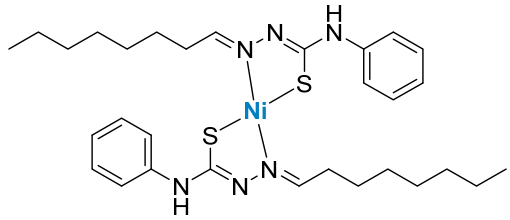

Bis(octanal-4-phenyl-3-thiosemicarbazonato)Ni(II) (84): 62 (0.10 g, 0.36 mmol), nickel(II) acetate (0.04 g, 0.18 mmol). Dark green powder. Yield: 81%. FT-IR (cm^{-1}): 1545 (s), 953 (m). ^{1}H-NMR (δ, ppm; DMSO-d^{6}): 0.85 (sb, 6H), 1.25 (sb, 16H), 1.44 (m, 4H), 2.25 (m, 4H), 7.32 (t, *J* = 8.0 Hz, 2H), 7.40 (d, *J* = 8.2 Hz, 4H), 7.57 (t, *J* = 8.2 Hz, 4H), 9.72 (s, 2H), 11.47 (s, 2H). ESI-MS (+) m/z calc. 612.54 found 612.17.

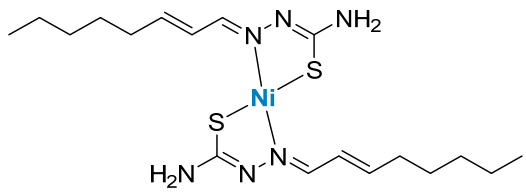

Bis(octenalthiosemicarbazonato)Ni(II) (85): 44 (0,13 g, 0.65 mmol), nickel(II) acetate (0.08 g, 0.32 mmol). Dark green solid. Yield: 86%. FT-IR (cm^{-1}): 1441 (s), 944 (m). ^{1}H-NMR (δ, ppm; DMSO-d^{6}): 0.86 (m, 6H), 1.24 (m, 8H), 1.38 (m, 4H), 2.15 (m, 4H), 6.29 (m, 2H), 6.71 (m, 6H), 6.95 (m, 2H). ESI-MS (+) m/z calc. 455.91 found 455.34.

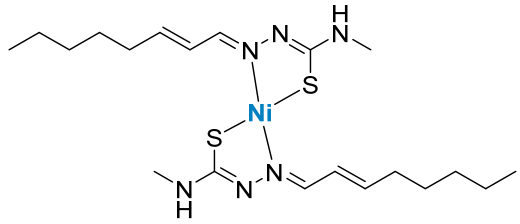

Bis(octenal-4-methyl-3-thiosemicarbazonato)Ni(II) (86): 63 (0.13 g, 0.59 mmol), nickel(II) acetate (0.07 g, 0.30 mmol). Dark brown powder. Yield: 79%. FT-IR (cm^{-1}): 1550 (s), 945 (m). ^{1}H-NMR (δ, ppm; DMSO-d^{6}): 0.88 (m, 6H), 1.26 (m, 8H), 1.38 (m, 4H), 2.15 (m, 4H), 3.51 (sb, 6H), 6.33 (m, 2H), 6.52 (m, 2H), 6.73 (m, 2H), 7.02 (m, 2H). ESI-MS (+) m/z calc. 483.93 found 483.26.

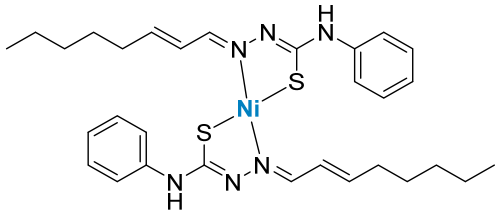

Bis(octenal-4-phenyl-3-thiosemicarbazonato)Ni(II) (87): 64 (0.10 g, 0.36 mmol), nickel(II) acetate (0.05 g, 0.18 mmol). Brown powder. Yield: 77%. FT-IR (cm^{-1}): 1560 (s), 957 (m). ^{1}H-NMR (δ, ppm; DMSO-d^{6}): 0.85 (t, *J* = 7.1 Hz, 6H), 1.30 (sb, 8H), 1.41 (m, 4H), 2.18 (sb, 4H), 6.24 (m, 4H), 7.30 (t, *J* = 8.0 Hz, 2H), 7.36 (d, *J* = 8.0 Hz, 4H), 7.50 (m, 4H), 7.71 (d, *J* = 8.0 Hz, 2H), 8.11 (d, *J* = 4.0 Hz, 2H). ESI-MS (+) m/z calc. 608.51 found 608.20.

12.1.2 Tridentate derivatives

General synthetic approach applied for the synthesis of the κ^{3}-TS

The desired thiosemicarbazones were obtained by mixing an equimolar amount of thiosemicarbazide with the proper aldehyde in methanol. The mixture was refluxed and stirred overnight, then the mixture was cooled at room temperature to precipitate the product. It was filtered, washed with cold ethanol and dried under *vacuum.*

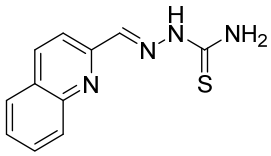

Quinoline-2-carboxaldehydethiosemicarbazone (88): thiosemicarbazide (0.10 g, 1.10 mmol), quinoline-2-carboxaldehyde (0.17 g, 1.10 mmol). Pale yellow powder. Yield: 53%. FT-IR (cm^{-1}): 1606 (s), 1110 (m), 838 (m). ^{1}H-NMR (δ, ppm; DMSO-d^{6}): 7.63 (t, *J* = 6.9 Hz, 1H), 7.78 (t, *J* = 7.1 Hz, 1H), 8.00 (m, 2H), 8.24 (s, 1H), 8.33 (s, 1H), 8.37 (d, *J* = 8.7 Hz, 1H), 8.44 (s, 1H), 8.46 (m, *J* = 8.7 Hz, 1H), 11.80 ppm (1H, s). ESI-MS (+) m/z calc. 231.39 found 231.09.

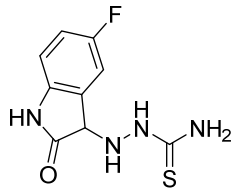

5-Fluoroisatinthiosemicarbazone (89): thiosemicarbazide (0.10 g, 1.10 mmol), 5-Fluoroisatin (0.18 g, 1.10 mmol). Orange powder. Yield: 83%. FT-IR (cm^{-1}): 1682 (s), 1619 (s), 1132 (m), 820 (m). ^{1}H-NMR (δ, ppm; DMSO-d^{6}): 6.93 (dd, *J* = 8.6 Hz, *J'* = 4.2 Hz, 1H), 7.19 (m, 1H), 7.51 (dd, *J* = 8.1 Hz, *J'* = 2.7 Hz, 1H), 8.76 (s, 1H), 9.12 (s, 1H), 11.20 (s, 1H), 12.36 (s, 1H). ESI-MS (+) m/z calc. 241.26 found 240.51.

Copper(II) complexes

The copper(II) complexes were obtained by mixing an equimolar amount of the desired κ^{3}-TS ligand with copper(II) acetate in methanol. The reagents were dissolved separately in two portion of methanol and then the solution containing the copper(II) salt was slowly dripped into the ligand solution. The colour turned immediately from clear to dark. The mixture was stirred at room temperature for 3 hours and finally the solvent was removed under reduced pressure and the solid obtained washed twice with diethylether and dried under *vacuum*.

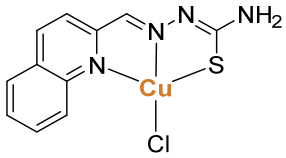

(Quinoline-2-carboxaldehydethiosemicarbazonato)Cu(II) chloride (90): 88 (0.05 g, 0.22 mmol), copper(II) chloride (0.04 g, 0.22 mmol). Dark green powder. Yield: 95%. FT-IR (cm^{-1}): 1618 (s), 1071 (m), 842 (m). ESI-MS (+) m/z $[M\text{-}Cl^{-}]^{+}$ calc. 292.83 found 292.29.

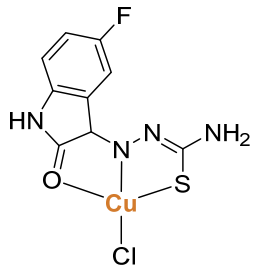

(5-Fluoroisatinthiosemicarbazonato)Cu(II) chloride (91): 89 (0.04 g, 0.17 mmol), copper(II) chloride (0.03 g, 0.17 mmol). Brown powder. Yield: 46%. FT-IR (cm^{-1}): 1658 (s), 1622 (m), 822 (m). ESI-MS (+) m/z $[M\text{-}Cl^-]^+$ calc. 301.78 found 301.30.

12.1.3 Tetradentate derivatives

General synthetic approach applied for the synthesis of tetradentate 2,3-butanedione derivatives

The desired 2,3-butanedione derivatives were obtained by mixing it with the proper thiosemicarbazide in ethanol. The mixture was refluxed and stirred until it turned from yellow to red (6 hours). Then, the mixture was transferred into a crystallizer and the product was isolated after the slow evaporation of the solvent.

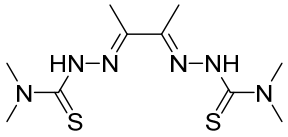

2,3-butanedione-bis-4,4-dimethyl-3-thiosemicarbazone (92): 4,4-dimethyl-3-thiosemicarbazide (0.20 g, 1.68 mmol), 2,3-butanedione (0.07 g, 0.84 mmol). Dark red powder. Yield: 83%. FT-IR (cm^{-1}): 3293 (m), 2926 (m), 1671 (s), 1536 (m), 927 (w). ^{1}H-NMR (δ, ppm; DMSO-d^6): 1.96 (s, 3H), 2.14 (s, 3H), 2.33 (s, 3H), 3.10 (s, 3H), 3.33 (s, 6H), 9.54 (s, 2H). ESI-MS (+) m/z calc. 289.43 found 289.09. E.A.% calc. (found): C 41.64 (41.15), H 6.99 (7.06), N 29.14 (29.34), S 22.23 (23.17).

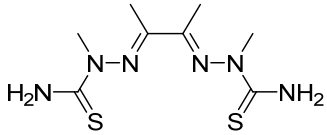

2,3-butanedione-bis-2-methyl-3-thiosemicarbazone (93): 2-methyl-3-thiosemicarbazide (0.20 g, 1.90 mmol), 2,3-butanedione (0.08 g, 0.95 mmol). Brown powder. Yield: 86%. FT-IR (cm^{-1}): 3400 (m), 3276 (m), 2925 (m), 1616 (s), 1571 (m), 935 (w). ^{1}H-NMR (δ, ppm; DMSO-d^{6}): 3.42 (s, 6H), 3.93 (s, 6H), 7.31 (s, 4H). ESI-MS (+) m/z calc. 261.38 found 261.69. E.A.% calc. (found): C 36.90 (37.05), H 6.19 (6.23), N 32.28 (32.18), S 24.63 (24.55).

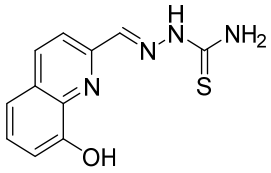

8-Hydroxy-2-quinolinecarboxaldehydethiosemicarbazone (94): The thiosemicarbazide (0.10 mg, 1.10 mmol) was dissolved in 30 mL of absolute ethanol at 60°C. Subsequently, an equimolar amount of 8-Hydroxy-2-quinolinecarboxaldehyde (0.19, 1.10 mmol), previously dissolved in 10 mL of absolute ethanol, was dripped in the thiosemicarbazide solution. The mixture was refluxed for 2 hours and the product precipitate as an orange solid during the reaction. It was collected by filtration, washed twice with diethylether and dried under *vacuum*. Orange powder. Yield: 85%. FT-IR (cm^{-1}): 1597 (s), 1083 (s), 840 (m). ^{1}H-NMR (δ, ppm; DMSO-d^{6}): 7.10 (dd, *J* = 7.4 Hz, *J'* = 1.4, 1H), 7.42 (m, 2H), 8.28 (m, 2H), 8.31 (s, 1H), 8.41 (s, 1H), 8.43 (d, *J* = 8.6 Hz, 1H), 9.84 (s, 1H), 11.85 (s, 1H). ESI-MS (+) m/z calc. 247.29 found 247.18.

Copper(II) complexes

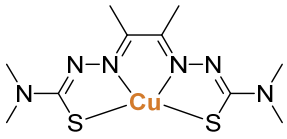

[2,3-butanedione-bis(4,4-dimethyl-3-thiosemicarbazato)]Cu(II) (95): 92 (0.21 g, 0.71 mmol) was dissolved in 40 mL of ethanol 95% under stirring. Copper(II) chloride (0.12

g, 0.71 mmol) was dissolved in 20 mL of ethanol 95% under stirring and was slowly added to the ligand solution. The resulting mixture was kept under stirring for 30 min and turned dark red-brown. It was then transferred to a crystallizer and left evaporating slowly at room temperature. The isolated solid brown product was recrystallized from a EtOH / H_2O 2 : 1 solution and characterized. Dark brown powder. Yield: 83%. FT-IR (cm^{-1}): 1634 (s), 1526 (w). ESI-MS (+) m/z calc. 350.97 found 351.17.

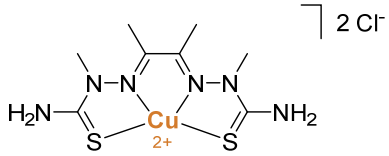

[2,3-Butanedione-bis(2-methyl-3-thiosemicarbazato)]Cu(II) di-chloride (96): 93 (0.14 g, 0.53 mmol) was dissolved in 50 mL of ethanol 95% under stirring. Copper(II) (0.02 g, 0.53 mmol) was dissolved in 20 mL of ethanol 95% under stirring and was slowly added to the ligand solution. The resulting mixture was kept under stirring for 1 hour at room temperature and turned dark red. Then it was transferred to a crystallizer and left to evaporate slowly. The powder obtained was then collected and characterized. Dark red powder. Yield 98%. FT-IR (cm^{-1}): 1606 (s), 1565 (m), 927 (w). ESI-MS (+) m/z calc. 323.93 found 324.89.

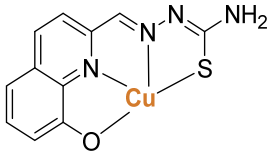

(8-Hydroxy-2-quinolinecarboxaldehydethiosemicarbazonato)Cu(II) (97): 94 (0.05 g, 0.20 mmol) was dissolved in 30 mL of ethanol 95% under stirring. Copper(II) (0.04 g, 0.20 mmol) was dissolved in 10 mL of ethanol 95% under stirring and was slowly added to the ligand solution. The resulting mixture was kept under stirring for 3 hours at room temperature and turned brown. Then the solvent was removed under reduced pressure and the solid dried under *vacuum*. Dark brown powder. Yield 87%. FT-IR (cm^{-1}): 1603 (s), 1110 (m), 839 (m). ESI-MS (+) m/z calc. 308.82 found 308.31.

12.1.4 Thiocarbohydrazones

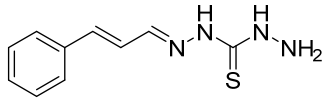

Cinnamaldehydemonothiocarbohydrazone (98): thiocarbohydrazide (0.10 g, 0.94 mmol) was dissolved in 30 mL of absolute ethanol at 60°C, then 0.5 mL of acetic acid were added. At the same time, the (*E*)-cinnamaldehyde (0.12 g, 0.94 mmol) was dissolved in 5 mL of absolute ethanol and it was dripped slowly in the thiocarbohydrazide solution. The solution turned immediately from colourless to yellow and clear. The mixture was refluxed and stirred for 15 minutes, cooled to room temperature and left at -4°C for 24 h. A solid appeared and it was collected by filtration, washed with hexane and dried under *vacuum*. White powder. Yield: 22%. FT-IR (cm^{-1}): 1622 (s), 1042 (s), 846 (m). ^{1}H-NMR (δ, ppm, 400 MHz, DMSO-d^6): 4.86 (s, 2H), 6.86 (dd, *J* = 16.2 Hz, *J'* = 8.9 Hz, 1H), 7.01 (d, *J* = 16.2 Hz, 1H), 7.32 (t, *J* = 7.3 Hz, 1H), 7.39 (t, *J* = 7.4 Hz, 2H), 7.55 (d, *J* = 7.3 Hz, 2H), 7.86 (d, *J* = 8.9, 1H), 9.43 (s, 1H), 11.39 (s. 1H). ESI-MS (+) m/z calc. 221.29 found 221.10.

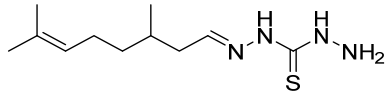

Citronellalmonothiocarbohydrazone (99): thiocarbohydrazide (0.10 g, 0.94 mmol) was dissolved in 30 mL of absolute ethanol at 60°C, then 0.5 mL of acetic acid were added. At the same time, the (*S*)-citronellal (0.15 g, 0.94 mmol) was dissolved in 8 mL of absolute ethanol and it was dripped slowly in the thiocarbohydrazide solution. The mixture was refluxed and stirred for 10 minutes, cooled to room temperature and left at -4°C for 24 h. A solid appeared and it was collected by filtration, washed with hexane and dried under *vacuum*. Pale yellow powder. Yield: 43%. FT-IR (cm^{-1}): 1537 (s), 1090 (s), 858 (m). ^{1}H-NMR (δ, ppm, 400 MHz, DMSO-d^6): 0.86 (d, *J* = 6.6 Hz, 3H), 1.19 (m, 2H), 1.33 (m, 2H), 1.57 (s, 3H), 1.60 (m, 1H), 1.65 (s, 3H), 1.92 (m, 2H), 3.46 (m, 1H), 4.69 (t, *J* = 10.5 Hz, 2H), 5.08 (m, 1H), 9.18 (s, 2H). ESI-MS (+) m/z calc. 243.39 found 243.12.

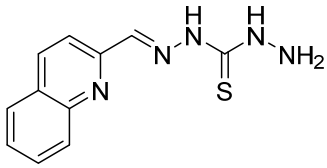

Quinoline-2-carboxaldehydemonothiocarbohydrazone (100): thiocarbohydrazide (0.20 g, 1.88 mmol) was dissolved in 50 mL of methanol at 50°C. At the same time, the quinoline-2-carbozaldehyde (0.30 g, 1.88 mmol) was dissolved in 5 mL of methanol and it was dripped slowly in the thiocarbohydrazide solution. The mixture was refluxed and stirred for 5 hours. The product precipitated during the reaction. The solution was cooled to room temperature and left at -4°C for 24 h. The product was collected by filtration, washed with hexane and dried under *vacuum*. Pale orange powder. Yield: 72%. FT-IR (cm^{-1}): 1597 8s), 1095 (m), 829 (s). ^{1}H-NMR (δ, ppm; DMSO-d^6): 4.97 (s, 2H), 7.62 (t, *J* = 7.4 Hz, 1H), 7.77 (t, *J* = 7.7 Hz, 1H), 7.99 (t, *J* = 8.8 Hz, 2H), 8.19 (s, 1H), 8.36 (d, *J* = 8.7 Hz, 1H), 8.55 (d, *J* = 8.7 Hz, 1H), 10.20 (s, 1H), 11.80 (s, 1H). ESI-MS (+) m/z calc. 246.30 found 246.42.

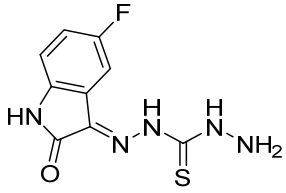

5-Fluoroisatinmonothiocarbohydrazone (101): The thiocarbohydrazide (0.10 g, 0.94 mmol) was dissolved in 30 mL of methanol at 50°C. At the same time, the 5-Fluoroisatin (0.16 g, 0.94 mmol) was dissolved in 10 mL of methanol and it was dripped slowly in the thiocarbohydrazide solution. The mixture was stirred for 6 hours at room temperature. The product precipitated during the reaction and it was collected by filtration, washed with hexane and dried under *vacuum*. Pale yellow powder. Yield: 41%. FT-IR (cm^{-1}): 1689 (s), 1628 (s), 841 (m). ^{1}H-NMR (δ, ppm; DMSO-d^6): 6.91 (dd, *J* = 8.5 Hz, *J'* = 4.3 Hz, 1H), 7.22 (m, 1H), 7.49 (m, 1H), 8.63 (s, 1H), 8.93 (s, 1H), 9.16(s, 1H), 11.39 (s, 1H), 12.36 (s, 1H). ESI-MS (+) m/z calc. 254.26 found 254.28.

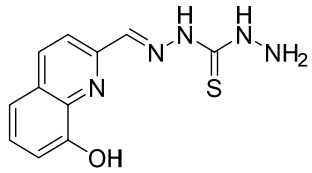

8-Hydroxy-2-quinolinecarboxaldehydemonothiocarbohydrazone (102): The thiocarbohydrazide (0.10 g, 0.94 mmol) was dissolved in 25 mL of methanol at 50°C. At the same time, the 8-Hydroxy-2-quinolinecarboxaldehyde (0.16 g, 0.94 mmol) was dissolved in 5 mL of methanol and it was dripped slowly in the thiocarbohydrazide solution. The mixture was refluxed and stirred for 5 hours. The product precipitated during the reaction. The solution was cooled to room temperature and the product was collected by filtration, washed with hexane and dried under *vacuum*. Yellow powder. Yield: 78%. FT-IR (cm^{-1}): 1598 (s), 1087 (s), 826 (m). ^{1}H-NMR (δ, ppm; DMSO-d^{6}): 4.96 (s, 2H), 7.10 (d, *J* = 7.3 Hz, 1H), 7.41 (m, 2H), 8.23 (s, 1H), 8.28 (d, *J* = 8.8 Hz, 1H), 8.52 (d, *J* = 8.8 Hz, 1H), 9.81 (s, 1H), 10.18 (s, 1H), 11.85 (s, 1H). ESI-MS (+) m/z calc. 262.30 found 262.16.

Synthesis of copper(II) complexes of bidentate mono-TC

The copper(II) complexes of **98** and **99** were obtained following the same procedure. Namely, a 2:1 ratio of ligand and copper(II) acetate were dissolved respectively in 10 and 5 mL of absolute ethanol. Subsequently, the copper-containing solution was dripped slowly into the ligand solution which turned to brown rapidly. The mixture was stirred at room temperature for 3 hours and then the solvent was removed under reduced pressure and the solid obtained was collected, washed with diethylether (2 x 7 mL) and finally dried under *vacuum*.

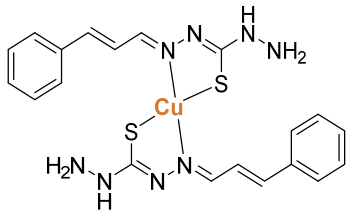

Bis(cinnamaldehydemonothiocarbohydrazonato)Cu(II) (103): 98 (0.02 g, 0.09 mmol), copper(II) acetate (0.01 g, 0,05 mmol). Brown powder. Yield: 78%. FT-IR (cm^{-1}): 1618 (s), 1071 (m), 810 (m). ESI-MS (+) m/z calc. 503.12 found 502.98.

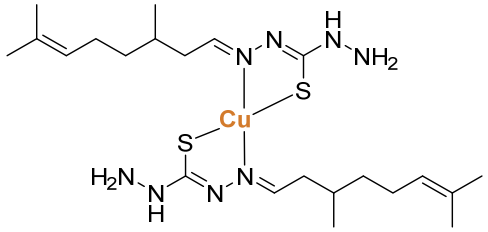

Bis(citronellalmonothiocarbohydrazonato)Cu(II) (104): **99** (0.05 g, 0.21 mmol), copper(II) acetate (0.02 g, 0,10 mmol). Brown powder. Yield: 42%. FT-IR (cm^{-1}): 1672 (s), 1131 (s), 827 (m). ESI-MS (+) m/z calc. 547.33 found 547.55.

Synthesis of copper(II) complexes of tridenate and tetradentate mono-TC

The copper(II) complexes of the κ^3-mono-TC **100** and **101** and of the κ^4-monoTC **102** were obtained following the same procedure. Namely, an equimolar amount of ligand and copper(II) chloride were dissolved respectively in 15 and 5 mL of methanol. Subsequently, the copper-containing solution was dripped slowly into the ligand solution which turned to brown rapidly. The mixture was stirred at room temperature for 2 hours and then the solvent was removed under reduced pressure and the solid obtained was collected, washed with diethylether (2 x 7 mL) and finally dried under *vacuum*.

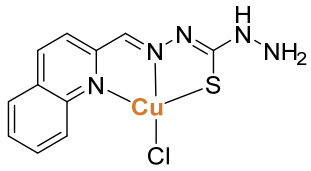

(Quinoline-2-carboxaldehydemonothiocarbohydrazonato)Cu(II) chloride (105): 100 (0.07 g, 0.29 mmol), copper(II) chloride (0.05 g, 0.29 mmol). Brown solid. Yield: 84%. FT-IR (cm^{-1}): 1606 (s), 1143 (m), 830 (m). ESI-MS (+) m/z calc. 307,84 found 309.31.

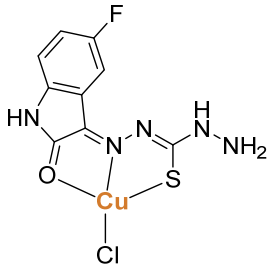

(5-Fluoroisatinmonothiocarbohydrazonato)Cu(II) chloride (106): 101 (0.04 mg, 0.17 mmol), copper(II) chloride (0.03 mg, 0.17 mmol). Brown powder. Yield: 77%. FT-IR (cm^{-1}): 1677 (s), 1623 (m), 812 (m). ESI-MS (+) m/z calc. 315.75 found 315.32.

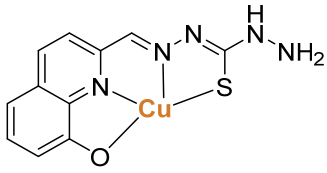

(8-Hydroxy-2-quinolinecarboxaldehydemonothiocarbohydrazonato)Cu(II) (107): 102 (0.05 mg, 0.19 mmol), copper(II) chloride (0.03 mg, 0.19 mmol). Brown powder. Yield: 64%. FT-IR (cm^{-1}): 1599 (s), 1088 (m), 840 (m). ESI-MS (+) m/z calc. 323.84 found 324.95.

12.1.5 Ru(II) half-sandwich with NI and TS/TC ligands

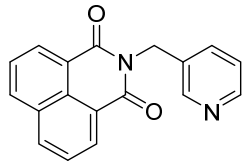

N-(3-methylenepyridyl)-1,8-naphthalimide (108): the 1,8-naphthalenic anhydride (0.80 g, 4.04 mmol), 3-picolylamine (0.52 mg, 4.04 mmol) and a catalytic amount of acetic acid were dissolved in 30 mL of dimethylformamide. The mixture was heated at 130°C for 24 hours using a Dean Stark condenser to remove water during the reaction. The mixture was cooled to room temperature obtaining a solid which was separated by filtration and dried under vacuum. Pale yellow microcrystalline solid. Yield: 87%. FT-IR (cm^{-1}): 1687 (s), 1646 (s), 1581 (m), 1225 (m). ^{1}H-NMR (δ, ppm, 400 MHz, $CDCl_3$): 5.43 (s, 2H), 7.34 (ddd, 1H, *J* = 8.0 Hz, *J'* = 5.2 Hz, *J''* = 2.1 Hz), 7.76 (t, 2H, *J* = 8.5 Hz), 8.02 (dt, 1H, *J* = 8.0 Hz, *J'* = 2.1 Hz), 8.24 (dd, 2H, *J* = 8.5 Hz, *J* = 1.0 Hz), 8.54 (dd, 1H, *J* = 5.2 Hz, *J* = 2.1 Hz), 8.62 (dd, 2H, *J* = 8.5 Hz, *J* = 1.0 Hz), 8.89 (d, 1H, *J* = 2.1 Hz). ESI-MS (+) m/z calc. 289.3 found 288.8.

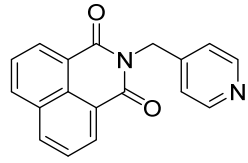

N-(4-methylenepyridyl)-1,8-naphthalimide (109): the procedure followed to synthesise this ligand was the same applied for **98**. 1,8-naphthalenic anhydride (0.50 g, 2.52 mmol), 4-aminopyridine (0.27 mg, 2.52 mmol). White microcrystalline solid. Yield: 83%. FT-IR (cm^{-1}): 1692 (s), 1658 (s), 1585 (m), 1234 (m). ^{1}H-NMR (δ, ppm, 400 MHz, DMSO-d^6): 5.28 (s, 2H), 7.33 (dd, J=7.5 Hz, J'=6.0 Hz, 2H), 7.88 (t, 2H), 8.47 (m, 6H). ESI-MS (+) m/z calc. 289.3 found 288.6.

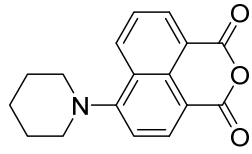

4-piperidinyl-1,8-naphthalicanhydride (110): the 4-bromo-1,8-naphthalicanhydride (0.30 g, 1.08 mmol) and the piperidine (0.18 g, 2.17 mmol) were refluxed and stirred in

3 mL of 2-methoxyethanol for 5 hours. The solution turned from pale brown to dark red during the reaction. The mixture was then cooled to room temperature and 10 mL of water were added to precipitate the product. Finally, the solid was centrifuged, washed with cold water (3 x 5 mL) and then dried under *vacuum*. Dark orange powder. Yield: 84%. ^{1}H-NMR (δ, ppm, 400 MHz, dmso-d^6): 1.68 (m, 2H), 1.83 (m, 4H), 2.26 (m; 4H), 7.33 (d, *J* = 8.2 Hz, 1H), 7.83 (dd, *J* = 8.5 Hz, *J'* = 7.3 Hz, 1H), 8.39 (d, *J* = 8.2 Hz, 1H), 8.45 (d, *J* = 8.5 Hz, 1H), 8.48 (d, *J* = 7.3 Hz, 1H). ESI-MS (+) m/z calc. 282.31 found 282.15.

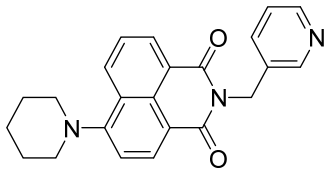

4-piperidinyl- N-(3-methylenepyridyl)-1,8-naphthalimide (111): 110 (0.20 g, 0.71 mmol) was dissolved in 15 mL of absolute ethanol and 3-picolylamine (0.08 g, 0.71 mmol) was added. The mixture was refluxed and stirred for 24 hours, then the solvent was removed under reduced pressure. The solid obtained was recrystallized twice using a 1:2 mixture of ethanol and water, filtered and then dried under *vacuum*. Yellow powder. Yield: 81%.^{1}H-NMR (δ, ppm, 400 MHz, acetone-d^6): 1.75 (m, 2H), 1.90 (m, 4H), 3.37 (m, 4H), 5.34 (s, 2H), 7.30 (m, 1H), 7.33 (d, *J* = 8.1 Hz, 1H), 7.80 (dd, *J* =8.5, *J'* = 7.4 Hz, 1H), 7.85 (d, *J* = 7.8 Hz, 1H), 8.46 (m, 2H), 8.51 (d, *J* = 8.5 Hz, 1H), 8.54 (d, *J* = 7.4 Hz, 1H). ESI-MS (+) m/z calc. 372.44 found 372.78.

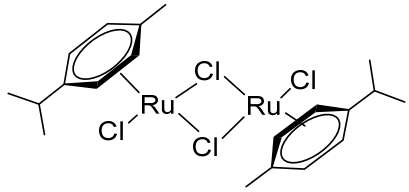

[(η^6-*p*-Cym)RuCl$_2$]$_2$ (112): 1.0 g of $RuCl_3 \cdot nH_2O$ was dissolved in 10 mL of methanol, then a large excess of α-phellandrene (3 mL) was added. The reaction was performed using a microwave reactor at 150 W and 140°C for 10 minutes. At the end, 10 mL of pentane were added to precipitate the product which was collected by filtration, washed with pentane (3 x 5 mL) and dried under *vacuum*. Dark red crystals. Quantitative yield. ^{1}H-NMR (δ, ppm, 400 MHz, $CDCl_3$): 5.35 (d, *J* = 6.0 Hz, 2H), 5.49 (d, *J* = 6.0 Hz, 2H).

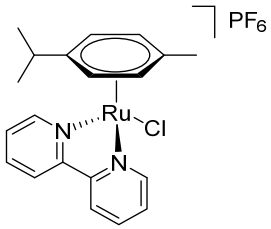

[(η^6-*p*-Cym)Ru(κ^2-bpy)Cl]PF$_6$ (113): 112 (0.150 g, 0.25 mmol), 2,2'-bipyridine (bpy) (0.076 g, 0.49 mmol) and KPF_6 (0.090 g, 0.49 mmol) were dissolved in dry methanol and stirred for 4 h in nitrogen atmosphere. The solution turned from clear and orange to turbid and yellow. The mixture was cooled to - 4 °C for 3 h and a yellow precipitate was formed. It was separated by filtration, washed with cold methanol and dried under *vacuum*. Yellow solid. Yield 71%. ^{1}H-NMR (δ, ppm, 400 MHz, acetone-d^6): 1.12 (d, *J* = 7.2 Hz, 6H), 2.33 (s, 3H), 2.80 (ept, J = 7.2 Hz, 1H), 6.02 (d, *J* = 6.0, 2H), 6.27 (d, *J* = 6.0, 2H), 7.85 (m, 2H), 8.36 (m, 2H), 8.65 (d, *J* = 8.4, 2H), 9.63 (d, *J* = 5.6, 2H). ^{19}F {^{1}H} NMR (δ, ppm, 400 MHz, acetone-d^6): -71.64 (d, J_{F-P} = 751.6). ESI-MS (+) [M-PF_6]$^+$ m/z calc. 426.9 found 426.9. E.A.% calc. (found): C 37.67 (36.98), H 3.51 (3.40), N 9.76 (9.44).

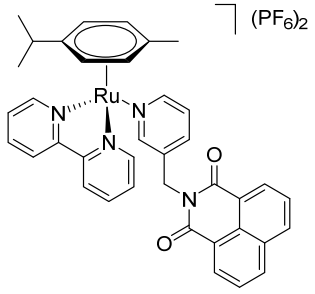

[(η^6-p-cym)Ru(N,N'-bpy)(108)](PF$_6$)$_2$ (114): 113 (0.100 g, 0.17 mmol) and $AgNO_3$ (0.029, 0.17 mmol) were dissolved in 10 mL of a 9:1 methanol/water solution using an aluminium-foil-covered flask to ensure a dark reaction environment. The mixture was left reacting overnight and the precipitated AgCl was removed by filtration. The ligand **108** (0.490 g, 1.7 mmol) was dissolved in 10 mL of CH_2Cl_2 and then slowly added to the ruthenium complex solution. The mixture was left stirring for 48 h and then 5 equiv. of KPF_6 were added to precipitate the product. The precipitate that formed was collected by filtration, washed with diethyl ether (2 x 5 mL) and CH_2Cl_2 (2 x 5 mL) and dried under *vacuum*. Yellow solid. Yield 17%. ^{1}H NMR (δ, ppm, 400 MHz, acetone-d^6): 1.01 (d, *J* = 6.8 Hz, 6H), 2.03 (s, 3H), 2.70 (ept, *J* = 6.8 Hz, 1H), 5.27 (s, 2H), 6.48 (d, *J* = 6.4, 2H), 6.84

(d, *J* = 6.4, 2H), 7.52 (dd, *J* = 7.8 Hz, *J'* = 5.8 Hz, 1H), 7.91 (t, *J* = 7.8 Hz, 2H), 8.10 (t, J = 7.8 Hz, 2H), 8.17 (d, *J* = 8.0 Hz, 1H), 8.39 (t, *J* = 7.9 Hz, 2H), 8.48 (d, *J* = 8.0 Hz, 2H), 8.53 (d, J = 8.2 Hz, 2H), 8.56 (d, *J* = 7.3 Hz, 2H), 8.66 (d, *J* = 5.6 Hz, 1H), 8.92 (s, 1H), 10.13 (d, 2H, *J* = 5.7 Hz, 2H).^{19}F {^{1}H} NMR (δ, ppm; acetone-d^{6}): -71.46 (d, J_{F-P} = 752.0). ESI-MS (+) [M-PF_6^-]$^+$ m/z calc. 824.7 found 825.1.

Crystals suitable for XRD analysis were obtained from slow evaporation of a saturated 1:1 methanol/dichlorometane solution of the complex.

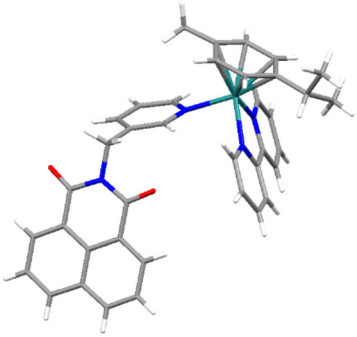

Space group P 2_1/c	
R 7.11%	
Z 16	
a 14.25608	**α** 90
b 55.8564	**β** 95.6131
c 19.05981	**γ** 90

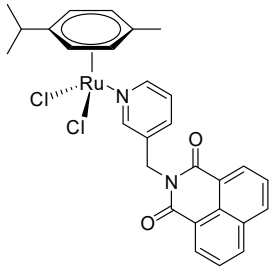

[(η^6-p-cym)Ru(108)Cl$_2$] (115): [(η^6-*p*-Cym)RuCl$_2$]$_2$ **112** (0.16 g, 0.26 mmol) and the ligand **108** (0.15 g, 0.52 mmol) were dissolved in 15 mL of CH_2Cl_2 dry in a Schlenk flask with nitrogen atmosphere. The mixture was stirred for 5 hours, then 10 mL of diethyl ether were added, and the solution was left al -4°C overnight. The precipitate was collected by filtration, washed with cold diethyl ether (2 x 5 mL) and dried under *vacuum*. Orange solid. Yield: 81%. ^{1}H NMR (δ, ppm, 400 MHz, $CDCl_3$): 1.30 (d, *J* = 6.9 Hz, 6H), 2.14 (s, 3H), 3.02 (ept, *J* = 6.9, 1H), 5.28 (d, *J* = 5.6 Hz, 2H), 5.39 (s, 2H), 5.46 (d, *J* = 5.6 Hz, 2H), 7.24 (m, 1H), 7.80 (dd, *J* = 8.1, *J'* = 7.3 Hz, 2H), 7.95 (d, *J* = 7.5 Hz, 1H), 8.27 (d, *J* = 8.1 Hz, 2H), 8.65 (d, *J* = 7.3 Hz, 2H), 8.95 (d, *J* = 5.3 Hz, 1H), 9.36 (s, 1H). ESI-MS (+) [M-Cl^-]$^+$ m/z calc. 559.04 found 559.08.

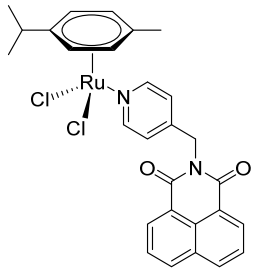

[(η^6-p-cym)Ru(109)Cl_2] (116): the procedure to synthesised this complex was the same used for complex **115**. [(η^6-*p*-Cym)$RuCl_2]_2$ **112** (0.10 g, 0.16 mmol), **109** (0.12 g, 0.32 mmol). Orange solid. Yield: 89%. ^{1}H NMR (δ, ppm, 400 MHz, $CDCl_3$): 1.30 (d, *J* = 6.9 Hz, 6H), 2.12 (s, 3H), 3,01 (ept, *J* = 6.9 Hz, 1H), 5.20 (d, *J* = 5.8 Hz, 2H), 5.41 (d, *J* = 5.8 Hz, 2H), 7.43 (d, *J* = 6.3 Hz, 2H), 7.80 (t, *J* = 7.8 Hz, 2H), 8.28 (d, *J* = 8.2 Hz, 2H), 8.63 (d, *J* = 7.2 Hz, 2H), 8.96 (d, *J* = 6.3 Hz, 2H). ESI-MS (+) $[M\text{-}Cl^-]^+$ m/z calc. 559.04 found 559.16.

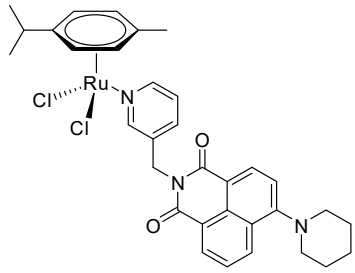

[(η^6-p-cym)Ru(111)Cl_2] (117): the procedure to synthesised this complex was the same used for complex **115**. [(η^6-*p*-Cym)$RuCl_2]_2$ **112** (0.10 g, 0.16 mmol), **111** (0.12 g, 0.32 mmol). Orange solid. Yield: 89%. Crystals suitable for XRD analysis were obtained for vapour diffusion of diethyl ether in a saturated dichlorometane solution of the complex. ^{1}H NMR (δ, ppm, 400 MHz, acetone-d^6):1.25 (d, *J* = 6.9 Hz, 6H), 1.76 (m, 2H), 1.91 (m, 4H), 2.02 (s, 3H), 2.92 (ept, *J* = 6.9 Hz, 1H), 3.30 (m, 4H), 5.26 (d, *J* = 6.0 Hz, 2H), 5.36 (s, 2H), 5.45 (d, *J* = 6.0 Hz, 2H), 7.36 (d, *J* = 8.1 Hz, 1H), 7.38 (m, 1H), 7.83 (dd, *J* = 8.5. *J'* = 7.3 Hz), 7.99 (d, *J* = 7.7 Hz, 1H), 8.50 (d, *J* = 8.1 Hz, 1H), 8.54 (dd, *J* = 8.5 Hz, *J'* = 1.1 Hz, 1H), 8.57 (dd, *J* = 7.3 Hz, *J'* = 1.1 Hz, 1H), 8.93 (d, *J* = 5.5 Hz, 1H), 9.27 (s, 1H). ESI-MS (+) $[M\text{-}Cl^-]^+$ m/z calc. 642.18 found 642.13.

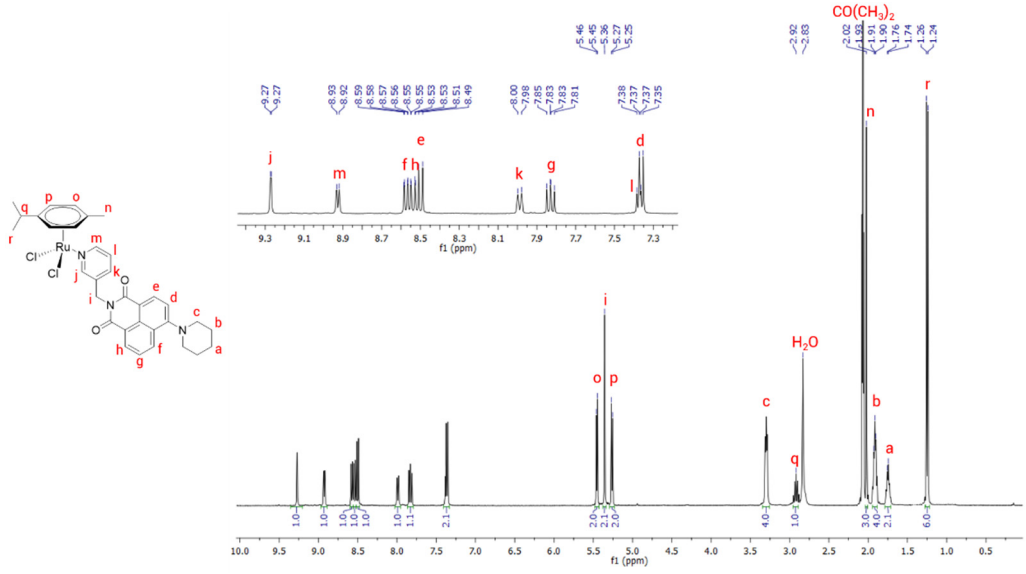

*^{1}H-NMR spectrum (400 MHz -acetone-d^6) of **117**.*

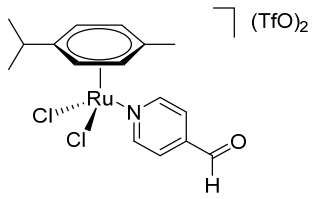

[(η^6-p-cym)Ru(4-formylpyridine)Cl$_2$] (118): the procedure to synthesised this complex was the same used for complex **115**. [(η^6-*p*-Cym)RuCl$_2$]$_2$ **112** (0.10 g, 0.16 mmol), 4-formylpyridine (0.03 g, 0.32 mmol). Orange microcrystalline solid. Yield: 90%. ^{1}H NMR (δ, ppm, 400 MHz, $CDCl_3$): 1.34 (d, *J* = 6.9 Hz, 6H), 2.14 (s, 3H), 3.02 (ept, *J* = 6.9 Hz, 1H), 5.28 (d, *J* = 6.0 Hz, 2H), 5.50 (d, *J* = 6.0 Hz, 2H), 7.73 (d, *J* = 6.5 Hz, 2H), 9.37 (d, *J* = 6.5 Hz, 2H), 10.13 (s, 1H). ESI-MS (+) [M-Cl$^-$]$^+$ m/z calc 377.85 found 377.51.

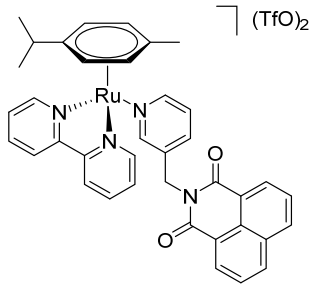

[(η^6-p-cym)Ru(N,N'-bpy)(108)](SO$_3$CF$_3$)$_2$ (119): 115 (0.10 g, 0.17 mmol) was dissolved in 15 mL of CH_2Cl_2 dry in a Schlenk flask with nitrogen atmosphere. At the same time, it was prepared an AgTfO (0.09 g, 0.34 mmol) solution in 3 mL of dry methanol in nitrogen atmosphere, and then it was dropped slowly into the ruthenium complex solution. The solution became turbid immediately and it was stirred for 2 h at room temperature, covering the flask with aluminium foil to keep the solution in dark conditions. Then, the AgCl formed was removed filtering the solution in a Schelnk filter and the clear orange solution obtained was dropped in a Schlenk flask with bipyridine (0.03 g, 0.17 mmol). The mixture was stirred overnight always in nitrogen and dark environment. In the end, the solvent was removed under reduced pressure and the orange solid obtained was washed with diethyl ether (3 x 10 mL) and dried under *vacuum*. Orange powder. Yield: 73%. ^{1}H NMR (δ, ppm, 400 MHz, acetone-d^6): 0.99 (d, *J* = 6.9 Hz, 6H), 2.01 (s, 3H), 2.68 (ept, *J* = 6.9 Hz, 1H), 5.26 (s, 2H), 6.48 (d, *J* = 6.0 Hz, 2H), 6.84 (d, *J* = 6.0 Hz, 2H), 7.50 (t, *J* = 6.7 Hz, 1H), 7.90 (t, *J* = 7.8 Hz, 2H), 8.07 (t, *J* = 6.7 Hz, 2H), 8.14 (d, *J* = 8.5 Hz, 1H), 8.38 (t, *J* = 8.0 Hz, 2H), 8.47 (d, *J* = 8.4 Hz, 2H), 8.54 (m, 4H),

8.75 (d, *J* = 5.3 Hz, 1H), 8.86 (s, 1H), 10.17 (d, *J* = 5.6 Hz, 2H). ESI-MS (+) $[M\text{-}TfO^-]^+$ m/z calc. 829.84 found 829.14. E.A.% calc. (found): C 49.12 (49.85), H 3.51 (3.43), N 5.73 (5.66).

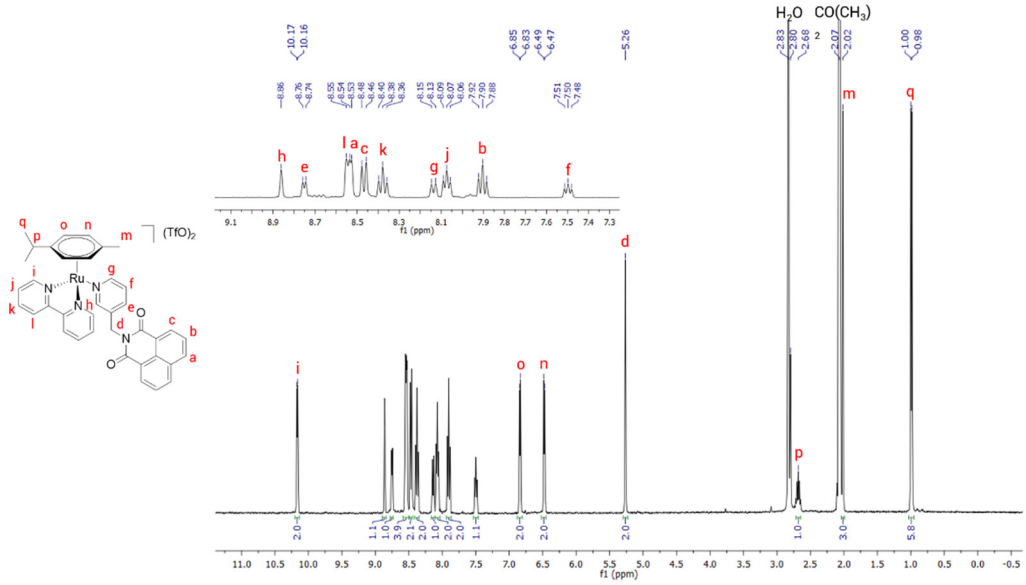

*^{1}H-NMR spectrum (400 MHz -acetone-d^6) of **119**.*

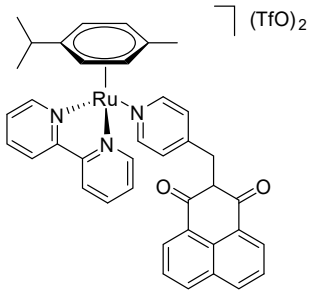

[(η^6-p-cym)Ru(N,N'-bpy)(109)](SO$_3$CF$_3$)$_2$ (120): the procedure to synthesised this complex was the same used for complex **119**. **116** (0.10 g, 0.17 mmol), AgTfO (0.09 g, 0.34 mmol), bipyridine (0.03 g, 0.17 mmol). Orange solid. Yield: 77%. ^{1}H NMR (δ, ppm, 400 MHz, acetone-d^6): 0.97 (d, *J* = 6.9 Hz, 2H), 1.96 (s, 3H), 2.65 (ept, *J* = 6.9 Hz, 1H), 5.37 (s, 2H), 6.41 (d, *J* = 6.5 Hz, 2H), 6.78 (d, *J* = 6.5 Hz, 2H), 7.55 (d, *J* = 6.6 Hz, 2H), 7.87 (m, 2H), 8.01 (m, 2H), 8.41 (t, *J* = 8.1 Hz, 2H), 8.46 (d, *J* = 8.4 Hz, 2H), 8.49 (d, *J* =7.3 Hz, 2H), 8.61 (m, 2H), 8.76 (d, *J* = 6.6 Hz, 2H), 10.13 (d, *J* = 5.7 Hz, 2H). ESI-MS (+) [M-TfO$^-$]$^+$ m/z calc. 829.84 found 829.15. E.A.% calc. (found): C 49.12 (48.21), H 3.51 (3.23), N 5.73 (5.52).

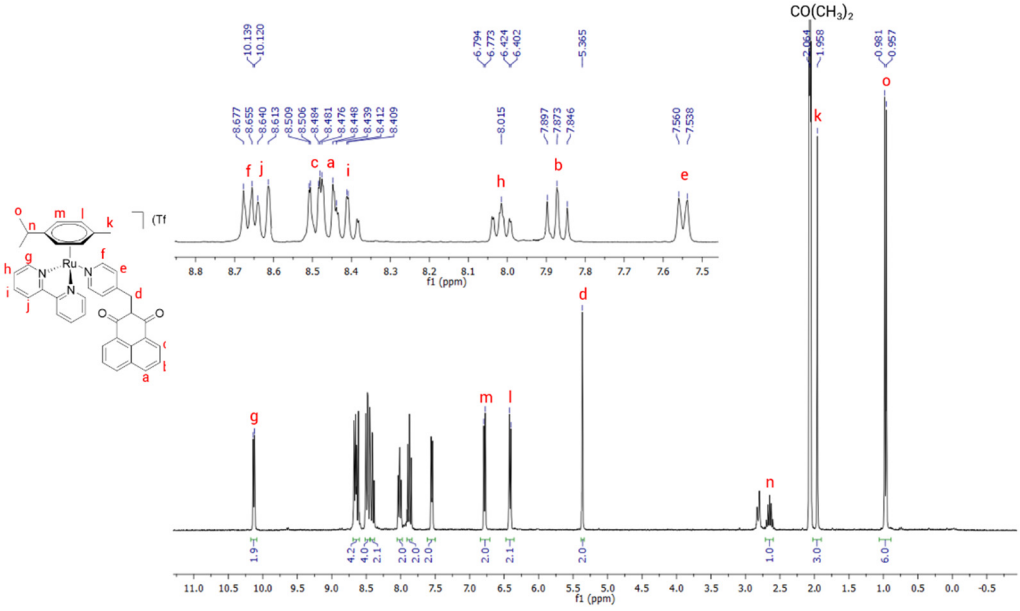

*^{1}H-NMR spectrum (400 MHz -acetone-d^6) of **120**.*

Crystals suitable for XRD analysis were obtained for vapour diffusion of diethyl ether in a saturated dichlorometane solution of the complex **120**.

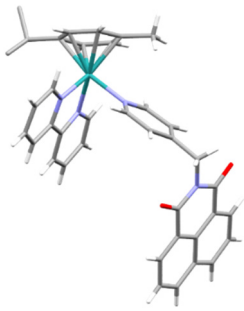

Space group P -1	
R 6.97%	
Z 2	
a 10.317	α 92.78
b 10.319	β 93.42
c 19.753	γ 97.58

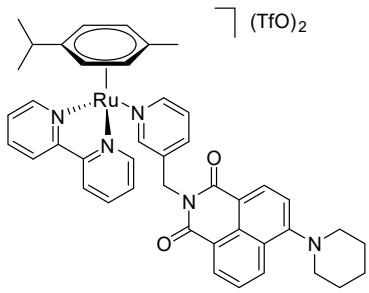

[(η⁶-p-cym)Ru(N,N'-bpy)(111)](SO₃CF₃)₂ (121): the procedure to synthesised this complex was the same used for complex **119**. **117** (0.12 g, 0.17 mmol), AgTfO (0.09 g, 0.35 mmol), bipyridine (0.03 g, 0.17 mmol). Orange solid. Yield: 91%. ^{1}H NMR (δ, ppm, 400 MHz, dmso-d^{6}): 0.81 (d, *J* = 6.9 Hz, 6H), 1.68 (m, 2H), 1.77 (s, 3H), 1.84 (m, 4H), 2.44 (m, 1H), 3.23 (m, 4H), 6.27 (d, *J* = 6.3 Hz, 2H), 6.66 (d, *J* = 6.3 Hz, 2H), 7.33 (d, *J* = 8.2 Hz, 1H), 7.43 (m, 1H), 7.84 (m, 1H), 7.95 (m, 3H), 8.29 (t, *J* = 7.8 Hz, 2H), 8.36 (m, 2H), 8.44 (m, 2H), 8.52 (m, 3H), 9.87 (d, *J* = 5.6 Hz, 2H). ESI-MS (+) [M-TfO^{-}]$^{+}$ m/z calc. 911.98 found 912.49.

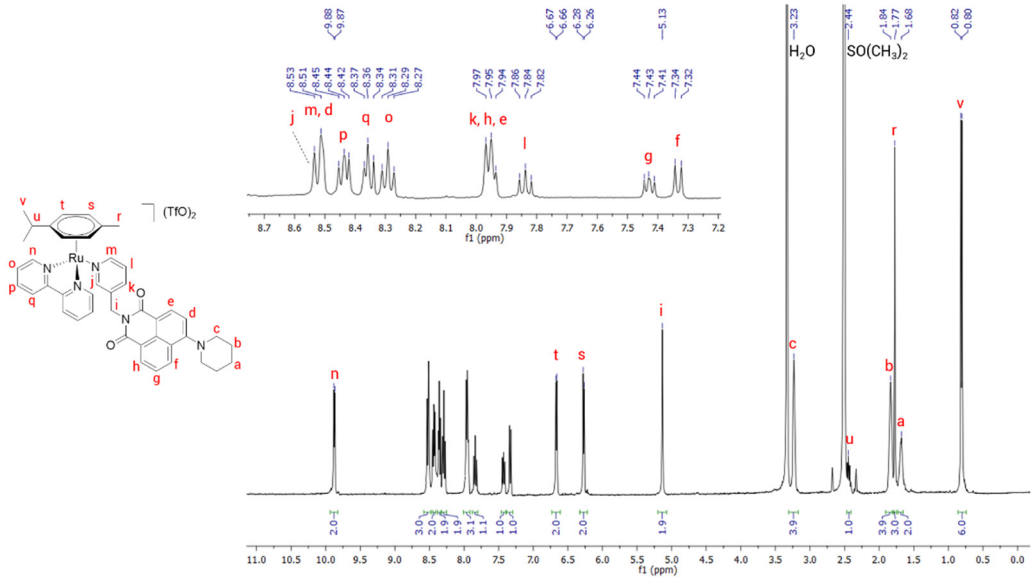

*^{1}H-NMR spectrum (400 MHz -dmso-d^{6}) of **121**.*

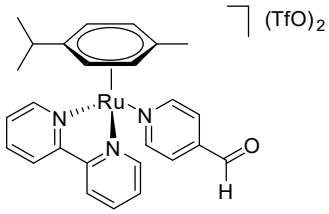

[(η^6-p-cym)Ru(N,N'-bpy)(4-formylpyridine)](SO_3CF_3)$_2$ (122): the procedure to synthesised this complex was the same used for complex **119**. **118** (0.10 g, 0.22 mmol), AgTfO (0,11 g, 0.43 mmol), bipyridine (0.03 g, 0.22 mmol). The ^{1}H-NMR of the product showed a mixture where the 62% was the desired complex, whereas the 38% was the complex with the aldehyde transformed in emiacetal due to the presence of methanol in the reaction environment. The product with the aldehyde was obtained pure through the crystallization of a saturated solution of the complex in CH_2Cl_2 with diffusion of diethyl ether. Orange crystals: Yield: 53%. ^{1}H NMR (δ, ppm, 400 MHz, acetone-d^6): 0.99 (d, *J* = 6.9 Hz, 6H), 1.97 (s, 3H), 2.67 (ept, *J* = 6.9 Hz, 1H), 6.47 (d, *J* = 6.3 Hz, 2H), 6.86 (d, *J* = 6.3 Hz, 2H), 7.90 (d, *J* = 6.2 Hz, 2H), 8.08 (m, 2H), 8.47 (t, *J* = 7.9 Hz, 2H), 8.68 (d, *J* = 8.0 Hz, 2H), 9.11 (d, *J* = 6.3 Hz, 2H), 10.13 (s, 1H), 10.19 (d, *J* = 5.8 Hz, 2H). ESI-MS (+) [M-TfO$^-$]$^+$ m/z calc. 647.65 found. 680.11 (emiacetal with methanol).

Crystals suitable for XRD analysis were obtained for vapour diffusion of diethyl ether in a saturated dichlorometane solution of the complex **122** (structure of the emiacetal).

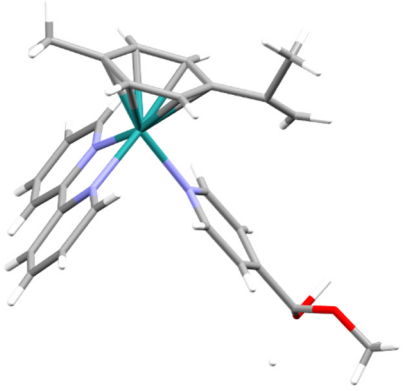

Space group *P*-1	
R 7.20%	
Z 2	
a 9.5969	α 98.127
b 9.7025	β 93.423
c 18.7046	γ 111.652

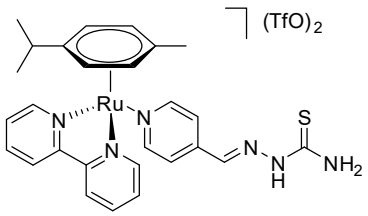

[(η^6-p-cym)Ru(N,N'-bpy)(N-4-formylpyridinethiosemicarbazone)](SO$_3$CF$_3$)$_2$ (123): 122 (0.10 g, 0.13 mmol) and thiosemicarbazide (0.01 g, 0.13 mmol) were dissolved in 15 mL of tetrahydrofuran dry in a Schlenk flask in nitrogen atmosphere. The mixture was stirred for 48 hours at room temperature covering the flask with aluminium foil to keep the solution in the dark. The mixture was then microfiltered on celite and the solvent of the clear solution obtained was removed under reduced pressure. Finally, the solid obtained was washed three times with diethyl ether and dried under *vacuum*. Orange solid. Yield: 72%. ^{1}H NMR (δ, ppm, 400 MHz, acetone-d^6): 1.00 (d, *J* = 6.8 Hz, 6H), 2.01 (s, 3H), 2.69 (ept, *J* = 6.8 Hz, 1H), 6.45 (d, *J* = 6.0 Hz, 2H), 6.82 (d, *J* = 6.0 Hz, 2H), 7.79 (s, 1H), 7.85 (d, *J* = 5.9 Hz, 3H), 8.13 (s, 1H), 8.46 (t, *J* = 7.8 Hz, 2H), 8.68 (m, 4H), 10,17 (d, *J* = 5.5 Hz, 2H), 10.87 (s, 1H). ESI-MS (+) [M-TfO$^-$]$^+$ m/z calc. 720.32 found 721.08.

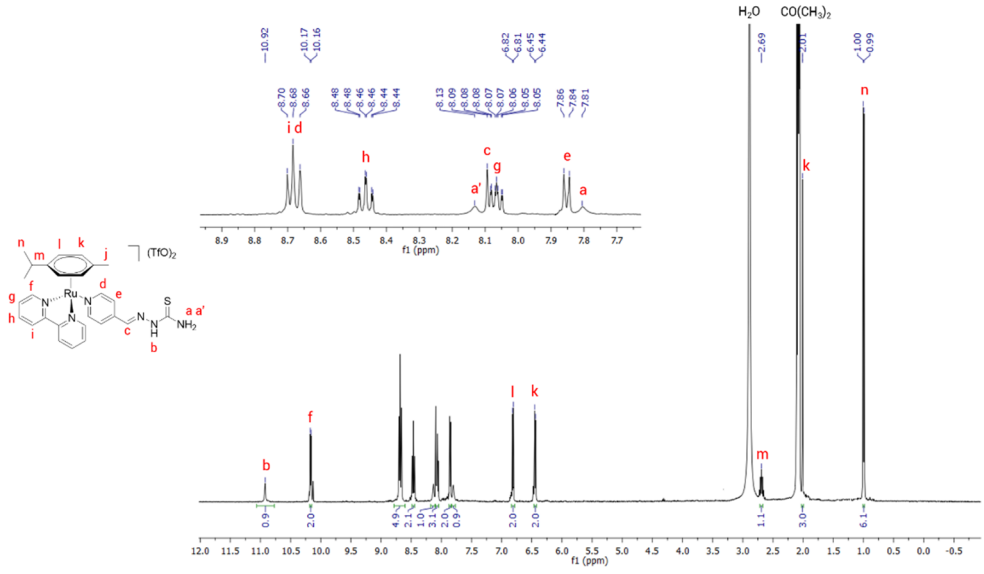

*^{1}H-NMR spectrum (400 MHz -acetone-d^6) of **123**.*

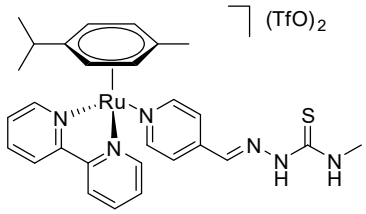

[(η^6-p-cym)Ru(N,N'-bpy)(N-4-formylpyridine-4-methyl-3-thiosemicarbazone)](SO$_3$CF$_3$)$_2$ (124): the procedure to synthesised this complex was the same used for complex **123**. **122** (0.10 g, 0.13 mmol), 4-methyl-3-thiosemicarbazide (0.01 g, 0.13 mmol). Orange solid. Yield: 63%. ^{1}H NMR (δ, ppm, 400 MHz, acetone-d^6): 1.00 (d, *J* = 6.9 Hz, 6H), 2.01 (s, 3H), 2.70 (m, 1H), 3.10 (s, 3H), 6.45 (d, *J* = 6.5 Hz, 2H), 6.81 (d, *J* = 6.5 Hz, 2H), 7.82 (d, *J* = 6.8 Hz, 2H), 8.04 (s, 1H), 8.07 (m, 2H), 8.46 (m, 2H), 8.54 (s, 1H), 8.67 (m, 4H), 10.17 (d, *J* = 5.2 Hz, 2H), 10.83 (s, 1H). ESI-MS (+) [M-TfO$^-$]$^+$ m/z calc. 734.82 found 735.27. E.A.% calc. (found): C 40.76 (41.38), H 3.65 (3.66), N 9.51 (9.28).

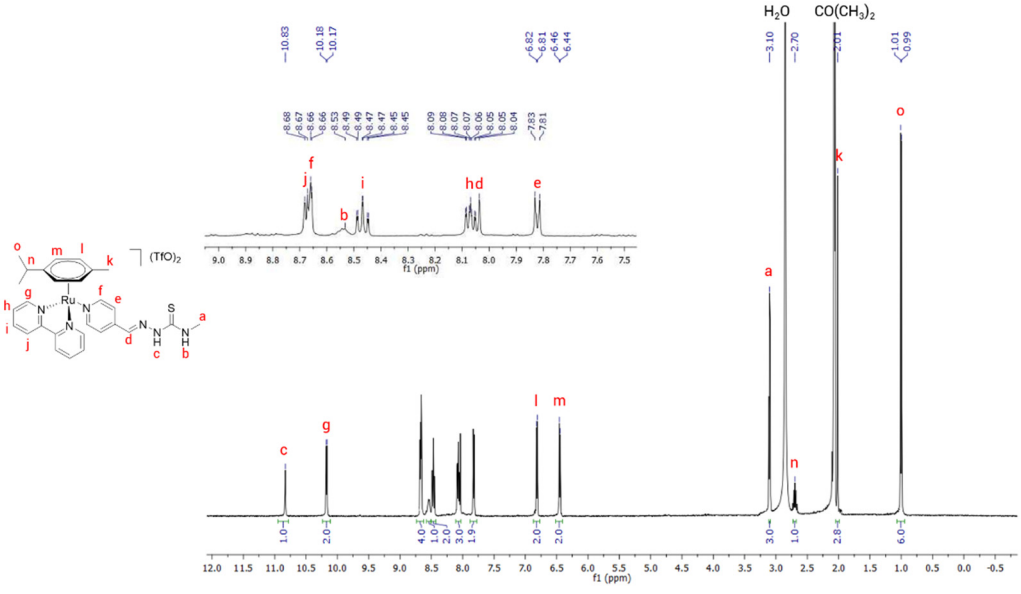

*^{1}H-NMR spectrum (400 MHz -acetone-d^6) of **124**.*

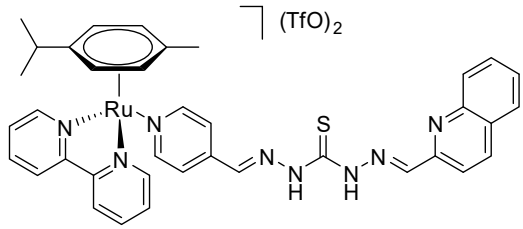

[(η^6-p-cym)Ru(N,N'-bpy)(N-4-formylpyridine-2-quinolinecarboxaldehydethiocarbohydrazone)](SO$_3$CF$_3$)$_2$(125): 122 (0.10 g, 0.13 mmol) and **100** (0.03 g, 0.13 mmol) were dissolved in 20 mL of tetrahydrofuran dry in a Schlenk flask in nitrogen atmosphere. The mixture was stirred for 24 hours at room temperature covering the flask with aluminium foil to keep the solution in the dark. The mixture was then microfiltered on celite and the solvent of the clear solution obtained was removed under reduced pressure. Finally, the solid obtained was washed three times with diethyl ether and dried under *vacuum*. Orange solid. Yield: 82%. ^{1}H NMR (δ, ppm, 400 MHz, acetone-d^6): 0.84 (d, *J* = 6.9 Hz, 6H), 1.82 (s, 3H), 2.48 (m, 1H), 6.26 (d, *J* = 6.4 Hz, 2H), 6.69 (d, *J* = 6.4 Hz, 2H), 7.67 (m, 2H), 7.82 (m, 2H), 8.05 (m, 6H), 8.41 (m, 4H), 8.46 (s, 1H), 8.49 (s, 1H), 9.89 (m, 2H), 12.21 (sb, 1H), 12.58 (sb, 1H). ESI-MS (+) [M-TfO$^-$]$^+$ m/z calc. 874.96 found 875.35.

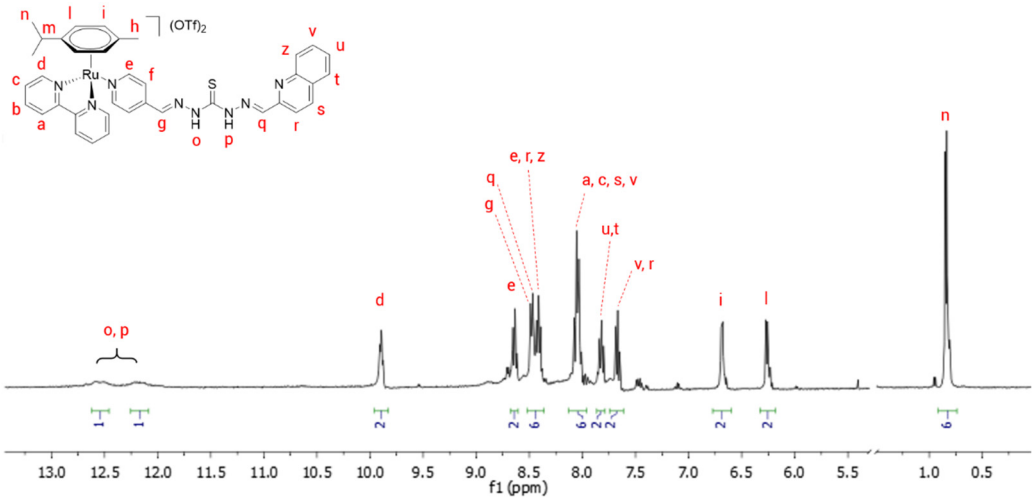

*^{1}H-NMR spectrum (400 MHz -acetone-d^6) of **125**.*

12.2 Biological test protocols

12.2.1 Cytotoxicity assessment

Drug effects on cell viability were analysed using a 3-(4,5-dimethylthiazol-2-yl)-2,5-diphenyltetrazolium bromide (MTT) colorimetric assay, based upon the ability of metabolically active cells to reduce MTT into formazan by the action of mitochondrial dehydrogenases. A549 (70,000 mL^{-1}), HeLa (75,000 mL^{-1}) and U937 (150,000 mL^{-1}) were seeded into 96-well plates overnight, and then exposed to compounds at indicated concentrations. At the end of the treatment, MTT was added (final concentration 0.5 mg/mL) for 3 hours at 37°C and formazan crystals were dissolved in 100 mL for each well of acidic isopropanol (0.08N HCl). After mixing, absorbance was evaluated using a Multiskan Ascent microwell plate reader equipped with a 550 nm filter (Thermo Labsystems, Helsinki, Finland). At least three independent experiments were performed with eight replicate wells per sample. The half maximal inhibitory concentration (IC_{50}) was determined as the concentration resulting in 50% cell growth reduction compared with untreated control cells.

Hypoxic treatments

During hypoxic experiments A549 cells were grown for 24 hours in an Anaerocult Cs mini system or in an Anaerobic Jar (Merck Millipore, Darmstadt, Germany) in which a hypoxic environment (oxygen concentration less than 7%) was produced. Hypoxia was confirmed by the colour change of the Anaerotests strip indicator (Merck Millipore, Darmstadt, Germany) located in the bag or jar.

Cell light irradiation

The evaluation of the effect of the photoactivation of our drug in cells were assayed by irradiating cells with an Auraglow Blue LED lamp (5 watt) for defined period, namely 0.5, 1.0, 1.5, 2.5, 3.0 and 24 hours. Since the exposure time of the sample was 24 hours, the cells were initially irradiated and then led in the dark for the remaining period. The effect

of the drugs at every irradiation time were determined using irradiated but not treated cells as a control in order to eliminate the potential effect of light on cells.

12.2.2 Cell cycle analysis

Flow cytometry was used to evaluate the cell phase distribution by determining the nuclear DNA content according with our published method[166]. Briefly, cells were collected, washed in PBS, and fixed in ethanol (96%) before staining with propidium iodide (PI 20 mg/mL in PBS containing RNase-A). Cells were sorted in a FC500t flow cytometer (Beckman Coulter, Brea, CA, USA), and percentages of cellular phases were calculated using FlowJo software (Ashland, OR, USA).

12.2.3 Assessment of apoptosis

Apoptosis in both the A549 and U937 cells was evaluated by using the annexin V–PI method. Briefly, cells exposed to different concentrations of compounds for 24 h were washed in PBS, incubated with annexin V–FITC and PI at room temperature for 15 min in the dark and analyzed using a FC500t flow cytometer (Beckman Coulter, Brea, CA, USA). The data analysis was performed using *FlowJo* software (Ashland, OR, USA). Apoptosis was calculated as the percentage of early and late apoptotic cells. Apoptosis analysis was completed by the quantification of caspase activity using fluorometric assay kits, according to the manufacturers' protocols. Cell lysates were incubated in the reaction buffer with the corresponding substrates: Ile-Glu-Thr-Asp (IETD)–AFC (7-amino-4-trifluoromethyl coumarin) for caspase-8, Leu-Glu-His-Asp (LEHD)–AFC for caspase-9 and rhodamine 110 bis-(N-CBZ-L-aspartyl-L-glutamyl- L-valyl-L-aspartic acid amide) (Z-DEVD-R110) for caspase-3. Enzymatic cleavage of the substrates produced fluorescent probes, which were quantified using a *Cary Eclipse* fluorescence spectrophotometer (Varian, Inc., Palo Alto, CA, USA). Enzymatic activity was referred to the protein content and expressed as the percentage of unexposed control.

12.2.4 Flow cytometry

Analysis of autophagy and in-cell fluorescence measurements

Autophagic activity at the cellular level was assessed using flow cytometry and fluorescence microscopy using a commercial assay, according to the producer's procedures. To quantitatively analyse autophagy, the cells were treated with compounds in the presence or absence of 3-methyladenine (3MA) (10 mM). After 24 h of treatment, the cells were collected, washed with PBS and subsequently incubated for 30 min at 37°C in the dark with the Cyto-ID Green Detection Reagent, diluted in culture medium without phenol red indicator and supplemented with 5%FBS. The probe was then removed via centrifugation and washed with PBS and the resuspended cells were immediately analyzed using a FC500t flow cytometer (Beckman Coulter, Brea, CA, USA). Analysis was performed using *FlowJo* software (Ashland, OR, USA). Flow cytometry allowed the monitoring of the changes in cellular physical parameters (SSC and FSC). To visualize autophagic vacuoles, lung cancer adherent cells were stained with the same specific autophagosome marker. Briefly, A549 cells were seeded and cultured on microscopy slides to approximately 70% confluence, before treatment with complexes at indicated concentrations. Untreated cells were used as negative controls. After 24 hours cells were carefully washed, and the dye diluted in assay buffer containing FBS 5% was applied to the slides for 30 minutes at 37°C. Then the cells were washed and fixed with 4% paraformaldehyde for 20 minutes before nuclear staining with DRAQ5s (Cell Signalling Technology, Danvers, MA, USA). The sample were observed using a confocal system (LSM 510 Meta scan head integrated with the Axiovert 200 M inverted microscope Carl Zeiss, Jena, Germany) with a 63x/1.30 oil objective. Image acquisition was carried out in the multitrack mode, namely through consecutive and independent optical pathways.

The flow cytometry was used also to monitor the changes in the cell internal fluorescence after the treatment with photoactivatable drugs. The procedure applied was the same used for the autophagic analysis and the emission signals was recorded using the FL1 detector. The analysis of the data was performed using *FlowJo* software (Ashland, OR, USA).

12.2.5 Oxidative stress measurement

The effects of compounds tested on intracellular redox equilibrium were assessed by the measurement of reactive oxygen species (ROS) and of lipid peroxidation. The generation of ROS in the cells following treatment was determined using 2,7-dichlorodihydrofluorescein diacetate (H2-DCFDA). The process involves elimination of the acetate groups (non-fluorescent) by intracellular esterases. DCFH can react with intracellular ROS to form the highly fluorescent 20,70-dichlorofluorescein (DCF). The cells were pre-treated for 30 minutes with H2-DCFDA (working concentration 10 mM) and rinsed with PBS before a brief incubation (30–60 minutes) with the tested compounds. After washing with PBS, the fluorescent cells were evaluated using a FC500t flow cytometer (Beckman Coulter, Brea, CA, USA) and data analysis was performed using *FlowJo* software (Ashland, OR, USA). The ''Thiobarbituric Acid Reactive Substances'' (TBARS) method is the validated assay chosen to evaluate lipid peroxidation: malondialdehyde (MDA) derived from polyunsaturated fatty acids condenses with two equivalents of thiobarbituric and the fluorescent product can be quantitatively evaluated using a *Cary Eclipse* fluorescence spectrophotometer (Varian, Inc., Palo Alto, CA, USA) (excitation 515 nm, emission 545 nm). The values were normalized for protein concentrations.

12.2.6 Protein determination

The BCA (bicinchoninic acid) Protein Assay was used for the colorimetric determination of protein concentration, according to the manufacturer's instructions. A standard curve of serial concentrations of bovine serum albumin was generated to cover the full assay range (0–200 mg/mL).

12.2.7 p53 analysis

Expression of p53 was assessed by using the specific FIT-Clabeled mouse monoclonal antibody anti-human p53. Adherent cells were fixed and permeabilized with a Per-Fix Kit, according to the manufacturer's instructions, and incubated with the fluorescent

antibodies for 30 minutes in the dark before flow cytometry analysis (FC500t flow cytometer, Beckman Coulter, Brea, CA, USA). Isotype controls were included.

12.2.8 Topoisomerase II inhibition *in vitro* test

The titration of topoisomerase II activity was made using the Human Topoisomerase II Assay Kit developed by *TopoGEN* following the protocol indicated by the manufacturer[167,168,169].

12.2.9 Statistical analysis

Data were analysed using GraphPad Prism v5 (GraphPad Inc., San Diego, CA, USA). The results are presented as the mean ± standard deviation of at least three independent experiments. Statistical analyses were carried out using one-way ANOVA, followed by Dunnett's or Turkey's *post hoc* tests. p values < 0.05 were considered as significant.

12.2.10 Metal uptake

Intracellular copper concentrations were determined over a 24-hour period of treatment in the cell lines U937 and A549. Briefly, the cell pellets were collected, re-suspended in 100 mL of water, freeze/thawed three times, and centrifuged (1200 g for 5 min). The supernatant was analysed by means of electrothermal atomic absorption with Zeeman effect background correction (ETAAS) using a Perkin Elmer Pin AAcle 900Z Atomic Absorption Spectrometer (Waltham, MA, USA). Certified standards were directly prepared in the supernatant of unexposed cells to reduce the matrix effect. The limit of detection (LOD), calculated as 3SD of the blank, was 0.5 mg/L. Cu concentrations were normalized for cell count and expressed as ng per 10^6 cells.

13 References

[1] *Patent - international*: C08F2/42; (IPC1-7): C08F1/82; C08F3/30.

[2] Ocean, A. J. et al. *Cancer Chemother. Pharmacol*. **2011**, 68(2), 379-88.

[3] Raman, N. et al. *Journal of Coordination Chemistry* **2009**, 691-709.

[4] Janardhan Reddy, J. et al. *Food Chemistry* **2007**, 101(2), 585-591.

[5] Vahma, H. S. et al. *J. Med. Chem*. **1967**, 10, 972–974.

[6] Padmanabhan, P. et al. *J Med Virol*. **2017**, 89(3), 546-552.

[7] Gingras, B. A. et al. *Pharmaceutical Sciences* **1965**, 54(11), 1674–1675.

[8] Degola, F. et al. Int. *J. Food Microbiol*. **2015**, 200, 104-111.

[9] Pelosi, G. *The Open Crystallography Journal* **2010**, 3, 16-28.

[10] Benns, B. G. et al. *Appl Microbiol.* **1960**, 8(6), 353-356.

[11] Araújo Neto, L. N. et al. *Chem Biol Interact.* **2017**, 272, 172-181.

[12] Brockman, R. W. et al. *Proc. Soc. Exp. Biol. Med*. **1970**, 133, 609-614.

[13] Shao, J. et al. *Mol. Cancer Ther*. **2006**, 5, 586-592.

[14] Hall, I. H. et al. *Pharmazie* **2000**, 55, 937-941.

[15] Yuan, J. et al. *Blood* **2004**, 104, 1450-1458.

[16] Richardson, D. R. et al. *J. Med. Chem.* **2006**, 49, 6510–6521.

[17] Kalinowski, D. S. et al. *J. Med. Chem*. **2007**, 50, 3716–3729.

[18] Jansson, P.J. et al. *J. Inorg. Biochem*. **2010**, 104, 1224–1228.

[19] Huang, H. et al. *J. Med. Chem*. **2010**, 53(8), 3048–3064.

[20] Zeglis, B. M. et al. *Med. Chem*. **2011**, 54(7), 2391–2398.

[21] Bisceglie, F. et al. *J Inorg. Biochem*. **2015**, 152, 10-19.

[22] Gorrini C. et al. *Nat. Rev. Drug. Discov*. **2013**, 12, 931–47.

[23] Malarz, K. et al. *Oncotarget*. **2018**, 9(25), 17689–17710.

[24] Sîrbu, A. et al. *Dalton Trans*. **2017**, 46, 3833-3847.

[25] Pessoto, F. S. et al. *Oxidative Medicine and Cellular Longevity* **2015**, 1-15.

[26] Biological Resource Center, NITE (NBRC).

[27] Bennett, J. W. et al. *Mycotoxins. Clin. Microbiol. Rev*. **2003**, 16, 497–516.

[28] Machida, M. et al. *DNA Res*. **2008**, 15, 173–183.

[29] ProAgrica database (https://www.allaboutfeed.net)

[30] Probst, C. et al. *Appl. Environ. Microbiol.* **2007**, 73, 2762–2764.

[31] Kabak, B. et al *Crit. Rev. Food Sci. Nutr*. **2006**, 46, 593–619.

[32] N.J. Mitchell. N.J. et al. Chem. Anal. Control Expo Risk Assess. **2016**, 33(3), 540–550.

[33] Wu., F. et al. *Toxin Reviews* **2008**, 27, 203–225.

[34] Thakare et al. *Sci. Adv*. **2017**, 3.

[35] Huvenne, H. et al. *J. Insect Physiol*. **2010**, 56, 227–235.

[36] Fairbairn, D. J. *Planta* **2007**, 226, 1525–1533.

[37] Yin, Y.N. et al. *Univ. Sci. B* **2008**, 9, 787–92.

[38] Degola, F. et al. *Int. J. Food Microbiol.* **2011**, 146, 235–243.

[39] Schmidt-Heydt, M. et al. *Int. J. of Food Microbiol.* **2013**, 166.

[40] Martin, D. et al. *Journal of Food Protection* **1982**, 45, Vol. 45(6), 519-526.

[41] Zjalic, S. et al. *Int. J. Food Microbiol.* **2006**, 107, 243–249.

[42] Tolaini, V. et al. *Int. J. Food Microbiol*. **2010**, 138, 243–249.

[43] Reverberi, M. et al. *Appl. Microbiol. and Biotechnol*. **2005**, 69, 207–215.

[44] Kim, J. et al. *Int. J. of Food Microbiol.* **2008**, 122, 49–60.

[45] Perrone, G. et al. *J. Agric. Food Chem*. **2007**, 55, 6807–6812.

[46] Chkuaseli, A. et al. *Annals of Agrarian Science* **2016**, 14(4), 295-298.

[47] Timothy, D. et al. *Natural Toxins* **1995**, 3(4), 204-213.

[48] Edrington, T. S. et al. *Toxicol. Lett*. **1996**, 89(2), 115-22.

[49] Ramírez, C. et al. *Fungal Biology* **2012**, 116(3), 452-463.

[50] Klich, M. *Mycologia* **2002**, 94, 21–27.

[51] Williams, J. H. et al. Am. Soc. Clin. Nutr. **2004**, 80, 1106–1122.

[52] Pietri, A. et al. *Food Addit. Contam.* **2004**, 21, 479–487.

[53] EFSA Opinion. *EFSA J.* **2004**, 89, 1–35.

[54] Geiser, D. M. et al. *Fungal Genet. Biol.* **2000**, 31, 169–179.

[55] *Agricultural Research Service (NRRL)*, Culture Collection Peoria.

[56] Ishikawa, A. T. *Toxins* **2017**, 9(11), 374.

[57] Newberneand, P. M. et al. *Cancer Research,* **1969**, 29, 236-250.

[58] Johnson, W. W. et al. *PNAS* **1997**, 94(12), 6121–6125.

[59] Fostera, P. L. et al. *Encyclopedia of Genetics*, **2001**.

[60] Chawanthayatham, S. et al. *PNAS* **2017**, 114(15), 3101-3109.

[61] Dunn, J. J. *Envirometal Mutagenesis* **1982**, 4, 19-2.

[62] Benns, B. G. et al. *Appl Microbiol.* **1960**, 8(6), 353-356.

[63] De Araújo Neto, L. N. et al. *Chem Biol Interact.* **2017**, 272, 172-181.

[64] Cuero, R. et al. *J Appl Microbiol*. **2005**, 98(3), 598-605.

[65] Holmes, R. A. et al. *Appl Microbiol Biotechnol.* **2008**, 78(4), 559-572.

[66] Wolber, G. et al *The Practice of Medicinal Chemistry – Chapter 21 (IV Edition)* **2015**, 489-510.

[67] Chang, P. K. et al. *Mycopathologia* **2002**, 153(1), 41-48.

[68] Grant, W. F. et al. *Mutation Research* **1982**, 99(6), 273-91.

[69] Chauhan, L.K.S. et al. *Environmental and Experimental Botany* **1999**, 42, 181-189.

[70] Shreaz, S. et al. *Fitoterapia* **2016**, 112,116–131.

[71] Xie, X. M. et al *Food Sci*. **2004**, 25, 32–34.

[72] Huang, L. et al. *J Mol Biol.* **2005** 351(3), 573–597.

[73] Sakuda, S. et al. *Toxins* **2014**, 6(4), 1193-200.

[74] De Graaf C. et al. *J. Med. Chem*. 48 **2005** 2308-2318.

[75] Nissink, J.et al. *Proteins: Structure, Function, and Genetics* **2002**, 49, 457-471.

[76] Kyte, J. et al., *J Mol Biol.* **1982**, 157(1), 105-132.

[77] Verdonk, M. L. et al. *Proteins: Structure, Function, and Genetics* **2003**, 52, 609–623.

[78] Eldridge, M. D. et al. *Journal of Computer-Aided Molecular Design* **1997**, 11(5), 425-445.

[79] Christensen, A et al. *PNAS* **2015**, 112(36), 11407-11412.

[80] Schaller, A. et al. *Phytochemistry* **2009**, 70, 1532–1538.

[81] Matsui, R. et al. *Scientific Reports* **2017**, 7, 6688, 1-9.

[82] Georgiou, C. D. et al. *Integrative and Comparative Biology* **2006**, 46(6), 691-712.

[83] Wilkinson, J. et al. *Chemistry and Biology* **2001**, 8(12), 1197-1208.

[84] Yolande, A. et al. *Nat Prod Rep*. **2009**, 26(1), 90–114.

[85] Zhang, Y. Q. et al. *Genetics* **2004**, 168(2), 785-794.

[86] Degola, F. et al. *Int. J. Food Microbiol.* **2011**, 146(3), 235-43.

[87] Degola, F. et al. *Letters in Applied Microbiology* **2012**, 55, 82–89.

[88] Choi, C. W. et al. *Plant Sci* **2002**, 163, 1161–1168.

[89] Kim, J. H. et al. *Appl. Microbiol. Biotechnol*. **2005**, 67, 807–815.

[90] Baruffini, E. et al. *Methods* **2010**, 51, 426–436.

[91] Maron, D. M. et al. *Mutat. Res.* **1983**, 113(3-4), 173-215.

[92] Mortelmans, K. et al. *Mutat. Res.* **2000**, 455(1-2), 29-60.

[93] Basrai, M.A. et al. *Microbiology* **1995**, 141(5), 1147-56.

[94] Cabaravdic, M. *Med. Arh.* **2010**, 64(4), 215-8.

[95] Bradford, M. M. et al. *Anal. Biochem* **1976**, 72, 248–254.

[96] Livak, K. J. et al. *Methods* **2001**, 25, 402–408.

[97] Jones, G. et al. *J. Mol. Biol.* **1997**, 267, 727-748.

[98] Eldridge, M. D. et al. *J. Computer-Aided Mol. Des.* **1997**, 11, 425-445.

[99] Baxter, C. A. et al. *Proteins* **1998**, 33, 367-382.

[100] Zhao, H. et al. *Gold Bulletin* **2001**, 34(1), 24–29.

[101] Dollwet H. H. A. et al. *Trace Elements in Medicine* **1985**, 2(2), 80-87.

[102] Debus, A. G. *Paracelsus and the Medical Revolution of the Renaissance* **1998**.

[103] Dilruba, S. et al. *Cancer Chemother. Pharmacol*. **2016**, 77(6), 1103-24.

[104]Nardon, C. et al. *Anticancer Res.* **2014**, 34(1), 487-92.

[105] Vock, C. A. et al. *J. Med. Chem.* **2007**, 50(9), 2166–2175.

[106] Ndagi, U. et al. *Drug Des. Devel. Ther.* **2017**, 11, 599–616.

[107] Rosemberg, B. et al. *Nature* **1965**, 205, 698.

[108] Stein, A. et al. *Expert. Opin. Pharmacother.* **2012**, 13(1), 125-37.

[109] Lentz, F. et al. *Anti-Cancer Drugs*. **2009,** 20(2), 97–103.

[110] Hartinger, C. G. et al. *Chemistry & Biodiversity* **2008**, 5(10): 2140–55.

[111] Wang, Y. et al. *Angew. Chem. Int. Ed. Engl.* **2015**, 54(35), 10230-10233.

[112] Cattaruzza, L. et al. *Int. J. Cancer*. **2011**, 128(1), 206-215.

[113] Health Effects of Excess Copper – Chapter 5, *National Academies Press (US)*, 2000.

[114] Health Effects of Excess Copper – Chapter 7, *National Academies Press (US)*, 2001.

[115] Koňarikováa, K. et al. *Pharmacological Reports* **2016**, 68(6), 1221-1224.

[116] Tabti, R. et al. *Med. Chem L.A.* **2017**, 7-5.

[117] Schnegg, A. et al. *Proceedings of the 3rd Intern. Symposium* **1978**, 236–243.

[118] Zambelli, B. et al. *Interrelations between Essential Metal Ions and Human Diseases – Chapter 10* **2013**, 321-357.

[119] Lauria, A. et al. *Dalton Trans.* **2014**, 43(16), 6108-6119.

[120] Dally, H. et al. *Carcinogenesis* **1997**, 18(5), 1021–1026.

[121] Lloyd, D. R. et al. *Mutat. Res.* **1999**, 424, 23-36.

[122] Pelosi, G. *The Open Crystallography Journal* **2010**, 3, 16-28.

[123] Bisceglie, F. et al. *Journal of Inorganic Biochemistry* **2014**, 140, 111-125.

[124] Bisceglie, F. et al. *Metallomics* **2013**, 5(11), 1510-1518.

[125] Buschini, A. et al. *Metallomics* **2014**, 6, 783-792.

[126] Helm, L. et al. *Chem. Rev*. **2005**, 105, 1923–1959.

[127] Degola, F. et al. *Int. J. Food Microbiol.* **2015**, 200, 104-111.

[128] Bisceglie, F. et al. *J. Inorg. Biochem*. **2015**, 152, 10-9.

[129] Zhang, H. et al. *J Biol Inorg Chem*. **2008**, 13(1), 47-55.

[130] Medina, R. A. et al. *J. Nucl. Med.* **2015**, 56, 921–926.

[131] Tanya, M. et al. *Seminars in Cancer Biology* **1998**, 8(5) 359-368.

[132] Tasdemir, E. et al. *Autophagy* **2008**, 4(6), 1-5.

[133] Shalini, S. et al. *Cell Death & Differentiation* **2015**, 22(4), 526–539.

[134] Sugimoto, K. et al. *Blood* **1992**, 79, 2378–2383.

[135] Lipinski, C. A. *Drug Discov. Today Technol*. **2004**, 1(4), 337-341.

[136] Thakur, D. et al. *Int. J. Pharm. Sci. and Nanotech.* **2011**, 4, 1173-1181.

[137] Zhang, Y. et al. *Acta Pharm. Sinica B*, **2018**, 8(1), 34-50.

[138] Singh, R. et al. *Exp Mol Pathol.* **2009**, 86(3), 215–223.

[139] Mroz, P. et al. *Cancers* **2011**, 3(2), 2516-2539.

[140] Oleinick, N.L et al. *Advances in Photodynamic Therapy: Basic, Translational and Clinical* **2008**, 115-133.

[141] Sun, Y. et al. *Mol. Pharmaceutics* **2018**, 15 (8), 3404–3416.

[142] Howerton, B. S. et al. *J. Am. Chem. Soc.* **2012**, 134(20), 8324-8327.

[143] Betanzos-Lara, S. et al. Organometallics **2012**, 31, 3466–3479.

[144] Tandon, R. et al. Chem. Rec. **2017**, 17, 956-993.

[145] Jia, X. et al. *Pure Appl. Chem.* **2014**, 86, 1237-1246.

[146] Gopikrishna, P. et al. *ACS Appl. Mater. Interfaces* **2018**, 10, 12081-12111.

[147] Rettig, M. et al. *Biomol.Chem.* **2010**, 8, 3179-3187.

[148] Bacchi, A. et al. *Chem. Select* **2017**, 2, 7000–7007.

[149] Yildirim, H. et al. Materials Science and Engineering: C 2014, 1-8.

[150] Fernández, M. et al. *Journal of Inorganic Biochemistry* **2015**, 153, 306–314.

[151] Floyd, A. et al. *Inorg Chem Commun.* **2009**, 12(11), 1094–1098.

[152] A. Gatti, et al. *Organometallics* **2018**, 37(6), 891–899.

[153] Duke, R. M. et al. *Chem. Soc. Rev.* **2010**, 39, 3936–3953.

[154] Grepioni, F. et al. *Journal of Materials Chemistry C* **2015**, 3, 9425.

[155] Tönnemann, J. et al. *Eur. J. Inorg. Chem*. **2013**, 4558–4562.

[156] Borenfreund, A. et al. *Annals of the New York Academy of Sciences* **1975**, 164- 171.

[157] Meenakshi, A. et al. *Mater Methods* **2013**, 3, 175.

[158] Kim, J. et al. *Chem. Eur. J.* **2013**, 19, 14768–1477.

[159] Díaz-Torres, R. et al. *Dalton Trans.* **2011**, 40, 10742.

[160] Sigel, A. et al. *Metallo-Drugs: Development and Action of Anticancer Agents* **2018**, 188-190.

[161] Tripathy, S. K. et al. *Dalton Trans.* **2014**, 43, 14546-14549.

[162] Kalayd, G. V. et al. *J. Med. Chem.* **2005,** 48, 16, 5191-5202.

[163] Christlieb, M. et al. *Dalton Trans*. **2007**, 5043–5054.

[164] Lukmantara, Y. et al. *Journal of Inorganic Biochemistry* **2014**, 141, 43-54.

[165] Singh, G. et al. *Inorganica Chimica Acta*, **1990**, 170, 177-180.

[166] Alinovi, R. *Toxicol. In Vitro* **2015**, 29, 426–437.

[167] Gardner, L. et al. *Breast Cancer Research* **2011**, 13(3), R53.

[168] Bower, J. J. et al. *Oncogene* **2010**, 29(34), 4787-4799.

[169] Polycarpou-Schwarz, M. et al. *Cancer Research* **2007**, 67, 4451-4458.

Acknowledgements

Bioinorganic lab members:

Prof. Giorgio Pelosi

Prof. Franco Bisceglie

Dott. Nicolò Orsoni

Other colleagues:

Prof. Mauro Carcelli, Prof. Paolo Pelagatti, Dott.ssa Dominga Rogolino, Prof. Francesco M. Restivo, Dott.ssa Francesca Degola, Dott. Giorgio Spadola, Dott.ssa Rossella Alinovi, Dott.ssa Silvana Pinelli, Dott.ssa Annamaria Buschini and Dott.ssa Serena Montalbano

Dott.ssa Claudia Zani and Dott.ssa Donatella Feretti

Prof. Peter J. Sadler

Dr. Isolda Romero-Canèlon

Dr. James Coverdale

Hannah E. Bridgewater

Prof. Guy Clarkson

Funding

Fondazione CARIPLO
TUTE SERVARE MUNIFICE DONARE • 1816

Rotary Club Parma Est

Instruments and analysis

UPO
UNIVERSITÀ DEL PIEMONTE ORIENTALE

Elemental analysis

Chiesi

X-ray facilities

CIM

NMR facilities

The end

Ma è davvero la fine?

Quando penso agli ultimi tre anni non mi sembra vero che il tempo sia volato così in fretta! Mi sembra davvero ieri quando sono entrata per la prima volta "da dottoranda" nel lab083. Mi sentivo proprio come all'inizio di avventura, e così è stata! Tre anni pieni, vivi, che mi hanno cambiata tantissimo. Mi hanno fatta crescere, o almeno avere un po' più consapevolezza di me, dei miei limiti e dei miei punti di forza. Il dottorato è un percorso e durante il mio percorso ho avuto la fortuna di fare tantissime esperienze diverse e soprattutto di conoscere tantissime persone meravigliose. Ognuna di queste persone mi ha lasciato qualcosa che porterò con me per sempre. Ciò che mi mancherà di più sarà l'ambiente famigliare del caro lab083, Franco, Nico e tutte le ragazze e i ragazzi che son passati da noi. Ma soprattutto mi mancherà l'avere una guida come Giorgio che mi ha sempre lasciata libera di essere me stessa, senza imposizioni, ma presente e alleato. Mi mancheranno tantissimo i gesti quotidiani, le pause caffè, le risate con i ragazzi dello stanzino, tutti quei momenti che rendono un luogo tuo.
Ho collezionato infiniti ricordi bellissimi, come il viaggio in Inghilterra. Sei mesi splendidi, la paura folle di partire, per poi scoprire che ovunque vai nel mondo, anche se sei da sola, basta un sorriso, una cena o un'uscita al pub e si costruiscono amicizie e legami indimenticabili. In questi tre anni sono successe tantissime cose, ma tra tutte sicuramente spicca l'aver conosciuto Nicolò, che mi ha cambiato la vita. Mi ha fatto capire che la vita non è sempre perfetta, ma sicuramente non può essere perfetta senza di lui. Adesso che questo viaggio è quasi terminato è ora di dire grazie. Grazie di cuore a tutte le persone incontrate durante questo cammino: lo avete reso davvero speciale, ma soprattutto grazie a tutti quelli che mi hanno supportato in ogni scelta e hanno sempre creduto in me.

"Nulla si crea, nulla si distrugge, ma tutto si trasforma" (A.L. Lavoisier).

Marianna